Advanced Electrode Models and Numerical Modelling for High Frequency Electrical Impedance Tomography Systems

Weida Zhang

A Thesis Submitted for the Degree of

Doctor of Philosophy

School of Engineering and Informatics

University of Sussex

February 2015

Declaration

I hereby declare that this thesis has not been and will not be, submitted in whole or in part to another University for the award of any other degree.

Signature:

Weida Zhang

Abstract

The thesis discusses various electrode models and finite element analysis methods for Electrical Impedance Tomography (EIT) systems. EIT is a technique for determining the distribution of the conductivity or admittivity in a volume by injecting electrical currents into the volume and measuring the corresponding potentials on the surface of the volume. Various electrode models were investigated for operating EIT systems at higher frequencies in the beta-dispersion band. Research has shown that EIT is potentially capable to distinguish malignant and benign tumours in this frequency band. My study concludes that instrumental effects of the electrodes and full Maxwell effects of EIT systems are the major issues, and they have to be addressed when the operating frequency increases.

In the thesis, I proposed 1) an Instrumental Electrode Model (IEM) for the quasi-static EIT formula, based on the analysis of the hardware structures attached to electrodes; 2) a Complete Electrode Model based on Impedance Boundary Conditions (CEM-IBC) that introduces the contact impedances into the full Maxwell EIT formula; 3) a Transmission line Port Model (TPM) for electrode pairs with the instrumental effects, the contact impedance, and the full Maxwell effects considered for EIT systems.

Circuit analysis, Partial Differential Equations (PDE) analysis, numerical analysis and finite element methods were used to develop the models. The results obtained by the proposed models are compared with widely used Commercial PDE solvers.

This thesis addresses the two major problems (instrumental effects of the electrodes and full Maxwell effects of EIT systems) with the proposed advanced electrode models. Numerical experiments show that the proposed models are more accurate in the high frequency range of EIT systems. The proposed electrode models can be also applicable to inverse problems, and the results show promising. Simple hardware circuits for verifying the results experimentally have been also designed.

Acknowledgments

I would like to thank many people for constantly supporting me for the past few years. First of all, I would like to thank my supervisors, Dr David Day-Uei Li and Prof Teng Long, for their guidance and support throughout the different stages of my doctoral study. They have been showing great enthusiasm for my work and offering positive advice. Without their invaluable help and generous encouragement, the present thesis would not have been accomplished.

Secondly, my special thanks go to Mr Rupert Lywood for funding on my research. Also the support given by Mr Stuart Lawson, Dr Charles Roberts, Dr Mike Cox and Dr Warris Bokhari from the investor's side, is immensely appreciated.

Thirdly, I appreciate the help and supervision given by Dr Phil Birch, Dr Helen Prance, Dr Rupert Young, Dr Daniel Roggen, Prof Chris Chatwin and Dr Lionel Ripley, during the four years of my study at the University of Sussex. I would also like to thank all the staff members from the department, and all the friends who have given me generous support and helpful advice during the past years. I have benefited a great deal from their suggestions.

Additionally, I would like to thank my friends Dr Nicolas Huber and Dr Mike Cox for proofreading some chapters of this thesis. Their helpful comments and advice are much appreciated. I am grateful for the encouragement from many, including Mr Michael He and Mr Chris Adams, and I hope they will become a PhD soon.

This work certainly wouldn't have been possible without the love and countenance from my family. I would like to dedicate this thesis to my beloved parents and girlfriend. Thank you for cheering me up on my bad days, for celebrating with me on the good days, and for loving me every day.

Table of Contents

List of Publications

Zhang, W. & Li, D., 2014. An instrumental electrode model for solving EIT forward problems. *Physiological Measurement,* 35(10), pp. 2001-2026.

Zhang, W. & Li, D., **to-be-submitted**. Inverse Problems for Instrumental Electrode Model of Electrical Impedance Tomography. *Electronics Letters.*

Zhang, W. & Li, D., **to-be-submitted**. Impedance Boundary Conditions for Electrodes in Electrical Impedance Tomography Forward Problems with Full Maxwell's Equations*., IEEE Transection on Biomedical Engineering.*

Zhang, W. & Li, D., **to-be-submitted**. Transmission Line Port Model for Electrical Impedance Tomography Forward Problems with Full Maxwell's Equations., *IEEE Transection on Biomedical Engineering.*

Li, D.-U., Poland, S., Coelho, S., Tyndall, D., **Zhang, W.**, Richardson, J., Henderson, R. & Ameer-Beg, S. 'Advanced Fluorescence Lifetime Imaging Algorithms for CMOS Single-Photon Sensor Based Multi-focal Multi-photon Microscopy,' in *the 35th Annual International Conference of the IEEE Engineering in Medicine and Biology Society (EMBC)*, Osaka, 2013.

Li, N., Xu, H., Wang, W. & **Zhang, W.** 'High-speed digital-controlled variable voltage source with current monitor for EIT application,' in *the 4th International Conference on Biomedical Engineering and Informatics (BMEI)*, Shanghai, 2011.

Zhang, W., Huber, N. & Wang, W. 'Modeling the Stainless Steel Electrode for EIT System of Saline Tank,' in *the 12th International Conference in Electrical Impedance Tomography (EIT-2011)*, Bath, 2011.

Li, N., **Zhang, W.**, Wang, W., Huber, N. & Xu, H. 'Bio-impedance Measurement Method Based on Digital Auto Balancing Bridge,' in *the 12th International Conference in Electrical Impedance Tomography (EIT-2011)*, Bath, 2011.

N. Béqo, N. Huber, R. Bilal, **W. Zhang**, G. Qiao and W. Wang, 'Fast method for artefact detection and breast boundary definition, ' in *The 12th International Conference in Electrical Impedance Tomography (EIT-2011)*, Bath, 2011.

List of Acronyms

ADC	Analogue-Digital Converter
BC	Boundary Condition
BMR	Breast Microwave Radar
BVP	Boundary Value Problem
CEM	Complete Electrode Model
DFT	Discrete Fourier Transform
ECT	Electrical Capacitance Tomography
EIDORS	Electrical Impedance and Diffuse Optical Reconstruction Software
EIT	Electrical Impedance Tomography
EMF	Electromagnetic Field
EMT	Electromagnetic Tomography
ENoB	Effective Number of Bits
ERT	Electrical Resistance Tomography
FEM	Finite Element Method
FFT	Fast Fourier Transform
GIC	Generalized Impedance Converters
GPR	Ground Penetrating Radar
IBC	Impedance Boundary Condition
IEM	Instrumental Electrode Model
LNA	Low Noise Amplifier
LS	Least Squares
MCMC	Markov Chain Monte Carlo
MIT	Magnetic Impedance Tomography (or Mutual Inductance Tomography)
MREIT	Magnetic Resonance Electrical Impedance Tomography
MWT	Microwave Tomography
NOSER	Newton's One-Step Error Reconstructor
PSD	Power Spectral Density
PEC	Perfect Electric Conductor
ODT	Optical Diffusion Tomography
OLS	Ordinary Least Squares
OpAmp	Operational Amplifier
RHS/LHS	Right/Left Hand Side (of an equation)
RMS	Root Mean Square

TPM	Transmission Line Port Model
TV	Total Variation
UWB	Ultra-Wide Band

List of Symbols

$\mathbf{E}, \mathbf{H}, \mathbf{X}$	Electric, Magnetic Field Intensity, or a field to present either $\mathbf{E}$ or $\mathbf{H}$ field
$\mathbf{D}$	Electric Displacement Field
$\mathbf{B}$	Magnetic Flux Density
$\mathbf{J}, \mathbf{M}$	Electric, Magnetic Current Density
$\mathbf{A}$	Vector Potential
Φ	Scalar Potential
ε	Permittivity Distribution
σ	Conductivity Distribution
μ	Permeability Distribution
ε^*	Admittivity (Complex Permittivity) Distribution
$\bar{}$	Complex Conjugate
t, f, ω, k	Time, Frequency, Angular Frequency and Wave Number
j	Imaginary Unit
ψ	Gauge Variable (Scalar Distribution)
v	Trial Function (Scalar Distribution)
$\phi_{i,j}$	Shape Functions (Scalar Distribution)
η	Contact Impedance
$\Omega, \partial\Omega$	3-D Region, Boundary of 3-D region
V, S, l	Volume, Area, Length
$\boldsymbol{S}, \boldsymbol{l}$	Vector Area, Vector Length
$\hat{\mathbf{n}}, \hat{\mathbf{t}_1}, \hat{\mathbf{t}_2}, \hat{}$	Unit Vectors
$U, I, \mathbf{Z}, G$	Voltage, Current, Impedance, Gain (Attenuation)

u, i	Voltage Noise Spectrum Density, Current Noise Spectrum Density
$\mathcal{n}, \sigma, \mu$	Gaussian Process, and its standard deviation and mean
t_0, f_s	Sampling Interval and Sampling frequency
$f_0, \omega_0, c_0, \varphi_0$	Frequency, Angular Frequency, Amplitude and Initial Phase of the Signal
n, k	Discretised Index in Time Domain, and in Frequency Domain
$\mathcal{F}\{x(t)\}$	Fourier Transform of $x(t)$
$r_{nn}(n)$	Autocorrelation Function
$S_{\mathcal{N}\mathcal{N}}(k)$	Power Spectral Density Function
k_B, T	Boltzmann's Constant and Temperature in Kelvin
q_0, Q_0	Quantisation Resolution, Total Quantisation Bits
$\mathbf{0}^{x\times y}, \mathbb{I}^x$	$x \times y$ Matrix of Zeroes, Identity Matrix of Size x
$\mathbb{C}^{x\times y}, \mathbb{R}^{x\times y}$	$x \times y$ Matrix of Complex or Real Entries
ξ_1, ξ_2, ξ_3	Variables of Barycentric Coordinate System
$\boldsymbol{A}, \boldsymbol{B}, \boldsymbol{C} \cdots$	Matrices (Single Character in Uppercase Bold Italic)
$[KK], [\boldsymbol{KK}]$	Matrices (Multi-Characters in Uppercase)
b, x, β	Vectors (in Lowercase)
$^\mathrm{T}, \ ^*$	Transport, Conjugate Transport of a Matrix
$\mathrm{u}_j, \Lambda_{xj}, \Lambda_{yj}, \Lambda_{zj}$	Discretised Scalar Potentials and Vector Potentials
n, N	Index and Total Number of Nodes
l, L	Index and Total Number of Electrodes
Γ_O	Reflection Coefficient

It is not the knowledge but the learning, not the possessing but the earning, not the being there but the getting there, which gives us the greatest pleasure.

- Carl Friedrich Gauss

Chapter 1 Introduction

The thesis discusses the electrode modelling for Electrical Impedance Tomography (EIT) systems. More accurate electrode models are proposed in the frequency range over which traditional models are not able to accurately describe the electrode.

This chapter provides a brief introduction to the field of study. The literatures are reviewed, the problems being investigated are stated here, as well as the contributions of this thesis. The background materials will be detailed in Chapter 2.

1.1 Characteristics and Classification

The Electromagnetic (EM) detection and imaging technique, is one of the major research areas which make uses of the electromagnetic fields or electromagnetic waves to obtain **medical images for diagnosis applications.** Different criterions are used for classifying the imaging techniques, including frequency ranges, radiators, target features, etc., or different types of algorithms as shown in Figure 1-1.

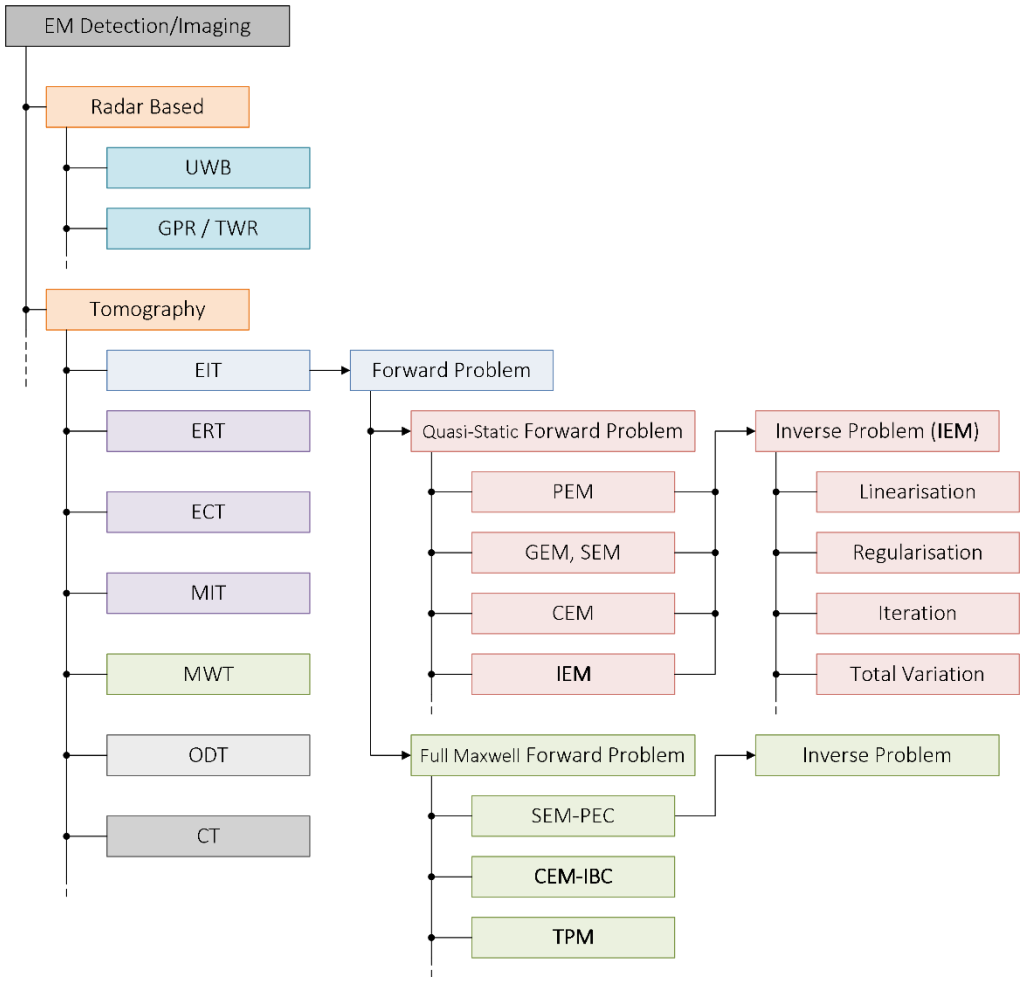

Figure 1-1 Divisions of Electromagnetic Detection and Imaging

The radar (RAdio-Detection-And-Ranging) based imaging methods, including Ultra-Wide Band (UWB) imaging methods, Through-the-Wall Radar (TWR) methods, etc. use the linear relationship between the target distances and the phase shift developed in the reflected signals to identify and localise the potential targets.

Tomography is to image by sections or slices. Generally, tomographic techniques are used to image the distribution of a specific property. For example, EIT is used to image the impedance distribution, while Computed Tomography (CT) is used to image the distribution of the *ability to block the X-ray beam*.

The tomographic techniques usually obtain images by evaluating the difference between the observation and the estimation. The estimation is obtained by solving the forward problem, which approximates the "observation" with a known image (e.g., typically start with an initial guess). The evaluation refers to the inverse problem, which feedbacks the difference to the observation to update the image.

Particularly, EIT (Barber & Brown, 1984; Webster, 1990; Metherall, et al., 1996; Cheney, et al., 1999; Saulnier, et al., 2001; Holder, 2005) is a technique for determining the distribution of the conductivity or admittivity in a volume by injecting electrical currents into the volume and measuring the corresponding potentials on the surface of the volume. A 3-D image of the admittivity distribution is generated by using inverse algorithms. The forward problem of EIT is capable of predicting the voltages on defined surface electrodes for a given admittivity distribution (Lionheart, 2004).

EIT is an important sub-division of the tomographic techniques. Other similar scenarios are using different excitations, or imaging different property distributions, or both. The Electric Resistance Tomography (ERT) (Daily, et al., 2004), is imaging the resistance distribution, while the Electric Capacitance Tomography (ECT) (Yang & Peng, 2003), is imaging the capacitance. Magnetic Induction Tomography (MIT) (Griffiths, 2001), is injecting magnetic fields or more precisely exciting the sample with the eddy current, and imaging the admittivity.

Microwave Tomography (MWT) (Semenov, 2009) has been investigated following the advances in numerical analysis, computational electromagnetism and inverse problems (such as EIT). The technique solves the full Maxwell's equations and obtaining all the three electromagnetic properties distributions.

However, although these scenarios have a similar tomography method to EIT, different forward problems and inverse problems are consequently performed based on the behaviours of the electromagnetic fields.

CT (X-ray CT) is the most commonly used tomographic technique. However, since the frequency of X-rays and visible light are too high, the forward problems of CT and also Optical Diffusion Tomography (ODT) degrade to projections (Herman, 2009). This property makes X-ray CT and ODT less in ill-posedness and better in imaging resolution. Magnetic Resonance Imaging (MRI) is another widely used medical imaging technique. Although it uses tomographic techniques in imaging, but MRI images the nuclear spinning instead of properties of electromagnetic fields, therefore is not discussed here.

Tomography techniques are unlike the radar based modalities, which aimed to detect the scatters and to locate the discontinuities of the intrinsic impedance. Tomography techniques obtain the property distributions as results.

However, the tomography techniques, such as EIT, MIT and MWT, have a number of disadvantages. As mentioned above, only the absorption that lies along the X-ray beam, affects the corresponding pixels in CT. This is a property of the modality called *local* (Holder, 2005). The EIT and other similar methods are *non-local*. At low frequencies, the excitation spreads all over the object non-linearly. Furthermore, the non-locality is deeply related to the ill-posed nature of the problem. The ill-posedness of the EIT means the uncertainties in the measurements taken on the boundary could map to an arbitrarily wide range of the admittivity causing artefacts easily. The features of the EIT and similar modalities, including non-local, non-linear and ill-posed, are resulting in that:

- Much lower resolution than modalities such as CT;
- Higher accuracy of observations is required;
- A priori information about the distribution is needed.

Due to the ill-posed nature of the inverse problem, the measureable information is insufficient for robust reconstruction of high-resolution admittivity images (Seo & Woo, 2011). The practical difficulties have led researches to searching for new ways to bypass the ill-posedness of the corresponding inverse problems. Dual-modality imaging methods such as ultra sound EIT, Magnetic Resonance EIT (MREIT) and Breast Microwave Radar (BMR) EIT etc., have been invested, and promising results have been obtained since 2008 (Hasanov, et al., 2008; Ammari, et al., 2008; Flores-Tapia, et al., 2011).

Overview and review of these modalities can be find in later sections.

1.2 Motivations

Researches have shown that a difference in admittivity and its spectrum between malignant and normal tissues can be observed in the beta dispersion band, the frequency range 0.1 MHz – 0.1 GHz (Schwan, 1957; Surowiec, et al., 1988; Gabriel, et al., 1996; Grimnes & Martinsen, 2008).

Dispersion is a phenomenon that the dielectric properties (permittivity) of materials are dependent on the frequency. The correspondent concept of dispersion in time domain is called relaxation. Permittivity is a measure of how much a material can be polarised, whereas relaxation is a measure of how fast it can be polarised (Grimnes & Martinsen, 2008).

Dispersions of biomaterials are divided in three groups based on different relaxation mechanisms: alpha-, beta-, and gamma-dispersion. The three groups are located at 100Hz, 1MHz and 10GHz on the frequency axis. For the gamma-dispersion being the fastest, its mechanism is considered as the polarisation of the dipoles *in* polar media such as water, solutions and proteins. The responses of the passive cell membranes, intracellular organelle membranes and the protein molecules, are the contributors to the beta-dispersion. Some other effects, mainly from large structures, are corresponding to the alpha-dispersion (Schwan, 1957).

A report (Surowiec, et al., 1988) about the dielectric properties of breast cancer tissues at the beta-dispersion band has been shown in Figure 1-2. The central and surrounding parts of the tumours are different from the normal tissues in both conductivity, permittivity and their spectrums. The possible interpretation is that, the cancer cells are different from normal ones for complicated and disorderly arranged membranes. These membranes correspond to the difference in the beta-dispersion band (Grimnes & Martinsen, 2008).

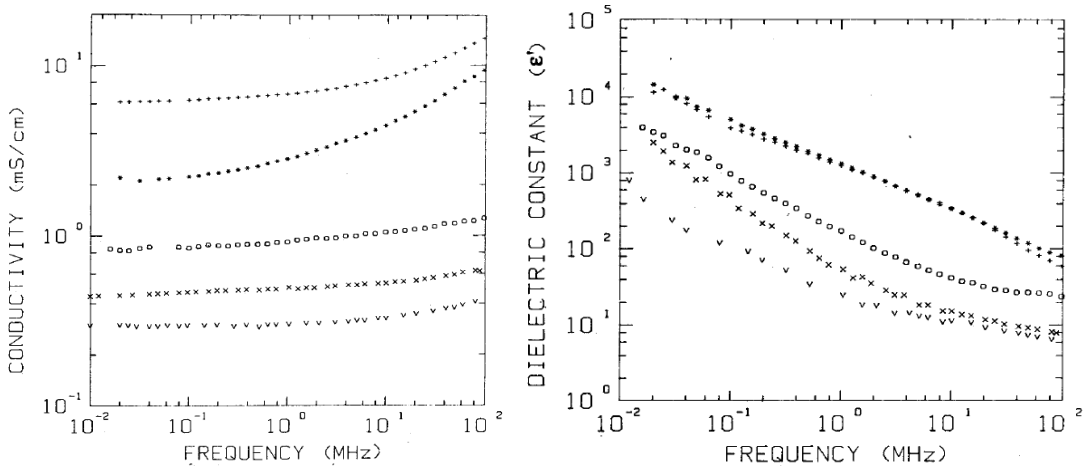

Figure 1-2 Beta Dispersion of Breast Cancer Tissue (*): central part of tumour; (+): tissue surrounding the tumour; (o): mainly fatty tissue containing infiltrating tumour cells; (x): peripheral sample located relatively far from central part of tumour; (v): normal breast tissue. Source: Dielectric Properties of Breast Carcinoma and the Surrounding Tissues (Surowiec, et al., 1988)

The dielectric properties of the breast tissues behave almost the same with water when the frequency is higher than the microwave band (300MHz – 300GHz). The distinguishability of the EM imaging modalities working at these frequency bands are therefore reduced.

For example, mammography, an X-ray based imaging technique widely used in breast cancer screening, provides overall high false-positive and false-negative rates, 5-15% and 10-50% respectively (Säbel & Aichinger, 1996). 40% and 26% of these rates were found in later reports (Bayford, 2006). Screening mammography is reported to be less sensitive for *dense* breast tissue in radiographic sense (Jackson, et al., 1993). Low contrasts in biological tissues of the X-ray to a variation less than 5%, has been reported and suspected to be the interpretation of the high false rates (Meeson, 1997).

Recent research results also show that malignant and benign can be distinguished using the low-microwave band up to 20GHz, lying in the gamma dispersion range. 10:1 contrast has been found in breast tissue samples which are adipose-dominant, however, only 10% difference were found between malignant and normal glandular/fibro-connective tissues (Lazebnik, et al., 2007).

The tomography imaging methods provide the electromagnetic properties in contrast to the radar based methods, which are obtaining reflection maps. The electromagnetic properties and the features in dispersion provide a foundation for EIT, MIT and MWT to detect cancerous tissues. Figure 1-3 provides a brief view of the frequency range used for different modalities of EM imaging. The EIT, ERT, ECT and MIT operate in the frequency range from a few kHz to a few MHz. The MWT has been reported to use over hundreds MHz (Meaney, et al., 2000). The radar

based techniques are using GHz range, while the ODT and CTs (including X-ray CT, PET and SPECT etc.) are using the frequencies up to the Gamma ray band.

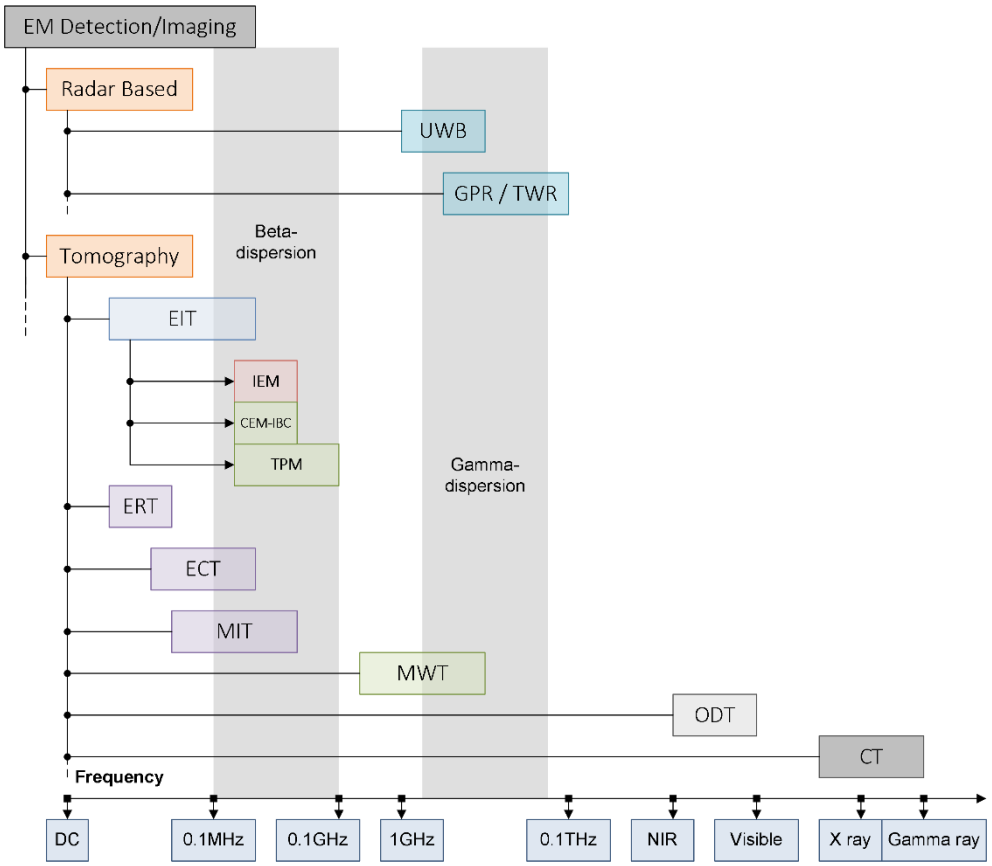

Figure 1-3 Frequencies Usage of Electromagnetic Detection and Imaging

In order to cover the beta-dispersion band, efforts have been made in extending the frequency range of EIT systems (or MIT systems). MWT uses the gamma dispersion band, has also attracted attention in recent years, for the potential of being capable of distinguishing different tumour types.

The motivation of this research is to investigate the flexibility of applying EIT systems in the whole beta-dispersion band. In this frequency range, EIT will be useful for cancer screening and diagnosis.

1.3 Literature Review and State-of-the-art

In this section, we will review the literature about EIT algorithms, EIT instruments, and also some of the similar modalities mainly tomography techniques and dual-modalities.

1.3.1 EIT Algorithms

The first EIT system was introduced in 1978, for obtaining impedance by spatial measurements of thorax (Henderson & Webster, 1978). 144 electrodes are placed as a square array on one

side of the body, with another large one on the other side. A complex impedance was measured, and a tissue impedance model was proposed as well. In 1980, Alberto Calderon's famous paper that laid the foundation for the mathematical study of the inverse conductivity boundary value problem (Calderon, 1980). However, it appeared only in a crudely typed conference proceeding, and was reprinted in Computational and Applied Mathematics in 2006.

Reconstructing the conductivity for medical imaging was first addressed in 1984 (Barber & Brown, 1984). A backprojection algorithm, which is similar to those used in CT, was proposed. A Finite Element Method (FEM) was first applied to EIT algorithms in 1985 (Murai & Kagawa, 1985).

Piecewise analytic conductivities can be determined by boundary measurements theoretically (Kohn & Vogelius, 1985) and was mathematically proved in 1985. A smooth complex conductivity distribution can be determined by boundary measurements with infinite precision if the distribution is isotropic (Sylvester & Uhlmann, 1987), and this was proved in the research of seeking complex geometrical optics solutions for Schrödinger equations.

Also in 1987, different algorithms are compared, and two are concluded to be most robust and efficient (Yorkey, et al., 1987): *Standard* (Yorkey, 1986) and *Compensation Theorem* (Murai & Kagawa, 1985). The two are found to be the same in later literatures with the Newton-Raphson method.

The distinguishability of conductivity was first defined and analysed (Isaacson, 1986). The criteria for determining the measurement precision and selecting current driving patterns, were presented. Similarly, the sensitivity and resolution of EIT were assessed (Seagar, et al., 1987). The smallest detectable object and contrast (to the background) were given by levels of noise in the measurements. Following the previous work, the spectral properties of the forward problem operators were analysed (Gisser, et al., 1990), and the work presents the way of choosing a proper driving pattern, electrode size and number of electrodes for EIT systems.

The instability of EIT problems was analysed (Breckon & Pidcock, 1988) using Singular Value Decomposition (SVD). A 2-D disc with driving electrode pairs has been found extremely ill-posed. The data errors that affect the EIT algorithms, were investigated using their Levenberg-Marquardt methods (Breckon & Pidcock, 1988).

A set of boundary conditions was first proposed for EIT forward problems, called the gap model in the later literatures (Wexler, 1988). The Complete Electrode Model (CEM) was proposed in 1989 to include the effect of the contact impedance (Cheng, et al., 1989). The

accuracy of 0.1% has been reported at the frequency of 15 kHz, whereas the previous researches using point, gap and shunt electrode models were struggled with the model accuracies. The existence and uniqueness of the forward problem solutions using CEM (Somersalo, et al., 1992) is proved in 1992.

Newton's One-Step Error Reconstructor (NOSER), which is the most commonly used approach based on Gaussian-Newton algorithm for EIT reconstruction, was proposed (Cheney, et al., 1990). The reconstructed conductivity was not accurate, however for the reason of one step (only one iteration), most of the calculation can be done prior to reconstructions.

A robust image reconstruction algorithm using Hachtel's augmented matrix has been proposed (Woo, et al., 1993), and it is found more accurate than the Newton-Raphson method (Yorkey, et al., 1987). Different from most iterative non-linear inverse methods, a single iteration algorithm was proposed (Somersalo, et al., 1991), which attempted to solve the conductivity from the boundary to inner layers by inserting *boundary* surfaces to the inner layers.

A priori information of the conductivity distribution, which is assumed to be blocky, was first incorporated into EIT formulations (Dobson & Santosa, 1994). The research led to the Total Variation (TV) regularised method, by applying Markov Chain Monte Carlo (MCMC) methods to solve the TV regularised inverse problems (Somersalo, et al., 1997). The efficient and stable solution of the TV regularised EIT problems was addressed later (Borsic, et al., 2001; Borsic, 2002).

An algorithm based on backprojection of Lagrange multipliers was proposed with experimental validations (Bayford, et al., 1995), which overcomes the ringing artefact in previous backprojection algorithms. A direct sensitivity matrix approach for fast 3-D image reconstruction was proposed (Morucci, et al., 1995) using the boundary element method (BEM).

3-D EIT experiments were performed with the Sheffield system (Brown & Seagar, 1987) based on the point electrode model (Metherall, et al., 1996). 3-D EIT experiments were then performed with cylindrical saline filled tank based on CEM, obtaining both difference and static images (Vauhkonen, et al., 1999).

A new method to include the prior information of the conductivities in the optimization algorithm was presented (Vauhkonen, et al., 1997). The method is compared with their later proposed (Vauhkonen, et al., 1998) Subspace Regularization Method (SSRM) together and the NOSER (single step) method (Cheney, et al., 1990). The SSRM was found to be better.

A Matlab toolkit was developed for 2-D reconstruction and released in 2000, called Electrical Impedance and Diffuse Optical Reconstruction Software (EIDORS). The later version of the EIDORS (Polydorides & Lionheart, 2002) supporting 3-D reconstruction was released in 2002.

The Nachman's proof, first introduced in 1996, says that the coefficients of 2-D elliptic equation (the governing equation of an EIT system) can be uniquely determined by the corresponding Dirichlet-to-Neumann map on the boundary. The D-Bar method was proposed (Mueller, et al., 2002) based on the Nachman's proof although only in 2-D but showing promising results, with a number of reports (Isaacson, et al., 2004).

Anisotropic smoothness constraints and spatial prior information were applied to the regularisation methods of EIT inverse problems. Better results were found than those using the identity regularisation, no worse results can be obtained using incorrect prior information comparing with those regularised with identity matrices (Kaipio, et al., 1999). The conductivity patterns can be still found in the reconstruction results even the patterns violated the prior information (Borsic, et al., 2002).

The EIT problem was brought in the framework of Bayesian statistics with MCMC integration methods for searching the maximum *a posteriori* estimate (Kaipio, et al., 2000). Research had been done to address the relation between the number of electrodes and the number of the mesh elements (Tang, et al., 2002). It concluded that increasing the electrode number improves the ill-posed conditions and the image areas closer to the boundary rather than the centre. It also concluded that increasing the mesh density worsens the ill-posed conditions.

A scheme, using the level set method for the representation of interface between regions with different conductivities (Chung, et al., 2005), was proposed upon the TV regularisation. An EIT reconstruction algorithm with 4D regularisation was proposed (Dai, et al., 2008) which took electrode movements into consideration as the 4^{th} dimension.

To take the advantage of beta dispersion, frequency-different EIT (fdEIT) was shown interesting. Feasibility study (Seo, et al., 2008) had been done and experiments (Jun, et al., 2009) were reported.

The full Maxwell's algorithm was proposed (Soni, et al., 2006) with simulation and experimental results for 2-D EIT. It followed the early investigations in MWT, and made a progress in numerically solving the Maxwell's equations (Paulsen, et al., 1992; Boyse & Paulsen, 1997). This algorithm is then applied to the EIT applications with full Maxwell's equations as forward problems.

A consensus linear reconstruction framework, called GREIT (Graz consensus Reconstruction algorithm for EIT) was proposed for lung EIT. The framework consists of: FEM models of a representative adult and neonatal thorax; consensus on the performance figures of merit for EIT image reconstruction; and a systematic approach to optimize a linear reconstruction matrix to desired performance measures (Adler, et al., 2009).

Different from the 4D regularisation, an approximation error approach was proposed to compensate for the modelling errors caused by inaccurately known body shape (Nissinen, et al., 2011). The approach was demonstrated with experimental data obtained with body movements. A sparsity regularisation incorporating with a Tikhonov functional was recently proposed with promising 2-D simulated results (Jin, et al., 2012), based on the assumption of sparsity of the inhomogeneity.

1.3.2 EIT Instruments

A number of EIT systems have been developed since the first EIT experiment was performed, including Sheffield Marks, OxB-ACTs, and ACTs, etc. These systems had been reviewed previously (Boone & Holder, 1996).

Multi-frequency EIT systems with voltage sources were demonstrated in 2004 (Halter, et al., 2004), and later improved in 2008 (Halter, et al., 2008), where calibration methods were proposed to increase the hardware accuracy. The “KHU Mark I” was developed in 2007 (Oh, et al., 2007) with the second version (Oh, et al., 2011) reported later in 2011. Parallel driving and measuring hardware were developed, with Generalized Impedance Converters (GIC) included for increasing the output impedance of the current sources to be larger than 1 MΩ at 495 kHz.

Hardware errors especially for multi-frequency EIT systems were reviewed (McEwan, et al., 2007) which concluding that the major sources of error are common-mode voltages, stray capacitance and contact impedance, all of which are frequency and load dependent.

1.3.3 Other Modalities and Dual-Modalities

Different modalities (from those using electrical current sources) were first proposed between 1992 and 1993 in a few conferences including MIT, Mutual Inductance Tomography (also MIT) and magnetiostatic permeability tomography or Electromagnetic Tomography (EMT) (Peyton, et al., 1996). A system was reported employing a parallel excitation magnetic field generated by two pairs of large coils (Yu, et al., 1993) and obtaining coarse images from experiments. A reconstruction algorithm based on general backprojection technique was used with forward problems solved by an experimental method. A fundamental work was carried out a year later

on the sensitivity of MIT (Dyck, et al., 1994), derived from Tellegen's theorem (Penfield, et al., 1970).

A single-channel MIT system operating at 10 MHz was detailed for measuring biomedical tissues (Griffiths, et al., 1999). Eddy currents were induced in the object, and images were reconstructed with a backprojection algorithm. A multi-coils system for MIT was reported later with experimental results (Korjenevsky, et al., 2000), operating at 20MHz with images reconstructed with the filtered backprojection algorithm. At that time, MIT was still using linear reconstruction methods such as backprojection. However, as an ill-posed non-linear problem similar to EIT, it was suggested to be solved non-linearly.

The developments of Ground Penetrating Radar (GPR) and edge FEM had advanced MIT technologies. The sensitivity matrix was deriving by an adjoint field method (Dorn, et al., 1999), whereas the forward problem is discretised from Maxwell's equations with finite-difference frequency-domain (FDFD) method. The edge-element FEM on vector and scalar potentials was first proposed (Bíró, 1999) for solving eddy current problems in the same year.

Based on the breakthroughs in GPR and edge FEM earlier, MIT forward problems with numerical solutions were reported (Merwa, et al., 2003), and Gaussian-Newton reconstruction algorithms were proposed (Merwa, et al., 2005) with simulation data. It followed by iterative reconstruction algorithm proposed (Soleimani & Lionheart, 2005) with numerical results, which solves the inverse problems of MIT non-linearly. Experimental results were reported (Soleimani, et al., 2006) with 3-D reconstructed images.

The MWT, however, was investigated following the introduction of ultra-sound diffraction tomography and X-ray CT. An algorithm called Born or Rytov approximations was proposed (Devaney, 1983) and used for electromagnetic imaging at microwave frequencies (Semenov, et al., 1998; Souvorov, et al., 1998). Although the inverse problems of MWT are using Newton iteration scheme similar to EIT, the solutions of the forward problems (called direct problems in MWT) are obtained from the approximation of Hankel functions (Bessel functions in 2-D). Another research following the progress made in hybrid element method, which solves the forward problems numerically, was reported (Meaney, et al., 1998). This is the first simplified version of the full Maxwell's EIT method.

The MREIT is a dual-modality imaging method, closely related to EIT and MRI. It adopted the current injection MRI techniques (Scott, et al., 1991) and magnetic resonance current density imaging (Scott, et al., 1992). In which, the magnetic flux densities in 3-D are detected to

reconstruct the induced current density under the quasi-static assumption. The induced current is corresponding to a low frequency bipolar current applied through electrodes.

Different algorithms are proposed for MREIT, including J-substitution (Kwon, et al., 2002; Khang, et al., 2002), current constrained voltage scaled reconstruction (Birgül, et al., 2003), equipotential line method (Kwon, et al., 2002) and current density impedance image (Hasanov, et al., 2008) method. All of these algorithms requires observation on the 3-D magnetic flux. In order to obtain all the components of magnetic flux, the object under test has to be rotated within the MRI scanner, which is causing mechanical difficulties.

The mechanical rotational-free MREIT method was proposed which requires the magnetic flux only on the axis direction (Seo, et al., 2003). This breakthrough allows the MREIT in vivo animal and human imaging experiments.

Another dual-modality algorithm, which obtained images using impedance tomography perturbed by ultrasound waves, was proposed (Ammari, et al., 2008), numerically illustrated and showing new directions for EIT applications.

Following the rapid developments in UWB techniques, the Breast Microwave Radar (BMR) has shown its advantages as free from ionizing radiation and breast compression. BMR has been reported to integrate with EIT in a dual-modality, in which BMR is to obtain the reflection structure and EIT is (to extract the) admittivity distribution (Flores-Tapia, et al., 2011).

1.4 Problems

EIT has been applied to cancer diagnosis applications. Recently, several image reconstruction methods have been proposed to enhance the EIT contrast, but only in the frequency range of tens of kHz (Seo, et al., 2008; Jun, et al., 2009; Ahn, et al., 2010; Harrach, et al., 2010). In order to fully use the beta-dispersion band (generally higher than the frequency range of most of the EIT systems) some issues in EIT instruments and algorithms need to be addressed.

There are two major problems in extending the operating frequency of EIT systems. Firstly, it is difficult to obtain accurate measurements from experimental devices when the operating frequency increases. The instrumental effects including non-idealities of the sources, parasitic capacitance (from the cables, connectors or the electrodes themselves), etc., start to degrade the measurement accuracy at frequencies larger than hundreds of kHz. Secondly, the Laplace equation used by the EIT forward problem is an approximation derived from Maxwell's equations (Boyse, et al., 1992; Paulsen, et al., 1992; Boyse & Paulsen, 1997; Soni, et al., 2006) .

The “irrotational electric field” approximation tends to fail when the frequency increases, as the quasi-static assumption is no longer valid (Sheng & Song, 2012).

For the first problem, we found that the boundary conditions (BCs) used for forward problems are not sufficient for system modelling in the low MHz band. There are different kinds of BCs used in the EIT forward problems, including the Gap Model (Boyle & Adler, 2010), Shunt Electrode Model (Boyle & Adler, 2010) and Complete Electrode Model (CEM) (Boyle & Adler, 2010; Cheng, et al., 1989; Somersalo, et al., 1992; Vauhkonen, et al., 1999). The CEM constrains the electrical currents flowing on the electrode surfaces and on the boundary of the imaging volume. It also includes the contact impedance on the electrode surface and therefore accounts for the voltage difference between the electrode and the outer surface of the imaging volume. It has been reported that the CEM can match experimental results with a very high precision up to 0.1% (Somersalo, et al., 1992). To reconstruct accurate images from *in vivo* data an accurate electrode model is usually required, and thus, the CEM is generally preferred (Boyle & Adler, 2010).

The CEM, however, assumes that the system hardware is ideal and therefore does not consider the loading effects of the current excitation sources or the voltage measurement components. This assumption is only valid at frequencies much lower than 1 MHz. Several research groups have described design implementations, simulations and experiment results using hardware with current source output impedances measured in MΩ at frequencies up to hundreds of kHz (Denyer, et al., 1994). Usually the input impedance of the front-end amplifiers in voltage measurement components (such as op-amp follower (Oh, et al., 2011) or instrumentation amplifier (Oh, et al., 2007)) is around several GΩ.

To overcome the first problem, the requirements for high output/input impedance of the excitation/measurement circuits pose a significant challenge in hardware implementation, especially at high frequencies, and therefore impose a limitation on the effective use of the forward model. Recent research efforts have been devoted to enhancing the output impedance of current sources, such as using driven shields and generalized impedance converters (GIC) (Ross, et al., 2003). It has been shown that a GIC can increase the output impedance up to 2MΩ at 495kHz (Oh, et al., 2011). Another method for modelling and optimising the hardware of EIT systems has been proposed (Hartinger, et al., 2006) using a Howland current source and a bootstrapped follower to model the hardware effects and optimise the parameters of the circuit, but it only improved the performance at frequencies less than 100kHz. An image reconstruction method has been reported in which hardware

effects were modelled through modification of the system matrix used for the inversion (Hartinger, et al., 2007). However, the reported operating frequency was much lower than 500kHz as there was no optimisation of the forward model.

Several calibration algorithms have been proposed for correcting the measurement errors caused by hardware non-idealities (McEwan, et al., 2006; Halter, et al., 2008; Holder, 2005; Oh, et al., 2007). These effectively compensate the instrumental effect on driving electrodes but it is difficult to remove all instrumental effects (including measuring electrode error) in the frequency range we are considering.

For the quasi-static approximation, which is the second problem mentioned earlier, a finite element analysis method derived from the full Maxwell equations (called the $\mathbf{A} - \Phi$ formulation or four-potential formulation) has been proposed (Soni, et al., 2006) and the formulations (which did not apply the quasi-static assumption) have been applied to voltage source based systems operating up to 10MHz (Halter, et al., 2004; Halter, et al., 2008). Being derived from the full Maxwell equations, the formulation is very computationally intensive compared to a Laplace formulation. A calibration method is used for compensating the instrumental effects (which also appear in voltage source systems). However, the electrodes used in their algorithm are not carefully considered. An electrode model similar to the shunt electrode model, but for the full Maxwell's formula, was used in the algorithm. This implies that neither the contact impedance nor the instrumental effect is considered. Research on contact impedance of electrodes has shown the impedance degrading while the frequency increases (Mirtaheri, et al., 2005), which suggests the effect of contact impedance can be small in the frequency range. However, instrumental effects are generally increasing, with skin effects and reflections start to appear in the frequency range. At a frequency as high as 10MHz, electrodes are not able to derive the current into the imaging object unless the impedance between electrodes pair are controlled specially.

It is worth noting that although the two previously mentioned problems are normally combined when operating in the MHz frequency range, they do not necessarily occur together. The instrumental effect is due to hardware non-idealities and depends on the parameters of the hardware alone, while the full Maxwell effect is caused by the quasi-static assumption and depends on the admittivity and permeability of the material, the overall system geometry, and the scale size. In all none of the two is definitely happening prior to the other while increasing the operating frequency.

Furthermore, for applications at high enough frequencies (in the beta-dispersion range still), both the instrumental effects and the full Maxwell effect need to be addressed.

1.5 Objectives and Contributions

The research aims to address the two major problems stated in the previous section: 1) to investigate the electrode models and 2) to build a numerical model for the proposed electrode models for high frequency EIT systems.

The *high frequency* regards the frequencies that are higher than the frequency a general EIT system can obtain stable images, and it is supposed to be in the beta-dispersion band. A frequency range from 500 kHz to tens of MHz is to be covered.

The contributions of the research can be summarised as follows:

- An Instrumental Electrode Model (IEM) is proposed for general EIT forward problems, with instrumental effects considered; ('General' here refers to EIT algorithms with the quasi-static assumption.)
- A full Maxwell version of CEM, using Impedance Boundary Conditions (IBC), is proposed for full Maxwell EIT forward problems;
- A Transmission line Port Model (TPM) is proposed for full Maxwell EIT forward problems;
- An EIT inverse formula incorporated with IEM is derived and proposed with simulated results.

From Figure 1-1, there are two types of forward problems following the EIT block. The IEM is one of the electrode models that can be used for quasi-static EIT forward problems. The CEM-IBC and TPM are two models suitable for full Maxwell EIT forward problems. The IEM together with other forward problems lead to inverse problems, and a particular one derived from IEM is plotted with a block. The full Maxwell EIT forward problems also lead to their own inverse formulas, however these are not included in the research and are not detailed in the figure.

The proposed IEM considers the effects on the potential distribution in the volume caused by hardware non-idealities, especially at frequencies larger than 500 kHz. An extra boundary condition is introduced accordingly to the CEM in the forward problem. The IEM can provide a much more accurate representation of the overall system including instrumental effects introduced by the hardware (the first problem mentioned).

The CEM-IBC brought the CEM into forward problems of the full Maxwell EIT formula. The formula considers the full Maxwell effects which quasi-static approximation is not able to handle when the frequency increases (the second problem mentioned). The proposed CEM-IBC on four-potential is applied to the electrode surface to enable the contact impedance being included in the full Maxwell EIT formula.

The TPM is the model of electrode pairs in full Maxwell EIT formula. It is to model the surface of the transmission-line type of electrode pairs as well as the port impedance in between them. The pair has to be formed a transmission line port, so that the electromagnetic wave propagating in the line can reach the imaging object with the characteristic impedance well defined. This model considers the two problems mentions together.

From Figure 1-3, general EIT systems work in the frequency range from a few kHz to 500 kHz. For those systems in which the instrumental effects dominate, the proposed IEM enables them to work up to a few MHz. For those systems in which the full Maxwell effects dominate, the proposed CEM-IBC enables the systems to work up to a few MHz, till the instrumental effects become dominating. The proposed TPM with the full Maxwell EIT formula enables the systems to work when both effects (two problems mentioned) are notable.

1.6 Thesis Organisation

This thesis is divided into 6 Chapters. The first chapter introduces the EM detection/imaging techniques and their classifications. The motivations of the research are described in this chapter. Literatures on EIT and some other similar modalities are reviewed. Problems of the state-of-the-art systems are discussed. The goals and contributions of the research are briefed.

Chapter 2 is used to introduce the basis of the research. Methods that are generally used in EIT forward problems and inverse problems will be detailed. Hardware and instrumental systems will be also discussed, where the instrumental effects will be explained. The full Maxwell EIT formula for forward problems will be derived as the basis of the proposed CEM-IBC and TPM.

In Chapter 3, the proposed IEM for forward problems of quasi-static EIT (general EIT) formula will be detailed from derivations of the equations to numerical experiments.

In Chapter 4, CEM-IBC and TPM will be detailed for forward problems of full Maxwell EIT formula. Derivations of the proposed models and numerical experiments will be included.

In Chapter 5, IEM will be applied to inverse problems in a general EIT algorithm, and the derivations of the proposed models and numerical experiments will be included.

A conclusion and suggested future works will be given in Chapter 6, where some hardware design and experimental results will be presented as well.

Chapter 2 Background of Research

2.1 Introduction

In this chapter, I will describe general methods in establishing and solving the EIT problems. The physical models of EITs and their numerical methods are referred to as forward problems. The forward solutions are evaluated with the real measurements to obtain inverse solutions to the inverse problems.

The way EIT algorithms are proposed is known as an ill-posed problem. It means a small measurement inaccuracy or random noise can easily cause a deviation in the inverse results, as mentioned in Chapter 1. Therefore, regularisation and iterative methods performed in solving the inverse problems are introduced. To build a system operating at a higher frequency, the physical models need to undergo a full Maxwell's analysis in order to avoid quasi-static inaccuracy. Some fundamental work of the physical model, such as the potential Helmholtz formula, will be derived in this chapter. The instrumental effects that cause inaccuracy at high frequency will be analysed and discussed using general hardware analysis methods.

EIT is a technique used to calculate the impedance distribution in the volume of an object by measuring the potential distribution on the surface when the object is excited electrically. The EIT algorithm can be simply defined as,

$$U(x) \underset{\text{EIT}}{\longrightarrow} \varepsilon^*(\Omega).$$

Equation 2-1

It solves for the admittivity distribution in the region Ω, with the voltages measured on finite positions x, where ε^* is the admittivity, the positions x are on the outer surface of object, and U is a set of measured differential voltages between pairs of electrodes.

There is no obvious way to solve the problem directly. Usually, EIT employs a forward problem and an inverse problem to solve it instead,

$$F[\varepsilon^*(\Omega)] = U(x), \qquad F^{-1}[U(x)] = \varepsilon^*(\Omega),$$

Equation 2-2 (a - b)

where $F[\quad]$ and $F^{-1}[\quad]$ refer to the forward problem and the inverse problem, respectively. The benefit is that there are well-established physical models for the forward problems, and also there are optimization techniques for solving the non-linear inverse problems.

The physical model of the forward problem (usually called forward model) is used to describe the relation between the electromagnetic fields and a known property distribution (it can be conductivity, permittivity and permeability).

The inverse problem is solved by linearising the problem and solving the difference, as,

$$F^{-1}\left[U_{\varepsilon^*{}_0}\right] = \varepsilon^*{}_0, \qquad F^{-1}\left[U_{\varepsilon^*{}_0+\Delta\varepsilon^*}\right] = \varepsilon^*{}_0 + \Delta\varepsilon^*,$$

$$\lim_{\Delta\varepsilon^*\to 0} U_{\varepsilon^*{}_0+\Delta\varepsilon^*} = F(\varepsilon^*{}_0) + \frac{\partial F(\varepsilon^*{}_0)}{\partial\varepsilon^*}\Delta\varepsilon^*.$$

Instead of directly solving the non-linear Equation 2-2, the problem is linearised by expanding with the first order Taylor series. The derivative of the forward problem with respect to the admittivity is used to calculate the perturbation. $\Delta\varepsilon^*$ is the variation of the admittivity.

$$\Delta\varepsilon^* = \left[\frac{\partial F(\varepsilon^*{}_0)}{\partial\varepsilon^*}\right]^{-1}\left[U_{\varepsilon^*{}_0+\Delta\varepsilon^*} - F(\varepsilon^*{}_0)\right].$$

Equation 2-3

Equation 2-3 holds under the assumption that $\Delta\varepsilon^* \to 0$. Based on Equation 2-3, a general working procedure of an EIT algorithm (Yorkey, et al., 1987) can be given. Figure 2-1 shows a block diagram of an EIT algorithm structure. Applications using differences of measured voltages to obtain $\Delta\varepsilon^*$ are usually called difference imaging or dynamic imaging. However, applications are called static imaging or absolute imaging if they start with an initial state, and iteratively approach the observation (only the foreground). A "switch" in the block of the inverse problem is placed to illustrate the difference between these two approaches.

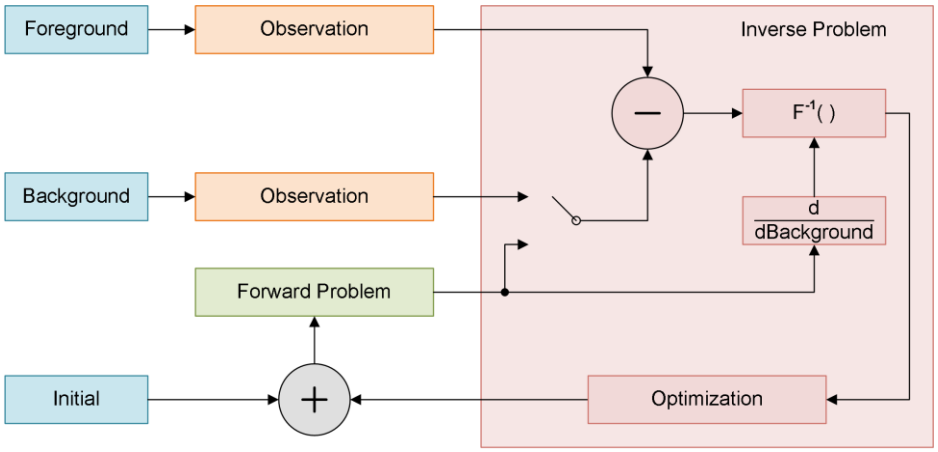

Figure 2-1 Structure of EIT Algorithm

In this chapter, the forward problems (the green block in Figure 2-1), will be introduced in Section 2.2. The inverse problems (the pink block in Figure 2-1), will be introduced in

Section2.3. The fundamental work of the full Maxwell's analysis, the potential Helmholtz-like formula, and the boundary conditions previously used will be introduced in Section 2.4. The instrumental effects that appear in the orange blocks in Figure 2-1, will be analysed and discussed in Section 2.5.

This chapter will introduce some previously published methods proposed by other research groups. My research will be based on these methods, and I will introduce my main contributions in the next few chapters.

2.2 Forward Problem

The EIT forward problem is a kind of Boundary Value Problems (BVP). It provides the relationship between a known admittivity distribution and simulated voltages based on Maxwell's equations.

In this section we will apply quasi-static approximation to the physics model and derived the governing Laplace equation of an EIT system. We will describe the full Maxwell's equations without applying the quasi-static assumption in another section.

2.2.1 Quasi-static Maxwell's Equation

From the harmonic Maxwell's equations (Stratton, 1941; Harrington, 1961),

$$\nabla \times \mathbf{E} = -\mathrm{j}\omega\mu\mathbf{H},$$

$$\nabla \times \mathbf{H} = \mathbf{J} + \mathrm{j}\omega\varepsilon\mathbf{E},$$

$$\nabla \cdot \varepsilon\mathbf{E} = \rho,$$

$$\nabla \cdot \mu\mathbf{H} = 0.$$

Equation 2-4 (a - d)

where ω is the angular frequency, $\mathbf{E}$ is electric field intensity, $\mathbf{B}$ is the magnetic flux density, $\mathbf{H}$ is magnetic field intensity, $\mathbf{J}$ is the electric current density (vector field), ρ, σ, ε and μ are the charge density, conductivity, permittivity and permeability distribution, respectively. The time convention $e^{i\omega t}$ is used. The continuity equation and medium-dependent equations are given as Equation 2-5 (a - c),

$$\nabla \cdot \mathbf{J} = -\mathrm{j}\omega\rho, \qquad \mathbf{B} = \mu\mathbf{H},$$

$$\mathbf{J} + \mathrm{j}\omega\varepsilon\mathbf{E} = \sigma\mathbf{E} + \mathrm{j}\omega\varepsilon\mathbf{E} = \varepsilon^{*}\mathbf{E}.$$

Equation 2-5 (a - c)

The EIT forward problem is to map a known ε^*distribution to the electric potential on the surface of a volume to be solved.

The solution to an EIT forward problem is a set of voltages, defined from the potentials of electromagnetic fields. A vector potential $\mathbf{A}_0$ is defined as (Sheng & Song, 2012),

$$\nabla \times \mathbf{A}_0 = \mathbf{B}.$$

Equation 2-6

$\mathbf{A}_0$ is also called magnetic vector potential in contrast to the electric scalar potential which is defined as follows. Substituting the above definition into Maxwell's equations, we obtain,

$$\nabla \times \mathbf{E} = -\mathrm{j}\omega\mu\mathbf{H} = -\mathrm{j}\omega\nabla \times \mathbf{A}_0,$$

$$\nabla \times (\mathbf{E} + \mathrm{j}\omega\mathbf{A}_0) = 0,$$

$$\nabla\Phi_0 = -(\mathbf{E} + \mathrm{j}\omega\mathbf{A}_0).$$

The subscription of 0 is attached because these potentials are not unique. The uniqueness will be discussed in later sections.

Applying divergence and replacing the electric field with the potentials, the map between the admittivity and the potential can be given as,

$$\nabla \times \mathbf{H} = \varepsilon^*\mathbf{E},$$

Equation 2-7

$$\nabla \cdot \varepsilon^*\mathbf{E} = \nabla \cdot \nabla \times \mathbf{H} = 0,$$

$$\mathbf{E} = -\nabla\Phi_0 - \mathrm{j}\omega\mathbf{A}_0,$$

Equation 2-8

$$\nabla \cdot \varepsilon^*(\nabla\Phi_0 + \mathrm{j}\omega\mathbf{A}_0) = 0.$$

Equation 2-9

The approximation is based on the quasi-static assumption, which states that the electric field can be considered as an irrotational field in a low frequency electromagnetic system,

$$\nabla \times \mathbf{E} = -\mathrm{j}\omega\nabla \times \mathbf{A}_0 \cong \mathbf{0}.$$

Equation 2-10

With this assumption, the map between the admittivity and the scalar potential distribution degrades to the Laplace equation,

$$\nabla \cdot \varepsilon^*\nabla\Phi = 0,$$

Equation 2-11

which is also called the governing equation for the EIT forward problem. We use Φ without the subscription as, for an EIT system, the differential voltages between pairs of electrodes are used (instead of using the electric potential).

Further, we will provide detailed derivations of the condition for with or without (full Maxwell forward problem) using the quasi-static assumption in later chapters.

With the governing equation, the forward problem can be solved by numerical technique and boundary conditions, which will be detailed in the following section.

2.2.2 Numerical Techniques and FEM

FEM is one of the well-developed numerical techniques for solving differential equations. The idea of FEM is to discretise the continuous problem in infinite dimensions, and solve the problem in finite number of small domains (Strang & Fix, 1973).

There are different types of FEMs, and we choose to introduce the Galerkin's method and use it in later derivations. It says, for a Hilbert space $\mathcal{U}$, to find $u \in \mathcal{U}$ such that for all $\phi \in \mathcal{U}$, there is,

$$a(u, \phi) = f(\phi).$$

Equation 2-12

Here, $\mathcal{U}$ is the domain of the problem, $a(,)$ is a bilinear form, and f is a bounded linear function on $\mathcal{U}$. u is the solution of the problem and ϕ can be any arbitrary function. To solve the problem in finite dimensions, domain discretisation is applied to give the subspace $\mathcal{U}_\mathrm{N} \subset \mathcal{U}$. The problem becomes to find $\mathrm{u}_\mathrm{N} \in \mathcal{U}_\mathrm{N}$ such that for all $\phi_\mathrm{N} \in \mathcal{U}_\mathrm{N}$, as Equation 2-13.

$$a(\mathrm{u}_\mathrm{N}, \phi_\mathrm{N}) = f(\phi_\mathrm{N}), \qquad \phi_\mathrm{N} = \sum_{i=1}^{N} \phi_i\,, \qquad \mathrm{u}_\mathrm{N} = \sum_{j=1}^{N} \mathrm{u}_j \phi_j$$

$$a\left(\sum_{i=1}^{N} \mathrm{u}_i\, \phi_i, \phi_j\right) = \sum_{i=1}^{N} \mathrm{u}_i a(\phi_i, \phi_j) = f(\phi_j), \qquad j \in [1,2,\cdots N].$$

Equation 2-13

Here, $\phi_\mathrm{N} \in \mathcal{U}_\mathrm{N}$ can be any arbitrary function on $\mathcal{U}_\mathrm{N}$, and the bilinear form allows to bring the coefficients u_j outside $a(,)$. The solution u_N is the approximation to u on discretised domain $\mathcal{U}_\mathrm{N}$. The Galerkin's method uses the sum of the bases in $\mathcal{U}_\mathrm{N}$ as the ϕ_N, we use Figure 2-2 to show a typical 1-D problem.

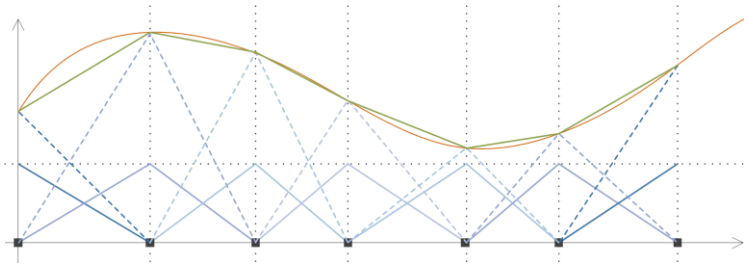

Figure 2-2 the Galerkin's Method

In Figure 2-2, the horizontal axis is the continuous domain $\mathcal{U}$ and the brown curve is the solution u on it. The square dots are the discretised domain $\mathcal{U}_{\mathrm{N}}$, and the green polyline is the FEM approximation u_{N}. Each of the blue lines is one of the bases ϕ_j of $\mathcal{U}_{\mathrm{N}}$, and the dashed lines are the weighted bases $\mathrm{u}_j\phi_j$. A basis can be a higher-order polynomial; linear bases are plotted in Figure 2-2, and u_{N} appears to be piecewise linear on the figure consequently.

In order to solve the forward problems with FEM techniques, the governing equation has to be changed to a bilinear form. An arbitrary trial function and BCs are added to make a bilinear form as in Equation 2-12.

2.2.3 Weak Formula and Boundary Conditions

In order to solve Equation 2-11 with the FEM, the corresponding bilinear form $a(,)$ and bounded linear function f needs to be found. A weak formula consists of $a(,)$, and f is therefore introduced as the governing equation standing for the strong formula. Applying the vector derivative identity, Green's identity and divergence theorem, respectively, we obtain the weak form,

$$v\nabla\cdot\varepsilon^*\nabla\Phi = \nabla\cdot v\varepsilon^*\nabla\Phi - \varepsilon^*\nabla\Phi\cdot\nabla v,$$

$$\int_\Omega v\nabla\cdot\varepsilon^*\nabla\Phi\,\mathrm{d}V = \int_\Omega \nabla\cdot v\varepsilon^*\nabla\Phi\,\mathrm{d}V - \int_\Omega \varepsilon^*\nabla\Phi\cdot\nabla v\,\mathrm{d}V = 0,$$

$$\int_\Omega \nabla\cdot v\varepsilon^*\nabla\Phi\,\mathrm{d}V = \int_\Omega \varepsilon^*\nabla\Phi\cdot\nabla v\,\mathrm{d}V,$$

$$\int_\Omega \varepsilon^*\nabla\Phi\cdot\nabla v\,\mathrm{d}V = \oint_{\partial\Omega} v\varepsilon^*\nabla\Phi\cdot\hat{\mathbf{n}}\,\mathrm{d}S.$$

Equation 2-14

where v is an arbitrary scalar trial function, Ω is the volume of the object, V denotes the volume, $\partial\Omega$ is the outer surface of the object, S denotes the surface area, and $\hat{\mathbf{n}}$ is the unit vector pointing outward normal to the surface.

The weak formula allows solving the potential distribution by providing boundary conditions and discretizing the domain with Galerkin's method.

We first apply the boundary conditions (BCs) to the problem. In EIT applications, the BCs describe the relationship between the electrodes and the potential distributions on their surfaces. A set of multiple BCs is usually called an electrode model. It includes the electric currents going into and out of the electrode surfaces, and the differences in electric potentials (where present) between the object surface and the electrodes. Different electrode models have been proposed and used, as introduced in Chapter 1.

In this section the CEM (Cheng, et al., 1989; Somersalo, et al., 1992; Vauhkonen, et al., 1999) is explained as it is much more accurate than the PEM and closely related with our electrode model, the IEM (Chapter 3).

The CEM consists of the following equations,

$$\varepsilon^* \nabla\Phi \cdot \hat{\mathbf{n}} = 0 \text{ (position not on electrodes)},$$

$$\int_{S_l} \varepsilon^* \nabla\Phi \cdot \hat{\mathbf{n}}\, \mathrm{d}S = I_l \left(\text{position on } l^{\text{th}} \text{ electrode}\right),$$

$$\Phi + \eta_l \varepsilon^* \nabla\Phi \cdot \hat{\mathbf{n}} = U_l,$$

$$\sum_{l=1}^{L} I_l = 0,$$

$$\sum_{l=1}^{L} U_l = 0.$$

Equation 2-15 (a - e)

where S_l is the surface of the l^{th} electrode,

I_l is the current on the l^{th} electrode,

η_l is the contact impedance in $\Omega \cdot \mathrm{m}^2$ on the l^{th} electrode,

U_l is the voltage measured on the l^{th} electrode,

L is the total number of the electrodes.

Equation 2-15 (a) prevents the current from flowing through the surface other than electrodes. Equation 2-15 (b) defines the current on the driving electrodes. Both of Equation 2-15 (a) and Equation 2-15 (b) are Neumann conditions. Equation 2-15 (c) allows the potential on the surface to be different from the voltage on the electrode circuit node, caused by the contact

impedance on the surface of electrodes, which is a Cauchy boundary condition. Equation 2-15 (d) and Equation 2-15 (e) ensure the existence and uniqueness of the solution.

To apply the CEM to Equation 2-14, the surface integral is divided into integrals on the electrode and non-electrode surfaces,

$$\int_{\Omega} \varepsilon^* \nabla\Phi \cdot \nabla v \, \mathrm{d}V = \int_{\partial\Omega \notin S_l} v\varepsilon^* \nabla\Phi \cdot \hat{\mathbf{n}} \, \mathrm{d}S + \sum_{l=1}^{L} \int_{S_l} v\varepsilon^* \nabla\Phi \cdot \hat{\mathbf{n}} \, \mathrm{d}S \,,$$

substituting the Non-Electrode surface BC Equation 2-15 (a),

$$\int_{\Omega} \varepsilon^* \nabla\Phi \cdot \nabla v \, \mathrm{d}V = \sum_{l=1}^{L} \int_{S_l} v\varepsilon^* \nabla\Phi \cdot \hat{\mathbf{n}} \, \mathrm{d}S \,.$$

The additional unknowns U_l are added to the system equations, the potential on the electrodes. We use Equation 2-15 (c) to add an extra unknown U_l,

$$\int_{\Omega} \varepsilon^* \nabla\Phi \cdot \nabla v \, \mathrm{d}V = \sum_{l=1}^{L} \int_{S_l} v \frac{U_l - \Phi}{\eta_l} \mathrm{d}S \,,$$

$$\int_{\Omega} \varepsilon^* \nabla\Phi \cdot \nabla v \, \mathrm{d}V + \sum_{l=1}^{L} \frac{1}{\eta_l} \int_{S_l} v\Phi \, \mathrm{d}S - \sum_{l=1}^{L} \frac{U_l}{\eta_l} \int_{S_l} v \, \mathrm{d}S = 0 \,.$$

To constrain U_l, Equation 2-15 (c) is substituted into Equation 2-15 (b) to establish extra equations for U_l,

$$\int_{S_l} \frac{U_l - \Phi}{\eta_l} \mathrm{d}S = I_l \,.$$

Combining the above equations to obtain,

$$\int_{\Omega} \varepsilon^* \nabla\Phi \cdot \nabla v \, \mathrm{d}V + \sum_{l=1}^{L} \frac{1}{\eta_l} \int_{S_l} v\Phi \, \mathrm{d}S - \sum_{l=1}^{L} \frac{U_l}{\eta_l} \int_{S_l} v \, \mathrm{d}S = 0 \,,$$

$$\int_{S_l} \frac{U_l - \Phi}{\eta_l} \mathrm{d}S = I_l \,.$$

Equation 2-16 (a - b)

Equation 2-16 is in the form of Equation 2-12, which is a bilinear form on the Left Hand Side (LHS), with a bounded linear function on the Right Hand Side (RHS). Galerkin's method can then be applied by replacing v and Φ with ϕ_{N} and u_{N} to achieve the FEM formula for EIT forward problems.

2.3 Inverse Problem

The general idea of an inverse problem is given in Section 2.1, with Equation 2-3. We rewrite the formula here again as,

$$\Delta\varepsilon^* = \left[\frac{\partial F(\varepsilon^*{}_0)}{\partial \varepsilon^*}\right]^{-1} \left[U_{\varepsilon^*{}_0+\Delta\varepsilon^*} - F(\varepsilon^*{}_0)\right].$$

The inverse problem needs the derivative of the forward problem, with respect to the admittivity distribution. To do so, the forward formula is perturbed with $\Delta\varepsilon^*$. The corresponding derivative forms are usually called the Jacobian matrix.

We will introduce the procedure of obtaining the Jacobian matrix first. As the problem is ill-posed, the inversion results are easily affected by measurements or numerical errors. Consequently, by simply inversing the Jacobian matrix, it is not able to find a meaningful $\Delta\varepsilon^*$. General methods for obtaining stable solutions, such as regularisation etc., are introduced following the Jacobian section.

2.3.1 Perturbation and Jacobian Matrix

We take the weak formula given in Equation 2-14 and use a potential distribution Φ^v in the place of v the arbitrary function of distribution,

$$\int_\Omega \varepsilon^* \nabla\Phi \cdot \nabla\Phi^v \mathrm{d}V = \int_{\partial\Omega} \Phi^v \varepsilon^* \nabla\Phi \cdot \hat{\mathbf{n}} \mathrm{d}S.$$

Φ^vcan be the same one or different from Φ, and we use v as superscript to emphasise that it is used as the trial function.

To determine a potential distribution, an excitation set with related boundary conditions is required, which is a set of I_l in Equation 2-16 (b). Here, we use the superscription d, δ for identifying different exciting sets (driving). Φ^d is the potential distribution driven by the current injection set $\mathbf{i}^d = [I^d{}_1, I^d{}_2, \cdots I^d{}_L]^{\mathrm{T}}$, whereas Φ^δ is a different distribution by a different excitation $\mathbf{i}^\delta = \left[I^\delta{}_1, I^\delta{}_2, \cdots I^\delta{}_L\right]^{\mathrm{T}}$. The weak formula then becomes,

$$\int_\Omega \varepsilon^* \nabla\Phi^d \cdot \nabla\Phi^\delta \mathrm{d}V = \int_{\partial\Omega} \Phi^\delta \varepsilon^* \nabla\Phi^d \cdot \hat{\mathbf{n}} \mathrm{d}S.$$

CEM boundary conditions are used to obtain,

$$\Phi^d + \eta_l \varepsilon^* \nabla\Phi^d \cdot \hat{\mathbf{n}} = U^d{}_l, \qquad \Phi^\delta + \eta_l \varepsilon^* \nabla\Phi^\delta \cdot \hat{\mathbf{n}} = U^\delta{}_l,$$

$$\int_{S_l} \varepsilon^* \nabla \Phi^d \cdot \hat{\mathbf{n}}\, dS = {I^d}_l, \qquad \int_{S_l} \varepsilon^* \nabla \Phi^\delta \cdot \hat{\mathbf{n}}\, dS = {I^\delta}_l.$$

Similarly, ${U^d}_l$ is the voltage on the l^{th} electrode when the excitation set $\mathbf{i}^d$ is applied, and the relative voltage measurement vector is expressed as $\mathbf{u}^d = [{U^d}_1, {U^d}_2, \cdots {U^d}_L]^{\mathrm{T}}$.

By substituting the BC under different excitations, we can obtain,

$$\int_\Omega \varepsilon^* \nabla \Phi^d \cdot \nabla \Phi^\delta \mathrm{d}V + \sum_{l=1}^{L} \eta_l \int_{S_l} \left(\varepsilon^* \nabla \Phi^\delta \cdot \hat{\mathbf{n}}\right)\left(\varepsilon^* \nabla \Phi^d \cdot \hat{\mathbf{n}}\right)\mathrm{d}S = \sum_{l=1}^{L} {U^\delta}_l {I^d}_l.$$

Equation 2-17

Usually, an EIT system uses a single pair of current injections, which means that for a specific $\mathbf{i}^d$only two of the ${I^d}_l$ on the L electrodes are non-zeroes. This means that the RHS can be further simplified.

When the driving pattern $\mathbf{i}^d$ is applied, the measured voltages are $\mathbf{u}^d = [{U^d}_1, {U^d}_2, \cdots {U^d}_{l^+}, \cdots {U^d}_{l^-}, \cdots {U^d}_L]^{\mathrm{T}}$, where l^+ and l^- are electrode numbers. Then another driving pattern $\mathbf{i}^\delta$ is used, the current is applied on the two electrodes mentioned l^+ and l^- only. Describing this procedure with equations we have,

$$\int_\Omega \varepsilon^* \nabla \Phi^d \cdot \nabla \Phi^\delta \mathrm{d}V + \sum_{l=1}^{L} \eta_l \int_{S_l} \left(\varepsilon^* \nabla \Phi^\delta \cdot \hat{\mathbf{n}}\right)\left(\varepsilon^* \nabla \Phi^d \cdot \hat{\mathbf{n}}\right)\mathrm{d}S$$
$$= \sum_{l=1}^{L} {U^d}_l {I^\delta}_l = \left({U^d}_{l^+} {I^\delta}_{l^+}\right) + \left({U^d}_{l^-} {I^\delta}_{l^-}\right).$$

In this way, as $\mathbf{i}^\delta \neq \mathbf{i}^d$, $\mathbf{u}^d$ has to be obtained from current being injected from a set of electrodes other than the l^+ and l^- pair used by $\mathbf{i}^\delta$. Therefore, only voltages on electrodes l^+ and l^- contribute to the RHS. This special design of the EIT procedure can avoid affecting the algorithm with an unknown contact impedance. If $\mathbf{i}^\delta = \mathbf{i}^d$ instead, the contact impedance of the electrodes l^+ and l^- are contributing to the RHS, which can be observed by substituting Equation 2-15 (b - c) into the RHS.

However, the assumption of not introducing contact impedance uncertainty is only for ideal systems. In reality, it is impossible to have ${I^\delta}_l$ being exactly zero due to non-ideal instrumental loading. A model considering non-ideal instrumental effects will be discussed later.

To obtain the first order partial derivative of $F({\varepsilon^*}_0)$, perturbation approaches are performed as $\varepsilon^* \to \varepsilon^* + \Delta\varepsilon^*$, $\Phi^d \to \Phi^d + \Delta\Phi^d$, $\Phi^\delta \to \Phi^\delta + \Delta\Phi^\delta$ and ${U^\delta}_l \to {U^\delta}_l + \Delta{U^\delta}_l$. The excited current is kept the same to ensure the existence of the solution. By ignoring the higher order terms, and removing the reference terms, we have,

$$\int_\Omega \varepsilon^* \nabla\left(\Delta\Phi^d\right) \cdot \nabla\Phi^\delta + \varepsilon^* \nabla\Phi^d \cdot \nabla\left(\Delta\Phi^\delta\right) + \Delta\varepsilon^* \nabla\Phi^d \cdot \nabla\Phi^\delta \mathrm{d}V$$

$$+ \sum_{l=1}^{L} \eta_l \int_{S_l} {\varepsilon^*}^2 \frac{\partial\Delta\Phi^\delta}{\partial n}\frac{\partial\Phi^d}{\partial n} + {\varepsilon^*}^2 \frac{\partial\Phi^\delta}{\partial n}\frac{\partial\Delta\Phi^d}{\partial n} + 2\Delta\varepsilon^*\varepsilon^* \frac{\partial\Phi^\delta}{\partial n}\frac{\partial\Phi^d}{\partial n} \mathrm{d}S$$

$$= \sum_{l=1}^{L} \Delta{U^\delta}_l {I^d}_l.$$

By evaluating the weak formula with $v = \Delta\Phi^d, \Delta\Phi^\delta$, we have,

$$\int_{\partial\Omega} \Delta\Phi^\delta \varepsilon^* \nabla\Phi^d \cdot \hat{\mathbf{n}} \mathrm{d}S + \int_{\partial\Omega} \Delta\Phi^d \varepsilon^* \nabla\Phi^\delta \cdot \hat{\mathbf{n}} \mathrm{d}S + \int_\Omega \Delta\varepsilon^* \nabla\Phi^d \cdot \nabla\Phi^\delta \mathrm{d}V$$

$$+ \sum_{l=1}^{L} \eta_l \int_{S_l} {\varepsilon^*}^2 \frac{\partial\Delta\Phi^\delta}{\partial n}\frac{\partial\Phi^d}{\partial n} + {\varepsilon^*}^2 \frac{\partial\Phi^\delta}{\partial n}\frac{\partial\Delta\Phi^d}{\partial n} + 2\Delta\varepsilon^*\varepsilon^* \frac{\partial\Phi^\delta}{\partial n}\frac{\partial\Phi^d}{\partial n} \mathrm{d}S = \sum_{l=1}^{L} \Delta{U^\delta}_l {I^d}_l .$$

Applying the vector derivative identity, Green's identity and divergence theorem again as what we did to obtain Equation 2-14, then inserting the perturbed BC Equation 2-15 (c) and BC Equation 2-15 (b), we can finally derive,

$$\int_\Omega \Delta\varepsilon^* \nabla\Phi^d \cdot \nabla\Phi^\delta \mathrm{d}V = -\sum_{l=1}^{L} \int_{S_l} \varepsilon^* \frac{\partial\Phi^\delta}{\partial n} \Delta{U^d}_l \mathrm{d}S = -\sum_{l=1}^{L} \Delta{U^d}_l {I^\delta}_l.$$

Equation 2-18

Equation 2-18 is the general formula of EIT inverse problems with the CEM as the BC set. We apply to a simple case to explain the usage. By assuming the measuring pattern to be $\mathbf{i}^\delta = \left[{I^\delta}_0, -{I^\delta}_0, 0, \cdots 0\right]^{\mathrm{T}}$, which means ${I^\delta}_1 = -{I^\delta}_2 = {I^\delta}_0$ and ${I^\delta}_l\big|_{3\sim L} = 0$, we have,

$$\int_\Omega \Delta\varepsilon^* \nabla\Phi^d \cdot \nabla\Phi^\delta \mathrm{d}V = -\sum_{l=1}^{L} \Delta{U^d}_l {I^\delta}_l = -\left(\Delta{U^d}_1 - \Delta{U^d}_2\right){I^\delta}_0 .$$

$\Delta{U^d}_1 - \Delta{U^d}_2$ is the difference between two measured differential voltages as,

$$\Delta{U^d}_1 - \Delta{U^d}_2 = [{U^d}_1(\varepsilon^* + \Delta\varepsilon^*) - {U^d}_2(\varepsilon^* + \Delta\varepsilon^*)] - [{U^d}_1(\varepsilon^*) - {U^d}_2(\varepsilon^*)].$$

The difference $\Delta {U^d}_1 - \Delta {U^d}_2$ is caused by $\Delta\varepsilon^*$. Here, $\Delta {U^d}_1 - \Delta {U^d}_2$ should not be confused with ${U^d}_1 - {U^d}_2$. The latter one is the voltage difference measured across the two electrodes of the measuring pattern, numbered 1 and 2. We call this ${U^d}_1 - {U^d}_2$ the measured differential voltage.

The perturbation technique provides the relationship between $\Delta\varepsilon^*$ and $\Delta {U^d}_1 - \Delta {U^d}_2$ in Equation 2-18. It is then formed as the derivative of the voltage measurements with respect to $\Delta\varepsilon^*$, and it is discretised from the volume Ω to $\sum_{e=1}^{E} V_e$.

$$\sum_{e=1}^{E} \Delta {\varepsilon^*}_e \int_{V_e} \nabla\Phi^d \cdot \nabla\Phi^\delta dV = -\sum_{l=1}^{L} \Delta {U^d}_l {I^\delta}_l$$

$$\sum_{l=1}^{L} \frac{\Delta {U^d}_l {I^\delta}_l}{\Delta {\varepsilon^*}_e} = -\int_{V_e} \nabla\Phi^d \cdot \nabla\Phi^\delta dV$$

Equation 2-19

Here $\Delta {\varepsilon^*}_e$ is the $\Delta\varepsilon^*$on the e^{th} element.

This formula is suitable for any excitation and measurement setting, and some simplifications can be made for those applications using driving and measuring electrodes in pairs. Assume that the measuring pattern $\mathbf{i}^\delta$ is on a pair of electrodes l^+ and l^-, while the driving pattern $\mathbf{i}^d$ is on a pair of electrodes *not* l^+ and l^-, with the current $\pm {I^d}_0$. The resulted potential distribution in the object is Φ^d. The voltages on the measuring electrode pair (the measuring pattern $\mathbf{i}^\delta$) are then ${U^d}_{l^+}$ and ${U^d}_{l^-}$. Equation 2-19 then becomes

$$\frac{\partial U_{d,\delta}}{\partial {\varepsilon^*}_e} \equiv \frac{\partial \left({U^d}_{l^+} - {U^d}_{l^-}\right)}{\partial {\varepsilon^*}_e} = \frac{-1}{{I^\delta}_0} \int_{V_e} \nabla\Phi^d \cdot \nabla\Phi^\delta \mathrm{d}V$$

Equation 2-20

A new notation $U_{d,\delta}$ is defined here for the LHS, which is the change of differential voltage due to $\Delta {\varepsilon^*}_e$. This change is measured on electrodes l^+ and l^- (pattern $\mathbf{i}^\delta$) with the object excited with I^d. The RHS says, this ratio can be determined by $\nabla\Phi^d$ and $\nabla\Phi^\delta$. ${I^\delta}_0$ is kept as constant for all measuring patterns (can be considered as a normaliser).

Both of the potential distributions are established without the admittivity change. The first potential distribution Φ^d is excited with I^d, on the driving electrode pair. The second potential distribution Φ^δ is excited by I^δ, on the measuring electrode pair. In EIT algorithms, a number of driving pairs and measuring pairs are used to solve the inverse problem. These driving and

measuring pairs comprise the so called *driving and measuring patterns*. The notation $U_{d,\delta}$, uses subscript d and δ to denote the related driving and measuring pattern, respectively.

With the partial derivative given, the Jacobian matrix can be easily obtained. The formula is similar to the forward problem, and many of the matrixes can be reused in calculating the Jacobian matrix. We eliminate the need for deriving this by only explaining the procedure.

Equation 2-20 is the contribution from an element to a driving and measuring pattern. The Jacobian matrix is built up by columns being the contribution of elements and rows being the contribution of patterns. The FEM is applied on the RHS of Equation 2-20 to provide the Jacobian matrix, replacing the gradient with combinations of the FEM bases.

We now name a row of the Jacobian matrix following the naming $\boldsymbol{J}^{d,\delta}$, which is related to the contribution of all the elements in the object to a specific driving and measuring pattern d, δ, as follows,

$$\boldsymbol{J}^{d,\delta} = \left[\frac{\partial U_{d,\delta}}{\partial \varepsilon^*{}_1} \quad \cdots \quad \frac{\partial U_{d,\delta}}{\partial \varepsilon^*{}_{\mathrm{E}}}\right] \in \mathbb{C}^{1\times \mathrm{E}}.$$

Then, the overall Jacobian matrix is made up as below,

$$\boldsymbol{J} = \begin{bmatrix} \boldsymbol{J}^{d1,\delta 1} \\ \vdots \\ \boldsymbol{J}^{dC,\delta 1} \\ \vdots \\ \boldsymbol{J}^{d1,\delta M} \\ \vdots \\ \boldsymbol{J}^{dC,\delta M} \end{bmatrix} \in \mathbb{C}^{(MC)\times E}.$$

where there is a total of C drive patterns $d1 \sim dC$, each of which driving patterns works with M measurement patterns $\delta 1 \sim \delta M$.

The Jacobian matrix is an essential part in establishing many numerical problems. The accuracy of calculation is closely related to the ill-posed problem in hand. Furthermore, the efficiency of calculating the Jacobian matrix is also important. In many EIT applications, iterative solvers are involved in solving the inverse problems, which require calculating the Jacobian matrix in each iteration.

2.3.2 Regularisation and Iterative Method

Equation 2-3 is the relationship between measurements and admittivity, and it can be replaced with the Jacobian matrix as,

$$\boldsymbol{J}[\Delta\varepsilon^*] = \frac{-1}{I^{\delta}{}_0}\begin{bmatrix} \int_{V_1} \nabla\Phi^{d1}\cdot\nabla\Phi^{\delta 1}\mathrm{d}V & \cdots & \int_{V_E} \nabla\Phi^{d1}\cdot\nabla\Phi^{\delta 1}\mathrm{d}V \\ & \vdots & \\ \int_{V_1} \nabla\Phi^{d1}\cdot\nabla\Phi^{\delta M}\mathrm{d}V & \cdots & \int_{V_E} \nabla\Phi^{d1}\cdot\nabla\Phi^{\delta M}\mathrm{d}V \\ & \vdots & \\ \int_{V_1} \nabla\Phi^{dC}\cdot\nabla\Phi^{\delta 1}\mathrm{d}V & \cdots & \int_{V_E} \nabla\Phi^{dC}\cdot\nabla\Phi^{\delta 1}\mathrm{d}V \\ & \vdots & \\ \int_{V_1} \nabla\Phi^{dC}\cdot\nabla\Phi^{\delta M}\mathrm{d}V & \cdots & \int_{V_E} \nabla\Phi^{dC}\cdot\nabla\Phi^{\delta M}\mathrm{d}V \end{bmatrix} [\Delta\varepsilon^*] = \begin{bmatrix} \Delta U_{d1,\delta 1} \\ \vdots \\ \Delta U_{d1,\delta M} \\ \vdots \\ \Delta U_{dC,\delta 1} \\ \vdots \\ \Delta U_{dC,\delta M} \end{bmatrix} \in \mathbb{C}^{MC\times 1},$$

$$\boldsymbol{J}[\Delta\varepsilon^*] = \left[\widetilde{U}_{d,\delta}(\varepsilon^*{}_0 + \Delta\varepsilon^*) - U_{d,\delta}(\varepsilon^*{}_0)\right],$$

$$\boldsymbol{J}[\Delta\varepsilon^*] = \left[\widetilde{U}_{d,\delta}(\varepsilon^*{}_\mathrm{F}) - \widetilde{U}_{d,\delta}(\varepsilon^*{}_\mathrm{B})\right].$$

Equation 2-21 (a - c)

Here $[\Delta\varepsilon^*] \in \mathbb{C}^{E\times 1}$ is a finite dimensions estimation of $\Delta\varepsilon^*$. The symbol $\widetilde{\ }$ means the observations in contrast to the forward solutions. $\varepsilon^*{}_\mathrm{F}$ and $\varepsilon^*{}_\mathrm{B}$ are the admittivities of the foreground (after admittivity changes) and the background (before changes), respectively.

For absolute imaging, Equation 2-21 (b) is used. When voltage measurements of the foreground and the background are both available, the difference imaging can be applied with Equation 2-21 (c).

By inverting the Jacobian matrix, $[\Delta\varepsilon^*]$ can be obtained from Equation 2-22.

$$[\Delta\varepsilon^*] = \boldsymbol{J}^{-1}\left[\widetilde{U}_{d,\delta}(\varepsilon^*{}_0 + \Delta\varepsilon^*) - U_{d,\delta}(\varepsilon^*{}_0)\right].$$

Equation 2-22

However, due to the fact that the EIT inverse problem is ill-posed, the solution of Equation 2-22 is obtained using special techniques for solving inverse problems, discussed below.

2.3.2.1 Linear Least Squares and Regularisation

Equation 2-22 can be seen as a typical inverse problem in the form of $x = \boldsymbol{A}^{-1}b$. It can be easily recognised as an Ordinary Least Squares (OLS) problem as,

$$x_{\mathrm{OLS}} = \arg\min_x\left\{\|\boldsymbol{A}x - b\|_2{}^2\right\}.$$

Here $\|\ \ \|_2$ is the Euclidean norm, $\arg\min_x\{\ \ \}$ is the denotation of an optimisation problem, and x_{OLS} is the estimation of the parameter x, which minimizes the square norm. The OLS

searches the estimations by taking the derivative of the sum of the squared errors (residuals) with respect to x.

$$S(x) = \|\boldsymbol{A}x - b\|_2{}^2 = [b - \boldsymbol{A}x]^*[b - \boldsymbol{A}x].$$

The estimation x_{OLS} minimises the optimisation problem by finding a solution to the following form.

$$\frac{\partial S(x)}{\partial x} = \frac{\partial [b^*b - x^*\boldsymbol{A}^*b - b^*\boldsymbol{A}x + x^*\boldsymbol{A}^*\boldsymbol{A}x]}{\partial x} = 0$$

$$x_{\mathrm{OLS}} = (\boldsymbol{A}^*\boldsymbol{A})^{-1}\boldsymbol{A}^*b$$

However, a small residual r_{E} exists, contributed to by noise and errors, limiting the usage of OLSs in ill-posed problems. Suppose there is an OLS estimation for a problem, the measurement of which is perturbed by r_{E},

$$\boldsymbol{A}x = b - r_{\mathrm{E}}, \qquad \|\boldsymbol{A}x_{\mathrm{OLS}} - b\|_2{}^2 < \|\boldsymbol{A}x_0 - b\|_2{}^2 = \|r_{\mathrm{E}}\|_2{}^2.$$

Here, x_{OLS} minimises the residuals of the optimisation problem. However, the observation is perturbed, and x_{OLS} may not be close to the true parameter x_0 of $\boldsymbol{A}x - b + r_{\mathrm{E}}$ (as ill-posed problems are sensitive to r_{E}).

In order to overcome the problem, regularisation techniques are used. We take the Tikhonov regularisation as example, which states as,

$$x_{\mathrm{TR}} = \arg\min_x \left\{\|\boldsymbol{A}x - b\|_2{}^2 + \|\boldsymbol{\Gamma}x\|_2{}^2\right\}.$$

Equation 2-23

When a proper Tikhonov matrix $\boldsymbol{\Gamma}$ is used, the best estimation $x_{\mathrm{TR}} \to x_0$ can be found as,

$$\|\boldsymbol{A}x_{\mathrm{TR}} - b\|_2{}^2 + \|\boldsymbol{\Gamma}x_{\mathrm{TR}}\|_2{}^2 = \|\boldsymbol{A}x_0 - b\|_2{}^2 + \|\boldsymbol{\Gamma}x_0\|_2{}^2 = \|r_{\mathrm{E}}\|_2{}^2 + \|\boldsymbol{\Gamma}x_0\|_2{}^2.$$

The problem becomes to seek an estimation which potentially minimises the squared residuals, by the use of a penalty term.

Equation 2-23 is the Tikhonov regularisation in the form of optimisation problems. It can also be treated as an OLS problem, by letting the objective function $S(x)$ to be the norm of the residuals.

$$S(x) = \|\boldsymbol{A}x - b\|_2{}^2 + \|\boldsymbol{\Gamma}x\|_2{}^2 = \|r(x)\|_2{}^2,$$

$$r(x) = \begin{bmatrix} \boldsymbol{A} \\ \boldsymbol{\Gamma} \end{bmatrix} x - \begin{bmatrix} b \\ 0 \end{bmatrix}.$$

The estimator can be found by solving $\nabla S(x) = 0$. The solution is given by the normal equations (also known as regularised normal equations) as,

$$\frac{\partial S(x)}{\partial x} = \nabla S(x) = 2\boldsymbol{A}^*\boldsymbol{A}x - 2\boldsymbol{A}^*b + 2\boldsymbol{\Gamma}^*\boldsymbol{\Gamma}x = 0.$$

$$\boldsymbol{A}^*\boldsymbol{A}x + \boldsymbol{\Gamma}^*\boldsymbol{\Gamma}x = \boldsymbol{A}^*b, \qquad x_{\mathrm{TR}} = (\boldsymbol{A}^*\boldsymbol{A} + \boldsymbol{\Gamma}^*\boldsymbol{\Gamma})^{-1}\boldsymbol{A}^*b.$$

Equation 2-24 (a – b)

The Tikhonov Matrix is usually normalised as $\boldsymbol{\Gamma} = \lambda \boldsymbol{L}$. λ is a real value, called the regularisation parameter. The normal equations become,

$$x_{\mathrm{TR}} = \arg\min_x \left\{ \|\boldsymbol{A}x - b\|_2{}^2 + \lambda^2 \|\boldsymbol{L}x\|_2{}^2 \right\}, \qquad \boldsymbol{A}^*\boldsymbol{A}x + \lambda^2 \boldsymbol{L}^*\boldsymbol{L}x = \boldsymbol{A}^*b$$

Equation 2-25 (a – b)

We bring back Equation 2-22 and insert it in the normal equation of the Tikhonov regularisation. Here, we use x_0 to present the initial $\varepsilon^*{}_0$, Δx to present $[\Delta\varepsilon^*]$ in order to avoid confusing with conjugate transport symbol, and we have,

$$\Delta x_{\mathrm{TR}} = \arg\min_{\Delta x} \left\{ \left\| \boldsymbol{J}\Delta x - \left(\widetilde{U}_{d,\delta}(x_0 + \Delta x) - U_{d,\delta}(x_0) \right) \right\|_2{}^2 + \lambda^2 \|\boldsymbol{L}x\|_2{}^2 \right\}$$

$$= \arg\min_{\Delta x} \left\{ \left\| \begin{bmatrix} \boldsymbol{J} \\ \lambda \boldsymbol{L} \end{bmatrix} \Delta x - \begin{bmatrix} \widetilde{U}_{d,\delta}(x_0 + \Delta x) - U_{d,\delta}(x_0) \\ 0 \end{bmatrix} \right\|_2{}^2 \right\},$$

$$\Delta x_{\mathrm{TR}} = [\boldsymbol{J}^*\boldsymbol{J} + \lambda^2 \boldsymbol{L}^*\boldsymbol{L}]^{-1}\boldsymbol{J}^*\left[\widetilde{U}_{d,\delta}(x_0 + \Delta x) - U_{d,\delta}(x_0)\right].$$

2.3.2.2 Typical Iterative Inverse Methods

The OLS, however, is not capable of finding the solution of EIT inverse problems in the general sense. In Section 2.1 we mentioned that Equation 2-3 can be sustained under the assumption of $\Delta\varepsilon^* \to 0$. The assumption suggests $\partial F / \partial \varepsilon^*$ used in Newton's method (which is the Jacobian matrix used in the OLS normal equation) is *local* to $\varepsilon^*{}_0$. Therefore, *global* methods for EIT inverse problems are needed such as nonlinear Least Squares (LS).

Nonlinear LS approaches usually solve the EIT inverse problems iteratively (Lionheart, 2004). In each iteration, the OLS solves a linearised problem. Equation 2-2 (a - b) is linearised iteratively as,

$$\varepsilon^*{}_{k+1} = \varepsilon^*{}_k + \left[\frac{\partial F(\varepsilon^*{}_k)}{\partial \varepsilon^*}\right]^{-1} \left[U_{\varepsilon^*{}_0+\Delta\varepsilon^*} - F(\varepsilon^*{}_k)\right].$$

Equation 2-26

Equation 2-26 is the iterative version of Equation 2-3, with the derivative referring to Equation 2-20 and the forward operation referring to Equation 2-16. In each iteration, the derivative and the forward operation are evaluated with $\varepsilon^*{}_k$, and the OLS updates $\varepsilon^*{}_k$ to $\varepsilon^*{}_{k+1}$.

The nonlinear LS is formulated by expending Equation 2-26 with normal equations of the OLS, as,

$$x_{k+1} = x_k + \beta_{\mathrm{LS}}, \qquad \beta_{\mathrm{LS}} = \arg\min_{\beta}\left\{\left\|\boldsymbol{J}_k\beta - \widetilde{U}_{d,\delta}(x_0+\Delta x) + U_{d,\delta}(x_k)\right\|_2{}^2\right\},$$

$$x_{k+1} = x_k + ([\boldsymbol{J}_k]^*[\boldsymbol{J}_k])^{-1}[\boldsymbol{J}_k]^*\left[\widetilde{U}_{d,\delta}(x_0+\Delta x) - U_{d,\delta}(x_k)\right].$$

Equation 2-27

Equation 2-27 is a general formula of the Gauss-Newton algorithm for solving the nonlinear LS problems. It is also called the *modified Newton-Raphson method* in some literature (Yorkey, et al., 1987). The latter was derived from Newton's method of iterative optimisation and the Newton-Raphson algorithm for nonlinear LS. The modification was made on the Hessian matrix, by neglecting the terms involving second derivatives.

However, each iteration is also ill-posed if the nonlinear problem is ill-posed (Kaltenbacher, et al., 2008). Therefore, regularisations upon the nonlinear LS approach are required.

Applying the Tikhonov regularisation to each iteration leads to the Levenberg-Marquardt method (Marquardt, 1963; Moré, 1978; Kaltenbacher, et al., 2008). It takes the form of the optimisation problem, and adds penalty terms as additional information,

$$x_{k+1} = x_k + \beta_{\mathrm{LMR}},$$

$$\beta_{\mathrm{LMR}} = \arg\min_{\beta}\left\{\left\|\boldsymbol{J}_k\beta - \widetilde{U}_{d,\delta}(x_0+\Delta x) + U_{d,\delta}(x_k)\right\|_2{}^2 + \alpha_k{}^2\|\boldsymbol{D}\beta\|_2{}^2\right\},$$

$$x_{k+1} = x_k + ([\boldsymbol{J}_k]^*[\boldsymbol{J}_k] + \alpha_k{}^2\boldsymbol{D}^*\boldsymbol{D})^{-1}[\boldsymbol{J}_k]^*\left[\widetilde{U}_{d,\delta}(x_0+\Delta x) - U_{d,\delta}(x_k)\right].$$

Equation 2-28 (a - c)

Here, $\boldsymbol{D}$ is any given non-singular matrix, diagonal matrix for scaling by default, and α_k is the Levenberg-Marquardt parameter, which is iteration-dependent. An appropriate solution of x_{k+1} is obtained by carefully choosing the sequence and values of the regularisation parameters α_k.

Similar to the Levenberg-Marquardt method, another iteratively regularised Gauss-Newton method (Bakushinskii, 1992; Holder, 2005; Kaltenbacher, et al., 2008) is to minimise the optimisation problems and solve the normal equations, as below,

$$x_{k+1} = x_k + \beta_{\mathrm{GNR}},$$

$$\beta_{\mathrm{GNR}} = \arg\min_{\beta} \left\{ \left\| \boldsymbol{J}_k \beta - \widetilde{U}_{d,\delta}(x_0 + \Delta x) + U_{d,\delta}(x_k) \right\|_2^{\,2} + \lambda^2 \| \boldsymbol{L}[\beta - (x_0 - x_k)] \|_2^{\,2} \right\}.$$

$$([\boldsymbol{J}_k]^*[\boldsymbol{J}_k] + \lambda^2 \boldsymbol{L}^*\boldsymbol{L})[x_{k+1} - x_k] = [\boldsymbol{J}_k]^* \left[\widetilde{U}_{d,\delta}(x_0 + \Delta x) - U_{d,\delta}(x_k) \right] + \lambda^2 \boldsymbol{L}^*\boldsymbol{L}(x_0 - x_k).$$

Equation 2-29 (a - c)

Compared to the Levenberg-Marquardt method, Equation 2-29 (b) uses a constant regularisation parameter through the iterations. The residual functions show that the penalty term of the Levenberg-Marquardt method is applied on the step of the current iteration (concept of a *trust region*), and the penalty term of Equation 2-29 (b) is applied on the steps of all the iterations (Holder, 2005; Kaltenbacher, et al., 2008).

$$r(\beta_{\mathrm{LMR}}) = \begin{bmatrix} \boldsymbol{J}_k \\ \alpha_k \boldsymbol{D} \end{bmatrix} \beta - \begin{bmatrix} \widetilde{U}_{d,\delta}(x_0 + \Delta x) - U_{d,\delta}(x_k) \\ 0 \end{bmatrix},$$

$$r(\beta_{\mathrm{GNR}}) = \begin{bmatrix} \boldsymbol{J}_k \\ \lambda \boldsymbol{L} \end{bmatrix} \beta - \begin{bmatrix} \widetilde{U}_{d,\delta}(x_0 + \Delta x) - U_{d,\delta}(x_k) \\ \lambda(x_0 - x_k) \end{bmatrix}.$$

The two methods are identical for the first iteration. The iteratively regularised Gauss-Newton method Equation 2-29 is better in getting convergence, from the second iteration onwards, but it relies on initial guesses. The Levenberg-Marquardt method however, is relies on the chosen trust region $\alpha_k \boldsymbol{D}$ instead of the initial guesses. The method used in Chapter 5 is the iteratively regularised Gauss-Newton method based on Equation 2-29.

2.4 Full Maxwell's Equations in Potential Formula

Numerical methods for solving electromagnetic field (EMF) problems have been investigated over many decades. Similar to the forward problem in EIT applications, these field solvers calculate fields from given property distributions and applied excitations. However, the quasi-static assumption is not made, and the Laplace equations are not used. As far as the primary EMFs are interested, electric potential distributions are usually not directly solved.

Furthermore, due to the spurious modes and vector parasites found in EMF solutions from curl-curl equations (Davies, et al., 1982; Lynch & Paulsen, 1991), different modification of numerical methods are proposed. The main reason for these "fake" solutions is the

discontinuity of the prime fields. The penalty method (Strang & Fix, 1973; Rahman & Davies, 1984), the edge-element FEM (Barton & Cendes, 1987) and the Helmholtz-like potential formula (Paulsen, et al., 1992) are some of the major approaches to overcome the spurious modes and vector parasites problems.

We choose to use the potential formula in the Helmholtz-like equation method, which has been reported to have succeeded in overcoming the spurious and parasitic problems. More important, the penalty methods and edge-element approaches modify the governing formula or the FEM shape functions. These modifications are conflicting with the inverse problem of EIT currently in use. On the other hand, the EMF solved using a potential formula has the benefit of directly obtaining the potentials, whereas prime fields are solutions of the penalty method and edge-element FEM.

The disadvantage of using the potential formula is that the processes of gauge fixing and gauge BCs are rather complicated, which have seriously limited the usage of the formula.

The Helmholtz-like potential formula (Soni, et al., 2006) was first used in an EIT algorithm in 2006, based on the research (Lynch & Paulsen, 1991; Paulsen, et al., 1992; Boyse, et al., 1992; Boyse & Paulsen, 1997) done in the 1990's. My contributions are based on their work, including deriving the 3-D FEM formula for EIT applications and proposing more accurate electrode models for the problem. In the following sections, I will introduce their method, and leave my work detailed in Chapter 4.

2.4.1 Maxwell's Equations in Potential Fields and Gauge Fixing

To obtain Maxwell's equations in potential fields, the curl-curl formula is first derived by inserting Equation 2-4 (a) into Equation 2-4 (b),

$$\nabla \times \mathbf{H} = -\frac{1}{\mathrm{j}\omega}\nabla \times \frac{1}{\mu}\nabla \times \mathbf{E} = \varepsilon^{*}\mathbf{E}\,,$$

$$\nabla \times \frac{1}{\mu}\nabla \times \mathbf{E} + \mathrm{j}\omega\varepsilon^{*}\mathbf{E} = 0\,.$$

Equation 2-30

By replacing the electric field with Equation 2-8 and removing the term that performs a curl operation on scalar field Φ_0, we obtain,

$$\nabla \times \frac{1}{\mu}\nabla \times \mathbf{A}_0 + \varepsilon^{*}(\mathrm{j}\omega\mathbf{A}_0 + \nabla\Phi_0) = 0\,,$$

Equation 2-31

Together with Equation 2-9, the potential formulation of Maxwell's equations can be found. As we have mentioned earlier, the potential fields are not uniquely defined. For any arbitrary scalar function ψ, there is a pair of potential fields $\mathbf{A}_1$ and Φ_1 obeying the definition but different from $\mathbf{A}_0$ and Φ_0, as shown below,

$$\nabla \times \mathbf{A}_1 = \nabla \times (\mathbf{A}_0 + \nabla\psi) = \mathbf{B}, \qquad \mathbf{A}_1 = \mathbf{A}_0 + \nabla\psi,$$

$$\nabla\Phi_1 = -(\mathbf{E} + \mathrm{j}\omega\mathbf{A}_1) = \nabla\Phi_0 - \mathrm{j}\omega\nabla\psi, \qquad \Phi_1 = \Phi_0 - \mathrm{j}\omega\psi.$$

Equation 2-32 (a - b)

The arbitrary scalar function ψ, which has provided the extra freedom, is brought by the definition of the potential fields. According to the Helmholtz theorem, a vector field is uniquely specified with its divergence and curl, if the field reaches zero at infinity (Griffiths, 1998). In order to uniquely define the potentials, the divergence of the vector potential field has to be defined. The process is called gauge fixing (Van Bladel, 1964), meaning to settle down the potentials, and remove the extra degrees of freedom.

The gauge fixes the potentials $\mathbf{A}$ and Φ from arbitrary function ψ, so called the gauge function. As the potentials are not observable, it does not change the EMF intensities by choosing different gauges. Therefore, the chosen gauge only needs to benefit the derivation of the EMF potential formula.

The Lorenz Gauge is used in the Helmholtz-like equations, and it states,

$$\nabla \cdot \mathbf{A} = -\varepsilon^*\mu\Phi\,.$$

Equation 2-33

In order to insert Equation 2-33 into the potential formulation of Maxwell equations, the gradient is taken and the vector identities are applied to it to obtain,

$$-\left(\nabla\frac{1}{\mu}\nabla \cdot \mathbf{A} + \Phi\nabla\varepsilon^*\right) = \varepsilon^*\nabla\Phi\,.$$

By substituting the gauge into Equation 2-31, the potential fields are no longer arbitrary and we use $\mathbf{A}$ and Φ without the subscription to denote them, and we have,

$$\nabla \times \frac{1}{\mu}\nabla \times \mathbf{A} + \mathrm{j}\omega\varepsilon^*\mathbf{A} - \nabla\frac{1}{\mu}\nabla \cdot \mathbf{A} - \Phi\nabla\varepsilon^* = 0$$

Equation 2-34

For Equation 2-9, the vector identity is applied on the vector potential and Equation 2-33 is directly plugged in to obtain,

$$\varepsilon^{*2}\mu\Phi - \frac{1}{\mathrm{j}\omega}\nabla\cdot\varepsilon^{*}\nabla\Phi - \mathbf{A}\cdot\nabla\varepsilon^{*} = 0$$

Equation 2-35

For homogenous admittivity applications, the gradient of ε^{*} vanishes in both Equation 2-34 and Equation 2-35. The potential fields are therefore completely decoupled. These decoupled formulas lead to the general electromagnetic wave equations. However, for EIT applications, the heterogeneity of the admittivity distribution is the key property for imaging, therefore we do not have the benefit of decoupled equations.

2.4.2 Weak Formula on Potential Helmholtz-like Equations

In order to numerically solve the potential formula, Equation 2-34 and Equation 2-35 have to appear in bilinear form as Equation 2-12. The weak formula therefore is derived in a potential form by integrating the equations with an arbitrary scalar trial function v over the region.

$$\int_{\Omega} v\nabla\times\frac{1}{\mu}\nabla\times\mathbf{A}\mathrm{d}V + \int_{\Omega}\mathrm{j}\omega v\varepsilon^{*}\mathbf{A}\mathrm{d}V - \int_{\Omega} v\nabla\frac{1}{\mu}\nabla\cdot\mathbf{A}\mathrm{d}V - \int_{\Omega} v\Phi\nabla\varepsilon^{*}\mathrm{d}V = 0$$

$$\int_{\Omega} v\varepsilon^{*2}\mu\Phi\mathrm{d}V - \int_{\Omega} v\frac{1}{\mathrm{j}\omega}\nabla\cdot\varepsilon^{*}\nabla\Phi\mathrm{d}V - \int_{\Omega} v\mathbf{A}\cdot\nabla\varepsilon^{*}\mathrm{d}V = 0$$

Equation 2-36 (a - b)

All the second order derivatives on field variables should be replaced with the product of first order derivatives on field variables and on the trial function. Vector identities provide these equalities for us as,

$$v\nabla\times\frac{1}{\mu}\nabla\times\mathbf{A} = \nabla\times v\frac{1}{\mu}\nabla\times\mathbf{A} - \nabla v\times\frac{1}{\mu}\nabla\times\mathbf{A}\,,$$

$$v\nabla\frac{1}{\mu}\nabla\cdot\mathbf{A} = \nabla v\frac{1}{\mu}\nabla\cdot\mathbf{A} - \frac{1}{\mu}\nabla\cdot\mathbf{A}\nabla v\,.$$

Considering the discretise procedure, the electromagnetic properties are approximated with discontinuous constant values in every element. Any derivative on admittivity or permeability would therefore cause singularity in the FEM formula, and these derivatives need to be avoided by moving the gradient onto other functions, as,

$$\nabla(\varepsilon^{*}v\Phi) = (v\Phi)\nabla\varepsilon^{*} + \varepsilon^{*}\nabla(v\Phi) = (v\Phi)\nabla\varepsilon^{*} + \varepsilon^{*}v\nabla\Phi + \varepsilon^{*}\Phi\nabla v\,.$$

Plugging in the reformed terms into Equation 2-36 (a) we have,

$$\int_\Omega \nabla \times v\frac{1}{\mu}\nabla \times \mathbf{A}\mathrm{d}V - \int_\Omega \nabla v \times \frac{1}{\mu}\nabla \times \mathbf{A}\mathrm{d}V + \int_\Omega \mathrm{j}\omega v\varepsilon^* \mathbf{A}\mathrm{d}V - \int_\Omega \nabla\left(v\frac{1}{\mu}\nabla \cdot \mathbf{A}\right)\mathrm{d}V$$
$$+ \int_\Omega \frac{1}{\mu}\nabla \cdot \mathbf{A}\nabla v\mathrm{d}V - \int_\Omega \nabla(\varepsilon^* v\Phi)\mathrm{d}V + \int_\Omega \varepsilon^* v\nabla\Phi\mathrm{d}V + \int_\Omega \varepsilon^*\Phi\nabla v\mathrm{d}V = 0$$

Equation 2-36 (a - b) are free of source, and the excitations have to be attached on the boundary. In order to have boundary conditions plugged in, the Stokes' theorem, divergence theorem and Green's identities are used for moving the integrals to the surface, so that the terms,

$$\nabla \times v\frac{1}{\mu}\nabla \times \mathbf{A}, \qquad \nabla\left(v\frac{1}{\mu}\nabla \cdot \mathbf{A}\right), \qquad \nabla(\varepsilon^* v\Phi)$$

become surface integrals. In all, the weak formula for Equation 2-34 is given as,

$$\int_\Omega \left(\frac{1}{\mu}\nabla \times \mathbf{A}\right) \times \nabla v\mathrm{d}V + \int_\Omega \frac{1}{\mu}\nabla \cdot \mathbf{A}\nabla v\mathrm{d}V + \int_\Omega \mathrm{j}\omega v\varepsilon^* \mathbf{A}\mathrm{d}V + \int_\Omega \varepsilon^* v\nabla\Phi\mathrm{d}V + \int_\Omega \varepsilon^*\Phi\nabla v\mathrm{d}V$$
$$= -\oint_{\partial\Omega} \hat{\mathbf{n}} \times v\frac{1}{\mu}\nabla \times \mathbf{A}\,\mathrm{d}S + \oint_{\partial\Omega}\left(v\frac{1}{\mu}\nabla \cdot \mathbf{A}\right)\hat{\mathbf{n}}\,\mathrm{d}S + \oint_{\partial\Omega}(\varepsilon^* v\Phi)\hat{\mathbf{n}}\,\mathrm{d}S\,.$$

Equation 2-37

Similarly, the steps of exchanging derivation variables and moving to boundary integrals are performed on Equation 2-36 (b) as,

$$\int_\Omega \frac{1}{\mathrm{j}\omega}v\nabla \cdot \varepsilon^*\nabla\Phi d\mathrm{V} = \oint_{\partial\Omega}\frac{1}{\mathrm{j}\omega}v(\varepsilon^*\nabla\Phi \cdot \hat{\mathbf{n}})dS - \int_\Omega \frac{1}{\mathrm{j}\omega}\varepsilon^*\nabla\Phi \cdot \nabla v d\mathrm{V}\,,$$

$$\int_\Omega v\mathbf{A} \cdot \nabla\varepsilon^* d\mathrm{V} = \oint_{\partial\Omega}\varepsilon^*(v\mathbf{A} \cdot \hat{\mathbf{n}})dS - \int_\Omega \varepsilon^*\nabla \cdot (v\mathbf{A})d\mathrm{V}\,,$$

$$\nabla \cdot (v\mathbf{A}) = v\nabla \cdot \mathbf{A} + \mathbf{A} \cdot \nabla v\,.$$

The weak formula of Equation 2-35 is then obtained as,

$$\int_\Omega v{\varepsilon^*}^2\mu\Phi\mathrm{d}V + \int_\Omega \frac{1}{\mathrm{j}\omega}\varepsilon^*\nabla\Phi \cdot \nabla v\mathrm{d}V + \int_\Omega \varepsilon^* v\nabla \cdot \mathbf{A}\mathrm{d}V + \int_\Omega \varepsilon^*(\mathbf{A} \cdot \nabla v)\mathrm{d}V$$
$$= +\oint_{\partial\Omega}\varepsilon^*(v\mathbf{A} \cdot \hat{\mathbf{n}})\mathrm{d}S + \frac{1}{\mathrm{j}\omega}\oint_{\partial\Omega}v(\varepsilon^*\nabla\Phi \cdot \hat{\mathbf{n}})\mathrm{d}S$$

Equation 2-38

2.4.3 Boundary Conditions for EIT in Full Maxwell's Equations

The FEM formula based on the weak formulas in Equation 2-37 and Equation 2-38 is implemented in 2-D (Soni, et al., 2006), with boundary conditions given. The electrode model

used is the Shunt Electrode Model (SEM), which describes the electrode as a perfect electric conductor (PEC). For the non-electrode boundary, a perfect magnetic conductor (PMC) and Impedance boundary conditions (IBC) (Senior, 1960) were used. In this thesis the above two sets of BCs are called SEM-PMC and SEM-IBC respectively. It also has been mentioned that CEM can be applied based on IBC (Soni, et al., 2006), without implementing it.

For electrode regions, the BCs were implemented as,

$$\hat{\mathbf{n}} \times (\nabla\Phi + \mathrm{j}\omega\mathbf{A}) = \mathbf{M}_\mathrm{s} = \mathbf{0}\,,$$

$$\int_{S_l} \left(\phi_i \frac{1}{\mu} \nabla \cdot \mathbf{A}\right) \hat{\mathbf{n}}\,\mathrm{d}S + \int_{S_l} (\varepsilon^* \phi_i \Phi)\hat{\mathbf{n}}\,\mathrm{d}S = 0\,,$$

$$\Phi = U_l\,.$$

Equation 2-39 (a - c)

Infinite conductivity on the metal electrode is enforced by setting $\mathbf{M}_\mathrm{s}$ to vanish, which is the PEC condition in Equation 2-39 (a). The Dirichlet condition on the gauge function is used in Equation 2-39 (b), which is one of the possible gauge conditions. The potentials on the electrodes are set to voltage U_l, as voltage sources are used. As a PEC condition is used, the contact impedance is not considered. Non-exciting electrodes are not mentioned in these methods.

For the non-electrode boundary, two types of BCs are used, so called the mixed condition and IBC. The mixed condition states,

$$\int_{S_\mathrm{O}} \hat{\mathbf{n}} \times \phi_i \frac{1}{\mu} \nabla \times \mathbf{A}\,\mathrm{d}S = \int_{S_\mathrm{O}} \phi_i \mathbf{J}_\mathrm{s}\,\mathrm{d}S = 0\,,$$

$$\frac{1}{\mathrm{j}\omega} \int_{S_\mathrm{O}} \phi_i \varepsilon^* (\mathrm{j}\omega\mathbf{A} + \nabla\Phi) \cdot \hat{\mathbf{n}} dS = 0,$$

$$\mathbf{A} \cdot \hat{\mathbf{n}} = 0\,.$$

Equation 2-40 (a - c)

S_O is the non-electrode surface. The surface current density on the boundary is enforced to vanish by Equation 2-40 (a), which leads to a PMC condition. The homogeneous Neumann condition on the gauge function is used in Equation 2-40 (b). The gradient of scalar potential on normal direction is set to vanish to avoid the outward electric current with Equation 2-40 (c). The mixed condition behaves as PMC, and the spreading of the EMF is not considered.

The IBC is then used for the non-electrode boundary and compared with the SEM-PMC. IBC allows to truncate the mesh and generate a closed numerical model by adding constrains

between electric and magnetic fields (Soni, et al., 2006). It is derived based on the impedance Z of the imperfect conductive medium (Senior, 1960).

$$\mathbf{E} - (\hat{\mathbf{n}} \cdot \mathbf{E})\hat{\mathbf{n}} = \mathrm{j}Z\hat{\mathbf{n}} \times \mathbf{H}, \qquad Z = \sqrt{\frac{\mu}{\varepsilon - \mathrm{j}\frac{\sigma}{\omega}}}$$

Equation 2-41

Based on Equation 2-41, the condition is translated in terms of potentials.

$$-\mathrm{j}\omega\mathbf{A} - \nabla\Phi - (-\mathrm{j}\omega\mathbf{A} \cdot \hat{\mathbf{n}} - \nabla\Phi \cdot \hat{\mathbf{n}})\hat{\mathbf{n}} = \mathrm{j}Z\hat{\mathbf{n}} \times \frac{1}{\mu}\nabla \times \mathbf{A}$$

Separating the components in Equation 2-41 gives,

$$\frac{\partial \mathbf{E}_{t1}}{\partial t_1} = \mathrm{j}Z\frac{\partial \mathbf{H}_{t2}}{\partial t_1}, \qquad \frac{\partial \mathbf{E}_{t2}}{\partial t_2} = -\mathrm{j}Z\frac{\partial \mathbf{H}_{t1}}{\partial t_2},$$

$$-\nabla_s \cdot [\mathrm{j}\omega\mathbf{A} + \nabla\Phi - (\mathrm{j}\omega\mathbf{A} \cdot \hat{\mathbf{n}} + \nabla\Phi \cdot \hat{\mathbf{n}})\hat{\mathbf{n}}] = \nabla_s \cdot \mathbf{E} = \mathrm{j}Z\hat{\mathbf{n}} \cdot \nabla \times \mathbf{H} = \mathrm{j}Z\hat{\mathbf{n}} \cdot \nabla \times \frac{1}{\mu}\nabla \times \mathbf{A}\,.$$

So the boundary terms can be obtained as,

$$-(\mathrm{j}\omega\mathbf{A}_s + \nabla_s\Phi) = \mathrm{j}Z\mathbf{J}_s = \mathrm{j}Z\hat{\mathbf{n}} \times \frac{1}{\mu}\nabla \times \mathbf{A}$$

$$-\nabla_s \cdot (\mathrm{j}\omega\mathbf{A}_s + \nabla_s\Phi) = -\mathrm{j}Z\varepsilon^*(\mathrm{j}\omega\mathbf{A} + \nabla\Phi) \cdot \hat{\mathbf{n}}$$

Equation 2-42 (a - b)

Equation 2-42 (a) provides the surface electric current density. Equation 2-42 (b) is a Neumann condition for gauge function, which also gives the outward field based on the impedance Z.

The SEM-IBC gives better modelling for the high frequency EIT systems compared to the SEM-PMC (Soni, et al., 2006). However, the electrode model (SEM) holds back the performance.

Our FEM formula based on the weak formulas in Equation 2-37 and Equation 2-38 as implemented in 3-D is detailed in Chapter 4. The full set of gauge conditions also will be detailed in Chapter 4, where we discuss the choosing of the gauge conditions based on available extra information. Furthermore, more accurate electrode models for high frequency EIT systems are proposed and detailed, including CEM-IBC and TPM, with numerical cases studied.

2.5 Hardware and Instrument

Hardware and Instruments of EIT systems provide voltage observations on the object and excitation to the object (the orange blocks in Figure 2-1). A set of EIT hardware usually consists

of electrical sources, voltage measurement devices, digitisers, switch networks and electrodes, etc.

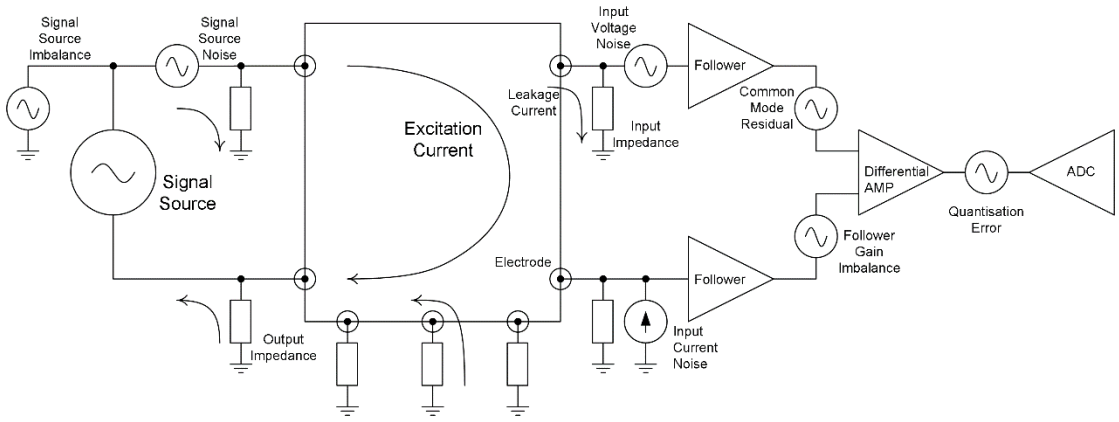

Figure 2-3 EIT System Instrument

Figure 2-3 provides general idea of an EIT instrumentation system, together with major instrumental effects and sources of inaccuracy. EIT instruments are designed to work with the algorithm in Equation 2-20. The current excitation $\mathbf{i}^d$ is implemented by applying signal sources on the object under test through electrodes. The signal sources can be current sources or current monitored voltage sources. Differential voltages ${U^d}_{l^+} - {U^d}_{l^-}$ are taken with differential amplifiers, sampled and quantised with Analog-Digital Converters (ADCs). In order to access many electrodes according to the driving and measuring patterns, a switch network is often used. As switches generally only contribute gain errors to the whole system, they are not plotted in the figure for simplicity.

The quantised signals of each driving measuring pattern compose a set of time series. The Fast Fourier Transform (FFT) is then applied to the series to separate the signals with most of the noise falling into different frequency bins. The FFT extracts the amplitudes and the phases of the quantised signals, which are fed into inverse problems (the pink block in Figure 2-1).

However, as explained, instruments of EIT systems are riddled with inaccuracies, especially for high frequency applications. Efforts are made to reduce these inaccuracies as reviewed in Section 1.3. In this section, we detail some of the major issues in the instrumentation described above.

In the EIT instrument signal chain, two types of inaccuracy occur, including deterministic errors and noise of stochastic processes. The deterministic errors are usually presented as ratios or percentages to the ideal signals, including:

- Scaling errors between the sources in any chosen pair and also between the pairs;

- The current which is leaked partially through the impedance attached on the electrodes to ground;
- The gain errors between the inputs of a differential amplifier and those across differential amplifiers.

The uncertainty caused by stochastic processes is expressed as a Power Spectral Density (PSD), as the amplitudes and phases are unpredictable. In EIT system, this uncertainty is contributed to by:

- The thermal noise in the object and all the types of impedance in the system;
- The noise of the electronic devices;
- The quantisation errors of the ADCs.

2.5.1 Deterministic Errors

2.5.1.1 The Sources

The sources scaling errors are significantly dependent on the design of the sources. The EIT systems with current sources are setting the voltage-current convertion ratio with a matched resistors network, e.g., a Howland current source (Ross, et al., 2003). However the matched ratios of resistance are hardly reaching 0.01%, and the mismatch reactance ratios are even lower at high frequencies.

The exciting current is injected through the driving electrodes only, and accurately controlled. However, as frequency increases, the output impedance of the current sources reduces. The output current partially flows through the output impedance, without having interacted with the object. The GIC and other circuits are designed to increase the output impedance of current sources. However, it is a challenge to achieve that at high frequencies, as mentioned in Chapter 1.

Using current monitored voltage sources is an approach which can potentially solve the problem. These systems include voltage sources that are monitoring the current by a monitor resistor. Operational Amplifiers (OpAmps) are used for including the monitor resistor in the feedback loop, so that the output impedance of the sources does not increase (Holder, 2005). The monitoring circuit is attached on the monitor resistor to measure the voltage difference across the monitor resistor. However, the accuracies of the monitor resistors are finite. Also there is capacitance attached to the monitoring circuit in the form of distributed parameters. When the frequency increases, the monitor resistor and distributed capacitance both cause inaccuracies.

The gains of the OpAmps also vary when frequency increases. The gain error reduces the accuracy of the current monitored voltage sources. The gain equation (Hayt, et al., 2011) of a negative feedback OpAmp is given with input terminal voltages $U_{\mathrm{i}+}$ and $U_{\mathrm{i}-}$, differential mode signal gain G_{D}, common mode gain G_{C}, source impedance $\mathbf{Z}_{\mathrm{S}}$, input impedance $\mathbf{Z}_{\mathrm{i}+}$ and $\mathbf{Z}_{\mathrm{i}-}$, gain resistor $\mathbf{Z}_{\mathrm{G}}$, feedback resistor $\mathbf{Z}_{\mathrm{F}}$ and output impedance $\mathbf{Z}_{\mathrm{O}}$ as,

$$G_{\mathrm{D}}(U_{\mathrm{i}+} - U_{\mathrm{i}-}) + G_{\mathrm{C}}\left(\frac{U_{\mathrm{i}+} + U_{\mathrm{i}-}}{2}\right) = U_{\mathrm{O}},$$

$$U_{\mathrm{i}-} = U_{\mathrm{O}}\frac{\mathbf{Z}_{\mathrm{i}-} \parallel \mathbf{Z}_{\mathrm{G}}}{(\mathbf{Z}_{\mathrm{i}-} \parallel \mathbf{Z}_{\mathrm{G}}) + \mathbf{Z}_{\mathrm{O}} + \mathbf{Z}_{\mathrm{F}}}, \qquad U_{\mathrm{i}+} = U_{\mathrm{I}}\frac{\mathbf{Z}_{\mathrm{i}+}}{\mathbf{Z}_{\mathrm{i}+} + \mathbf{Z}_{\mathrm{S}}},$$

$$G_{\mathrm{OpAmp}} = \frac{U_{\mathrm{O}}}{U_{\mathrm{I}}} = \left(\frac{G_{\mathrm{D}} + \frac{G_{\mathrm{C}}}{2}}{G_{\mathrm{D}} - \frac{G_{\mathrm{C}}}{2}}\right)\left(\frac{\mathbf{Z}_{\mathrm{i}+}}{\mathbf{Z}_{\mathrm{i}+} + \mathbf{Z}_{\mathrm{S}}}\right)\frac{(\mathbf{Z}_{\mathrm{i}-} \parallel \mathbf{Z}_{\mathrm{G}}) + \mathbf{Z}_{\mathrm{O}} + \mathbf{Z}_{\mathrm{F}}}{\frac{(\mathbf{Z}_{\mathrm{i}-} \parallel \mathbf{Z}_{\mathrm{G}}) + \mathbf{Z}_{\mathrm{O}} + \mathbf{Z}_{\mathrm{F}}}{G_{\mathrm{D}} - \frac{G_{\mathrm{C}}}{2}} + (\mathbf{Z}_{\mathrm{i}-} \parallel \mathbf{Z}_{\mathrm{G}})} \approx 1 + \frac{\mathbf{Z}_{\mathrm{F}}}{\mathbf{Z}_{\mathrm{G}}}.$$

Equation 2-43

As we are considering the non-idealities at high frequencies, the reactance of resistors in the circuit is included by using impedances. Equation 2-43 is approximated based on the assumption the G_{C} and $\mathbf{Z}_{\mathrm{O}}$ are close to zero while G_{D}, $\mathbf{Z}_{\mathrm{i}+}$ and $\mathbf{Z}_{\mathrm{i}-}$ are infinite.

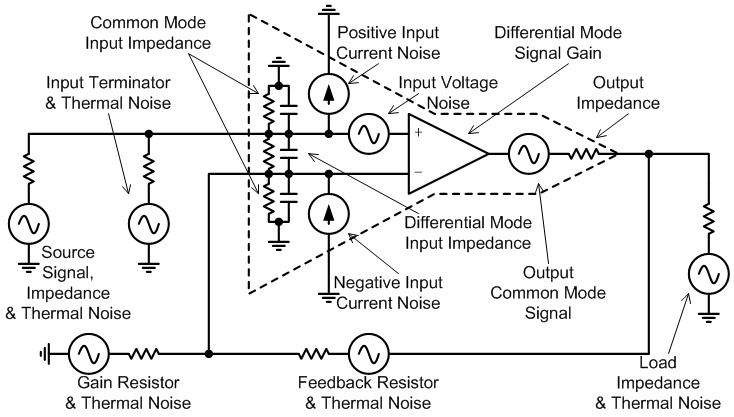

Figure 2-4 A Typical OpAmp and its Non-idealities in a Negative Feedback Setting

On the OpAmp datasheets, G_{D} is given as the open loop gain, and the common mode rejection rate is given in $-\mathrm{dB}(G_{\mathrm{C}})$. The input impedances $\mathbf{Z}_{\mathrm{i}+}$ and $\mathbf{Z}_{\mathrm{i}-}$ are given in the form of differential and common mode input impedances, as is also shown in Figure 2-4. It can be seen from datasheets these parameters are functions of frequency. When the frequency is high, none of them can be considered as infinite. Consequently, the gains of the OpAmp circuits are inaccurate and vary from device to device.

2.5.1.2 The Measuring Devices

On the voltage measuring circuits, when the frequency increases, the input impedance of the differential amplifiers is not high enough to be considered as infinite. Current is flowing through the path formed by these input impedances, driven by the potential difference between electrodes. Especially, these potential differences are not in the form of an ideal voltage source. They are not capable of maintaining the potential differences as constants. As a result, the current injected to the object is partially leaked through these measuring electrodes. The potential distribution in the object is interfered by the electrodes on the object's point of view.

In order to increase the input impedance of the measuring circuits, followers, i.e. unity gain OpAmps, are added between the differential amplifiers and the measuring electrodes. This is shown in Figure 2-3. The followers achieve high impedances, but only when the frequency does not reach the MHz range. By adding these followers, the gain errors on the measuring channels also increases, this being another disadvantage of adding the followers.

For an EIT algorithm, a great number of measurements is needed on the object surface. In order to reduce the acquisition time, multi-channel systems are usually used. For a multi-channel system, at least one differential amplifier is used in each acquisition channel. Differential amplifiers, which are responsible for obtaining the voltage differences, usually introduce significant gains. These gains of the differential amplifiers are set by on-board resistors or by on-chip feedback networks. Therefore, the accuracy of these gains needs to be considered.

Between the electrodes and each differential amplifier, there can be found the follower and switch network. As analysed, these components contribute to the inaccuracy since the gains they introduce are not identical.

2.5.2 Stochastic Processes

2.5.2.1 Thermal Noise and Noise of Devices

The power of the thermal noise P_{n} on a frequency range is given by,

$$P_{\mathrm{n}} = 4k_{\mathrm{B}}T\Delta f.$$

Equation 2-44

Here k_{B} is Boltzmann's constant, T is the temperature in kelvin, and Δf is the bandwidth. Thermal noises are considered as white and stationary, having uniform PSD and constant

probability distribution through time. Therefore the Root Mean Square (RMS) voltage can be given as,

$$U_{\mathrm{RMS}}(R) = \sqrt{P_{\mathrm{n}} R} = \sqrt{\lim_{\tau\to\infty} \frac{1}{2\tau} \int_{-\tau}^{\tau} \frac{{U_{\mathrm{n}}}^2(t)}{R} \mathrm{d}t \, R} = \sqrt{4k_{\mathrm{B}} T R \Delta f}$$

However, the voltage noise cannot be established at high frequency, due to the existence of stray capacitance (Sarpeshkar, et al., 1993). Therefore the RMS voltage on impedance $\boldsymbol{Z}$ in a bandwidth of Δf can be given as,

$$\boldsymbol{Z} = \boldsymbol{Z}_{\mathrm{C}} \parallel R, \quad U_{\mathrm{RMS}}(\boldsymbol{Z}) = \sqrt{\lim_{\tau\to\infty} \frac{1}{2\tau} \int_{-\tau}^{\tau} \frac{{U_{\mathrm{n}}}^2(t)}{R} \mathrm{d}t \, R \left(\frac{\boldsymbol{Z}_{\mathrm{C}}}{\boldsymbol{Z}_{\mathrm{C}} + R}\right)^2} = \sqrt{4k_{\mathrm{B}} T R \Delta f} \left|\frac{\boldsymbol{Z}_{\mathrm{C}}}{\boldsymbol{Z}_{\mathrm{C}} + R}\right|$$

Equation 2-45

Similar to the passive components, the uncertainty introduced by the electronic devices can be expressed through the PSD, but using different expressions. The noise generated by an OpAmp itself is referred to its input terminals, called “input referred current/voltage noise”. It means virtual noise sources are applied on the inputs of noise-free OpAmps. These noise sources are used for assessing the noise generated and measured at the output of the OpAmp, as shown in Figure 2-4. For example, an OpAmp in the setting of Figure 2-4 treats the negative input-referred current density in the following way. The current density i_{iN} is applied to Equation 2-43 as,

$$u_{\mathrm{in-}} = u_{\mathrm{iN}} + i_{\mathrm{iN}}[\mathbf{Z}_{\mathrm{i-}} \parallel \mathbf{Z}_{\mathrm{G}} \parallel (\mathbf{Z}_{\mathrm{O}} + \mathbf{Z}_{\mathrm{F}})].$$

Here $u_{\mathrm{in-}}$ is the input voltage noise density, and u_{iN} is the negative input-referred voltage noise density. The input referred current and voltage noise density can be found in the datasheets of the OpAmps, and for a specific circuit design (such as EIT systems), the output noise density can be calculated.

2.5.2.2 ADC Non-idealities and Quantisation Errors

The differential mode signals extracted by the differential amplifiers are then acquired by an ADC. Typical non-idealities, which degrade the acquisition quality, include quantisation error, Integral Linearity Error (INL), Differential Linearity Error (DNL), offset and gain errors etc.

The quantisation error $q(t)$ is the difference between the signal $U(t)$ and the quantised finite states series, and it is depended on the input signal of the ADC. The maximum amplitude $q(t)$ is the quantisation resolution of the ADC q_0.

$$q(t) = U_{d,\delta}(t) - x(n) \otimes \mathrm{rect}(t/t_0), \qquad q(t) \in (0, q_0).$$

Equation 2-46

$x(n)$ is the sampled finite states series, and n is the index of the samples. $\mathrm{rect}(t/t_0)$ is the sampling window, t_0 is the sampling interval, $\otimes$ is the convolution operator.

Though the quantisation errors of sine waves do not exhibit a clear interdependence, periodicity yields a discrete spectrum, thus whiteness (uniform spectrum) in the strict sense certainly does not hold (Widrow & István, 2008). Investigations have shown, when quantising a sine wave, the PSD of the $q(t)$ is quasi-uniform with spikes appearing at the frequencies f_{Spurious}, (Claasen & Jongepier, 1981), as follows,

$$f_{\mathrm{Spurious}} = \frac{2\pi A}{q_0} m f_0.$$

Equation 2-47

Here, m is any integer number, while A is the amplitude of the signal being quantised and f_0 is the frequency of the sine wave. Therefore, once the signal frequency, amplitude and the quantisation resolution together have avoided the spurious frequencies, the quantisation error can be considered quasi-uniform.

The DNL is the error between the actual voltage of two adjacent quantised states and q_0, which is the voltage it is supposed to be ideally. Similarly, the INL is the error between the actual voltage of all the quantised states and the straight line $q_0 d$, where $d = [0,1,\cdots,2^D - 1]$ is the index of the quantised states (digital codes) and D is the total quantisation bits (IEEE-SA Standards Board, 2000). The error of DNL and INL is due to the implementation of the ADCs, in contrast to $q(t)$, which is a fundemantal error. DNL and INL contribute to the quantised series by adding uncertenties on every sample. The Effective Number of Bits (ENoB) instead of D is usually used for assessment of whether to include the influence of the DNL and INL (Flores, et al., 2004; Platonov, et al., 2006).

$$q_0 = A_{\mathrm{FS}} 2^{-D}, \qquad q_{0\mathrm{ENoB}} = A_{\mathrm{FS}} 2^{-\mathrm{ENoB}}.$$

For those ADCs sampling at hundreds of MHz, clock jitter and phase noise play an important role in the ENoB. We ignore it here for low sampling rate systems.

2.5.3 Analysis and Discussions

In order to analyse the inaccuracies contributed by the EIT instruments, we introduce the typical procedure of extracting the amplitude and phase of the EIT measurements.

In EIT systems, linear relationship holds for both algorithms (can be seen from Equation 2-16) and instruments (can be seen from Figure 2-3). Therefore the frequency of the measured signal is not spread or shifted from the excited frequency, ideally. The signal bandwidth can be designed very narrow, and a Fourier transform can be used for analysing this narrow bandwidth signal.

ADCs are used for not only quantising but also sampling the signal (Pelgrom, 2010) to produce discrete time serises $x(n)$, as shown in Equation 2-46. The amplitudes and phases of $x(n)$ are extracted by applying the discrete Fourier transform (DFT). Furthermore, the length of the sampling series N, is normally designed to be $N = 2^M$ to use the FFT algorithm, where M is an integer,

$$X(k) = \sum_{n=0}^{N-1} x(n) e^{-\mathrm{j}2\pi k\frac{n}{N}}, \qquad N = 2^M .$$

Equation 2-48 (a - b)

Here, k is the index in the discrete frequency domain, and n is the index in the sampled time domain. The amplitudes and phases of the sampled signal become the coefficients of the frequency bases given by the FFT, as shown in Figure 2-5.

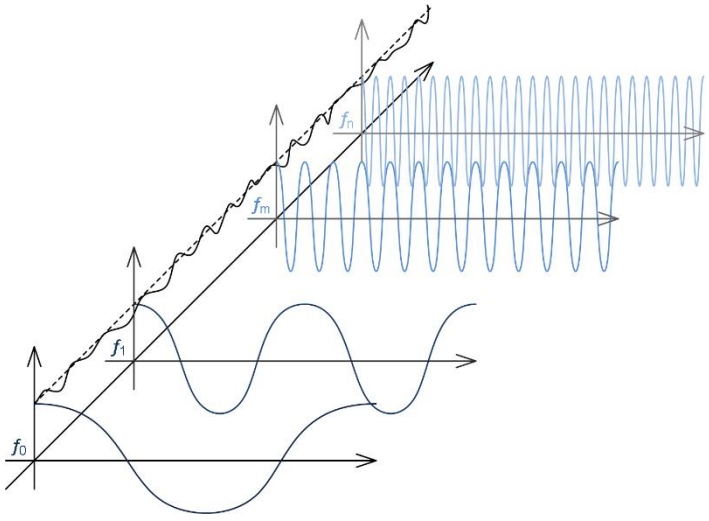

Figure 2-5 Fourier Transforms of a Signal with Quasi-Uniform Spectrum

According to previous discussions, the quantised signal can be assumed to be

$$x(n) = \mathrm{Real}\{G_{\mathrm{ADC}} c_0 e^{\mathrm{j}\varphi_0} e^{\mathrm{j}\omega_0 n t_0}\} + G_{\mathrm{ADC}} n(nt_0) + q(nt_0) .$$

Equation 2-49

Here, G_{ADC} is the gain of the ADC, c_0 is the amplitude of the *signal*, φ_0 is the phase of the *signal* and ω_0 is the angular frequency of the *signal*. The signal here is the sum of all the

deterministic components. It includes the scaling and gain errors, and also the current that is partially leaked through unknown paths. $n(nt_0)$ are the noises resulted by the system and sampled by the ADC. $q(nt_0)$ is the quantisation error in every sample.

Fourier analysis provides the amplitudes and phases of each frequency basis as,

$$X(k) = \sum_{n=0}^{N-1} x(n) e^{-\mathrm{j}2\pi k \frac{n}{N}}.$$

So the signal $\mathrm{Real}\{c_0 e^{\mathrm{j}\varphi_0} e^{\mathrm{j}\omega_0 n t_0}\}$ is transferred into the $(k_0+1)^{\mathrm{th}}$ bin (and another bin for the imaginary part with Euler's equation) in the discrete frequency domain as,

$$k_0 = \left[\frac{\omega_0 t_0 N}{2\pi}\right]_{\mathrm{Int}} = \left[\frac{f_0 N}{f_\mathrm{s}}\right]_{\mathrm{Int}},$$

$$X(k_0) = \frac{N}{2} G_{\mathrm{ADC}} c_0 e^{\mathrm{j}\varphi_0} + G_{\mathrm{ADC}} \sum_{n=0}^{N-1} n(nt_0) e^{-\mathrm{j}2\pi k_0 \frac{n}{N}} + \sum_{n=0}^{N-1} q(nt_0) e^{-\mathrm{j}2\pi k_0 \frac{n}{N}}.$$

Equation 2-50 (a - b)

The length of the sampling series N determines the frequency resolution of $X(k)$. By assuming the bandwidth of the signal is the same to the frequency resolution $f_\mathrm{s} N^{-1}$, the uncertainties added to $X(k_0)$ are modelled by $n(nt_0)$ and $q(nt_0)$.

We assume $n(t)$ to be a Gaussian white noise, which is a normal (Gaussian) distributed serially uncorrelated stationary stochastic process, denoted by $n^{0,\sigma_\mathrm{n}}(t)$, with expectation $\mu = 0$ and standard deviation $\sigma = \sigma_\mathrm{n}$. Stationary processes yield σ_n to not be a function of t (Jones & Smith, 2010). However, in general the Fourier transform of stationary stochastic processes does not exist, as invariance the σ_n will result in infinite energy (Vasilescu, 2006). On the other hand, an infinite bandwidth uniform spectrum signal does not exist, which also results in infinite power (Iniewski, 2008).

In practice however, a finite observation time and a finite signal (or noise) power can be analysed, such as Equation 2-50, which truncates the time period to be $[0, t_0 N]$. Also, Equation 2-45 shows the bandwidth $n(t)$ is limited when establishing it based on impedances.

Therefore $n(t)$ is assumed as stationary in $[0, t_0 N]$, of uniform spectrum in $[0, f_\mathrm{s}]$, with Gaussian distributed noise with zero mean and variance ${\sigma_\mathrm{n}}^2$, and its uncertainty contributed to $X(k_0)$ can be given as a sinc function, and is approximately equal to σ_n (Jerri, 1977).

The stochastic processes $q(nt_0)$ can be assumed as $q_\mathrm{s}(t)$ is stationary in $[0, t_0 N]$ and of uniform spectrum in $[0, f_\mathrm{s}]$, as discussed in Equation 2-47. The uniform distribution is

commonly used for the quantisation error, and results in the contribution to $X(k_0)$ being $q_0/2\sqrt{3}$ (Widrow & István, 2008).

In all, Equation 2-50 (b) becomes Equation 2-51, with $e^{i\varphi_n}$ and $e^{i\varphi_q}$ indicating the uncertain phase of the noise and the quantisation error.

$$X(k_0) \approx \frac{N}{2} G_{\mathrm{ADC}} c_0 e^{i\varphi_0} + G_{\mathrm{ADC}} \sigma_n e^{i\varphi_n} + \frac{q_0}{2\sqrt{3}} e^{i\varphi_q}.$$

Equation 2-51

There is one more inaccuracy effect, but more related to the EIT systems design, known as spetral leakage. Recalling Equation 2-50 (b), $c_0 e^{i\varphi_0}$ are obtained relying on the spectrum of $x_0(n)$ to fall in a single FFT bin. However, if the integer requirement in Equation 2-50 (a) is not satisfied, the spectrum of $x_0(n)$ shall leak to other FFT bins.

Spetral leakage can be partially avoided by carefuly choosing the signal frequencies, by considering Equation 2-48 (b), Equation 2-50 (a) and Equation 2-47 together. Other methods used in obtaining accurate amplitudes and phases include applying windows and apFFT (Fu, et al., 2012; Li, 2014), etc.

Considering Equation 2-51, the differential voltages $U_{d,\delta}(t)$, and all the deterministic errors go into $c_0 e^{i\varphi_0}$. Together, the gain by $NG_{\mathrm{ADC}}/2$ is applied to them. The noises, contributed by the thermal noise and the electronic devices, go into $\sigma_n e^{i\varphi_n}$. G_{ADC} as gain is applied to them, but not accumulated by N. The quantisation errors appear in $\left(q_0 e^{i\varphi_q}\right)/2\sqrt{3}$, which is limited to the same order of magnitude as the quantisation resolution q_0.

We discuss these signals based on the expression, some calculations and some basic assumptions of EIT systems,

- Intuition concepts suggest that the more samples aquired, the more accurate the result obtained by the accumulation processing. But a long acquisition time for each measurement is not appropriate for EIT system, as the admittivity distribution may vary on a longer time scale. Also a significent amount of data may be produced as a reconstruction process requires thousands of measurements.
- G_{ADC} applies to only the input signals of the ADCs, not quantisation errors, which means a large gain is equivalent to reducing the quantisation error. But normally it is a relatively small number compared to N, and it is not easy to make it too large without saturating the input signal or generating non-linear terms.

- Based on the input-referred noises of some commonly used components from the datasheets, we calculated the overall RMS noise σ_{n} is of the order of $10\mu\mathrm{V}$.
- The quantisation error of a typical ADC chip (ADC14L020, 20Msps 14-bit resolution), can be calculated from its ENoB and its full scale range. It is to the order of $100\mu\mathrm{V}$.
- Compared to the quantisation errors and the noises, the signal amplitude $NG_{\mathrm{ADC}}c_0/2$ is normally much larger. This implies the deterministic errors are much larger than the uncertainty caused by stochastic processes.
- The scaling errors across the sources, and the gain errors across measurement channels can be as large as 1%. However, these errors can be calibrated out in a carefully designed system. Figure 2-3 and analysis show that these errors are not dependent on the admittivity distribution.
- The current leakages however, have to be handled differently, as their effect relies on the unknown admittivity of the object. Calibration processes can only obtain the output impedances of the sources and input impedances of the measurement circuits. These impedances are needed for solving the current leakages together with the forward problems.

2.6 Summary

In this chapter, we have introduced the general problem EIT is solving, and the procedure of the EIT algorithm.

The typical forward problem and inverse problem are detailed, including the concepts of electrode models, ill-posed problems, regularisation and iterative methods. We introduced the full Maxwell's equations in potential formula form for solving EIT forward problems.

We then analysed typical EIT hardware systems. Comparisons between different kinds of inaccuracies were made. We have concluded that current leakages, as one of the instrumental effects, have to be considered for higher accuracy systems at higher frequencies. They need to be modelled and solved together with the forward problems.

In the following chapters, we will detail the methods of solving instrumental effects together with different forward problems, and also the inverse problem.

Chapter 3 EIT Forward Problems with IEM

This chapter is based on Zhang, W. & Li, D., 2014. An instrumental electrode model for solving electrical impedance tomography forward problems. *Physiological Measurement.* (Zhang & Li, 2014).

3.1 Introduction

In the Chapter 1, we have introduced the state of the art of the EIT problems. Two major problems in extending the frequency usage of EIT has been brought forward, including the electrode models are not suitable for high frequencies, and the quasi-static assumption conflicts with the extending the frequency. In the previous chapter, we have introduced the typical EIT problems and algorithms, and also analysed general hardware systems of EIT. We have concluded that the instrumental effects have to be considered, modelled in the electrode models when solving the forward problems.

In this chapter, we will detail the method we used for solving the forward problems with instrumental effects considered. The proposed instrumental electrode model (IEM) considers the effects on the potential distribution in the volume caused by hardware non-idealities, at higher frequencies. An extra boundary condition is introduced accordingly to the CEM in the forward problem.

In this chapter, the concept of the instrumental impedance is first introduced. Numerical methods of solving forward problems with IEM are detailed in Section 3.3, which is modified from the commonly used CEM numerical methods. Cases studies are in Section 3.4, including two different EIT problems, and comparisons across different forward solvers. Full Maxwell's analysis is also done to check the effectiveness of the quasi-static assumption (the second major problem mentioned). Summaries and conclusions take place in the Section 3.5. For the reason that analysis is done for current sources, an IEM which is suitable for voltage sources has been given as Appendix in Section 3.6.

3.2 IEM Boundary Conditions

To solve the partial differential Equation 2-14, proper boundary conditions should be applied to describe the current injection and model the behaviour of electrodes. The CEM (Cheng, et al., 1989; Somersalo, et al., 1992; Vauhkonen, et al., 1999) is commonly used and has been experimentally proven to be accurate in low frequency EIT systems, and detailed in Section 2.2.3. The proposed IEM is based on the CEM, but instrumental non-ideality is given additional

consideration within the electrode model. The CEM boundary conditions can be understood from Figure 3-1,

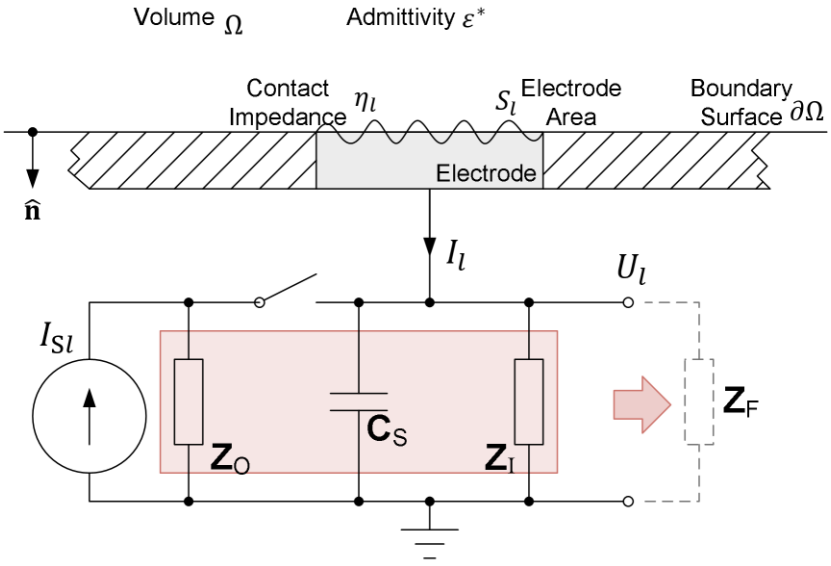

Figure 3-1 EIT electrode geometry and circuit model. (Zhang & Li, 2014)

where Ω is the volume to be solved,

$\partial\Omega$ is the surface of the volume,

I_{Sl} is the current output by the current source which is connected with the l^{th} electrode,

$\mathbf{Z}_O$ is the output impedance of the current source,

$\mathbf{C}_S$ is the total parasitic capacitance of the cable, PCB trace and electrode itself,

$\mathbf{Z}_I$ is the input impedance of the voltage measurement device, and

$\mathbf{Z}_F$ is the virtual impedance, equivalent to the total effect of the above impedance.

For the remaining symbols in the figure we kept the previous definitions.

Referring to the EIT electrode model in Figure 3-1, each electrode can be configured either as a driving electrode (with the switch closed and the current source connected to the electrode) or as a measuring electrode (with the switch opened and the current source disconnected). The current source has an output impedance $\mathbf{Z}_O$ with the electrode contributing some parasitic capacitance $\mathbf{C}_S$ to ground, and the measurement circuit can be modelled with an input impedance $\mathbf{Z}_I$. The current source generates a current of I_{Sl}.

In the ideal situation, $\mathbf{Z}_O$ and $\mathbf{Z}_I$ are assumed to be infinite, $\mathbf{C}_S$ to be zero, and all of the current generated from the source goes into the electrode, $I_{Sl} = I_l$, when the switch is closed. When the switch is opened (the circuit acts as a measurement circuit), $I_l = 0$.

The frequency of interest for many EIT applications extends up to several MHz, and difficulties therefore emerge when applying the CEM. Some of the assumptions in the ideal situation mentioned above need to be re-examined and modified, since non-ideal loading effects are not negligible in the MHz frequency range.

Firstly, the output impedance $\mathbf{Z}_{\mathrm{O}}$ of the current source and input impedance $\mathbf{Z}_{\mathrm{I}}$ of the measurement circuit are not infinitely high. The circuit front-ends can easily contribute a few pF of parasitic capacitance contributed by the devices, therefore reducing input/output impedances and degrading the performance in the MHz range. In addition the parasitic capacitance of the cable, PCB trace and electrode itself (modelled by $\mathbf{C}_{\mathrm{S}}$ in general) is not negligible. Although $\mathbf{C}_{\mathrm{S}}$ almost remains constant across the frequency range, the equivalent impedance of the capacitance $1/\mathrm{j}\omega\mathbf{C}_{\mathrm{S}}$ reduces and starts loading the front-ends as the frequency increases.

At high frequencies, the electrode current flows therefore behave differently. In contrast to the assumption made by the CEM, at high frequencies some portion of I_{Sl} flows through $\mathbf{Z}_{\mathrm{O}}$, $\mathbf{Z}_{\mathrm{I}}$ and $\mathbf{C}_{\mathrm{S}}$ (this part is negligible when the frequency is low) rather than entirely into the electrode. Also, for electrodes in measuring mode (with the switch open), there is some current flowing through $\mathbf{Z}_{\mathrm{I}}$ and $\mathbf{C}_{\mathrm{S}}$ to ground, as I_l, even though there is no driving current I_{Sl}.

Analytical calculations based on typical circuit parameters provide some indication of typical input and output impedances. When the operating frequency is 1MHz, the output impedance $\mathbf{Z}_{\mathrm{O}}$ typically comprises a resistance of 5MΩ in parallel with a capacitance of 4pF and the input impedance $\mathbf{Z}_{\mathrm{I}}$ comprises a resistance of 10MΩ in parallel with a capacitance 4pF (This comes from an easily accessible front-end amplifier, for example, 4.5pF from the Analog Devices AD8065 or 6pF from the Texas Instruments OPA2365.) and a parasitic capacitance $\mathbf{C}_{\mathrm{S}}$ of 2pF. At 1MHz, the overall instrumental effect is modelled with a virtual impedance $\mathbf{Z}_{\mathrm{F}}$, as shown in Figure 3-1, and becomes 16 kΩ in driving mode and 26 kΩ in measuring mode, which is *far* from infinite.

For EIT systems working at lower frequencies (< 500kHz), the GIC (Oh, et al., 2007; Ross, et al., 2003; Oh, et al., 2011) is widely used to alleviate the effects of capacitive loading, but it performs poorly at frequencies higher than 500kHz.

From the above calculations, it is obvious that there is a significant “leakage current” flowing through the instrumental path (with an equivalent impedance of $\mathbf{Z}_{\mathrm{F}}$) from the current source

(in the driving mode) or from the imaging volume (in the measuring mode) and for accurate representation this leakage current must be included when solving the system matrix.

We can reformulate the electrode model to include the "leakage currents" in the forward problem. We obtain, in the driving mode,

$$I_{Sl} + \frac{U_l - U_{\mathrm{GND}}}{\mathbf{Z}_{\mathrm{F}}} + I_l = 0\,,$$

and in the measuring mode,

$$\frac{U_l - U_{\mathrm{GND}}}{\mathbf{Z}_{\mathrm{F}}} + I_l = 0\,,$$

combined as

$$I_{Sl} + \frac{U_l}{\mathbf{Z}_{\mathrm{F}}} + I_l = 0\,.$$

Equation 3-1

Together with the CEM BCs, we have the IEM as

$$\varepsilon^* \nabla\Phi \cdot \hat{\mathbf{n}} = 0 \text{ (Surface not on electrodes)},$$

$$\int_{S_l} \varepsilon^* \nabla\Phi \cdot \hat{\mathbf{n}}\, \mathrm{d}S = I_l \left(\text{Surface on } l^{\mathrm{th}} \text{ electrode}\right),$$

$$\Phi + \eta_l \varepsilon^* \nabla\Phi \cdot \hat{\mathbf{n}} = U_l,$$

$$I_{Sl} + \frac{U_l}{\mathbf{Z}_{\mathrm{F}}} + I_l = 0,$$

$$\sum_{l=1}^{L} I_l = 0.$$

Note that, with the external circuit attached, the total current generated from current sources $\sum_{l=1}^{L} U_l$ may not be balanced any more (as $\mathbf{Z}_{\mathrm{F}}$ on different driving electrodes may vary), but the total charge in the volume to be solved $\sum_{l=1}^{L} I_l$ has to be zero.

In our IEM formulations, the potential balance condition $\sum_{l=1}^{L} U_l = 0$ used in CEM is removed. As the CEM does not have a reference ground, whereas the IEM embeds one in the instrumental circuit.

When the operating frequency is low enough, the current flowing through the instrumental path $\mathbf{Z}_{\mathrm{F}}$ is negligible, in which case the IEM will behave just like the CEM.

The IEM provides a method for describing non-ideal hardware behaviours and is therefore able to obtain accurate solutions of the forward problem with knowledge of the hardware, unlike the CEM which assumes perfect hardware.

3.3 Numerical Implementation and Finite Element Method

Finite element methods (FEM) are used for solving the forward model with the IEM. Our programs were developed based on the software package EIDORS (Electrical Impedance and Diffuse Optical Reconstruction Software). EIDORS is a Matlab toolkit for three-dimensional EIT (Polydorides & Lionheart, 2002; Adler & Lionheart, 2006). To apply our IEM model, similar formulations were derived, but with modifications.

3.3.1 Numerical Modelling with IEM

We take the same steps which deriving CEM forward problems have taken until Equation 2-16 (a - b). And to constrain I_l in Equation 2-16 (b), we have the additional Equation 3-1, with the known instrument impedance as the factor,

$$\frac{U_l}{\mathbf{Z}_{\mathrm{F}}} + I_l = -I_{\mathrm{S}l}.$$

Equation 3-2

Imposing the constraint of charge balance, Equation 3-2 becomes

$$\frac{U_L}{\mathbf{Z}_{\mathrm{F}}} - \sum_{l=1}^{L-1} I_l = -I_{\mathrm{S}l}.$$

Equation 3-3

Finally, we obtain

$$\begin{cases} \int_{\Omega} \varepsilon^* \nabla v \cdot \nabla \Phi \, \mathrm{d}V + \sum_{l=1}^{L} \frac{1}{\eta} \int_{S_l} v\Phi \, \mathrm{d}S - \sum_{l=1}^{L} \frac{U_l}{\eta} \int_{S_l} v \, \mathrm{d}S = 0 \,, \\ \int_{S_l} \frac{U_l - \Phi}{\eta} \mathrm{d}S - I_l = 0 \,, \\ \frac{U_l}{\mathbf{Z}_{\mathrm{F}}} + I_l = -I_{\mathrm{S}l} \,, l = 1,2,3, \dots, L-1, \\ \frac{U_L}{\mathbf{Z}_{\mathrm{F}}} - \sum_{l=1}^{L-1} I_l = -I_{\mathrm{S}l}. \end{cases}$$

Equation 3-4 (a - d)

3.3.2 Discretisation and Shape Function

The governing equation of EIT forward problems has been reduced to Equation 3-4 with a trial function and IEM BCs. Equation 3-4 is in the weak form of Equation 2-12, which can be discretised using Galerkin's method to the form of Equation 2-13. In Equation 2-13, there are bases of the domain ϕ_js. In FEM, the bases in each element are also known as the shape functions which are determined by the coordinates of the nodes. The number of nodes in an element (discretised small domain) is defined by the order of the shape functions and the physical dimension of the problem. In our models, the first order shape functions tetrahedron elements in 3-D are used.

The method called the *Isoparametric*, which isolate the global coordinate system from the local element, is used. The local element is represented in Barycentric coordinate system, which looks the same to each element. The shape functions (Strang & Fix, 1973) for tetrahedrons in Barycentric coordinate are given as,

$$\phi_1(x,y,z) = \xi_1(x,y,z)$$

$$\phi_2(x,y,z) = \xi_2(x,y,z)$$

$$\phi_3(x,y,z) = \xi_3(x,y,z)$$

$$\phi_4(x,y,z) = 1 - \xi_1(x,y,z) - \xi_2(x,y,z) - \xi_3(x,y,z)$$

Equation 3-5

$$\begin{bmatrix} \frac{\partial \phi_i}{\partial x} \\ \frac{\partial \phi_i}{\partial y} \\ \frac{\partial \phi_i}{\partial z} \end{bmatrix} = \begin{bmatrix} \frac{\partial x}{\partial \xi_1} & \frac{\partial y}{\partial \xi_1} & \frac{\partial z}{\partial \xi_1} \\ \frac{\partial x}{\partial \xi_2} & \frac{\partial y}{\partial \xi_2} & \frac{\partial z}{\partial \xi_2} \\ \frac{\partial x}{\partial \xi_3} & \frac{\partial y}{\partial \xi_3} & \frac{\partial z}{\partial \xi_3} \end{bmatrix}^{-1} \begin{bmatrix} \frac{\partial \phi_i}{\partial \xi_1} \\ \frac{\partial \phi_i}{\partial \xi_2} \\ \frac{\partial \phi_i}{\partial \xi_3} \end{bmatrix} = \mathbf{J}^{-1} \begin{bmatrix} \frac{\partial \phi_i}{\partial \xi_1} \\ \frac{\partial \phi_i}{\partial \xi_2} \\ \frac{\partial \phi_i}{\partial \xi_3} \end{bmatrix} = \begin{bmatrix} x_1 - x_4 & y_1 - y_4 & z_1 - z_4 \\ x_2 - x_4 & y_2 - y_4 & z_2 - z_4 \\ x_3 - x_4 & y_3 - y_4 & z_3 - z_4 \end{bmatrix}^{-1} \begin{bmatrix} \frac{\partial \phi_i}{\partial \xi_1} \\ \frac{\partial \phi_i}{\partial \xi_2} \\ \frac{\partial \phi_i}{\partial \xi_3} \end{bmatrix}$$

Equation 3-6

And the integral under Barycentric coordinates in triangle and tetrahedron elements, is given as follows (Eisenberg & Malvern, 1973)

$$\int_{\mathrm{S}} {\xi_1}^a {\xi_2}^b (1 - \xi_1 - \xi_2)^c \mathrm{dS} = \frac{a!\, b!\, c!}{(a+b+c+2)!} 2|\mathrm{S}|$$

$$\int_{\mathrm{V}} {\xi_1}^a {\xi_2}^b {\xi_3}^c (1 - \xi_1 - \xi_2 - \xi_3)^d \mathrm{dV} = \frac{a!\, b!\, c!\, d!}{(a+b+c+d+3)!} 6|\mathrm{V}|$$

Equation 3-7 (a - b)

3.3.3 FEM Forward Problem in Matrix Form

With the help of Barycentric coordinate system, we, here, explain the process of bring the forward problem in to matrix form with FEM.

Equation 3-4 (a - d) gives the weak formula of the problem with the boundary conditions inserted. With the Galerkin method, we discretize the potential distribution Φ into piecewise linear distribution Φ_{N}, which can be represented by the bases ϕ_j, as following,

$$\Phi_N = \sum_{j=1}^{N} \mathrm{u}_j \phi_j,$$

And replace the trial function v with shape functions ϕ_i, so obtain,

$$\int_{\Omega} \varepsilon^* \nabla\phi_i \cdot \nabla \sum_{j=1}^{N} \mathrm{u}_j \phi_j \,\mathrm{d}V + \sum_{l=1}^{L} \frac{1}{\eta_l} \int_{S_l} \phi_i \sum_{j=1}^{N} \mathrm{u}_j \phi_j \,\mathrm{d}S - \sum_{l=1}^{L} \frac{U_l}{\eta_l} \int_{S_l} \phi_i \,\mathrm{d}S = 0\,,$$

$$\frac{1}{\eta_l} \int_{S_l} \left(U_l - \sum_{j=1}^{N} \mathrm{u}_j \phi_j \right) \mathrm{d}S - I_l = 0\,,$$

$$\frac{U_l}{\mathbf{Z}_{\mathrm{F}}} + I_l = -I_{\mathrm{S}l}, \qquad l = 1,2,3,\ldots,L-1\,,$$

$$\frac{U_L}{\mathbf{Z}_{\mathrm{F}}} - \sum_{l=1}^{L-1} I_l = -I_{\mathrm{S}l}.$$

Following the steps of Galerkin method as shown in Equation 2-13, the sum is taken out of the bilinear form, and gives,

$$\sum_{j=1}^{N} \mathrm{u}_j \int_{\Omega} \varepsilon^* \nabla\phi_i \cdot \nabla\phi_j \,\mathrm{d}V + \sum_{l=1}^{L} \sum_{j=1}^{N} \mathrm{u}_j \frac{1}{\eta_l} \int_{S_l} \phi_i \phi_j \,\mathrm{d}S - \sum_{l=1}^{L} \frac{U_l}{\eta_l} \int_{S_l} \phi_i \,\mathrm{d}S = 0\,,$$

$$-\sum_{j=1}^{N} \frac{\mathrm{u}_j}{\eta_l} \int_{S_l} \phi_j \mathrm{d}S + \frac{U_l}{\eta_l} S_l - I_l = 0\,,$$

$$\frac{U_l}{\mathbf{Z}_{\mathrm{F}}} + I_l = -I_{\mathrm{S}l}, \qquad l = 1,2,3,\ldots,L-1\,,$$

$$\frac{U_L}{\mathbf{Z}_{\mathrm{F}}} - \sum_{l=1}^{L-1} I_l = -I_{\mathrm{S}l}.$$

Equation 3-8 (a - d)

Then, taking the unknowns u_j, U_l and I_l out of the inner products, and it leads to the system matrix in the form

$$\begin{bmatrix} \boldsymbol{A}+\boldsymbol{B} & \boldsymbol{C} & \mathbf{0}^{N\times L} \\ \boldsymbol{C}^{\mathrm{T}} & \boldsymbol{D} & -\mathbb{I}^{L} \\ \mathbf{0}^{L\times N} & \boldsymbol{E} & \boldsymbol{F} \end{bmatrix} \begin{bmatrix} \mathbf{u} \\ \mathbf{v} \\ \mathbf{i} \end{bmatrix} = \begin{bmatrix} \mathbf{0}^{(N+L)\times 1} \\ -\mathbf{i_S} \end{bmatrix},$$

$$\boldsymbol{A} = \int_{\Omega} \varepsilon^{*} \nabla\phi_i \cdot \nabla\phi_j \,\mathrm{d}V \in \mathbb{C}^{N\times N},$$

$$\boldsymbol{B} = \sum\nolimits_{l=1}^{L} \frac{1}{\eta_l} \int_{S_l} \phi_i \phi_j \,\mathrm{d}S \in \mathbb{C}^{N\times N},$$

$$\boldsymbol{C} = -\frac{1}{\eta_l} \int_{S_l} \phi_i \,\mathrm{d}S \in \mathbb{C}^{N\times L}, \qquad \boldsymbol{D} = \mathrm{diag}\left\{\frac{S_l}{\eta_l}\right\} \in \mathbb{C}^{L\times L},$$

$$\boldsymbol{E} = \mathrm{diag}\left\{\frac{1}{\mathbf{Z}_{\mathrm{F}}}\right\} \in \mathbb{C}^{L\times L}, \qquad \boldsymbol{F} = \begin{bmatrix} 1 & 0 & 0 & 0 \\ 0 & 1 & 0 & 0 \\ 0 & 0 & \ddots & 0 \\ -1 & -1 & \cdots & 0 \end{bmatrix} \in \mathbb{C}^{L\times L},$$

Equation 3-9

where $\mathbb{I}^{L}$ is identity matrix, $\mathbf{u}^{N\times 1}$ is the nodal potential vector (made up with u_j), $\mathbf{v}^{L\times 1}$ is the electrode voltage vector(made up with U_l), $\mathbf{i}^{L\times 1}$ is the electrode current vector (made up with I_l), $\mathbf{i_S}^{L\times 1}$ is the source injection current vector (made up with $I_{\mathrm{S}l}$), $\phi_{i,j}$ is the shape functions, *N* is the total number of the vertices, and i, j are the index of vertices.

In the Equation 3-9, the left up corner of the system matrix consists with $\boldsymbol{A}+\boldsymbol{B}$, $\boldsymbol{C}$, $\boldsymbol{C}^{\mathrm{T}}$ and $\boldsymbol{D}$ are the same to the system matrix given by the boundary conditions CEM. Compared with the CEM, our IEM adds the matrix $\mathbb{I}^{L}$ providing extra freedom to the electrode current, and regulates the electrode current by $\boldsymbol{E}$ and $\boldsymbol{F}$. When the frequency increases with the $\mathbf{Z}_{\mathrm{F}}$ reduced, $\boldsymbol{E}\mathbf{v}$ increases and therefore reduces the current applied on the products $\boldsymbol{C}^{\mathrm{T}}\mathbf{u}$ and $\boldsymbol{D}\mathbf{v}$ in the driving mode. For the measuring mode, (although the imposed source current $I_{\mathrm{S}l}$ is zero) $\boldsymbol{E}\mathbf{v}+\boldsymbol{F}\mathbf{i}$ allows the current to flow through electrodes. While on the other hand, if the frequency is low, $\mathbf{Z}_{\mathrm{F}}$ tends to infinity and the system matrix is equivalent to the CEM. In addition, the process to find the ground node is removed, as the ground node is embedded in the IEM formulations.

To assemble the FEM matrix form, we take the first term $\boldsymbol{A}$ first. The formula, which consists inner product of the gradient of shape functions, is usually called stiffness matrix in stress applications of FEM, and we borrow the name here. By inserting the gradient of the shape function respect to global coordinates then, we have,

$$\sum_{j=1}^{N} \mathrm{u}_j \int_{\Omega} \varepsilon^* \nabla\phi_i \cdot \nabla\phi_j \, \mathrm{d}V = \sum_{j=1}^{N} \mathrm{u}_j \int_{\Omega} \varepsilon^* \begin{bmatrix} \frac{\partial\phi_i}{\partial x} \\ \frac{\partial\phi_i}{\partial y} \\ \frac{\partial\phi_i}{\partial z} \end{bmatrix}^{\mathrm{T}} \begin{bmatrix} \frac{\partial\phi_j}{\partial x} \\ \frac{\partial\phi_j}{\partial y} \\ \frac{\partial\phi_j}{\partial z} \end{bmatrix} \mathrm{d}V,$$

and for the fact that the derivative of the shape functions in every element is constant, the integral is removed therefor,

$$\sum_{j=1}^{N} \mathrm{u}_j \int_{\Omega} \varepsilon^* \begin{bmatrix} \frac{\partial\phi_i}{\partial x} \\ \frac{\partial\phi_i}{\partial y} \\ \frac{\partial\phi_i}{\partial z} \end{bmatrix}^{\mathrm{T}} \begin{bmatrix} \frac{\partial\phi_j}{\partial x} \\ \frac{\partial\phi_j}{\partial y} \\ \frac{\partial\phi_j}{\partial z} \end{bmatrix} \mathrm{d}V = \sum_{j=1}^{N} \mathrm{u}_j \sum_{e=1}^{\mathrm{E}} \varepsilon^{*e} V^e \begin{bmatrix} \frac{\partial\phi^e{}_i}{\partial x} \\ \frac{\partial\phi^e{}_i}{\partial y} \\ \frac{\partial\phi^e{}_i}{\partial z} \end{bmatrix}^{\mathrm{T}} \begin{bmatrix} \frac{\partial\phi^e{}_j}{\partial x} \\ \frac{\partial\phi^e{}_j}{\partial y} \\ \frac{\partial\phi^e{}_j}{\partial z} \end{bmatrix}$$

Here, ε^{*e} is the admittivity of the element e, V^e is the volume and $\phi^e{}_i$ is part of the ϕ_i which is the element e. By extend the sum of the node index j in the equation, there is,

$$\sum_{j=1}^{N} \mathrm{u}_j \sum_{e=1}^{\mathrm{E}} \varepsilon^{*e} V^e \begin{bmatrix} \frac{\partial\phi^e{}_i}{\partial x} \\ \frac{\partial\phi^e{}_i}{\partial y} \\ \frac{\partial\phi^e{}_i}{\partial z} \end{bmatrix}^{\mathrm{T}} \begin{bmatrix} \frac{\partial\phi^e{}_j}{\partial x} \\ \frac{\partial\phi^e{}_j}{\partial y} \\ \frac{\partial\phi^e{}_j}{\partial z} \end{bmatrix}$$

$$= \sum_{e=1}^{\mathrm{E}} \begin{bmatrix} \frac{\partial\phi^e{}_i}{\partial x} \\ \frac{\partial\phi^e{}_i}{\partial y} \\ \frac{\partial\phi^e{}_i}{\partial z} \end{bmatrix}^{\mathrm{T}} \begin{bmatrix} \varepsilon^{*e} V^e & 0 & 0 \\ 0 & \varepsilon^{*e} V^e & 0 \\ 0 & 0 & \varepsilon^{*e} V^e \end{bmatrix} \begin{bmatrix} \frac{\partial\phi^e{}_1}{\partial x} & \cdots & \frac{\partial\phi^e{}_N}{\partial x} \\ \frac{\partial\phi^e{}_1}{\partial y} & & \frac{\partial\phi^e{}_N}{\partial y} \\ \frac{\partial\phi^e{}_1}{\partial z} & & \frac{\partial\phi^e{}_N}{\partial z} \end{bmatrix} \begin{bmatrix} \mathrm{u}_1 \\ \vdots \\ \mathrm{u}_N \end{bmatrix}$$

Then extending the sum of the element index e, and defining the matrix $[\varepsilon V L^e]$, $\boldsymbol{\phi}_i^e$ and $\boldsymbol{\phi}^e$, we have,

$$\sum_{j=1}^{N} \mathrm{u}_j \sum_{e=1}^{\mathrm{E}} \varepsilon^{*e} V^e \begin{bmatrix} \frac{\partial\phi^e{}_i}{\partial x} \\ \frac{\partial\phi^e{}_i}{\partial y} \\ \frac{\partial\phi^e{}_i}{\partial z} \end{bmatrix}^{\mathrm{T}} \begin{bmatrix} \frac{\partial\phi^e{}_j}{\partial x} \\ \frac{\partial\phi^e{}_j}{\partial y} \\ \frac{\partial\phi^e{}_j}{\partial z} \end{bmatrix} = \sum_{e=1}^{\mathrm{E}} \boldsymbol{\phi}_i^{e\,\mathrm{T}} [\varepsilon V L^e] \boldsymbol{\phi}^e \begin{bmatrix} \mathrm{u}_1 \\ \vdots \\ \mathrm{u}_N \end{bmatrix}$$

$$= \begin{bmatrix} \boldsymbol{\phi}_i^1 \\ \vdots \\ \boldsymbol{\phi}_i^E \end{bmatrix}^{\mathrm{T}} \operatorname{diag}\begin{bmatrix} \varepsilon VL^1 \\ \vdots \\ \varepsilon VL^E \end{bmatrix} \begin{bmatrix} \boldsymbol{\phi}_1^1 & \cdots & \boldsymbol{\phi}_N^1 \\ \vdots & & \vdots \\ \boldsymbol{\phi}_1^E & & \boldsymbol{\phi}_N^E \end{bmatrix} \begin{bmatrix} \mathrm{u}_1 \\ \vdots \\ \mathrm{u}_N \end{bmatrix} = \boldsymbol{K}_i{}^{\mathrm{T}} [\varepsilon VL] \boldsymbol{K} \begin{bmatrix} \mathrm{u}_1 \\ \vdots \\ \mathrm{u}_N \end{bmatrix}.$$

Here, the three matrices are defined as,

$$[\varepsilon VL^e] = \begin{bmatrix} \varepsilon^{*e} V^e & 0 & 0 \\ 0 & \varepsilon^{*e} V^e & 0 \\ 0 & 0 & \varepsilon^{*e} V^e \end{bmatrix}, \qquad \boldsymbol{\phi}_i^e = \begin{bmatrix} \dfrac{\partial \phi^e{}_i}{\partial x} \\ \dfrac{\partial \phi^e{}_i}{\partial y} \\ \dfrac{\partial \phi^e{}_i}{\partial z} \end{bmatrix}, \qquad \boldsymbol{\phi}^e = \begin{bmatrix} \dfrac{\partial \phi^e{}_1}{\partial x} & \cdots & \dfrac{\partial \phi^e{}_N}{\partial x} \\ \dfrac{\partial \phi^e{}_1}{\partial y} & & \dfrac{\partial \phi^e{}_N}{\partial y} \\ \dfrac{\partial \phi^e{}_1}{\partial z} & & \dfrac{\partial \phi^e{}_N}{\partial z} \end{bmatrix}.$$

And we also define,

$$\boldsymbol{K}_i = \begin{bmatrix} \boldsymbol{\phi}_i^1 \\ \vdots \\ \boldsymbol{\phi}_i^E \end{bmatrix}, \qquad [\varepsilon VL] = \operatorname{diag}\begin{bmatrix} [\varepsilon VL^1] \\ \vdots \\ [\varepsilon VL^E] \end{bmatrix}, \qquad \boldsymbol{K} = \begin{bmatrix} \boldsymbol{\phi}_1^1 & \cdots & \boldsymbol{\phi}_N^1 \\ \vdots & & \vdots \\ \boldsymbol{\phi}_1^E & & \boldsymbol{\phi}_N^E \end{bmatrix}.$$

The derivative of shape functions, which appeared in $\boldsymbol{K}$ and its components, can be given by the Barycentric coordinate system. Recall Equation 3-6, $[DE^e]$ can be easily given by column operation, and also $[DE]$.

$$\begin{bmatrix} \dfrac{\partial \phi^e{}_{e1}}{\partial x} & \cdots & \dfrac{\partial \phi^e{}_{e4}}{\partial x} \\ \dfrac{\partial \phi^e{}_{e1}}{\partial y} & & \dfrac{\partial \phi^e{}_{e4}}{\partial y} \\ \dfrac{\partial \phi^e{}_{e1}}{\partial z} & & \dfrac{\partial \phi^e{}_{e4}}{\partial z} \end{bmatrix} = [\boldsymbol{J}^e]^{-1} \begin{bmatrix} \dfrac{\partial \phi^e{}_{e1}}{\partial \xi_1{}^e} & \cdots & \dfrac{\partial \phi^e{}_{e4}}{\partial \xi_1{}^e} \\ \dfrac{\partial \phi^e{}_{e1}}{\partial \xi_2{}^e} & & \dfrac{\partial \phi^e{}_{e4}}{\partial \xi_2{}^e} \\ \dfrac{\partial \phi^e{}_{e1}}{\partial \xi_3{}^e} & & \dfrac{\partial \phi^e{}_{e4}}{\partial \xi_3{}^e} \end{bmatrix}$$

$$= \begin{bmatrix} x_1^e - x_4^e & y_1^e - y_4^e & z_1^e - z_4^e \\ x_2^e - x_4^e & y_2^e - y_4^e & z_2^e - z_4^e \\ x_3^e - x_4^e & y_3^e - y_4^e & z_3^e - z_4^e \end{bmatrix}^{-1} \begin{bmatrix} 1 & 0 & 0 & -1 \\ 0 & 1 & 0 & -1 \\ 0 & 0 & 1 & -1 \end{bmatrix},$$

$$[DE^e] = \begin{bmatrix} \operatorname{diag}\begin{pmatrix} \dfrac{\partial \phi^e{}_{e1}}{\partial x} \\ \dfrac{\partial \phi^e{}_{e1}}{\partial y} \\ \dfrac{\partial \phi^e{}_{e1}}{\partial z} \end{pmatrix} & \cdots & \operatorname{diag}\begin{pmatrix} \dfrac{\partial \phi^e{}_{e4}}{\partial x} \\ \dfrac{\partial \phi^e{}_{e4}}{\partial y} \\ \dfrac{\partial \phi^e{}_{e4}}{\partial z} \end{pmatrix} \end{bmatrix}, \qquad [DE] = \begin{bmatrix} DE^1 & \mathbf{0} & \mathbf{0} \\ \mathbf{0} & DE^e & \mathbf{0} \\ \mathbf{0} & \mathbf{0} & DE^{\mathrm{E}} \end{bmatrix}.$$

Equation 3-10

It can be seen however, in first order tetrahedron FEM mesh, each element contents 4 nodes. This means $[DE^e] \in \mathbb{R}^{3\times 12}$, which hardly forms $\boldsymbol{K}$ in dimensions of $(3E) \times N$. Also it should be notice that $[\boldsymbol{\phi}^e]$ which is consisting $\boldsymbol{K}$, is a sparse matrix. For those nodes which are not in the element e, the corresponding columns are filled with zeroes. So we use connection

matrix $[EN_i]$ to build these sparse matrices, by converting the local node index (which is defined within the element) and global node index.

$[EN_i]$ is in the matrix which connects the element to the nodes. Assume node i is shared by 3 different elements, $e1$, $e2$ and $e3$. And it is the 2nd, 1st and 4th node of these 3 elements respectively. Then we can have $[EN_i]$ made up with E blocks in a column, corresponding to all the E elements. Each block has 4 sub-blocks placed in the column, corresponding to the 4 nodes of the element. The node i is shared by blocks $e1$, $e2$ and $e3$, where the 2nd, 1st and 4th sub-blocks are 3×3 identity matrices respectively.

$$[EN_i] = \begin{matrix} \vdots \\ e1 \\ \vdots \\ e2 \\ \vdots \\ e3 \\ \vdots \end{matrix} \begin{matrix} \vdots \\ 1 \\ 2 \\ 3 \\ 4 \\ \vdots \\ 1 \\ 2 \\ 3 \\ 4 \\ \vdots \\ 1 \\ 2 \\ 3 \\ 4 \\ \vdots \end{matrix} \begin{matrix} \vdots \\ \\ \\ \\ \\ \\ \\ \\ \\ \\ \\ \\ \\ \\ \\ \\ \\ \end{matrix} \begin{matrix} \\ \\ \rightarrow \\ \\ \\ \\ \\ \rightarrow \\ \\ \\ \\ \\ \\ \\ \\ \rightarrow \\ \\ \end{matrix} \begin{bmatrix} \vdots \\ \mathbf{0}^{3\times3} \\ \mathbb{I}^3 \\ \mathbf{0}^{3\times3} \\ \mathbf{0}^{3\times3} \\ \vdots \\ \mathbb{I}^3 \\ \mathbf{0}^{3\times3} \\ \mathbf{0}^{3\times3} \\ \mathbf{0}^{3\times3} \\ \vdots \\ \mathbf{0}^{3\times3} \\ \mathbf{0}^{3\times3} \\ \mathbf{0}^{3\times3} \\ \mathbb{I}^3 \\ \vdots \end{bmatrix} \in \mathbb{R}^{12E\times3}, \qquad [DE][EN_i] = \begin{bmatrix} \frac{\partial \phi^1{}_i}{\partial x} & 0 & 0 \\ 0 & \frac{\partial \phi^1{}_i}{\partial y} & 0 \\ 0 & 0 & \frac{\partial \phi^1{}_i}{\partial z} \\ & \vdots & \\ \frac{\partial \phi^E{}_i}{\partial x} & 0 & 0 \\ 0 & \frac{\partial \phi^E{}_i}{\partial y} & 0 \\ 0 & 0 & \frac{\partial \phi^E{}_i}{\partial z} \end{bmatrix},$$

Equation 3-11 (a -b)

As $[EN_i]$ provides map from global nodes to element local nodes, we can have the product $[DE][EN_i]$ in Equation 3-11 (b) in the form which is similar to the $[\boldsymbol{K}_i]$. With the help of the tool vector $[SV_0]$ which squeezes diagonal matrices to vectors, we then have,

$$[DE][EN_i][SV_0] = [\boldsymbol{K}_i], \qquad [SV_0] = \begin{bmatrix} 1 \\ 1 \\ 1 \end{bmatrix},$$

$$[EN] = [[EN_1] \quad \cdots \quad [EN_N]], \qquad [DE][EN][SV] = \boldsymbol{K}, \qquad [SV] = \operatorname{diag}\begin{bmatrix} [SV_0] \\ \vdots \\ [SV_0] \end{bmatrix} \in \mathbb{R}^{3N\times N}$$

Equation 3-12

And together the stiffness matrix,

$$\sum_{j=1}^{N} \mathrm{u}_j \int_{\Omega} \varepsilon^* \nabla \phi_i \cdot \nabla \phi_j \, \mathrm{d}V = \boldsymbol{K}^{\mathrm{T}} [\varepsilon V] \boldsymbol{K} \begin{bmatrix} \mathrm{u}_1 \\ \vdots \\ \mathrm{u}_N \end{bmatrix}$$

$$= [SV]^{\mathrm{T}}[EN]^{\mathrm{T}}[DE]^{\mathrm{T}}[\varepsilon V][DE][EN][SV]\begin{bmatrix}\mathrm{u}_1\\ \vdots \\ \mathrm{u}_N\end{bmatrix}, \qquad i = 1,2,\cdots,N.$$

Equation 3-13

And further, for the second term $\boldsymbol{B}$, the mass matrix, in Equation 3-9, it can be extend as,

$$\sum_{l=1}^{L}\sum_{j=1}^{N}\mathrm{u}_j\frac{1}{\eta_l}\int_{S_l}\phi_i\phi_j\,\mathrm{d}S = \sum_{l=1}^{L}\left(M_i^l\begin{bmatrix}\mathrm{u}_1\\ \vdots \\ \mathrm{u}_N\end{bmatrix}\right),$$

$$M_i^l\begin{bmatrix}\mathrm{u}_1\\ \vdots \\ \mathrm{u}_N\end{bmatrix} = \frac{1}{\eta_l}\sum_{j=1}^{N}\mathrm{u}_j\int_{S_l}\phi_i\phi_j\,\mathrm{d}S = \frac{1}{\eta_l}\begin{bmatrix}\int_{S_l}\phi_i\phi_1\,\mathrm{d}S\\ \vdots \\ \int_{S_l}\phi_i\phi_N\,\mathrm{d}S\end{bmatrix}^{\mathrm{T}}\begin{bmatrix}\mathrm{u}_1\\ \vdots \\ \mathrm{u}_N\end{bmatrix}.$$

In contrast to the element-to-node matrix $[EN]$ in composing the stiffness matrix Equation 3-13, here we use $[BN]$ which connects the boundary faces to the nodes. $[BN]$ is made up with $[BN_i]$ which indicate the existence and location of the node i in each boundary face.

$$[BN_i] = \begin{matrix}\vdots & \vdots & \vdots\\ \vdots & 1 & \vdots\\ b1 & 2 & \rightarrow\\ \vdots & 3 & \vdots\\ \vdots & \vdots & \vdots\\ \vdots & 1 & \rightarrow\\ b2 & 2 & \vdots\\ \vdots & 3 & \vdots\\ \vdots & \vdots & \vdots\\ \vdots & 1 & \vdots\\ b3 & 2 & \vdots\\ \vdots & 3 & \rightarrow\\ \vdots & \vdots & \vdots\end{matrix}\begin{bmatrix}\vdots\\ \mathbf{0}^{3\times3}\\ \mathbb{I}^3\\ \mathbf{0}^{3\times3}\\ \vdots\\ \mathbb{I}^3\\ \mathbf{0}^{3\times3}\\ \mathbf{0}^{3\times3}\\ \vdots\\ \mathbf{0}^{3\times3}\\ \mathbf{0}^{3\times3}\\ \mathbb{I}^3\\ \vdots\end{bmatrix} \in \mathbb{R}^{9B\times3}, \qquad [BN] = \begin{bmatrix}[BN_1]^{\mathrm{T}}\\ \vdots \\ [BN_N]^{\mathrm{T}}\end{bmatrix}^{\mathrm{T}} \in \mathbb{R}^{9B\times3N}$$

Equation 3-14 (a -b)

Each 3 columns, which is $[BN_i]$, in the $[BN]$ related to the node i in the whole volume. The 3 columns in $[BN_i]$ are related to the 3 axes. Each 9 rows in $[BN_i]$ is associated with a boundary face on the outer boundary. The 9 rows are consist with 3 blocks of 3×3 matrices, each one of them represents one of the 3 nodes of the face. And if the node i is on the face, identity matrix is used as the block, empty matrix otherwise.

With $[BN_i]$ and $[BN]$, which bring the global node index to the local boundary face node index, M_i^l can be expressed as,

$$M_i^l = \frac{1}{\eta_l}[SV_0]^{\mathrm{T}}[BN_i]^{\mathrm{T}}[BS^l]^{\mathrm{T}}[PS][BS^l][BN][SV],$$

$$[PS] = \mathrm{diag}\begin{bmatrix}[PS_1]\\ \vdots \\ [PS_B]\end{bmatrix}, \qquad [PS_b] = \begin{bmatrix} \int_{S_b} {\phi^b}_{b1}{\phi^b}_{b1}\,\mathrm{d}S & \cdots & \int_{S_b} {\phi^b}_{b1}{\phi^b}_{b3}\,\mathrm{d}S \\ \vdots & \ddots & \vdots \\ \int_{S_b} {\phi^b}_{b3}{\phi^b}_{b1}\,\mathrm{d}S & \cdots & \int_{S_b} {\phi^b}_{b3}{\phi^b}_{b3}\,\mathrm{d}S \end{bmatrix}.$$

Equation 3-15

Here, B is the number of boundary faces and b is the index of these boundary faces. $[BS^l]$ is a matrix which indicates whether the boundary face b is on the electrode l. $[PS_b]$ is localised to each boundary face, and the entries in it are the integrals of shape functions. By Equation 3-7 (a), the entries can be given, and we have,

$$[BS^l] = \frac{1}{3}\mathrm{diag}\begin{bmatrix}[SV_0]^{\mathrm{T}}\\ \vdots \\ [SV_0]^{\mathrm{T}}\end{bmatrix} \in \mathbb{R}^{3B\times 9B}, \qquad [PS_b] = \frac{|S_b|}{12}\begin{bmatrix}2 & 1 & 1\\ 1 & 2 & 1\\ 1 & 1 & 2\end{bmatrix} \in \mathbb{R}^{3\times 3}.$$

The third term $\boldsymbol{C}$, in Equation 3-9, can be treated similar to the mass matrix as,

$$\sum\nolimits_{l=1}^{L} \frac{U_l}{\eta_l}\int_{S_l} \phi_i\,\mathrm{d}S = \sum\nolimits_{l=1}^{L}\left(\left[MM_i^l\right]\begin{bmatrix}U_1\\ \vdots \\ U_L\end{bmatrix}\right),$$

$$\left[MM_i^l\right] = \frac{1}{\eta_l}\int_{S_l} \phi_i\,\mathrm{d}S = \frac{1}{\eta_l}[SV_0]^{\mathrm{T}}[BN_i]^{\mathrm{T}}[BS^l]^{\mathrm{T}}[PPS],$$

$$[PPS] = \begin{bmatrix}[PPS_1]\\ \vdots \\ [PPS_B]\end{bmatrix}, \qquad [PPS_b] = \begin{bmatrix}\int_{S_b} \phi_{b1}\,\mathrm{d}S\\ \vdots \\ \int_{S_b} \phi_{b3}\,\mathrm{d}S\end{bmatrix} = \frac{|S_b|}{3}[SV_0].$$

Equation 3-16

Finally, the matrix formula of FEM system Equation 3-9 is assembled with Equation 3-13, Equation 3-15 and Equation 3-16. Matrices $\boldsymbol{D}$, $\boldsymbol{E}$ and $\boldsymbol{F}$ do not involve in assembling process, as they are isolated with the shape functions but only associated with U_l and I_l to form inner products.

The FEM formula of a Laplace equation is quite often appeared in computational technique or numerical problems text book, and the EIT forward problem with CEM or IEM boundary conditions is basically in the Laplace formula, with only the electrodes part modified a bit. The reasons we detailed it here are that, first, the stiffness matrix is reused in the inverse problem, and we are going to discuss it in Chapter 5; second, we introduced a set of different boundary conditions to fine the forward problem solution corresponding to the hardware non-ideal

effects, and it is different from the FEM formula given by CEM; third, in order to extend the frequency usage of the EIT applications, we derived the EIT forward problem from the Maxwell's equation in Chapter 4, it needs the FEM-Laplace formula as the foundation and for comparison with as well.

3.4 Case Studies and Discussions

The following sections illustrate solutions of the forward model for two different geometry models and compare the results obtained using different solution methods.

3.4.1 Lumped Model

The first geometry model, called "Lumped Model," is a cylinder with two electrodes at each end. The cylinder is filled with materials to simulate breast tissues (Surowiec, et al., 1988) and placed in free space as Figure 3-2 defines.

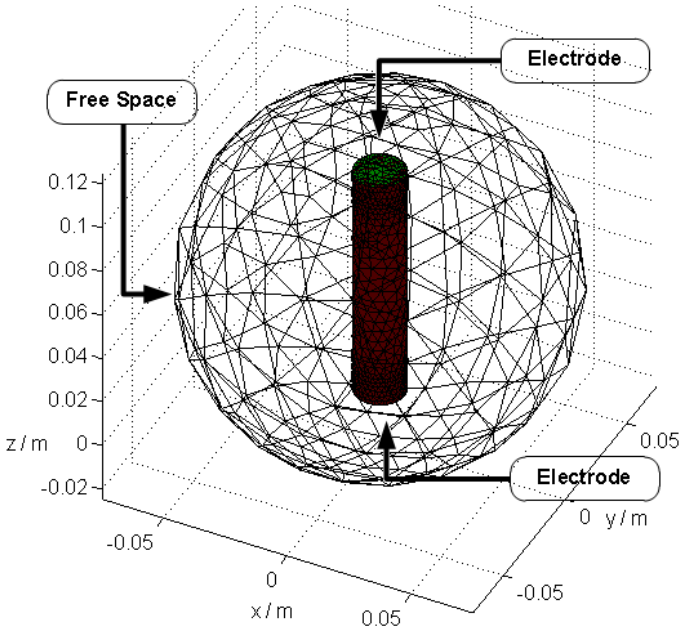

Figure 3-2 the geometry of the Lumped Model

In contrast to typical EIT models, the Lumped Model is clearly not able to predict the impedance distribution inside the volume without the prior knowledge of its homogeneity, as there are not enough electrodes. The free space outside the cylinder is usually ignored. The benefit of the Lumped Model is that as long as the free space (in the sphere) is removed, then it can be verified analytically by considering the model as a lumped circuit containing a parallel-plate capacitor C_S in parallel with a resistor R_S. As the material in the cylinder is homogeneous, the circuit components are given as

$$R_S = \frac{L}{\sigma \times S} \quad , \qquad C_S = \frac{\varepsilon \times S}{L},$$

$$\mathbf{Z}_{\mathrm{S}} = \frac{\mathrm{R}_{\mathrm{S}} \frac{1}{\mathrm{j}\omega \mathrm{C}_{\mathrm{S}}}}{\mathrm{R}_{\mathrm{S}} + \frac{1}{\mathrm{j}\omega \mathrm{C}_{\mathrm{S}}}} = \frac{L}{\varepsilon^* S},$$

where R_{S}, C_{S} and $\mathbf{Z}_{\mathrm{S}}$ are the equivalent resistor, capacitor and impedance of the material,

σ, ε and ε^* are the conductivity, permittivity and admittivity of the material,

S is the surface area of the electrode (also the top/bottom surface area of the cylinder),

L is the distance between the electrodes (also the length of the cylinder).

In addition, on each electrode, a circuit unit consisting of a resistor R_{F} and a capacitor C_{F} can be attached to simulate the instrumental impedance $\mathbf{Z}_{\mathrm{F}}$ we proposed in the IEM. Because there are only two electrodes in the model, current sources are applied on both of them in opposite direction and no measuring electrode is included.

When the surrounding free space is considered, the two electrodes form another capacitor (reflecting the interaction with the free space electric field) connected in parallel with $\mathbf{Z}_{\mathrm{S}}$. We denote it as C_{A} or its reactance $\mathbf{X}\mathrm{C}_{\mathrm{A}}$, and solve it numerically.

As mentioned in section 2.2.1, the Laplace equations under the quasi-static approximation are not sufficient to obtain accurate solutions for the frequency range of interest. Here we denote the difference between the solutions obtained from the full Maxwell equations and the Laplace equations as the full Maxwell effect, and we use a circuit unit $\mathbf{Z}_{\mathrm{M}}{}^{+}$ to model this effect although a simplistic equivalent impedance cannot fully represent this effect.

The equivalent circuit of the Lumped Model is shown in Figure 3-3(a).

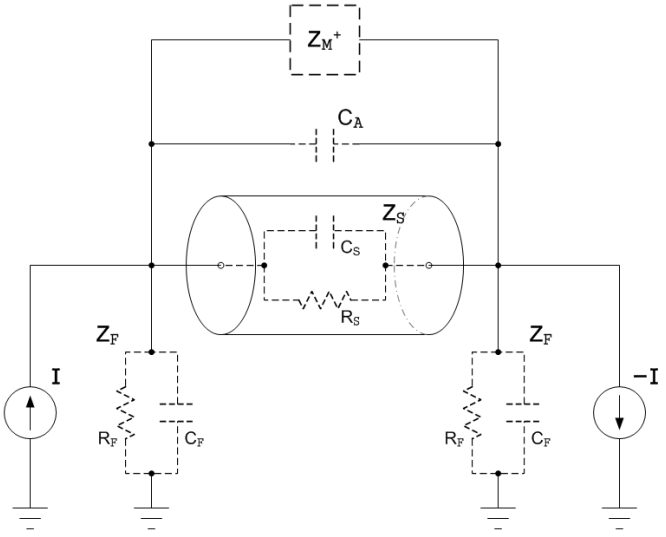

Figure 3-3(a). The equivalent circuit for Lumped Model

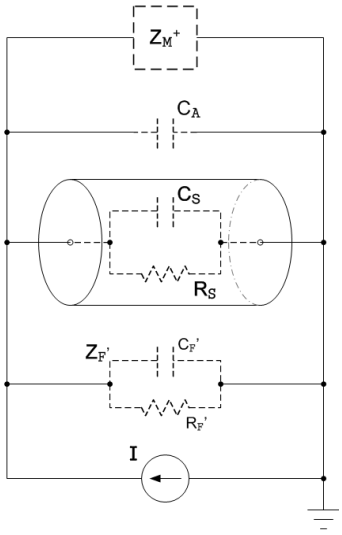

Figure 3(b). The equivalent circuit for method h) and i)

In our simulations, three main effects are included in the Lumped Model for solving the forward models. Note that we are not trying to quantify these effects, as they vary with geometries and materials, but merely to use the combinational effects to verify the IEM. These three effects are:

- Instrumental effect, $\mathbf{Z}_{\mathrm{F}}$;
- Volume Cut-off effect, $\mathbf{X}\mathrm{C}_{\mathrm{A}}$;
- Full Maxwell's effect, ${\mathbf{Z}_{\mathrm{M}}}^{+}$.

We obtained the simulation results by using the following nine methods (forward problem solvers or BCs sets) and cross-compared the results to assess the accuracy of the IEM implementation. The methods are:

a) analytical lumped method

   An analytical solution based on an equivalent circuit of the cylinder and current sources.

b) analytical lumped method with the instrumental effect $\mathbf{Z}_{\mathrm{F}}$

   Similar to a), but the instrumental impedance effect $\mathbf{Z}_{\mathrm{F}}$ is also included in the analysis.

c) CEM by EIDORs (Polydorides & Lionheart, 2002) without considering the free space (no $\mathbf{X}\mathrm{C}_{\mathrm{A}}$)

   An FEM forward model of the cylinder solved with the CEM. This models the potential distribution in the cylinder, contact impedance and the potentials on the two electrodes. Only the cylinder (coloured in dark red in Figure 3-2) is meshed and solved without considering the surrounding free space (or $\mathbf{X}\mathrm{C}_{\mathrm{A}}$).

d) CEM by EIDORs with $\mathbf{X}\mathrm{C}_{\mathrm{A}}$

   Similar to c), but with the free space (in Figure 3-2) included and solved. Note that the governing Equation 2-11 and the derivation in Section 3.3.1 are free of sources inside the volume, which differs from the configuration for this simulation (the source electrodes are inside the finite elements volume). They are equivalent mathematically, but we do not need to detail the equations here.

e) IEM without considering the free space (no $\mathbf{X}\mathrm{C}_{\mathrm{A}}$)

Similar to c), but using the IEM we proposed in the Sections 3. It models the potential distribution in the cylinder, contact impedance on the two electrodes with the instrumental effect $\mathbf{Z}_{\mathrm{F}}$ included.

f) IEM with $\mathbf{X}\mathrm{C}_{\mathrm{A}}$

Similar to e), but the free space ($\mathbf{X}\mathrm{C}_{\mathrm{A}}$) is included in the simulations.

g) $\mathbf{A}-\Phi$ forward model in Helmholtz-like equations

An FEM forward model that solves the full Maxwell equations. It models the vector potential ($\mathbf{A}$) and scalar potential (Φ) distribution in the cylinder and also the surrounding free space shown in Figure 3-2, but the contact impedance or instrumental effect is not considered. We derived the formula of the $\mathbf{A}-\Phi$ method based on a previously published 2-D work (Soni, et al., 2006), and the data structure in Matlab is based on EIDORS using the mesh generating software NETGEN. A description of the forward model formulation can be found in the Chapter 4.

h) COMSOL Multiphysics without the instrumental effect $\mathbf{Z}_{\mathrm{F}}$

The solution is obtained by COMSOL Multiphysics (well-known commercial finite-element software developed for solving differential equations in different applications, denoted as COMSOL hereafter). It models the electric field distribution in the cylinder and the surrounding free space (perfect matching layer, PML, is usually used in solving Maxwell's equations).

i) COMSOL Multiphysics with $\mathbf{Z}_{\mathrm{F}}$

Similar to h), but we included the instrumental effect $\mathbf{Z}_{\mathrm{F}}$ on electrodes.

Table 3-1 summarises the methods we used.

Table 3-1 List of the effects considered by each method

Index	Name	Effect $\mathbf{Z}_{\mathrm{F}}$	Effect $\mathbf{X}\mathrm{C}_{\mathrm{A}}$	Effect $\mathbf{Z}_{\mathrm{M}}{}^{+}$
a)	Analytical	No	No	No
b)	Analytical w/ $\mathbf{Z}_{\mathrm{F}}$	**Yes**	No	No
c)	CEM	No	No	No
d)	CEM w/ $\mathbf{X}\mathrm{C}_{\mathrm{A}}$	No	**Yes**	No
e)	IEM	**Yes**	No	No
f)	IEM w/ $\mathbf{X}\mathrm{C}_{\mathrm{A}}$	**Yes**	**Yes**	No

g)	$\mathbf{A} - \Phi$	No	**Yes**	**Yes**
h)	COMSOL	No	**Yes**	**Yes**
i)	COMSOL w/ $\mathbf{Z}_{\mathrm{F}}$	**Yes**	**Yes**	**Yes**

Note: The contact impedance in c) – f) is set to be $1 \times 10^{-6}\ \Omega \cdot \mathrm{m}^2$ in order to compare with other methods which the contact impedance are not considered.

For all methods the dimensions of the cylinder, conductivity, permittivity, instrumental impedance, stimulation and frequencies are kept constant to allow fair comparison. The parameters are:

- Material conductivity, 0.03S/m, (Surowiec, et al., 1988)
- Material relative permittivity, 40, (Surowiec, et al., 1988)
- Cylinder radius, 0.01m
- Cylinder length, 0.10m
- Current source driving current, 1mA
- Frequency range, 250kHz – 20MHz.

Various other parameters apply to some of the individual methods:

- The equivalent impedance of the cylinder $\mathbf{Z}_{\mathrm{S}}$ in a) and b) is calculated from the material property and cylinder dimension above.
- The resistive part of the instrumental impedance, R_{F}, in methods b), e) and f) is 5MOhm
- The capacitive part of the instrumental impedance, C_{F}, in methods b), e) and f) is 10pF
- The diameter of the free space sphere in methods d), f) and g) is 0.15m.
- The diameter of the free space plus PML sphere in method h) and i) is 0.15m.
- Method h) and i) which uses COMSOL requires a uniform “port” defined as field excitation, so the two opposing electrodes are considered as a single “port”, and the instrumental impedance, which is attached on each electrode in methods b), e) and f), is combined into a single effective impedance connected in parallel with the port, as shown in Figure 3-3(b) (with the impedance doubled to maintain equivalence with Figure 3-3(a)).

Figure 3-4 and Figure 3-5 show the differential voltage in magnitude and phase obtained by the methods, a) – i).

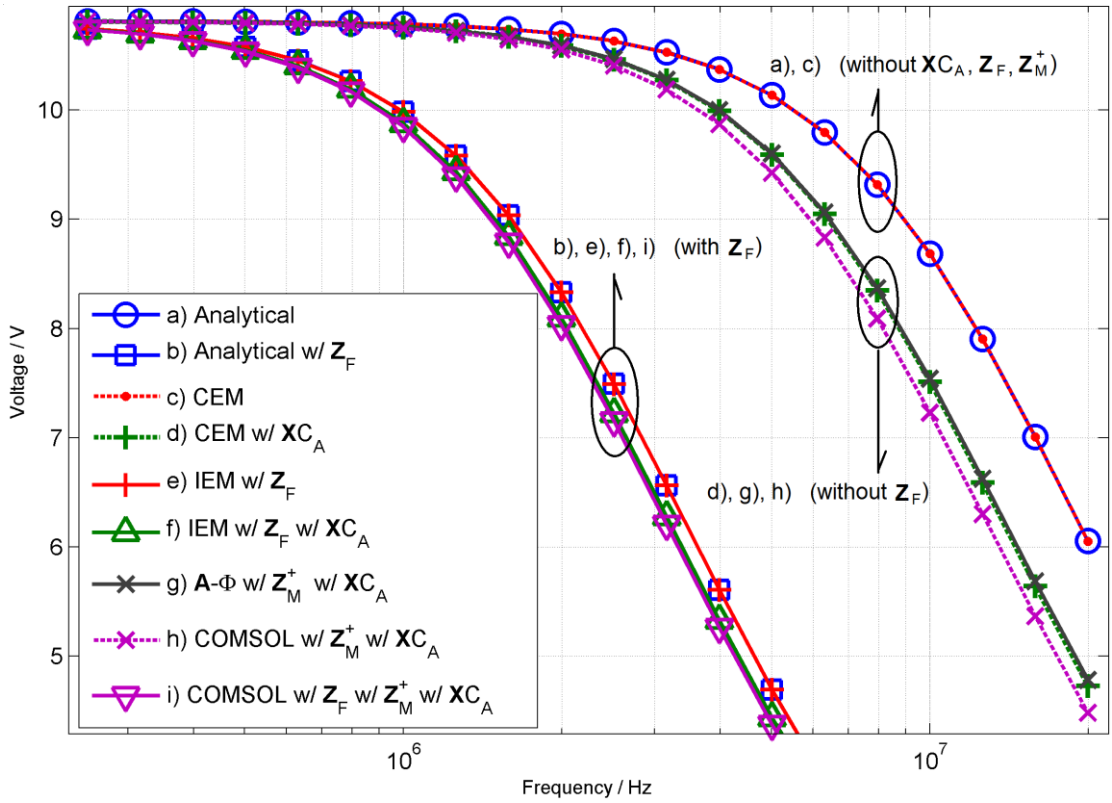

Figure 3-4 Solutions in magnitude of the forward problem obtained by using methods a) – i)

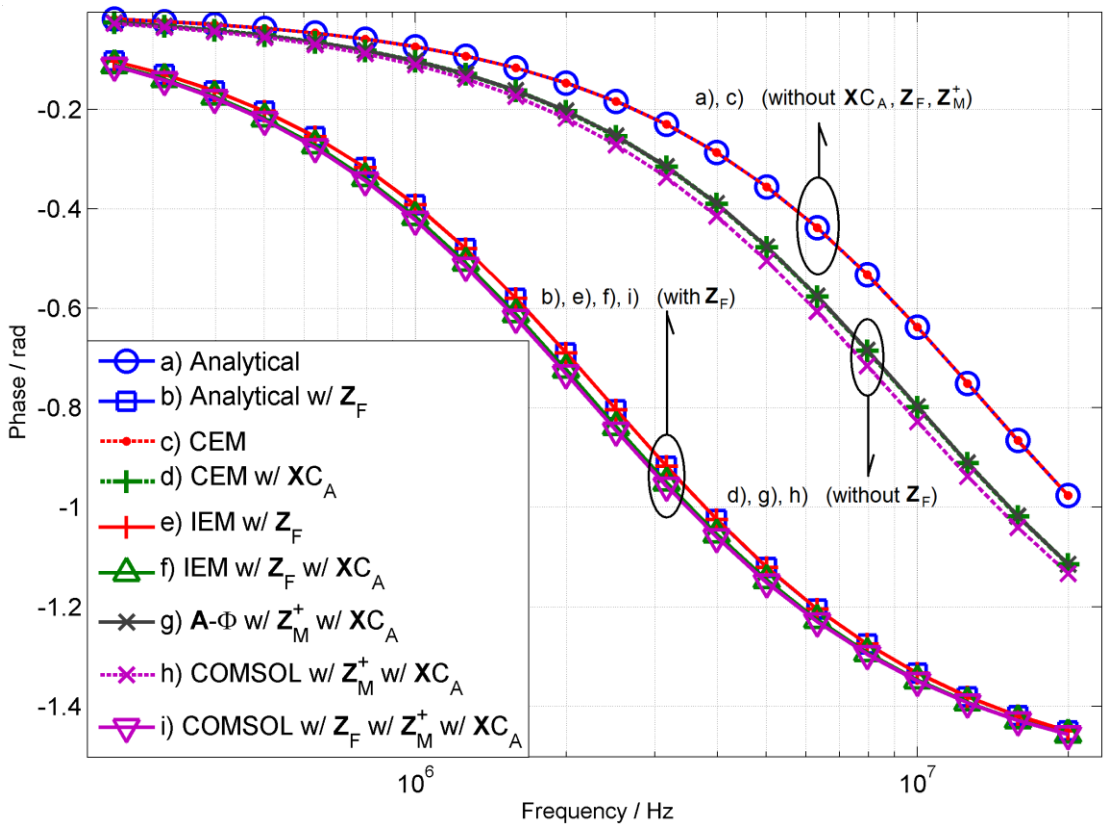

Figure 3-5 Solutions in phase of the forward problem obtained by using methods a) – i)

Key findings from the various solution methods are as follows:

- The results from a), analytical method, and c), FEM with CEM BCs are almost the same, as they describe the same problem in analytical and numerical ways.
- The results from b), analytical method with $\mathbf{Z}_{\mathrm{F}}$, and e), FEM with IEM BCs are in a good agreement, as they discribe the same problem. And this shows our IEM describes the instrumental effect correctly.
- Both b) and e) start to attenuate at a much lower frequency than a) and c). This comes from the instrumental effect, where $\mathbf{Z}_{\mathrm{F}}$ provides an extra path for the current and reduces the current injected into the cylinder.
- Similarly, the results for d), FEM with CEM BCs and $\mathbf{X}\mathrm{C}_{\mathrm{A}}$, attenuate in magnitude at a lower frequency than the a) and c) results. This illustrates the volume cut-off effect. The capacitance contributed by the free space is not considered in a) and is numerically chopped off in c), which provides an extra path for the current.
- Similarly, the results for f), FEM with IEM BCs and $\mathbf{X}\mathrm{C}_{\mathrm{A}}$, also shows the volume cut-off effect, but are not so different from the results for b) and e). This demonstrates that the instrument effect dominates in this case.
- The results for g), FEM of $\mathbf{A}-\Phi$ problem with $\mathbf{X}\mathrm{C}_{\mathrm{A}}$, are very similar to the results for d), FEM with CEM BCs and $\mathbf{X}\mathrm{C}_{\mathrm{A}}$. This shows that the full Maxwell effect ${\mathbf{Z}_{\mathrm{M}}}^{+}$ is not obvious for the structure we chose in this frequency range.
- The h) curves (obtained using COMSOL, but without considering $\mathbf{Z}_{\mathrm{F}}$) are similar to the d) curves, showing further that the Maxwell effect is not significant. The error between g) and h) will be discussed shortly.
- The results for i) using COMSOL (including $\mathbf{Z}_{\mathrm{F}}$) show the combined effects of $\mathbf{Z}_{\mathrm{F}}$, $\mathbf{X}\mathrm{C}_{\mathrm{A}}$ and ${\mathbf{Z}_{\mathrm{M}}}^{+}$, and they are close to the results for f).

From the above, we conclude that:

- The numerical methods match the analytical methods perfectly; a) with c) and b) with e).
- The volume cut-off effect, $\mathbf{X}\mathrm{C}_{\mathrm{A}}$, contributed by the free space surrounding the cylinder, is observable, based on the comparison between groups d), g) and h) and groups a) and c) (groups are circled in the figures).
- The instrumental effect, $\mathbf{Z}_{\mathrm{F}}$, is significant. Based on comparisons between a) and b), c) and e), d) and f), and h) and i) in both magnitude and phase plots.

- The Maxwell effect, $\mathbf{Z_M}^+$, is insignificant, for the geometry and material property we chose.
- The two different Maxwell solvers (COMSOL and $\mathbf{A}-\Phi$) give similar but not identical results. Both methods solve full Maxwell equations and are mathematically equivalent, and theoretically should obtain the same results. Potential reasons for the small discrepancy are:
    - In method g), the $\mathbf{A}-\Phi$ method solves Helmholtz-like equations with nodal FEM, as described in section 2.4, while in method h), COMSOL solves curl-curl Equation 3-17 with edge element FEM (in which ϵ_r, μ_r, ϵ_0 and k_0 are relative permittivity, relative permeability, permittivity in free space and propagation constant) (Firoozabadi & Miller, 2010).

$$\nabla \times \mu_\mathrm{r}^{-1}(\nabla \times \mathbf{E}) - k_0^2\left(\epsilon_\mathrm{r} - \frac{\mathrm{j}\sigma}{\omega\epsilon_0}\right)\mathbf{E} = \mathbf{0}$$

Equation 3-17

    - COMSOL builds the numeric problem, meshes the geometry and solves the matrix differently compared to method g) (which uses NETGEN and Matlab).

3.4.2 Tank Model and Discussion

For the second forward problem we use a simple cylinder tank as shown in Figure 3-6 (relatively simple to model but complicated enough to illustrate the differences between the IEM and the other methods). There are six electrodes located at the vertical mid-point of the cylinder wall with free space surrounding the tank. Each electrode is modelled as a small circle distributed around the perimeter of the cylinder tank at a uniform 60-degree angular spacing.

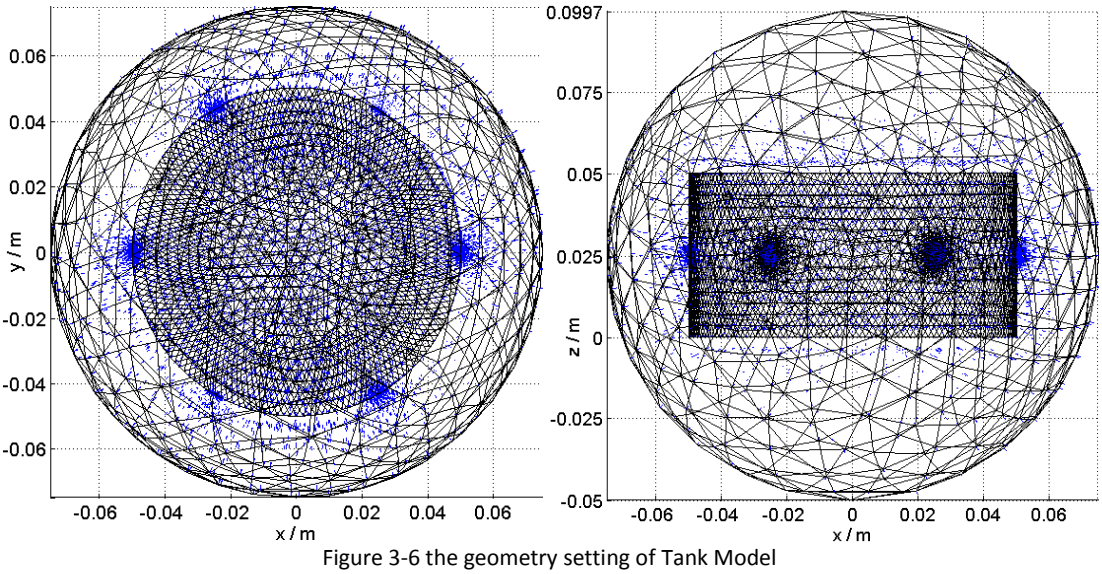

Figure 3-6 the geometry setting of Tank Model

Furthermore, a more realistic contact impedance is introduced in this forward problem. The electrochemical (polarization) impedance part of the contact impedance (Kolehmainen, et al., 1997) is considered. Based on experimental measurements of polarization impedance (Mirtaheri, et al., 2005), we set the contact impedance of electrodes in the Tank Model using 0.9%-saline-gold data measured at 1kHz. It is the highest frequency measured in the report and the experimental results suggest that the impedance tends to reduce with increasing frequency (Mirtaheri, et al., 2005), so we can expect the effect of contact impedance is less significant in the frequency range considered here. The contact impedance is given by,

$$\eta = \mathbf{Z}_{\mathrm{C}} S = \left(\mathrm{R}_{\mathrm{C}} + \frac{1}{\mathrm{j}2\pi f \mathrm{C}_{\mathrm{C}}}\right) S_{\mathrm{C}}$$

where R_{C} is the resistive part measured in the contact impedance experiment (Mirtaheri, et al., 2005),

C_{C} is the capacitive part,

$\mathbf{Z}_{\mathrm{C}}$ is the measured impedance,

$f = 1\mathrm{kHz}$ is the frequency,

S_{C} is the electrode surface area, 0.07 cm^2.

In a similar fashion to the Lumped Model described previously, we use several methods to solve the forward problem, and make cross-comparisons to verify the results obtained from IEM, subject to the following effects,

- Instrumental effect, $\mathbf{Z}_{\mathrm{F}}$;
- Volume Cut-off effect, $\mathbf{X}\mathrm{C}_{\mathrm{A}}$;
- Full Maxwell's effect, ${\mathbf{Z}_{\mathrm{M}}}^{+}$.

Figure 3-7 illustrates the equivalent circuit for the Tank Model. A pair of ideal current sources are attached to two electrodes of the tank. Each of these sources comes with its instrumental impedance $\mathbf{Z}_{\mathrm{FD}}$, consisting of R_{F} and C_{FD}. The sources drive the tank through the contact impedance η_{D} (expressed as an impedance $\eta_{\mathrm{D}} S^{-1}$ where S is the electrode surface area). The impedances $\eta_{\mathrm{D}} S^{-1}$ are shown with dashed lines, as the true locations are at the surface of the electrodes. Two electrodes (No. 4 and No. 5 on the right hand side) constitute the measurement circuit with the differential voltage between them (DV_{45}) measured down-stream from the contact impedance ($\eta_{\mathrm{M}} S^{-1}$) and with their instrumental impedance attached ($\mathbf{Z}_{\mathrm{FM}}$ to ground comprising R_{F} and C_{FM} in parallel). The model includes instrumental impedances for all six electrodes ($\mathbf{Z}_{\mathrm{FM}}$for measuring and $\mathbf{Z}_{\mathrm{FD}}$ for driving) although these are

not all shown on the diagram. Once again the model uses simplistic equivalent impedance representations for the volume cut-off effect (represented by capacitor C_A) and the full Maxwell effect (represented by the two port network $\mathbf{Z_M}^+$). In simulations, the driving and measuring pattern can be varied to use any of the available electrode pairs.

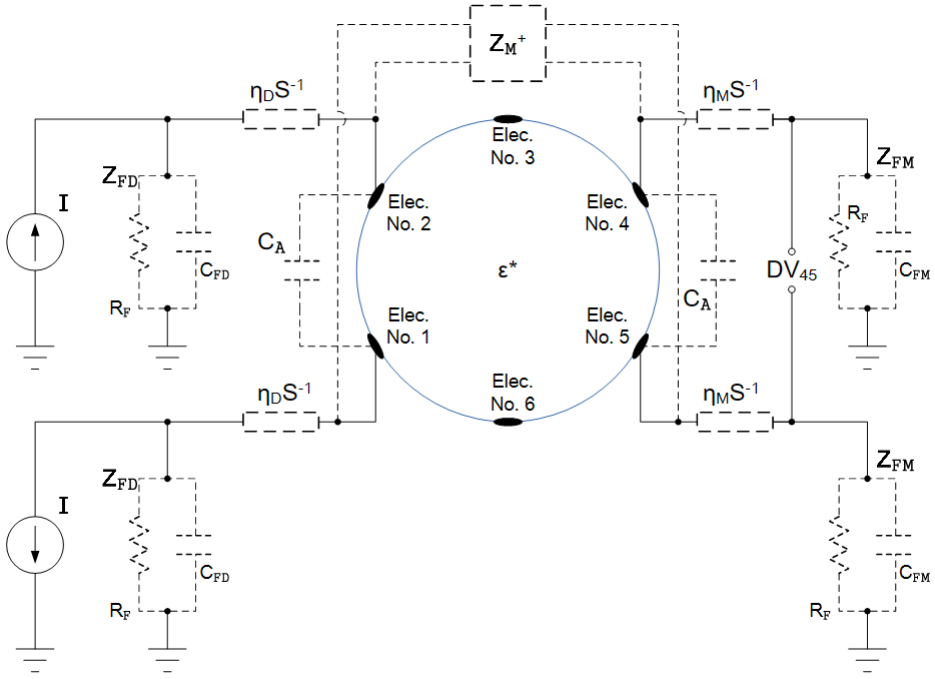

Figure 3-7 Equivalent circuit of Tank Model including instrumental effects

We obtained the results using the following solution methods:

a) CEM using EIDORs
b) CEM including the outer free space using EIDORs
c) IEM including the outer free space and instrumental effects
d) $\mathbf{A} - \Phi$ forward model in Helmholtz-like equations
e) COMSOL without the instrumental effect
f) COMSOL including the instrumental effect

The model parameters are:

- Material conductivity, 0.03S/m
- Material relative permittivity, 40
- Tank radius, 0.05m
- Tank height, 0.05m
- Electrode radius, 0.002m
- Driving current, 1mA

- An electrode drive pattern based on opposite driving (1 and 4) and measuring electrodes (2 and 5) is used.

Together with some parameters which apply to particular solution methods,

- For method c), $\mathrm{R_F}$ = 5MOhm, $\mathrm{C_{FD}}$ (the capacitive part of the instrumental impedance on driving electrodes) $=$ 10pF, and $\mathrm{C_{FM}}$ (the capacitive part of the instrumental impedance on measuring electrodes) = 6pF.
- The diameter of the free space sphere in methods b) - f) is 0.15m.
- The BC used in d), $\mathbf{A} - \Phi$ forward model, is similar to the shunt electrode model (Boyle & Adler, 2011) (see section 2.4) and does not include the contact impedance or instrumental impedance.
- Contact impedance is not applicable in COMSOL Electromagnetic simulation, and is not applied in methods e) and f).
- For methods a) – c), the contact impedance on measuring electrodes,

$$\eta_{\mathrm{M}} = 7 \times 10^{-4} - \mathrm{j}5 \times 10^{-4} \Omega \cdot \mathrm{m}^2.$$

- For methods a) – c), the contact impedance on driving electrodes,

$$\eta_{\mathrm{D}} = 1 \times 10^{-6} \Omega \cdot \mathrm{m}^2.$$

  For all three methods the contact impedance of the driving electrodes is set to the same small value used for the Lumped Model, so that the measured voltage difference is comparable with methods d) – f) which do not include contact impedance. (The contact impedance on driving electrodes is in series with the impedance of the whole tank, which reduces the current flowing through the driving electrodes when a finite instrumental impedance is present at the electrodes.) The contact impedance on the driving electrodes exacerbates the instrumental effects but here we ignore it to show the instrumental effects caused by the measuring electrodes.

Table 3-2 summarises the methods we used.

Table 3-2 List of the effects considered by each method

Index	Name	η_D	η_M	Effect $\mathbf{Z}_F$	Effect $\mathbf{X}C_A$	Effect $\mathbf{Z}_M^+$
a)	CEM	Small	**Yes**	No	No	No
b)	CEM w/ $\mathbf{X}C_A$	Small	**Yes**	No	**Yes**	No
c)	IEM w/ $\mathbf{X}C_A$	Small	**Yes**	**Yes**	**Yes**	No
d)	$\mathbf{A}-\Phi$	No	No	No	**Yes**	**Yes**
e)	COMSOL	No	No	No	**Yes**	**Yes**
f)	COMSOL w/ $\mathbf{Z}_F$	No	No	**Yes**	**Yes**	**Yes**

Figure 3-8 and Figure 3-9 show magnitude and phase for the measured differential voltage for methods a) – f) (driving at electrode No. 1 and 4 and measuring at No. 2 and 5).

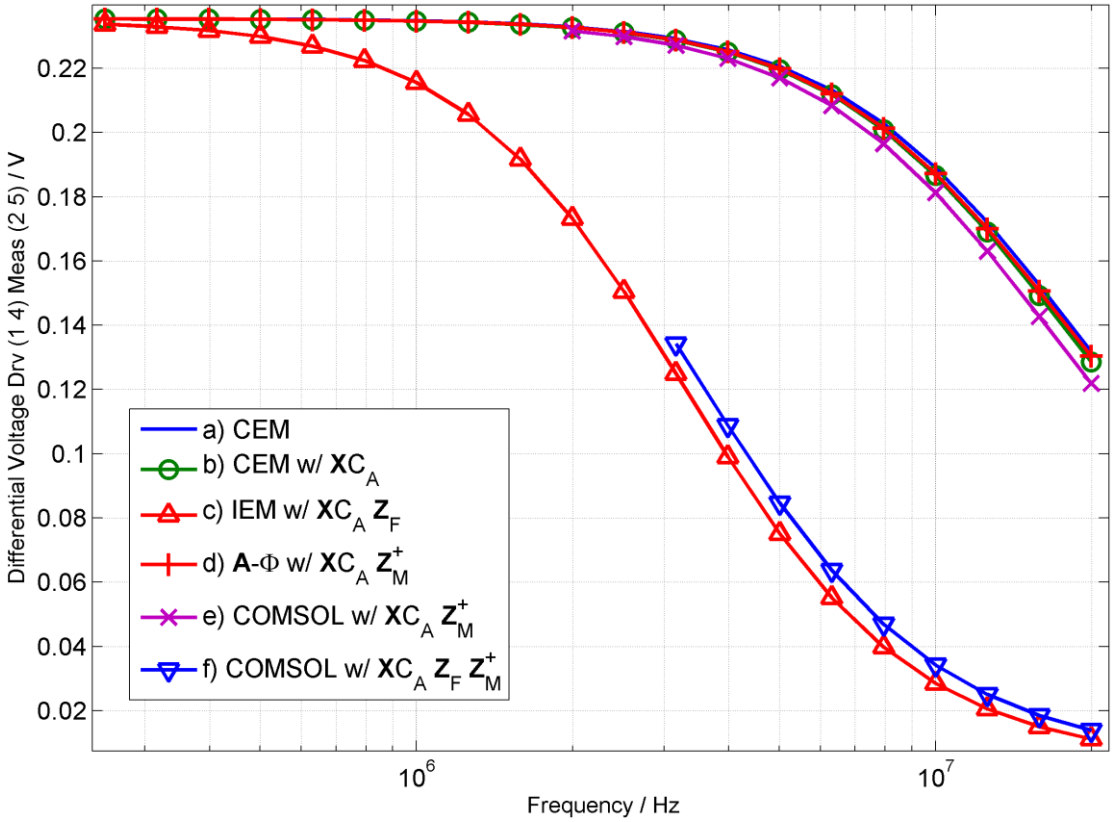

Figure 3-8 Voltage difference (magnitude) on measuring electrodes

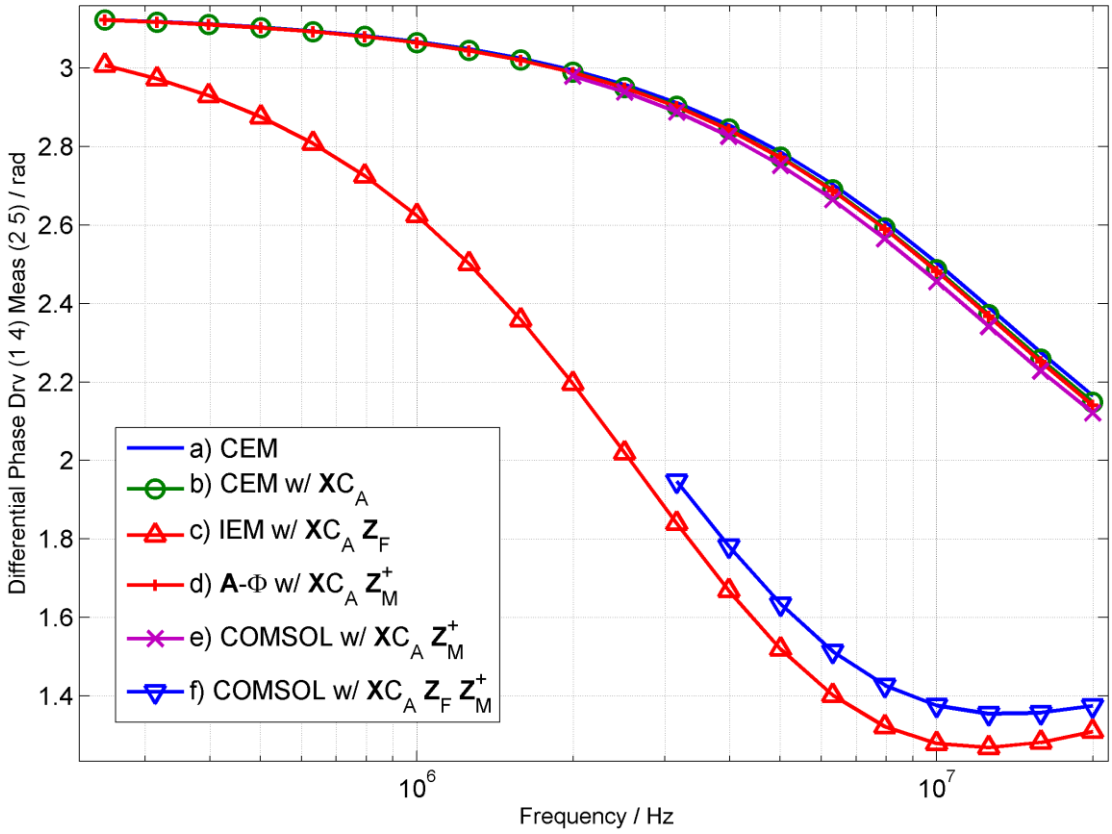

Figure 3-9 Voltage difference (phase) on measuring electrodes

From Figure 3-8 and Figure 3-9 we found:

- The volume cut-off effect, $\mathbf{XC}_A$, due to the free space surrounding the tank, is not easily observed until the frequency exceeds 5MHz. See curves a) and b).
- The full Maxwell effect, $\mathbf{Z}_M{}^+$, is not easily observed until the frequency exceeds 5MHz. See curves b), d) and e).
- The instrumental effect, $\mathbf{Z}_F$, can be easily observed from f > 300kHz. See curves b), c) and f).
- The observed discrepancy between d) and e) may be due to numerical differences in the methods for $\mathbf{A} - \Phi$ and COMSOL (as discussed previously for the Lumped Model).
- The difference between c) and f) could result from a combination of the full Maxwell effect, lack of contact impedance in f) and differences in numerical methods (different mesh, nodal/edge elements, solver, etc.), but it is not significant
- Results e) and f) obtained using COMSOL do not converge for frequencies lower than 2MHz (3MHz for f)). These results illustrate the limitations of COMSOL.

It is desirable to check at high frequencies whether the Laplace equation with our IEM model is adequate to predict the potential distribution without resorting to the full Maxwell equations, especially at frequencies where the quasi-static hypothesis tends to fail. In other words, we

check here whether the instrumental effect is the effect dominates the full Maxwell effect across the frequency range of interest.

Figure 3-10 and Figure 3-11 show contour plots (logarithmic scale) for the electric potential obtained by different methods with opposite and adjacent electrode drive at f = 5.01MHz. The three subplots illustrate results for (a) the $\mathbf{A} - \Phi$ method, (b) CEM with $\mathbf{X}\mathrm{C}_{\mathrm{A}}$ and (c) IEM.

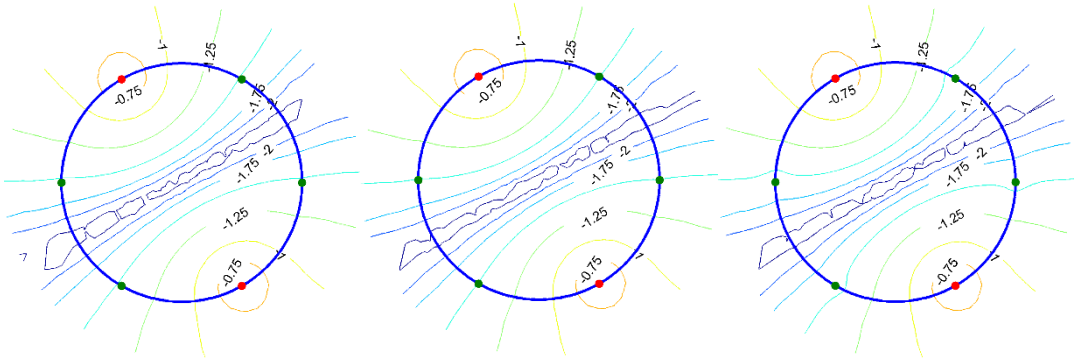

Figure 3-10 Contours of potential with opposite electrode drive at frequency 5.01MHz

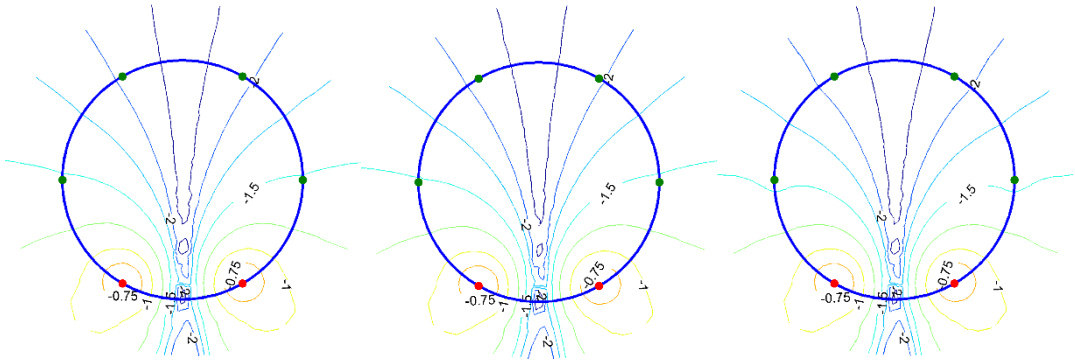

Figure 3-11 Contours of potential with adjacent electrode drive at frequency 5.01MHz

In Figure 3-10 and Figure 3-11, the contours are at z = 0.025m (electrodes slice, see Figure 3-6). The edge of the tank is in blue. The green dots in the plots represent electrodes and the red ones represent the driving electrodes.

The electric potentials obtained using the $\mathbf{A} - \Phi$ and CEM methods are similar, whereas the IEM method produces different results. It suggests the Maxwell effect does not contribute to the difference as much as the instrumental effect does for the parameters we chose. Hence if the instrumental effect is taken into account then the Laplace equations as implemented by the IEM should be used to predict the potential distribution.

3.5 Summary

This paper investigates the effects of non-ideal instrumentation on the performances of EIT front-end hardware. A more accurate electrode model for forward problems, IEM, is presented

which includes the instrumental loading effects in the electrode model. We conclude *that the instrument loading effects should be considered by both semi Maxwell and full Maxwell methods*, and the full Maxwell results (using the COMSOL with instrumental boundary conditions; see Figure 3-8 and Figure 3-9) confirm our argument.

Modelling demonstrates that the IEM model provides a more accurate representation in the frequency range from 500 kHz to a few MHz, a range where it is difficult for GIC circuits to overcome instrument effects at the driving electrodes and for calibration methods to compensate for effects at the measuring electrodes. Simulations show that an IEM formulation of the semi-Maxwell equations can provide a more accurate solution for the forward problems in situations where the full Maxwell effect is not the dominant effect in the frequency range. It is suggested to check with full Maxwell's solvers whether the material and frequency is suitable for the Laplace equations.

Table 3-3 summarises the general characteristics of the various solution methods investigated in this paper.

Table 3-3 Comparison of general characteristics of different methods for solving the forward problems

	Analytical	CEM	IEM	$\mathbf{A}-\Phi$ Method	COMSOL
Inversion	No	Capable	Capable	Capable	Difficult
Instrumental Effect	Yes	No	Yes	No	Yes
Maxwell's Effect	No	No	No	Yes	Yes
Complicated Geometry & Outer Space	No	Yes	Yes	Yes	Yes
Processing Density	Low	Normal	Normal	High	High
Low Frequency Stability	Good	Good	Good	Good	Poor
High Frequency Accuracy	Normal	Poor	Material Dependant	Material Dependant	Good

It is worth noting that the beta dispersion frequency used in some studies for distinguishing cancerous from normal tissues is reported to be fall in the same frequency range (100kHz to 10MHz) (Schwan, 1957; Grimnes & Martinsen, 2008; Surowiec, et al., 1988).

3.6 Appendix

As mentioned in Section 3.1, the IEM formula needs to be revised for voltage source EIT systems, and we derive it here including a simple example. Theoretically, there is no difference between voltage source and current source EIT systems, as voltage sources and current

sources can be made equivalent in circuits. However, using voltage source systems can avoid the situation where current source systems are not able to provide output impedance high enough to avoid from loading effects (Holder, 2005).

Although voltage source EIT systems can bring some benefits, the non-idealities, however, cannot be completely avoided. First, the input impedance between the voltage measuring electrode pairs cannot be infinite. Second, voltage source systems need to measure the currents on the exciting electrodes as it appears in inverse problems (Holder, 2005), but the current measurements can be inaccurate due to the finite impedance attached to electrodes.

Different approaches have been used for implementing EIT systems with voltage sources, including resistive sensors (Saulnier, et al., 2006; Halter, et al., 2008), bridges (Dutta, et al., 2001; Li, et al., 2013), etc. Typically, the voltage source system can be modelled as a collection of voltage sources, current measurement and voltage measurement components. We use Figure 3-12 to explain this, which is modified from Figure 3-1.

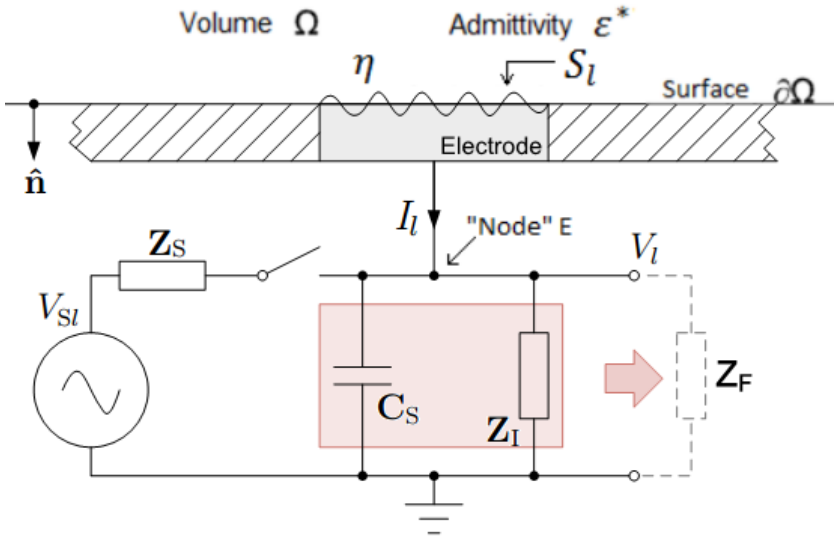

Figure 3-12 EIT electrode geometry and voltage source circuit model

In Figure 3-12, U_{Sl} is the voltage generated by the source, connected with the l^{th} electrode, $\mathbf{Z}_{\text{S}}$ is the impedance of the sensor resistor. For the remaining symbols in the figure we kept the previous definitions.

The switch controls the electrode to be in the exciting mode or measuring mode. In the exciting mode, an ideal voltage source is assumed and applied, generating a voltage U_{Sl}. A small resistor (connected between the source and the electrode) is used to measure the injected current. Similar to current source systems, not all the current measured by the sensor goes into the electrode especially when the operating frequency is high due to the finite

impedance attached to electrode (measurement circuit, switches and parasitic capacitor, etc.). These non-ideal instrumental effects result in inaccuracy. In the measuring mode, there are leakage currents flowing throughout the electrode and perturbing the potential distribution in the volume in a way similar to current source systems.

To derive the forward model for voltage source systems, the same procedure as in section 3.2 is used. We apply the current equation for the circuit node E to obtain,

$$\frac{U_l - U_{\mathrm{S}l}}{\mathbf{Z}_{\mathrm{S}}} + \frac{U_l - U_{\mathrm{GND}}}{\mathbf{Z}_{\mathrm{F}}} + I_l = 0,$$

in the driving mode, and

$$\frac{U_l - U_{\mathrm{GND}}}{\mathbf{Z}_{\mathrm{F}}} + I_l = 0\,,$$

in the measuring mode, where $\mathbf{Z}_{\mathrm{S}}$ denotes the sensing impedance of each electrode. Combining these two equations, we obtain (with $\mathbf{Z}_{\mathrm{S}} = \infty$ indicating the measuring mode),

$$\left(\frac{1}{\mathbf{Z}_{\mathrm{S}}} + \frac{1}{\mathbf{Z}_{\mathrm{F}}}\right) U_l + I_l = \frac{U_{\mathrm{S}l}}{\mathbf{Z}_{\mathrm{S}}}.$$

Equation 3-18

Substituting the above equation into the weak formula, we have,

$$\begin{cases} \int_{\Omega} \varepsilon^* \nabla v \cdot \nabla \Phi \, dV + \sum_{l=1}^{L} \frac{1}{\eta} \int_{S_l} v\Phi \, dS - \sum_{l=1}^{L} \frac{U_l}{\eta} \int_{S_l} v \, dS = 0\,, \\ \int_{S_l} \frac{U_l - \Phi}{\eta} dS - I_l = 0\,, \\ \left(\frac{1}{\mathbf{Z}_{\mathrm{S}l}} + \frac{1}{\mathbf{Z}_{\mathrm{F}l}}\right) U_l + I_l = \frac{U_{\mathrm{S}l}}{\mathbf{Z}_{\mathrm{S}l}}\,, l = 1,2,3,\ldots,L-1, \\ \left(\frac{1}{\mathbf{Z}_{\mathrm{S}L}} + \frac{1}{\mathbf{Z}_{\mathrm{F}L}}\right) U_L - \sum_{l=1}^{L-1} I_l = \frac{U_{\mathrm{S}L}}{\mathbf{Z}_{\mathrm{S}L}}. \end{cases}$$

Equation 3-19

With $\mathbf{Z}_{\mathrm{S}} = [\mathbf{Z}_{\mathrm{S}1} \quad \cdots \quad \mathbf{Z}_{\mathrm{S}L}]^{\mathrm{T}}$ and $\mathbf{v_S} = [U_{\mathrm{S}1} \quad \cdots \quad U_{\mathrm{S}L}]^{\mathrm{T}}$ the FEM matrix can be,

$$\begin{bmatrix} \boldsymbol{A} + \boldsymbol{B} & \boldsymbol{C} & \mathbf{0}^{N\times L} \\ \boldsymbol{C}^{\mathrm{T}} & \boldsymbol{D} & -\mathbf{I}^{L\times L} \\ \mathbf{0}^{L\times N} & \boldsymbol{G} & \boldsymbol{F} \end{bmatrix} \begin{bmatrix} \mathbf{u} \\ \mathbf{v} \\ \mathbf{i} \end{bmatrix} = \begin{bmatrix} \mathbf{0}^{(N+L)\times 1} \\ \frac{\mathbf{v_S}}{\mathbf{Z}_{\mathrm{S}}} \end{bmatrix},$$

$$\boldsymbol{G} = \mathrm{diag}\left\{\frac{1}{\mathbf{Z}_{\mathrm{S}l}} + \frac{1}{\mathbf{Z}_{\mathrm{F}l}}\right\} \in \mathbb{C}^{L\times L}.$$

In the measuring mode, $1/\mathbf{Z}_S$ is set to zero. The formula is very similar to the current source IEM but more complicated than the voltage source CEM. In addition, it predicts the current on the sensing resistor, but it requires the information of instrumental impedance $\mathbf{Z}_F$ and sensing impedance $\mathbf{Z}_S$.

We use the tank model with the following parameters to show the difference between the voltage source CEM and the voltage source IEM.

- Driving Voltages: +/-2V
- An electrode-driving pattern based on the opposite driving (1 and 4) and measuring electrodes (2 and 5) is used.
- In order for comparison, the voltage across the driving electrode pair is monitored.
- For IEM R_F = 5MOhm, C_{FM} = C_{DM} = 6pF, and $\mathbf{Z}_S$ = 10 Ohm for voltage driving electrodes.
- The contact impedance on both driving and measuring electrodes,

$$\eta = 7 \times 10^{-4} - \mathrm{j}5 \times 10^{-4} \Omega \cdot \mathrm{m}^2.$$

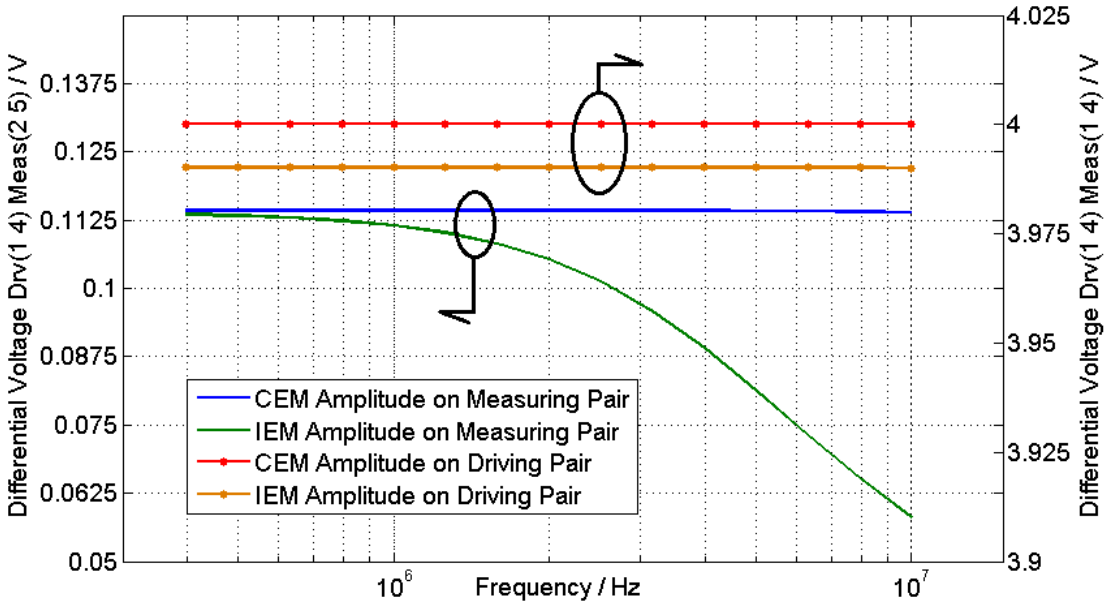

Figure 3-13 Voltage Difference on Electrode Pairs, with Voltage Source Setup.

Simulation results are shown in Figure 3-13. The instrumental effect on driving electrodes, contributed by the measuring circuits and parasitic capacitors, is not significant. The difference between the voltages on the CEM driving pair (red dot curve) and the IEM driving pair (orange dot curve) is caused by the sensor impedance, and we ignore it for simplicity here. On the other hand, it suggests that the CEM solutions can be significantly inaccurate on the measuring

electrode pairs due to the instrumental effects. The CEM shows an almost constant voltage across the frequency band (blue curve), whereas the IEM concludes that the input impedance of the measuring pair varies with frequency (green curve), and it changes the potential distribution inside the object accordingly.

Furthermore, the current measurements in the voltage source systems affected by hardware non-idealities can be more serious than what the simulation shows, especially when the sensing impedance contains a significant capacitive component. This problem is system dependent and closely related to the inverse problem, but we would like to discuss it in a different report.

Chapter 4 EIT Forward Problems with Full Maxwell's Equations

4.1 Introduction

In order to extend the frequency range of the EIT for better covering the beta-dispersion band, the quasi-static assumption has to be revised. With the full Maxwell's equations applied, the EIT forward problem becomes a full-vectorial analysis instead of an electro-quasi-static problem (Larsson, 2007).

I have mentioned a few different modalities including UWB and MWT in Chapter 1 which use frequencies higher than the beta-dispersion or even gamma-dispersion band. For these high frequency applications, full Maxwell's equations are solved. However, a background medium with a uniform distribution of electromagnetic properties (including admittivity, permeability, etc.) has to be assumed to avoid complicated FEM analysis (Semenov, 2009).

The difficulty in the FEM analysis of electromagnetic fields is mainly due to the discontinuities of the $\mathbf{E}$ and $\mathbf{H}$ fields (the prime fields). It can be successfully handled by the Edge-Element FEM methods (Barton & Cendes, 1987). However, the discontinuous functions are incompatible with inverse schemes (Somersalo, et al., 1992), which can be also seen from Equation 2-3.

A traditional EIT solves electric scalar potentials in forward problems and obtains the distribution of the admittivity by inversing the forward solutions under the quasi-static assumption. In this way, the discontinuities of the prime fields are not involved.

Solving the potential formula of the full Maxwell's equations with nodal-element FEM (Soni, et al., 2006) is an appropriate method for high frequency EIT applications. It obtains full-vectorial forward solutions without including the discontinuities of the prime fields. However, to propose realistic BCs for both the potentials and gauge functions can be challenging, for two reasons. Firstly, the potentials themselves are not observable, extra degrees of freedom are embedded in the definition of potentials. Gauge fixing has to be performed to remove the arbitrariness. Secondly, proper methods for injecting electromagnetic field are needed, and the contact impedance and instrumental impedance have to be modelled by the proper BCs.

Table 4-1 summarises different methods for solving forward problems.

Table 4-1 Comparison between different methods for solving forward problems

	Inversion	Contact Impedance	Instrumental Effect	Maxwell's Effect	Processing Density	Low Frequency Stability	High Frequency Accuracy
CEM	**Yes**	**Yes**	No	No	**Low**	**Yes**	Poor
IEM	**Yes**	**Yes**	**Yes**	No	**Low**	**Yes**	Normal
SEM-IBC	**Yes**	No	No	**Yes**	High	**Yes**	Normal
CEM-IBC	**Yes**	**Yes**	No	**Yes**	High	**Yes**	Normal
TPM	**Yes**	**Yes**	**Yes**	**Yes**	High	**Yes**	**Good**
COMSOL	No	No	**Yes**	**Yes**	High	No	**Good**

In this chapter, we will introduce the difference between the quasi-static assumption and full Maxwell's equations. The continuity of the EMF is introduced in Section 4.2. The derivations the 3-D potential formula, the potential BCs and the gauge fixing are described in Section 4.3. I proposed two sets of BCs for high frequency EIT applications including CEM-IBC and TPM, and they will be detailed in Section 4.4. They model the effects of the contact impedance and the instrumental impedance. A tank structure similar to the model in Section 3.4.2, will be studied with different sets of BCs, and with the results discussed in Section 4.5.

4.2 Fundamental of Electromagnetic Field and Potentials

4.2.1 Quasi-static Approximation

The quasi-static approximation is made in Chapter 2 (Equation 2-9), and it says that at a low frequency, the electric field can be considered as an irrotational field. This assumption simplifies an EIT forward problem to a Laplace equation (Equation 2-10).

It is necessary to re-examine the quasi-static assumption when extending the frequency range of an EIT system, as we stated in earlier chapters.

It is not obvious to see the inaccuracy introduced by the approximation,

$$\nabla \cdot \varepsilon^* (\nabla \Phi_0 + \mathrm{j}\omega \mathbf{A}_0) \cong \nabla \cdot \varepsilon^* \nabla \Phi \,.$$

We can estimate the quasi-static error. Take a simple structure shown in Figure 4-1 as an example. The top and bottom circles are PEC plates, with radii being the same as R, separated by a distance of d. Between the two plates, there is a virtual circle with the radius of r. A virtual rectangular is placed between the two plates, perpendicular to the surfaces of the plates, with the height d and width $R - r$.

In order to describe the example, we use the cylindrical coordinates and let the vertical direction to be $\hat{x}$, the radial direction to be $\hat{r}$, and the direction tangent to the edge of the circle to be $\hat{\theta}$. The material in the geometry is assumed to be homogeneous and isotropic.

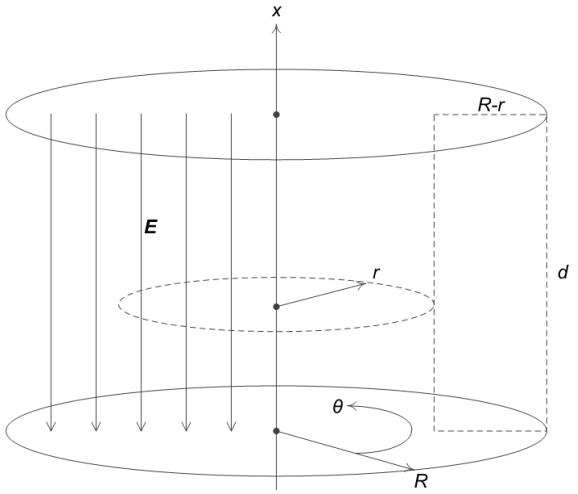

Figure 4-1 Simple Geometry Setup for Estimating the Quasi-static Error

Assume there is a source generating a voltage difference $U = U_0 e^{\mathrm{j}\omega_0 t}$ between the two plates. Under the quasi-static assumption, the electric field intensity between the plates can be approximated as,

$$\mathbf{E} = -\nabla\Phi - \mathrm{j}\omega\mathbf{A} \cong -\nabla\Phi, \qquad \mathbf{E} = E_0\hat{x} + E_\mathrm{r}\hat{r} \approx E_0\hat{x} = \frac{U}{d}\hat{x}.$$

At the edge of the plate E_r can exist, but we ignore it here for simplicity.

Recall the integral form of the Ampère's circuital law (with Maxwell's addition), and apply it on the electric field throughout the virtual circle. As the geometry is angular symmetrical and homogenous, the integral becomes

$$\oint_0^{2\pi} \mathbf{B}(r) \cdot \mathrm{d}\theta = \int_{\mathrm{vc}} \mu\varepsilon^* \mathbf{E} \cdot \mathrm{d}\boldsymbol{S}, \qquad \mathbf{H}(r) = \frac{\varepsilon^* E_0 r}{2}\theta.$$

Then we consider the magnetic field intensity throughout the virtual rectangle, apply the integral form the Maxwell-Faraday equation.

$$\oint_{\partial\mathrm{Rect}} \mathbf{E} \cdot \mathrm{d}l = -\int_{\mathrm{Rect}} \mathrm{j}\omega\mu\mathbf{H} \cdot \mathrm{d}\boldsymbol{S} = -\oint_{\partial\mathrm{Rect}} (\nabla\Phi + \mathrm{j}\omega\mathbf{A}) \cdot \mathrm{d}l.$$

Equation 4-1

Here the quasi-static error appears by inserting the potential definition equation. If the vector potential field $\mathbf{A}$ is ignored, the most RHS of the equation will vanish according to gradient theorem, which means the $\mathbf{H}$ filed does not contribute to the electric field.

$\mathbf{E}$ is perpendicular to the surfaces of the metal plates, so only the vertical paths contribute to the integral of the LHS of Equation 4-1. Therefore, we have,

$$\int_0^d \mathbf{E}(r) \cdot \mathrm{d}x + \int_d^0 \mathbf{E}(R) \cdot \mathrm{d}x = -\int_{\mathrm{Rect}} \mathrm{j}\omega\mu\mathbf{H} \cdot \mathrm{d}\boldsymbol{S},$$

$$= U_r - U_R = -\int_r^R \mathrm{j}\omega\mu \frac{\varepsilon^* E_0 r'}{2} d\mathrm{d}r' = -\mathrm{j}\omega\mu\varepsilon^* \frac{U}{4}(R^2 - r^2).$$

The integral on the LHS are replaced with the potential difference $U_r - U_R$, but it is different from the voltage generated by the source U. The equation says that the intensity of the electric field is re-distributed, due to the change of the magnetic field in the $\hat{\theta}$ direction, so does the potential.

In some circumstances, the difference between the potentials given by quasi-static and full Maxwell analysis can be ignored. These circumstances must obey the following relationship,

$$Q = \left|\frac{U_r - U_R}{U}\right| = \left|\frac{\omega\mu\varepsilon^*(r')^2}{4}\right| \ll 1$$

Equation 4-2

Equation 4-2 indicates that ω, μ, ε^* and r' affect the accuracy of the quasi-static assumption in different ways. Here r' is the distance from the voltage source to the position of the measurement.

We consider a cylinder of saline with the $R = 0.1$m, $\sigma = 0.1$S/m, relative permittivity = 81, and the relative permeability = 1. By evaluating Equation 4-2 with the assumption of $Q \leq 1\%$, the limit of the frequency is 5.212 MHz. Or for $Q \leq 0.1\%$, the limit becomes 1.018MHz.

In EIT applications, the admittivity or the size of the object can have a significant variation, and therefore it is difficult to ensure that the quasi-static assumption is valid.

In order to obtain accurate forward solutions for realistic EIT geometries, it is necessary to introduce the full Maxwell (non-quasi-static) formula with its numerical methods as well as their BCs in the following sections.

4.2.2 Continuity Conditions

It has been mentioned, that the curl-curl FEM formula (Davies, et al., 1982) can have spurious solutions due to the discontinuities of the prime fields. In this section, we will explain the continuity conditions of the EMF for the prime fields and the potentials.

The continuity conditions (or boundary conditions in some literatures) of the prime fields are well studied (Wangsness, 1986). The continuity conditions can be obtained with the integral form of the Maxwell's equations.

$$\hat{\mathbf{n}} \cdot (\mathbf{D}_1 - \mathbf{D}_2) = \rho_s$$

$$\hat{\mathbf{n}} \times (\mathbf{H}_1 - \mathbf{H}_2) = \mathbf{J}_s$$

$$\hat{\mathbf{n}} \times (\mathbf{E}_1 - \mathbf{E}_2) = \mathbf{0}$$

$$\hat{\mathbf{n}} \cdot (\mathbf{B}_1 - \mathbf{B}_2) = 0$$

Equation 4-3 (a - d)

Equation 4-3 (c - d) ensure that the tangential components of the electric field or the normal components of the magnetic field have to be continued across a boundary. But due to the surface charge density ρ_s or the surface current density $\mathbf{J}_s$, the normal component of the $\mathbf{D}$ field and the tangential component of the $\mathbf{H}$ field can be discontinuous.

Reviewing the FEM approach we introduced in Section 2.2.2, the unknown function $\mathcal{U}$ is approximated by the discrete functions $\mathcal{U}_N = \sum u_j \phi_j$. From the nodal-based shape function ϕ_j in Figure 2-2 (blue lines), the discretisation requires $\mathcal{U}$ to be smooth. The discontinuity in the $\mathbf{D}$ and $\mathbf{H}$ fields violates the requirements of the nodal-based FEM discretisation, and this violation produces spurious modes.

The continuity of potentials is different from the prime fields. As the potentials are defined by their derivatives in Equation 2-6, Equation 2-8 and Equation 2-33, they are naturally continuous and one order smoother than the prime fields.

4.3 Numerical Implementation of Helmholtz-like Equations

With the weak formula derived in Chapter 2, we apply discretisation and 3-D implementation in this section. The boundary coordinates are introduced and the typical BCs of the potentials formula are discussed. The derivations of the BCs specifically for EIT applications are detailed the next section.

4.3.1 FEM for Potential Formula

Apart from the piecewise linear distribution Φ_N used to approximate Φ in Chapter 2 and Chapter 3, now we add $\mathbf{A}_N$ for the vector potential.

$$\Phi_N = \sum_{j=1}^{N} \mathrm{u}_j \phi_j \,, \qquad \mathbf{A}_N = \sum_{j=1}^{N} \boldsymbol{\Lambda}_j \, \phi_j = \sum_{j=1}^{N} \left(\boldsymbol{\Lambda}_{xj} \hat{\mathbf{x}} + \boldsymbol{\Lambda}_{yj} \hat{\mathbf{y}} + \boldsymbol{\Lambda}_{zj} \hat{\mathbf{z}} \right) \phi_j$$

By inserting the discretised potentials, we have,

$$\begin{aligned} \sum_{j=1}^{N} \int_{\Omega} \frac{1}{\mu} \left[\nabla \times \left(\phi_j \boldsymbol{\Lambda}_j \right) \right] \times \nabla \phi_i \mathrm{d}V + \sum_{j=1}^{N} \int_{\Omega} \frac{1}{\mu} \nabla \cdot \left(\phi_j \boldsymbol{\Lambda}_j \right) \nabla \phi_i \mathrm{d}V \\ + \sum_{j=1}^{N} \mathrm{j}\omega \int_{\Omega} \varepsilon^* \phi_i \left(\phi_j \boldsymbol{\Lambda}_j \right) \mathrm{d}V + \sum_{j=1}^{N} \int_{\Omega} \varepsilon^* \phi_i \nabla \left(\phi_j \mathrm{u}_j \right) \mathrm{d}V \\ + \sum_{j=1}^{N} \int_{\Omega} \varepsilon^* \left(\phi_j \mathrm{u}_j \right) \nabla \phi_i \mathrm{d}V \\ = - \oint_{\partial\Omega} \hat{\mathbf{n}} \times v \frac{1}{\mu} \nabla \times \mathbf{A} \, \mathrm{d}S + \oint_{\partial\Omega} \left(v \frac{1}{\mu} \nabla \cdot \mathbf{A} \right) \hat{\mathbf{n}} \, \mathrm{d}S + \oint_{\partial\Omega} (\varepsilon^* v \Phi) \hat{\mathbf{n}} \, \mathrm{d}S \,, \end{aligned}$$

$$\begin{aligned} \sum_{j=1}^{N} \int_{\Omega} \varepsilon^{*2} \mu \phi_i \left(\phi_j \mathrm{u}_j \right) \mathrm{d}V + \sum_{j=1}^{N} \frac{1}{\mathrm{j}\omega} \int_{\Omega} \varepsilon^* \nabla \left(\phi_j \mathrm{u}_j \right) \cdot \nabla \phi_i \mathrm{d}V + \sum_{j=1}^{N} \int_{\Omega} \varepsilon^* \phi_i \nabla \cdot \left(\phi_j \boldsymbol{\Lambda}_j \right) \mathrm{d}V \\ + \sum_{j=1}^{N} \int_{\Omega} \varepsilon^* \left(\phi_j \boldsymbol{\Lambda}_j \right) \cdot \nabla \phi_i \mathrm{d}V = \oint_{\partial\Omega} \varepsilon^* (v \mathbf{A} \cdot \hat{\mathbf{n}}) \mathrm{d}S + \frac{1}{\mathrm{j}\omega} \oint_{\partial\Omega} v (\varepsilon^* \nabla \Phi \cdot \hat{\mathbf{n}}) \mathrm{d}S \,. \end{aligned}$$

Equation 4-4 (a - b)

Compared with Equation 2-11, Equation 4-4 (a - b) are much more complicated, and most of these terms are ignored by the quasi-static approximation.

We leave the surface integrals on the RHS for later discussions in BCs sections. In order to compose the FEM matrix in the form of a stiffness matrix and mass matrix, some of the terms need to be rearranged. The vectors, u_j and $\boldsymbol{\Lambda}_j$ are not functions of positions, so the gradients of u_j, the curls and divergences of $\boldsymbol{\Lambda}_j$ are vanished. Applying vector identities on the terms, we have,

$$\begin{aligned} \sum_{j=1}^{N} \boldsymbol{\Lambda}_j \int_{\Omega} \frac{1}{\mu} \nabla \phi_i \cdot \nabla \phi_j \mathrm{d}V + \sum_{j=1}^{N} \int_{\Omega} \frac{1}{\mu} \left[\left(\nabla \phi_j \cdot \boldsymbol{\Lambda}_j \right) \nabla \phi_i - \left(\nabla \phi_i \cdot \boldsymbol{\Lambda}_j \right) \nabla \phi_j \right] \mathrm{d}V \\ + \sum_{j=1}^{N} \mathrm{j}\omega \boldsymbol{\Lambda}_j \int_{\Omega} \varepsilon^* \phi_i \phi_j \mathrm{d}V + \sum_{j=1}^{N} \mathrm{u}_j \int_{\Omega} \varepsilon^* \left(\phi_i \nabla \phi_j + \phi_j \nabla \phi_i \right) \mathrm{d}V \\ = - \oint_{\partial\Omega} \hat{\mathbf{n}} \times v \frac{1}{\mu} \nabla \times \mathbf{A} \, \mathrm{d}S + \oint_{\partial\Omega} \left(v \frac{1}{\mu} \nabla \cdot \mathbf{A} \right) \hat{\mathbf{n}} \, \mathrm{d}S + \oint_{\partial\Omega} (\varepsilon^* v \Phi) \hat{\mathbf{n}} \, \mathrm{d}S \,, \end{aligned}$$

$$\sum_{j=1}^{N}\int_{\Omega}\varepsilon^{*}\left(\phi_i\nabla\phi_j+\phi_j\nabla\phi_i\right)\mathrm{d}V\cdot\boldsymbol{\Lambda}_j+\sum_{j=1}^{N}\frac{\mathrm{u}_j}{\mathrm{j}\omega}\int_{\Omega}\varepsilon^{*}\nabla\phi_j\cdot\nabla\phi_i\mathrm{d}V$$

$$+\sum_{j=1}^{N}\mathrm{u}_j\int_{\Omega}\varepsilon^{*2}\mu\phi_i\phi_j\mathrm{d}V=\oint_{\partial\Omega}\varepsilon^{*}(v\mathbf{A}\cdot\hat{\mathbf{n}})dS+\frac{1}{\mathrm{j}\omega}\oint_{\partial\Omega}v(\varepsilon^{*}\nabla\Phi\cdot\hat{\mathbf{n}})dS\,.$$

Equation 4-5 (a - b)

By expanding the components of $\boldsymbol{\Lambda}$, and insertting u, the unknown vector $[\mathrm{u}\boldsymbol{\Lambda}]$ is composed. In Electrodynamics (Westgard, 1997), the concept of 4-potentials $[\mathrm{u}\boldsymbol{\Lambda}]$ is commonly used for simplifying the description EMF, in contrast to the prime fields having 6 variables.

$$\boldsymbol{\Lambda}_j=[\boldsymbol{\Lambda}_{xj}\quad\boldsymbol{\Lambda}_{yj}\quad\boldsymbol{\Lambda}_{zj}]^{\mathrm{T}},\qquad[\mathrm{u}\boldsymbol{\Lambda}]=[\boldsymbol{\Lambda}_{1x}\quad\boldsymbol{\Lambda}_{1y}\quad\boldsymbol{\Lambda}_{1z}\quad\mathrm{u}_1\quad\cdots\quad\boldsymbol{\Lambda}_{Nx}\quad\boldsymbol{\Lambda}_{Ny}\quad\boldsymbol{\Lambda}_{Nz}\quad\mathrm{u}_N]^{\mathrm{T}},$$

Before implementing the FEM formula, we introduce a few matrices which are constantly used for composing the FEM matrix. The gradient to a shape function of the i^{th} node, within the element e has been placed in a 4 by 4 diagonal matrix as $[\boldsymbol{\phi\phi}_i^e]$.

$$[\boldsymbol{\phi\phi}_i^e]=\begin{bmatrix}\frac{\partial\phi^e{}_i}{\partial x}&0&0&0\\0&\frac{\partial\phi^e{}_i}{\partial y}&0&0\\0&0&\frac{\partial\phi^e{}_i}{\partial z}&0\\\multicolumn{4}{c}{\mathbf{0}^{1\times4}}\end{bmatrix},\qquad[EN_i]=\begin{matrix}\vdots\\e1\\\vdots\\\vdots\\e2\\\vdots\\\vdots\\e3\\\vdots\end{matrix}\begin{matrix}\vdots\\1\\2\\3\\4\\\vdots\\1\\2\\3\\4\\\vdots\\1\\2\\3\\4\\\vdots\end{matrix}\begin{matrix}\vdots\\\\\\\\\\\rightarrow\\\\\\\\\\\rightarrow\\\\\\\\\\\rightarrow\\\\\\\end{matrix}\begin{bmatrix}\vdots\\\mathbf{0}^{4\times4}\\\mathbb{I}^4\\\mathbf{0}^{4\times4}\\\mathbf{0}^{4\times4}\\\vdots\\\mathbb{I}^4\\\mathbf{0}^{4\times4}\\\mathbf{0}^{4\times4}\\\mathbf{0}^{4\times4}\\\vdots\\\mathbf{0}^{4\times4}\\\mathbf{0}^{4\times4}\\\mathbf{0}^{4\times4}\\\mathbb{I}^4\\\vdots\end{bmatrix}\in\mathbb{R}^{16E\times4}.$$

$[EN_i]$ is in the matrix which connects the element to the nodes, similar to the matrix we introduced in Equation 3-11 (a), Chapter 3, but here more dimensions are added, and it is modified respectively. Assume the node i is shared by three different elements, $e1$, $e2$ and $e3$. And it is the 2nd, 1st and 4th node of these 3 elements respectively. Then we can have $[EN_i]$ made up with E blocks in a column, corresponding to the elements. Each block has 4 sub-blocks placed in the column, corresponding to the 4 nodes of the element. The node i is shared by blocks $e1$, $e2$ and $e3$, where the 2nd, 1st and 4th sub-blocks are 4×4 identity matrices respectively.

$$[\boldsymbol{\phi\phi}^e] = [[\boldsymbol{\phi\phi}_1^e] \quad \cdots \quad [\boldsymbol{\phi\phi}_N^e]], \qquad [\boldsymbol{KK}_i] = \begin{bmatrix} [\boldsymbol{\phi\phi}_i^1] \\ \vdots \\ [\boldsymbol{\phi\phi}_i^E] \end{bmatrix},$$

$$[\boldsymbol{KK}] = [[\boldsymbol{KK}_1] \quad \cdots \quad [\boldsymbol{KK}_N]], \qquad [EN] = [[EN_1] \quad \cdots \quad [EN_N]]$$

The $[\boldsymbol{\phi\phi}_i^e]$ and $[EN_i]$ for different nodes and elements are together made up matrices named as above. Another two matrices are made for their functionalities, as,

$$[SV_0] = \begin{bmatrix} \mathbf{0}^{4\times3} & \begin{matrix}1\\1\\1\\0\end{matrix} \end{bmatrix}, \qquad [SS_0] = \begin{bmatrix} \mathbf{0}^{4\times3} & \begin{matrix}0\\0\\0\\1\end{matrix} \end{bmatrix}, \qquad [SS/V] = \mathrm{diag}\begin{bmatrix} [SS/V_0] \\ \vdots \\ [SS/V_0] \end{bmatrix} \in \mathbb{R}^{4N\times4N}.$$

These matrices are responsible for selecting the vector potentials or scalar potentials. The subscript 0 indicates that they are constant.

With the above matrices defined, the FEM matrix can be given as follows. The first one is the stiffness matrix for the vector potential.

$$\sum\nolimits_{j=1}^{N} \boldsymbol{\Lambda}_j \int_\Omega \frac{1}{\mu} \begin{bmatrix} \frac{\partial \phi_i}{\partial x} \\ \frac{\partial \phi_i}{\partial y} \\ \frac{\partial \phi_i}{\partial z} \end{bmatrix}^{\mathrm{T}} \begin{bmatrix} \frac{\partial \phi_j}{\partial x} \\ \frac{\partial \phi_j}{\partial y} \\ \frac{\partial \phi_j}{\partial z} \end{bmatrix} \mathrm{d}V = \sum_{j=1}^{N} \boldsymbol{\Lambda}_j \sum\nolimits_{e=1}^{\mathrm{E}} \frac{V^e}{\mu^e} \begin{bmatrix} \frac{\partial \phi^e{}_i}{\partial x} \\ \frac{\partial \phi^e{}_i}{\partial y} \\ \frac{\partial \phi^e{}_i}{\partial z} \end{bmatrix}^{\mathrm{T}} \begin{bmatrix} \frac{\partial \phi^e{}_j}{\partial x} \\ \frac{\partial \phi^e{}_j}{\partial y} \\ \frac{\partial \phi^e{}_j}{\partial z} \end{bmatrix}$$

$$= \left(\sum_{e=1}^{\mathrm{E}} [\boldsymbol{\phi\phi}_i^e]^{\mathrm{T}} [\mu V^e] [\boldsymbol{\phi\phi}^e] \right) [\mathrm{u}\boldsymbol{\Lambda}] = [\boldsymbol{KK}_i]^{\mathrm{T}} [\mu V] [\boldsymbol{KK}] [\mathrm{u}\boldsymbol{\Lambda}] ,$$

$$[\mu V^e] = \frac{V^e}{\mu^e} \mathbb{I}^4, \qquad [\mu V] = \mathrm{diag}\begin{bmatrix} [\mu V^1] \\ \vdots \\ [\mu V^E] \end{bmatrix}.$$

We arrange the stiffness matrix in four-potential form for compatibility, including the three vector potential dimensions and one scalar potential dimension, although the scalar potential is not involved in the operation.

The second stiffness matrix of $\boldsymbol{\Lambda}_j$,

$$\sum_{j=1}^{N}\int_{\Omega}\frac{1}{\mu}\left(\begin{bmatrix}\frac{\partial\phi_i}{\partial x}\\ \frac{\partial\phi_i}{\partial y}\\ \frac{\partial\phi_i}{\partial z}\end{bmatrix}\begin{bmatrix}\frac{\partial\phi_j}{\partial x}\\ \frac{\partial\phi_j}{\partial y}\\ \frac{\partial\phi_j}{\partial z}\end{bmatrix}^{\mathrm{T}}-\begin{bmatrix}\frac{\partial\phi_j}{\partial x}\\ \frac{\partial\phi_j}{\partial y}\\ \frac{\partial\phi_j}{\partial z}\end{bmatrix}\begin{bmatrix}\frac{\partial\phi_i}{\partial x}\\ \frac{\partial\phi_i}{\partial y}\\ \frac{\partial\phi_i}{\partial z}\end{bmatrix}^{\mathrm{T}}\right)\boldsymbol{\Lambda}_j\,\mathrm{d}V$$

$$=\sum_{j=1}^{N}\sum_{e=1}^{\mathrm{E}}\frac{V^e}{\mu^e}\left(\begin{bmatrix}\frac{\partial\phi^e{}_i}{\partial x}\\ \frac{\partial\phi^e{}_i}{\partial y}\\ \frac{\partial\phi^e{}_i}{\partial z}\end{bmatrix}\begin{bmatrix}\frac{\partial\phi^e{}_j}{\partial x}\\ \frac{\partial\phi^e{}_j}{\partial y}\\ \frac{\partial\phi^e{}_j}{\partial z}\end{bmatrix}^{\mathrm{T}}-\begin{bmatrix}\frac{\partial\phi^e{}_j}{\partial x}\\ \frac{\partial\phi^e{}_j}{\partial y}\\ \frac{\partial\phi^e{}_j}{\partial z}\end{bmatrix}\begin{bmatrix}\frac{\partial\phi^e{}_i}{\partial x}\\ \frac{\partial\phi^e{}_i}{\partial y}\\ \frac{\partial\phi^e{}_i}{\partial z}\end{bmatrix}^{\mathrm{T}}\right)\boldsymbol{\Lambda}_j$$

$$=\sum_{e=1}^{\mathrm{E}}\left([\boldsymbol{\phi}\boldsymbol{\phi}_i^e]^{\mathrm{T}}[\mu VB^e][\boldsymbol{\phi}\boldsymbol{\phi}^e]-[\boldsymbol{KRK}_i]\right)[\mathrm{u}\boldsymbol{\Lambda}]=\left([\boldsymbol{KK}_i]^{\mathrm{T}}[\mu VB][\boldsymbol{KK}]-[\boldsymbol{KRK}_i]\right)[\mathrm{u}\boldsymbol{\Lambda}]\,,$$

$$[\mu VB^e]=\frac{V^e}{\mu^e}\begin{bmatrix}1&1&1&0\\1&1&1&0\\1&1&1&0\\0&0&0&0\end{bmatrix},\qquad[\mu VB]=\mathrm{diag}\begin{bmatrix}[\mu VB^1]\\ \vdots\\ [\mu VB^E]\end{bmatrix},$$

$$[\boldsymbol{KRK}_i]=[[\boldsymbol{KK}_i]^{\mathrm{T}}[\mu VB][\boldsymbol{KK}_1]\quad\cdots\quad[\boldsymbol{KK}_i]^{\mathrm{T}}[\mu VB][\boldsymbol{KK}_N]]\,.$$

The mass matrix of $\boldsymbol{\Lambda}_j$ can be given with the similar method introduced in Section 3.3.3, and the integral of the shape functions can be given with Equation 3-7 (b),

$$\left(\sum_{e=1}^{\mathrm{E}}\mathrm{j}\omega\varepsilon^{*e}\begin{bmatrix}\int_{V^e}\phi_i\phi_1\,\mathrm{d}V\\ \vdots\\ \int_{V^e}\phi_i\phi_N\,\mathrm{d}V\end{bmatrix}^{\mathrm{T}}\right)[\mathrm{u}\boldsymbol{\Lambda}]=[EN_i]^{\mathrm{T}}[\varepsilon VM][EN][\mathrm{u}\boldsymbol{\Lambda}]$$

$$[\varepsilon VM^e]=\frac{\mathrm{j}\omega\varepsilon^{*e}V^e}{20}\begin{bmatrix}2\mathbb{I}^4&\cdots&\mathbb{I}^4\\ \vdots&\ddots&\vdots\\ \mathbb{I}^4&\cdots&2\mathbb{I}^4\end{bmatrix}\in\mathbb{C}^{16\times16},\qquad[\varepsilon VM]=\mathrm{diag}\begin{bmatrix}[\varepsilon VM^1]\\ \vdots\\ [\varepsilon VM^E]\end{bmatrix}.$$

The second mass matrix of $\boldsymbol{\Lambda}_j$ can be given as,

$$\sum_{e=1}^{\mathrm{E}}\left([SV_0]^{\mathrm{T}}\varepsilon^{**e}\int_{V^e}\phi_i^e\,\mathrm{d}V\,[\boldsymbol{\phi}\boldsymbol{\phi}^e]+[SV_0]^{\mathrm{T}}\varepsilon^{**e}\int_{V^e}\phi_j^e\,\mathrm{d}V\,[\boldsymbol{\phi}\boldsymbol{\phi}_i^e]^{\mathrm{T}}\right)[\mathrm{u}\boldsymbol{\Lambda}]$$

$$=\left([SV_0]^{\mathrm{T}}[EN_i]^{\mathrm{T}}[\varepsilon V^*][\boldsymbol{KK}]+[SV_0]^{\mathrm{T}}[\boldsymbol{KK}_i]^{\mathrm{T}}[\varepsilon V^*]^{\mathrm{T}}[EN]\right)[\mathrm{u}\boldsymbol{\Lambda}]$$

$$[\varepsilon V^{*e}] = \varepsilon^{**e}\frac{V^e}{4}\begin{bmatrix}\mathbb{I}^4\\ \mathbb{I}^4\\ \mathbb{I}^4\\ \mathbb{I}^4\end{bmatrix}, \qquad [\varepsilon V^*] = \operatorname{diag}\begin{bmatrix}[\varepsilon V^{*1}]\\ \vdots\\ [\varepsilon V^{*E}]\end{bmatrix}.$$

ε^{**} is the complex conjugate of admittivity where the conjugate is brought by the inner product. The product of this mass matrix is a scalar, but we made it into the four-potential form for compatibility.

The stiffness matrix of u_j can be the same from the Laplace forward problem in Equation 3-13, in Chapter 3. We made modifications to fit into the four-potential form.

$$\sum_{j=1}^{N}\frac{\mathrm{u}_j}{\mathrm{j}\omega}\int_\Omega \varepsilon^*\begin{bmatrix}\frac{\partial\phi_i}{\partial x}\\ \frac{\partial\phi_i}{\partial y}\\ \frac{\partial\phi_i}{\partial z}\end{bmatrix}^{\mathrm{T}}\begin{bmatrix}\frac{\partial\phi_j}{\partial x}\\ \frac{\partial\phi_j}{\partial y}\\ \frac{\partial\phi_j}{\partial z}\end{bmatrix}\mathrm{d}V = \left(\sum_{e=1}^{\mathrm{E}}[SV_0]^{\mathrm{T}}[\boldsymbol{\phi\phi}_i^e]^{\mathrm{T}}[\varepsilon VK^e][\boldsymbol{\phi\phi}^e][SV]\right)[\mathrm{u}\boldsymbol{\Lambda}]$$

$$= [SV_0]^{\mathrm{T}}[\boldsymbol{KK}_i]^{\mathrm{T}}[\varepsilon VK][\boldsymbol{KK}][SV][\mathrm{u}\boldsymbol{\Lambda}]$$

$$[\varepsilon VK^e] = \frac{\varepsilon^{*e}V^e}{\mathrm{j}\omega}\mathbb{I}^4, \qquad [\varepsilon VK] = \operatorname{diag}\begin{bmatrix}[\varepsilon VK^1]\\ \vdots\\ [\varepsilon VK^E]\end{bmatrix}$$

The first mass matrix for u_j can be given,

$$\left(\sum_{e=1}^{\mathrm{E}}\varepsilon^{*e2}\mu^e\begin{bmatrix}\int_{V^e}\phi_i\phi_1\,\mathrm{d}V\\ \vdots\\ \int_{V^e}\phi_i\phi_N\,\mathrm{d}V\end{bmatrix}^{\mathrm{T}}\right)[\mathrm{u}\boldsymbol{\Lambda}] = [SS_0]^{\mathrm{T}}[EN_i]^{\mathrm{T}}[\varepsilon VS][EN][SS][\mathrm{u}\boldsymbol{\Lambda}]$$

$$[\varepsilon VS^e] = \frac{\varepsilon^{*e2}\mu^eV^e}{20}\begin{bmatrix}2\mathbb{I}^4 & \cdots & \mathbb{I}^4\\ \vdots & \ddots & \vdots\\ \mathbb{I}^4 & \cdots & 2\mathbb{I}^4\end{bmatrix}\in\mathbb{C}^{16\times16}, \qquad [\varepsilon VS] = \operatorname{diag}\begin{bmatrix}[\varepsilon VS^1]\\ \vdots\\ [\varepsilon VS^E]\end{bmatrix}.$$

The second mass matrix for u_j can be given,

$$\sum_{e=1}^{\mathrm{E}}\varepsilon^{*e}\left(\int_{V^e}\phi_i\mathrm{d}V\left[\boldsymbol{\phi\phi}_j^e\right][SV] + [\boldsymbol{\phi\phi}_i^e]^{\mathrm{T}}\int_{V^e}\phi_j\mathrm{d}V\,[SV]\right)[\mathrm{u}\boldsymbol{\Lambda}]$$

$$= \left([EN_i]^{\mathrm{T}}[\varepsilon V][\boldsymbol{KK}][SV] + [\boldsymbol{KK}_i]^{\mathrm{T}}[\varepsilon V]^{\mathrm{T}}[EN][SV]\right)[\mathrm{u}\boldsymbol{\Lambda}]$$

The matrix $[\varepsilon V]$ is the conjugate of $[\varepsilon V^*]$ which has been defined earlier. In all, the FEM formula for the 3-D four-potential can be given in matrix form as,

$$\begin{pmatrix} [\boldsymbol{KK}_i]^{\mathrm{T}}[\mu V][\boldsymbol{KK}] \\ +[\boldsymbol{KK}_i]^{\mathrm{T}}[\mu VB][\boldsymbol{KK}] - [\boldsymbol{KRK}_i] \\ +[EN_i]^{\mathrm{T}}[\varepsilon VM][EN] \\ +[SV_0]^{\mathrm{T}}[EN_i]^{\mathrm{T}}[\varepsilon V^*][\boldsymbol{KK}] \\ +[SV_0]^{\mathrm{T}}[\boldsymbol{KK}_i]^{\mathrm{T}}[\varepsilon V^*]^{\mathrm{T}}[EN] \\ +[SV_0]^{\mathrm{T}}[\boldsymbol{KK}_i]^{\mathrm{T}}[\varepsilon VK][\boldsymbol{KK}][SV] \\ +[SS_0][EN_i]^{\mathrm{T}}[\varepsilon VS][EN][SS] \\ +[EN_i]^{\mathrm{T}}[\varepsilon V][\boldsymbol{KK}][SV] \\ +[\boldsymbol{KK}_i]^{\mathrm{T}}[\varepsilon V]^{\mathrm{T}}[EN][SV] \end{pmatrix} [\mathrm{u}\boldsymbol{\Lambda}] = \begin{pmatrix} \oint_{\partial\Omega} \left(\phi_i \frac{1}{\mu} \nabla \cdot \mathbf{A}\right) \hat{\mathbf{n}} \, \mathrm{d}S + \oint_{\partial\Omega} (\varepsilon^* \phi_i \Phi) \hat{\mathbf{n}} \, \mathrm{d}S \\ - \oint_{\partial\Omega} \hat{\mathbf{n}} \times \phi_i \frac{1}{\mu} \nabla \times \mathbf{A} \, \mathrm{d}S \\ \oint_{\partial\Omega} \varepsilon^* (\phi_i \mathbf{A} \cdot \hat{\mathbf{n}}) dS + \frac{1}{\mathrm{j}\omega} \oint_{\partial\Omega} \phi_i (\varepsilon^* \nabla\Phi \cdot \hat{\mathbf{n}}) dS \end{pmatrix}.$$

Equation 4-6

Reviewing the RHS of Equation 4-6, it can be found, the terms are in boundary coordinates, normal/tangential vectors instead of global coordinates, $\hat{\mathbf{x}} \quad \hat{\mathbf{y}} \quad \hat{\mathbf{z}}$. This suggests that one side of the equations has to be rotated before both sides are applied together. In practice, the system matrix (LHS) is transferred, due to the fact the boundary conditions usually use local coordinates.

We define the transform as $\boldsymbol{T}_i$, which is the transform for the i^{th} node. $\widehat{\mathbf{i}_n} = [\mathrm{i}_{nx} \quad \mathrm{i}_{ny} \quad \mathrm{i}_{nz}]^{\mathrm{T}}$ is the unit normal vector in the $\hat{\mathbf{x}} \quad \hat{\mathbf{y}} \quad \hat{\mathbf{z}}$ coordinates on the i^{th} node.

$$\boldsymbol{T}_i = \begin{bmatrix} \widehat{\mathbf{i}_n} & \widehat{\mathbf{i}_{t_1}} & \widehat{\mathbf{i}_{t_2}} & \mathbf{0}^{3\times1} \\ & \mathbf{0}^{1\times3} & & 1 \end{bmatrix} = \begin{bmatrix} \mathrm{i}_{nx} & \mathrm{i}_{t_1x} & \mathrm{i}_{t_2x} & 0 \\ \mathrm{i}_{ny} & \mathrm{i}_{t_1y} & \mathrm{i}_{t_2y} & 0 \\ \mathrm{i}_{nz} & \mathrm{i}_{t_1z} & \mathrm{i}_{t_2z} & 0 \\ 0 & 0 & 0 & 1 \end{bmatrix}.$$

Therefore, the coordinate transform can be obtained by multiplying the transform matrix,

$$[\boldsymbol{TT}] = \begin{bmatrix} \boldsymbol{T}_1 & \mathbf{0} & \mathbf{0} \\ \mathbf{0} & \ddots & \mathbf{0} \\ \mathbf{0} & \mathbf{0} & \boldsymbol{T}_N \end{bmatrix}.$$

Equation 4-7

For those elements not on the boundary, the corresponding $\boldsymbol{T}_i$ is the identity matrix.

4.3.2 Boundary Conditions for Potential Equations

In order to solve electromagnetic problems numerically, it is necessary to apply proper boundary conditions. According to the uniqueness, the boundary current density (electric or magnetic) needs to be properly defined over the boundaries (Stratton, 1941). But, for the potential formula, the BCs for the gauge are needed, which we will detail in this section.

Specifying BCs for an electromagnetic problem in the four-potential formula can be summarised in three steps as shown in Figure 4-2.

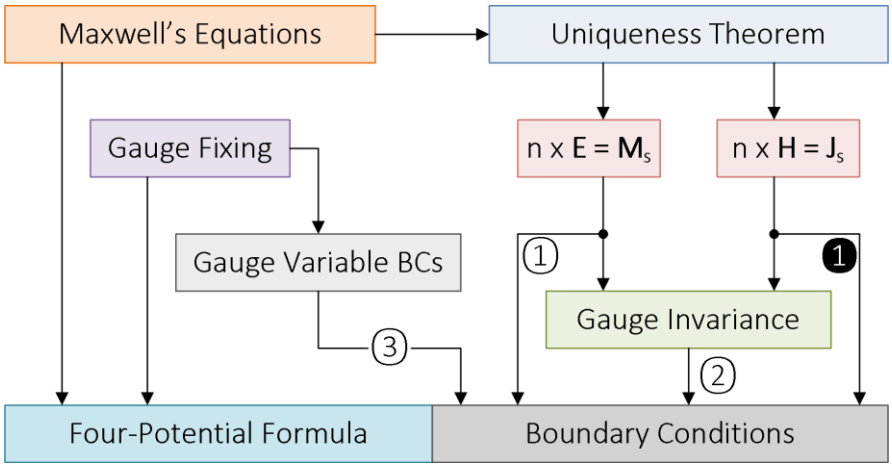

Figure 4-2 Specifying the BCs for four-potential formula

The BCs brought by the Maxwell's equations are in the form of tangential components, and among all the terms on RHS of Equation 4-6, the tangential components are,

$$\oint_{\partial\Omega} \hat{\mathbf{n}} \times \phi_i \frac{1}{\mu} \nabla \times \mathbf{A} \, \mathrm{d}S = \oint_{\partial\Omega} \phi_i \hat{\mathbf{n}} \times \mathbf{H} \, \mathrm{d}S = \oint_{\partial\Omega} \phi_i \mathbf{J}^{\mathbf{i}}{}_{\mathrm{s}} \, \mathrm{d}S \, .$$

Equation 4-8

The imposed surface electric current density is denoted by $\mathbf{J}^{\mathbf{i}}{}_{\mathrm{s}}$. This part meets the uniqueness theorem, which says the tangential components of the $\mathbf{H}$ field over the whole boundary completely define the EMF. This BC is shown as ❶ in Figure 4-2.

In practise however, the BCs in the form of $\mathbf{M}^{\mathbf{i}}{}_{\mathrm{s}}$ are sometimes required, which is not obvious in the potential formula. As the uniqueness theorem suggests tangential component of $\mathbf{E}$ over the boundary can specify the EMF as well, the BCs leading to $\mathbf{M}^{\mathbf{i}}{}_{\mathrm{s}}$ can be given as,

$$-\oint_{\partial\Omega} \phi_i \hat{\mathbf{n}} \times (\nabla\Phi + \mathrm{j}\omega\mathbf{A}) \, \mathrm{d}S = \oint_{\partial\Omega} \phi_i \hat{\mathbf{n}} \times \mathbf{E} \, \mathrm{d}S = \oint_{\partial\Omega} \phi_i \mathbf{M}^{\mathbf{i}}{}_{\mathrm{s}} \, \mathrm{d}S \, .$$

Equation 4-9

Although the LHS form of Equation 4-9 does not appear on the RHS of Equation 4-6, it can be imposed by removing the row related with ϕ_i and inserting the boundary values directly. This BC is shown as ① in Figure 4-2. Step ① (Equation 4-9) or ❶ (Equation 4-8) is the first step for specifying the BCs of the four-potential formula.

Re-examining Equation 4-6, there are terms other than the surface current density $\mathbf{J}^{\mathbf{i}}{}_{\mathrm{s}}$ or $\mathbf{M}^{\mathbf{i}}{}_{\mathrm{s}}$ on the RHS. The existence of these terms is due to the gauge.

Neither the imposed $\mathbf{J^i}_s$ nor $\mathbf{M^i}_s$ is constrained by the gauge, and they are both gauge invariant, see Equation 4-10 (a - b),

$$\hat{\mathbf{n}} \times \frac{1}{\mu} \nabla \times \mathbf{A} = \hat{\mathbf{n}} \times \frac{1}{\mu} \nabla \times (\mathbf{A} + \nabla\psi) = \mathbf{J^i}_s \,,$$

$$\hat{\mathbf{n}} \times (\nabla\Phi + \mathrm{j}\omega\mathbf{A}) = \hat{\mathbf{n}} \times [\nabla(\Phi - \mathrm{j}\omega\psi) + \mathrm{j}\omega(\mathbf{A} + \nabla\psi)] = \mathbf{M^i}_s \,.$$

Equation 4-10 (a - b)

Therefore, the gauge fixing has to be applied to $\mathbf{J^i}_s$ or $\mathbf{M^i}_s$ with another BC, and this is the second step of specifying the BCs for four-potential formula, which is shown as ② in Figure 4-2.

Applying the Lorenz gauge to the normal component of Equation 4-6, we have,

$$\oint_{\partial\Omega} \phi_i \left(\frac{1}{\mu} \nabla \cdot \mathbf{A} + \varepsilon^* \Phi \right) \hat{\mathbf{n}} \, \mathrm{d}S = 0 \,.$$

Equation 4-11

By evaluating the scalar component of Equation 4-6, the Lorenz gauge is also found but in a different form. Substituting Equation 2-32 into Equation 2-38,

$$\int_\Omega v{\varepsilon^*}^2 \mu\Phi + \frac{1}{\mathrm{j}\omega} \varepsilon^* \nabla\Phi \cdot \nabla v + \varepsilon^* v \nabla \cdot \mathbf{A} + \varepsilon^* \mathbf{A} \cdot \nabla v \mathrm{d}V + \int_\Omega v\varepsilon^* (\nabla \cdot \nabla\psi - \mathrm{j}\omega\varepsilon^*\mu\psi) \mathrm{d}V$$
$$= \frac{1}{\mathrm{j}\omega} \oint_{\partial\Omega} v \, \varepsilon^* (\mathrm{j}\omega\mathbf{A} + \nabla\Phi) \cdot \hat{\mathbf{n}} \mathrm{d}S \,.$$

Equation 4-12

From the gauge Equation 2-33, a Helmholtz equation of the gauge function ψ can be found as,

$$\nabla \cdot (\mathbf{A} + \nabla\psi) = -\varepsilon^* \mu (\Phi - \mathrm{j}\omega\psi) \,,$$

$$\nabla \cdot \nabla\psi = \mathrm{j}\omega\varepsilon^*\mu\psi \,.$$

Equation 4-13 (a - b)

Therefore the second volume integral in Equation 4-12 is equivalent to the Lorenz gauge as,

$$\int_\Omega v\varepsilon^* (\nabla \cdot \nabla\psi - \mathrm{j}\omega\varepsilon^*\mu\psi) \mathrm{d}V = \int_\Omega v\varepsilon^* (\nabla \cdot \mathbf{A} + \varepsilon^*\mu\Phi) \mathrm{d}V = 0 \,.$$

From Equation 4-12, the Lorenz gauge is satisfied only when the given scalar value of $\varepsilon^* (\mathrm{j}\omega\mathbf{A} + \nabla\Phi) \cdot \hat{\mathbf{n}}$ can cooperate with one of the tangential BCs in Equation 4-8 or Equation 4-9. The scalar value provides the gauge fixing for the tangential BCs. By applying the normal component of Equation 2-7 on the boundary surface,

$$\frac{1}{\mathrm{j}\omega}\oint_{\partial\Omega} v\,\varepsilon^*(\mathrm{j}\omega\mathbf{A}+\nabla\Phi)\cdot\hat{\mathbf{n}}\mathrm{d}S=\frac{1}{\mathrm{j}\omega}\oint_{\partial\Omega} v\left(\nabla\times\frac{1}{\mu}\nabla\times\mathbf{A}\right)\cdot\hat{\mathbf{n}}\mathrm{d}S$$

$$\frac{1}{\mathrm{j}\omega}\oint_{\partial\Omega} v\,\varepsilon^*(\mathrm{j}\omega\mathbf{A}+\nabla\Phi)\cdot\hat{\mathbf{n}}\mathrm{d}S=\frac{-1}{\mathrm{j}\omega}\oint_{\partial\Omega} v\nabla\cdot\mathbf{J}^{\mathbf{i}}{}_{\mathrm{s}}\,\mathrm{d}S$$

Equation 4-14

Therefore, both Equation 4-11 and Equation 4-14 can achieve the second step of specifying the BCs, which is shown as ② in Figure 4-2. The choice between the two equations depends on the knowledge about the scalar value $\varepsilon^*(\mathrm{j}\omega\mathbf{A}+\nabla\Phi)\cdot\hat{\mathbf{n}}$.

There is the third step to take shown as ③ in Figure 4-2. From Equation 4-13 (b), the Lorenz gauge is incomplete in the sense that there remains degrees of freedom on the gauge function ψ (Jackson, 2002). Every solution of the gauge function satisfying Equation 4-13 (b) corresponds to a 4-potential distribution. This suggests that, in order to have the potentials completely settled down, BCs for the gauge function are needed. Equation 4-13 (b) shows that, Lorenz gauge allows the gauge function ψ to propagate at the speed of light. For simplicity, $\psi=0$ throughout the region is clearly the solution of Equation 4-13 (b).

In order to specify the gauge function $\psi=0$, Equation 4-11 and Equation 4-14 are used again. Whenever Equation 4-11 is used, $\nabla\cdot\mathbf{A}$ or Φ needs to be set with the scalar component of Equation 4-6, whereas when Equation 4-14 is applied, $\mathbf{A}$ or $\nabla\Phi$ has to be defined with the normal component of Equation 4-6. Setting the scalar or normal component of Equation 4-6 achieves the third step of specifying the BCs, which is shown as ③ in Figure 4-2.

It is useful to list the conditions in a table, Table 4-1.

Table 4-2 Boundary Conditions for the Potential Formula

Type	LHS	Original RHS	BCs	Step	Extra Information	EIT Front-end Structure
A	Kept	$(\nabla\cdot\mathbf{A}+\varepsilon^*\mu\Phi)\hat{\mathbf{n}}$	Equation 4-11	②	N.A.	Surface Current Source
	Kept	$\hat{\mathbf{n}}\times\mu^{-1}\nabla\times\mathbf{A}$	Equation 4-8	①	$\mathbf{J}_s$	
	Replaced	$(\mathrm{j}\omega\mathbf{A}+\nabla\Phi)\cdot\hat{\mathbf{n}}$	N.A.	③	$\nabla\cdot\mathbf{A}$ / Φ	
B	Replaced	$(\nabla\cdot\mathbf{A}+\varepsilon^*\mu\Phi)\hat{\mathbf{n}}$	N.A.	③	$\mathbf{A}\cdot\hat{\mathbf{n}}$ / $\nabla\Phi\cdot\hat{\mathbf{n}}$	Floating Current Sources
	Kept	$\hat{\mathbf{n}}\times\mu^{-1}\nabla\times\mathbf{A}$	Equation 4-8	①	$\mathbf{J}_s$	
	Kept	$(\mathrm{j}\omega\mathbf{A}+\nabla\Phi)\cdot\hat{\mathbf{n}}$	Equation 4-14	②	$\hat{\mathbf{n}}\cdot(\varepsilon^*\mathbf{E})$	
C	Kept	$(\nabla\cdot\mathbf{A}+\varepsilon^*\mu\Phi)\hat{\mathbf{n}}$	Equation 4-11	②	N.A.	Voltage Source
	Replaced	$\hat{\mathbf{n}}\times\mu^{-1}\nabla\times\mathbf{A}$	Equation 4-9	①	$\mathbf{M}_s$	

	Replaced	$(j\omega\mathbf{A}+\nabla\Phi)\cdot\hat{\mathbf{n}}$	N.A.	③	$\nabla\cdot\mathbf{A}$ / Φ	
D	Replaced	$(\nabla\cdot\mathbf{A}+\varepsilon^{*}\mu\Phi)\hat{\mathbf{n}}$	N.A.	③	$\mathbf{A}\cdot\hat{\mathbf{n}}$ / $\nabla\Phi\cdot\hat{\mathbf{n}}$	Referenced Current Source
	Replaced	$\hat{\mathbf{n}}\times\mu^{-1}\nabla\times\mathbf{A}$	Equation 4-9	①	$\mathbf{M}_s$	
	Kept	$(j\omega\mathbf{A}+\nabla\Phi)\cdot\hat{\mathbf{n}}$	Equation 4-14	②	$\hat{\mathbf{n}}\cdot(\varepsilon^{*}\mathbf{E})$	

An extra type of BCs based on the IBC (Senior, 1960) is included to the potential formula (Boyse & Paulsen, 1997). We call it the Type E BC. Different from the Type A-D, the IBC achieves the first step by specifying the ratio between $\mathbf{M}^{i}{}_{s}$ and $\mathbf{J}^{i}{}_{s}$, namely the impedance.

Table 4-3 Impedance Boundary Conditions for the Potential Formula

Type	LHS	Original RHS	BCs	Step	Extra Information
E	Replaced	$(\nabla\cdot\mathbf{A}+\varepsilon^{*}\mu\Phi)\hat{\mathbf{n}}$	N.A.	③	$\mathbf{A}\cdot\hat{\mathbf{n}}$ / $\nabla\Phi\cdot\hat{\mathbf{n}}$
	Kept	$\hat{\mathbf{n}}\times\mu^{-1}\nabla\times\mathbf{A}$	Equation 2-42 (a)	①/❶	$-(jZ)^{-1}(j\omega\mathbf{A}_s+\nabla_s\Phi)$
	Kept	$(j\omega\mathbf{A}+\nabla\Phi)\cdot\hat{\mathbf{n}}$	Equation 2-42 (b)	②	$(jZ)^{-1}\nabla_s\cdot(j\omega\mathbf{A}_s+\nabla_s\Phi)$

The LHS marked as “Kept” in Table 4-2 and Table 4-3 means that without changing the LHS, the BC can be achieved by the formula on RHS. Whereas, those marked as “Replaced” mean that the LHS is changed based on the extra given information.

The BCs for the potential formula were not clarified when the potential formula was proposed. The types A-D were mentioned, but only Type B and Type C were derived (Boyse, et al., 1992). Type E for the potential formula was proposed and detailed in the IBC by Boyse and Paulsen (Boyse & Paulsen, 1997). The potential formula was first introduced to EIT systems using voltage sources (See Section 3.6 Appendix), where Type B and C BCs are for their SEM-PMC model, and Type C and E are for their SEM-IBC model (Soni, et al., 2006). Also we have reported the formula of Type B on EIT systems as a comparison group for proposing the IEM (Zhang & Li, 2014).

4.4 Boundary Conditions for EIT and Electrode Models

BCs and electrode models introduced in preceding sections and chapters will determine the accuracy of high frequency EIT systems. The previously proposed SEM-PMC and SEM-IBC conditions, however, are inaccurate due to the reasons below.

Firstly, the contact impedance is not modelled in the two models. Secondly, the measuring electrodes attached on the surface usually affect on the potential distributions in the object, similar to the instrumental effects discussed in Chapter 3. The loading effects of these

measuring electrodes are not considered in these two models. Thirdly, a single electrode attached on an object is not able to inject currents at the frequency of a few MHz. The EMF surrounding the electrode and its wire in this case is unbounded. A serial inductive impedance is therefore produced along the longitudinal direction of the wire and electrode. In other words, the imposed field is reflected.

In the following two sections, we will detail the electrode models proposed to overcome the above-mentioned issues.

4.4.1 Complete Electrode Model with Impedance Boundary Condition

Soni et al., mentioned that the contact impedance can be modelled with the IBC (Soni, et al., 2006), but without implementations. The effects caused by the contact impedance on the potential distribution can be large in the frequency range of the beta-dispersion. Therefore, we apply the contact impedance in the electrode model to derive the CEM-IBC.

By inserting Equation 2-42 (a) to the tangential components of Equation 4-6, and Equation 2-42 (b) to the scalar components of Equation 4-6, we have,

$$-\oint_{\partial\Omega}\frac{v}{\mathrm{j}\mathrm{Z}}(\mathrm{j}\omega\mathbf{A}_{\mathrm{s}}+\nabla_{\mathrm{s}}\Phi)\,\mathrm{d}S=\oint_{\partial\Omega}\hat{\mathbf{n}}\times v\frac{1}{\mu}\nabla\times\mathbf{A}\,\mathrm{d}S\,.$$

$$\frac{1}{\mathrm{j}\omega}\oint_{\partial\Omega}\frac{v}{\mathrm{j}\mathrm{Z}}\nabla_{\mathrm{s}}\cdot(\mathrm{j}\omega\mathbf{A}_{\mathrm{s}}+\nabla_{\mathrm{s}}\Phi)\,\mathrm{d}S=\frac{1}{\mathrm{j}\omega}\oint_{\partial\Omega}v\,\varepsilon^{*}(\mathrm{j}\omega\mathbf{A}+\nabla\Phi)\cdot\hat{\mathbf{n}}\mathrm{d}S\,.$$

Equation 4-15 (a - b)

The impedance Z is replaced with Z_{C}, the surface impedance of an electrode. The contact impedance η_{C} is assumed to be isotropic, and the surface impedance Z_{C}

$$\mathrm{Z}_{\mathrm{C}}=\frac{\eta_{\mathrm{C}}(\omega)}{S_l}.$$

In Section 2.3, it has been explained that the voltage differences across electrode pairs are measured and used in the inverse algorithm. Also an electrode is usually meshed to several elements with many nodes, unless the PEM is used. Therefore, it is much more convenient to have *a SINGLE* voltage attached on each electrode, instead of having a *GROUP* of potentials on each node. So that the voltage difference can be calculated easily. The potentials for every node on electrode surfaces are the same if the SEM-PMC is applied, however it is not the case if the CEM-IBC is applied. The surface current is allowed in the CEM-IBC, which leads to a potential variance. In order to obtain the voltage on the conductive electrode as *SINGLE* voltage value, an extra equation is added, similar to the CEM.

Therefore, for measuring electrodes, an extra equation for voltages and potentials can be given as,

$$\Phi + \mathrm{Z_C} S_l \varepsilon^* (\mathrm{j}\omega \mathbf{A} + \nabla\Phi) \cdot \hat{\mathbf{n}} = U_l \, .$$

Equation 4-16

Equation 4-16 suggests that the voltage on the electrode is the scalar potential on the electrode surface plus the voltage drop on the surface impedance.

4.4.1.1 Current Driving Electrodes

For the current driving electrodes, Equation 2-42 (b) needs to be re-evaluated. As the source attached, the normal projection needs to be revised.

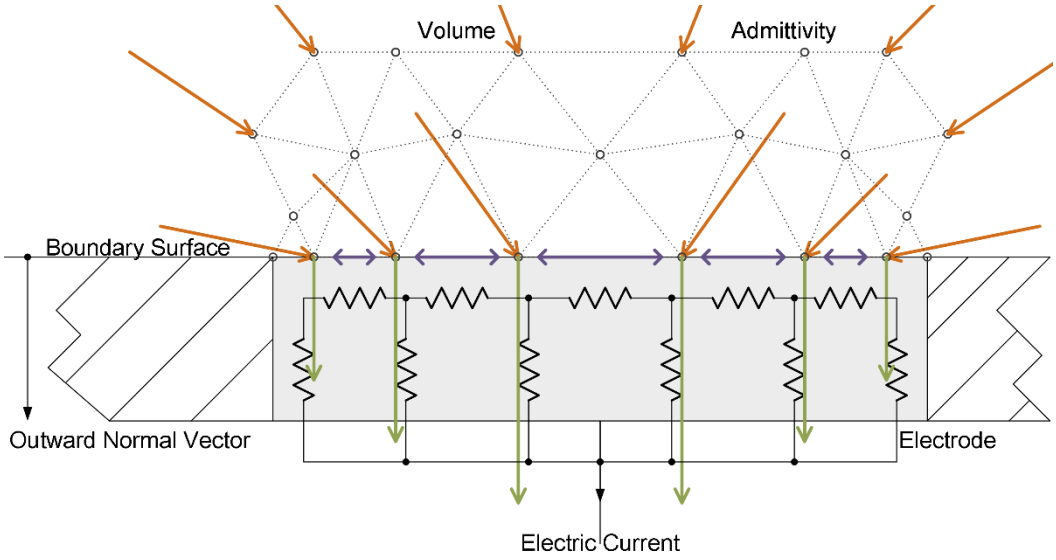

Figure 4-3 CEM-IBC Electrode Region

Figure 4-3 shows the current driving electrode region where the CEM-IBC is applied. Some of the nodes (circles) and elements (dot line) are plotted above the boundary surface, which consists of the electrode region (grey) and non-electrode regions (slashes). The CEM-IBC does not require the electric field (orange arrows) to be perpendicular to the electrode surface. A portion of the injected (or drained) current is contributed by $(\mathrm{j}\omega\mathbf{A} + \nabla\Phi) \cdot \hat{\mathbf{n}}$ (green arrows). The rest of the current is provided by the surface terms (purple arrows). This is different from the SEM-PMC (Section 2.4.3), as the SEM-PMC does not allow a surface current. It is also different from the measuring electrode, where the current throughout the electrode is zero.

Based on the analysis on the electrode region, for the current driving electrode, there is,

$$\mathbf{J}^{\mathbf{i}} \cdot \hat{\mathbf{n}} = \varepsilon^* \mathbf{E} \cdot \hat{\mathbf{n}} - \frac{1}{\mathrm{j}\mathrm{Z_C}} \nabla_{\mathrm{s}} \cdot \mathbf{E}_s = -\varepsilon^* (\mathrm{j}\omega\mathbf{A} + \nabla\Phi) \cdot \hat{\mathbf{n}} + \frac{1}{\mathrm{j}\mathrm{Z_C}} \nabla_{\mathrm{s}} \cdot (\mathrm{j}\omega\mathbf{A}_s + \nabla_{\mathrm{s}}\Phi)$$

$$-\frac{1}{\mathrm{j}\omega}\int_{S_l} v\,\varepsilon^*(\mathrm{j}\omega\mathbf{A}+\nabla\Phi)\cdot\hat{\mathbf{n}}\mathrm{d}S+\frac{1}{\mathrm{j}\omega}\int_{S_l}\frac{v}{\mathrm{j}Z_\mathrm{C}}\nabla_\mathrm{s}\cdot(\mathrm{j}\omega\mathbf{A}_\mathrm{s}+\nabla_\mathrm{s}\Phi)\,\mathrm{d}S=\frac{1}{\mathrm{j}\omega}\int_{S_l} v\,\mathbf{J}^\mathbf{i}\cdot\hat{\mathbf{n}}\mathrm{d}S\,.$$

Equation 4-17 (a - b)

In Equation 4-17 (a), $\mathbf{J}^\mathbf{i}$ is provided by the current source denoted with the superscript $\mathbf{i}$. $\varepsilon^*\mathbf{E}\cdot\hat{\mathbf{n}}$ is the complex electric current density inside the object. $Z_\mathrm{C}{}^{-1}\nabla_\mathrm{s}\cdot\mathbf{E}_s$ is the surface electric current density (complex) due to the surface impedance.

The most RHS of Equation 4-17 (a) is the complex electric densities in the potential formula. Equation 4-17 (a) can be derived from the original IBC formula (Senior, 1960) Equation 2-42 (b). Equation 4-17 (b) is the weak formula which will be inserted to the Equation 4-6 as a BC.

4.4.1.2 Voltage Driving Electrodes

For the voltage excitation electrodes, however, the voltages cannot be inserted directly by Dirichlet conditions for the scalar potentials similar to the SEM-PMC (Section 2.4.3). In the CEM-IBC, all the nodes on the electrode surfaces do not represent the metal surface, but a thin layer above the metal with a finite conductivity. Considering Figure 4-3, the purple arrows are on the surface, however the equipotential electrode is below the surface, and connected to the surface with the surface impedances. The relationship between both sides of this thin layer has to be established.

Re-examining Equation 4-16, the relationship can be established with the electric current density (complex current density),

$$\frac{\Phi-U_l}{\mathrm{Z_C}S_l}=\mathbf{J}^\mathbf{i}\cdot\hat{\mathbf{n}}=-\varepsilon^*(\mathrm{j}\omega\mathbf{A}+\nabla\Phi)\cdot\hat{\mathbf{n}}+\frac{1}{\mathrm{j}Z_\mathrm{C}}\nabla_\mathrm{s}\cdot(\mathrm{j}\omega\mathbf{A}_s+\nabla_\mathrm{s}\Phi)\,.$$

$$-\frac{1}{\mathrm{j}\omega}\int_{S_l} v\,\varepsilon^*(\mathrm{j}\omega\mathbf{A}+\nabla\Phi)\cdot\hat{\mathbf{n}}\mathrm{d}S+\frac{1}{\mathrm{j}\omega}\int_{S_l}\frac{v}{\mathrm{j}Z_\mathrm{C}}\nabla_\mathrm{s}\cdot(\mathrm{j}\omega\mathbf{A}_\mathrm{s}+\nabla_\mathrm{s}\Phi)\,\mathrm{d}S-\frac{1}{\mathrm{j}\omega}\int_{S_l}\frac{v\Phi}{\mathrm{Z_C}S_l}\mathrm{d}S$$
$$=-\frac{1}{\mathrm{j}\omega}\int_{S_l}\frac{vU_l}{\mathrm{Z_C}S_l}\mathrm{d}S\,.$$

Equation 4-18 (a - b)

Based on Equation 4-17 (a), Equation 4-18 (a) establishes the relation by replacing $\mathbf{J}^\mathbf{i}$ with the current provided by the voltage sources. This current is defined with the voltage difference and the surface impedance. Equation 4-18 (b) is the weak formula being inserted to the Equation 4-6 as a BC.

Together, the CEM-IBC provides the BCs for current exciting electrodes as Equation 4-15 (a) and Equation 4-17 (b); for voltage exciting electrodes as Equation 4-15 (a) and Equation 4-18 (b); and for measuring electrodes, the voltage can be given by Equation 4-16.

4.4.1.3 Implementation

In order to implement the CEM-IBC, the second order derivative of the scalar potential is needed, which appears in the BCs for both voltage and current driving electrodes (derived from Equation 4-15 (b)). As the first-order FEM is used, the second derivatives on shape functions have to be reformed. We apply the vector identities and the Green's theorem on Φ. The LHS of Equation 4-15 (b) becomes,

$$\frac{1}{\mathrm{j}\omega}\int_{S_l}\frac{v}{\mathrm{j}Z_\mathrm{C}}\nabla_\mathrm{s}\cdot(\mathrm{j}\omega\mathbf{A}_\mathrm{s}+\nabla_\mathrm{s}\Phi)\,\mathrm{d}S$$

$$=\int_{S_l}\frac{v}{\mathrm{j}Z_\mathrm{C}}\nabla_\mathrm{s}\cdot\mathbf{A}_\mathrm{s}\,\mathrm{d}S+\frac{1}{\mathrm{j}\omega}\int_{S_l}\left[\nabla_\mathrm{s}\cdot\left(\frac{v}{\mathrm{j}Z_\mathrm{C}}\nabla_\mathrm{s}\Phi\right)-\nabla_\mathrm{s}\Phi\cdot\nabla_\mathrm{s}\frac{v}{\mathrm{j}Z_\mathrm{C}}\right]\mathrm{d}S$$

$$=\int_{S_l}\frac{v}{\mathrm{j}Z_\mathrm{C}}\nabla_\mathrm{s}\cdot\mathbf{A}_\mathrm{s}\,\mathrm{d}S-\frac{1}{\mathrm{j}\omega}\int_{S_l}\nabla_\mathrm{s}\Phi\cdot\nabla_\mathrm{s}\frac{v}{\mathrm{j}Z_\mathrm{C}}\mathrm{d}S+\frac{1}{\mathrm{j}\omega}\oint_{\partial S_l}\frac{v}{\mathrm{j}Z_\mathrm{C}}\nabla_\mathrm{s}\Phi\cdot\widehat{\mathbf{n}_\mathrm{B}}\,\mathrm{d}l\,.$$

In which, $\widehat{\mathbf{n}_\mathrm{B}}$, is the normal unit vector. It is perpendicular to the edge of the boundary surface and it is in the surface plane. ∂S_l is the edge (1-D) of an electrode region.

However, as these components are boundary-coordinated variables, they cannot be directly inserted to the system matrix. Coordinate transformation from the boundary to global coordinate is needed.

To apply the discretisation of FEM, we replace the trial function v and the potentials with finite dimension vectors $\phi_{i,j}$. The typical method is modified to have surface components in the global coordinate system. A few matrices are repeatedly used in the later deriving for their functionalities. We denote them as following,

$$[TS]=\begin{bmatrix}0 & \mathbf{0}^{1\times2} & 0\\ \mathbf{0}^{2\times1} & \mathbb{I}^2 & \mathbf{0}^{2\times1}\\ 0 & \mathbf{0}^{1\times2} & 0\end{bmatrix},\qquad \left[\boldsymbol{TST}_j\right]=\boldsymbol{T}_j[TS]{\boldsymbol{T}_j}^\mathrm{T},\qquad [\boldsymbol{TST}]=\mathrm{diag}\begin{bmatrix}[\boldsymbol{TST}_1]\\ \vdots\\ [\boldsymbol{TST}_N]\end{bmatrix}.$$

Here, $\boldsymbol{T}_j$ is the coordinate transform matrix of the j^{th} node. $\left[\boldsymbol{TST}_j\right]$ is responsible for removing the normal component from a global coordinate vector.

$$\left[\boldsymbol{\phi\phi B}_i^b\right] = \begin{bmatrix} \frac{\partial \phi^b{}_i}{\partial x} & 0 & 0 & \\ 0 & \frac{\partial \phi^b{}_i}{\partial y} & 0 & \mathbf{0}^{3\times 1} \\ 0 & 0 & \frac{\partial \phi^b{}_i}{\partial z} & \\ & \mathbf{0}^{1\times 4} & & \end{bmatrix}, \qquad [\boldsymbol{KB}] = \begin{bmatrix} [\boldsymbol{\phi\phi B}_1^1] & \cdots & [\boldsymbol{\phi\phi B}_N^1] \\ \vdots & \ddots & \vdots \\ [\boldsymbol{\phi\phi B}_1^B] & \cdots & [\boldsymbol{\phi\phi B}_N^B] \end{bmatrix}.$$

$\left[\boldsymbol{\phi\phi B}_i^b\right]$ is the gradient matrix of the shape functions, with b denoting the boundary face and i denoting the node index. $\left[\boldsymbol{\phi\phi B}_i^b\right]$ is similar to $[\boldsymbol{\phi\phi}_i^e]$ we used in earlier sections, but for boundary faces only.

In contrast to the element-to-node matrix $[EN]$ in deriving the system matrix, here we use $[BN]$ which connects the boundary faces to the nodes. $[BN]$ is similar to the one we used in Equation 3-14, but with a different dimension.

$$[BN_i] = \begin{matrix} \vdots \\ \vdots \\ b1 \\ \vdots \\ \vdots \\ \vdots \\ b2 \\ \vdots \\ \vdots \\ \vdots \\ b3 \\ \vdots \\ \vdots \end{matrix} \begin{matrix} \vdots \\ 1 \\ 2 \\ 3 \\ \vdots \\ 1 \\ 2 \\ 3 \\ \vdots \\ 1 \\ 2 \\ 3 \\ \vdots \end{matrix} \begin{matrix} \vdots \\ \vdots \\ \rightarrow \\ \vdots \\ \vdots \\ \rightarrow \\ \vdots \\ \vdots \\ \vdots \\ \vdots \\ \vdots \\ \rightarrow \\ \vdots \end{matrix} \begin{bmatrix} \vdots \\ \mathbf{0}^{4\times 4} \\ \mathbb{I}^4 \\ \mathbf{0}^{4\times 4} \\ \vdots \\ \mathbb{I}^4 \\ \mathbf{0}^{4\times 4} \\ \mathbf{0}^{4\times 4} \\ \vdots \\ \mathbf{0}^{4\times 4} \\ \mathbf{0}^{4\times 4} \\ \mathbb{I}^4 \\ \vdots \end{bmatrix} \in \mathbb{R}^{12B\times 4}, \qquad [BN] = \begin{bmatrix} [BN_1]^{\mathrm{T}} \\ \vdots \\ [BN_N]^{\mathrm{T}} \end{bmatrix}^{\mathrm{T}} \in \mathbb{R}^{12B\times 4N}$$

For the surface components, which cannot be done in global coordinates, we discretise them in the following way, with the above matrices introduced.

$$\mathbf{A}_{\mathrm{s}} = (\widehat{\mathbf{t}_1}\cdot\mathbf{A})\widehat{\mathbf{t}_1} + (\widehat{\mathbf{t}_2}\cdot\mathbf{A})\widehat{\mathbf{t}_2} = \sum_{j=1}^{N} \phi_j \left[\boldsymbol{TST}_j\right] \begin{bmatrix} \boldsymbol{\Lambda}_{xj} \\ \boldsymbol{\Lambda}_{yj} \\ \boldsymbol{\Lambda}_{zj} \\ \mathrm{u}_j \end{bmatrix}.$$

The derivatives ($\nabla_{\mathrm{s}}\phi_i$, $\nabla_{\mathrm{s}}\cdot\mathbf{A}_{\mathrm{s}}$ and $\nabla_{\mathrm{s}}\Phi$) with respect to the boundary coordinates can be given by derivative of $\boldsymbol{T}_j$ as,

$$\nabla_{\mathrm{s}}\phi_i = \begin{bmatrix} \frac{\partial n}{\partial x} & \frac{\partial t_1}{\partial x} & \frac{\partial t_2}{\partial x} & 0 \\ \frac{\partial n}{\partial y} & \frac{\partial t_1}{\partial y} & \frac{\partial t_2}{\partial y} & 0 \\ \frac{\partial n}{\partial z} & \frac{\partial t_1}{\partial z} & \frac{\partial t_2}{\partial z} & 0 \\ 0 & 0 & 0 & 1 \end{bmatrix} [TS] \begin{bmatrix} \frac{\partial x}{\partial n} & \frac{\partial y}{\partial n} & \frac{\partial z}{\partial n} & 0 \\ \frac{\partial x}{\partial t_1} & \frac{\partial y}{\partial t_1} & \frac{\partial z}{\partial t_1} & 0 \\ \frac{\partial x}{\partial t_2} & \frac{\partial y}{\partial t_2} & \frac{\partial z}{\partial t_2} & 0 \\ 0 & 0 & 0 & 1 \end{bmatrix} \begin{bmatrix} \frac{\partial \phi_i}{\partial x} \\ \frac{\partial \phi_i}{\partial y} \\ \frac{\partial \phi_i}{\partial z} \\ 0 \end{bmatrix} = [\boldsymbol{TST}_i]\left[\boldsymbol{\phi\phi B}_i^0\right][SV_0].$$

$$\nabla_{\mathrm{s}} \cdot \mathbf{A}_{\mathrm{s}} = \sum_{j=1}^{N} \nabla_{\mathrm{s}} \phi_j \cdot \mathbf{\Lambda}_{\mathrm{s}j} = \sum_{j=1}^{N} [SV_0]^{\mathrm{T}} \left[\boldsymbol{TST}_j\right] \left[\boldsymbol{\phi\phi B}_j^0\right] \begin{bmatrix} \mathbf{\Lambda}_{xj} \\ \mathbf{\Lambda}_{yj} \\ \mathbf{\Lambda}_{zj} \\ \mathrm{u}_j \end{bmatrix},$$

$$\nabla_{\mathrm{s}} \Phi = \sum_{j=1}^{N} \nabla_{\mathrm{s}} \phi_j \mathrm{u}_j = \sum_{j=1}^{N} \left[\boldsymbol{TST}_j\right] \left[\boldsymbol{\phi\phi B}_j^0\right] [SV_0] \begin{bmatrix} \mathbf{\Lambda}_{xj} \\ \mathbf{\Lambda}_{yj} \\ \mathbf{\Lambda}_{zj} \\ \mathrm{u}_j \end{bmatrix}.$$

Substituting v, $\mathbf{A}_{\mathrm{s}}$ and Φ into Equation 4-15.The terms on the LHS in Equation 4-15 (a) are represented by the unknowns and appear on the LHS of the FEM as,

$$-\sum_{j=1}^{N} \sum_{b=1}^{B_l} \left(\frac{\mathrm{j}\omega}{\mathrm{j}{Z_{\mathrm{C}}}^{l}} \int_{S^b} \phi_i \phi_j \, \mathrm{d}S \left[\boldsymbol{TST}_j\right] + \frac{1}{\mathrm{j}{Z_{\mathrm{C}}}^{l}} \int_{S^b} \phi_i \, \mathrm{d}S \left[\boldsymbol{TST}_j\right] \left[\boldsymbol{\phi\phi B}_j^b\right] [SV_0] \right) \begin{bmatrix} \mathbf{\Lambda}_{xj} \\ \mathbf{\Lambda}_{yj} \\ \mathbf{\Lambda}_{zj} \\ \mathrm{u}_j \end{bmatrix}.$$

Equation 4-19

Here, S^b denotes the surface area of the b^{th} boundary face and B_l is the total boundary faces number for the l^{th} electrode. Note, the contact impedance ${Z_{\mathrm{C}}}^{l}$ used in CEM-IBC, is assumed uniform distributed on each electrode, so we use the superscript l to denote the electrode. Insert the discrete vectors to Equation 4-15 (b), we have,

$$\begin{aligned} &\sum_{j=1}^{N} \sum_{b=1}^{B_l} \left(\frac{1}{\mathrm{j}{Z_{\mathrm{C}}}^{l}} \int_{S^b} \phi_i \, \mathrm{d}S \, [SV_0]^{\mathrm{T}} \left[\boldsymbol{TST}_j\right] \left[\boldsymbol{\phi\phi B}_j^b\right] \right) \begin{bmatrix} \mathbf{\Lambda}_{xj} \\ \mathbf{\Lambda}_{yj} \\ \mathbf{\Lambda}_{zj} \\ \mathrm{u}_j \end{bmatrix} \\ &\quad - \frac{1}{\mathrm{j}\omega} \sum_{j=1}^{N} \sum_{b=1}^{B_l} \left([SV_0]^{\mathrm{T}} \left[\boldsymbol{\phi\phi B}_i^b\right]^{\mathrm{T}} [\boldsymbol{TST}_i] \frac{1}{\mathrm{j}{Z_{\mathrm{C}}}^{l}} \int_{S^b} \mathrm{d}S \left[\boldsymbol{TST}_j\right] \left[\boldsymbol{\phi\phi B}_j^b\right] [SV_0] \right) \begin{bmatrix} \mathbf{\Lambda}_{xj} \\ \mathbf{\Lambda}_{yj} \\ \mathbf{\Lambda}_{zj} \\ \mathrm{u}_j \end{bmatrix} \\ &\quad + \frac{1}{\mathrm{j}\omega} \sum_{j=1}^{N} \sum_{b=1}^{B_l} \left(\frac{1}{\mathrm{j}{Z_{\mathrm{C}}}^{l}} \oint_{\partial S^b} \phi_i \widehat{\mathbf{n}_{\mathrm{e}}} \, \mathrm{d}l \cdot \left[\boldsymbol{TST}_j\right] \left[\boldsymbol{\phi\phi B}_j^b\right] [SV_0] \right) \begin{bmatrix} \mathbf{\Lambda}_{xj} \\ \mathbf{\Lambda}_{yj} \\ \mathbf{\Lambda}_{zj} \\ \mathrm{u}_j \end{bmatrix} \end{aligned}$$

Equation 4-20

Here $\widehat{\mathbf{n}_{\mathrm{e}}}$ is the discretised version of $\widehat{\mathbf{n}_{\mathrm{B}}}$. The relationship between $\widehat{\mathbf{n}_{\mathrm{e}}}$, $\widehat{\mathbf{n}_{\mathrm{n}}}$ and $\hat{\mathbf{n}}$ can be found in Figure 4-4. The three normal vectors are the edge normal vector in the plane of the element face, the face normal vector, and the node normal vector respectively.

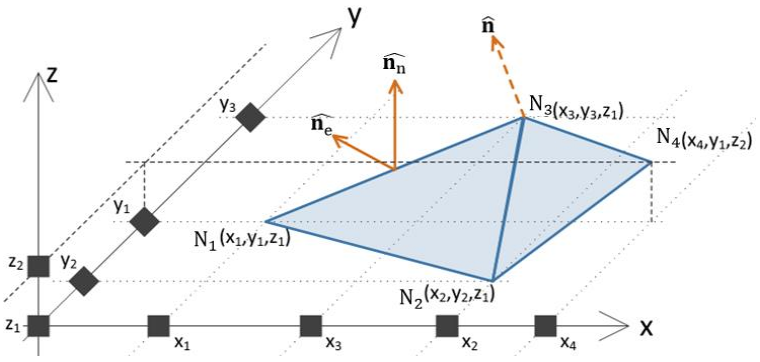

Figure 4-4 Difference in normal unit vector of element edge, face and surface

A procedure similar to the derivations of the FEM system matrix Equation 4-6 is applied to imposing the IBC. Equation 4-19 becomes the mass matrices.

$$-\begin{pmatrix}[BN_i]^{\mathrm{T}}[ZSM][BN][\boldsymbol{TST}]^{\mathrm{T}}\\ [BN_i]^{\mathrm{T}}[ZS][\boldsymbol{KKB}][SV]\end{pmatrix}[\mathrm{u}\boldsymbol{\Lambda}]$$

Equation 4-21

$$[ZSM^b]=\mathrm{j}\omega\frac{S^b}{12\mathrm{j}{Z_\mathrm{C}}^l}\begin{bmatrix}2\mathbb{I}^4 & \mathbb{I}^4 & \mathbb{I}^4\\ \mathbb{I}^4 & 2\mathbb{I}^4 & \mathbb{I}^4\\ \mathbb{I}^4 & \mathbb{I}^4 & 2\mathbb{I}^4\end{bmatrix}\in\mathbb{C}^{12\times12},\qquad [ZS]=\begin{bmatrix}\frac{S^1}{3\mathrm{j}{Z_\mathrm{C}}^l}\begin{bmatrix}\mathbb{I}^4\\ \mathbb{I}^4\\ \mathbb{I}^4\end{bmatrix} & \ddots & \\ & \ddots & \frac{S^B}{3\mathrm{j}{Z_\mathrm{C}}^l}\begin{bmatrix}\mathbb{I}^4\\ \mathbb{I}^4\\ \mathbb{I}^4\end{bmatrix}\end{bmatrix},$$

$$[ZSM]=\mathrm{diag}\begin{bmatrix}[ZSM^1]\\ \vdots\\ [ZSM^B]\end{bmatrix},\qquad [\boldsymbol{KKB}]=\begin{bmatrix}[\boldsymbol{TST}_1][\boldsymbol{\phi\phi B}_1^1] & \cdots & [\boldsymbol{TST}_N][\boldsymbol{\phi\phi B}_N^1]\\ \vdots & \ddots & \vdots\\ [\boldsymbol{TST}_1][\boldsymbol{\phi\phi B}_1^B] & \cdots & [\boldsymbol{TST}_N][\boldsymbol{\phi\phi B}_N^B]\end{bmatrix}.$$

The integral of the shape functions is given in Equation 3-7 (a) to determine the coefficients in $[ZSM]$ and $[ZS]$.

Equation 4-20 becomes,

$$\begin{pmatrix}[SV_0]^{\mathrm{T}}[BN_i]^{\mathrm{T}}[ZS][\boldsymbol{KKB}]\\ -[SV_0]^{\mathrm{T}}[\boldsymbol{KKB}_i]^{\mathrm{T}}[ZSK][\boldsymbol{KKB}][SV]\\ [BN_i]^{\mathrm{T}}[ZL][\boldsymbol{NE}][\boldsymbol{KKB}][SV]\end{pmatrix}[\mathrm{u}\boldsymbol{\Lambda}]$$

Equation 4-22

The stiffness term uses $[\boldsymbol{KKB}_i]$ is the columns in $[\boldsymbol{KKB}]$ corresponding to node i.

$$[\boldsymbol{KKB}_i]=\begin{bmatrix}[\boldsymbol{TST}_i][\boldsymbol{\phi\phi B}_i^1]\\ \vdots\\ [\boldsymbol{TST}_i][\boldsymbol{\phi\phi B}_i^B]\end{bmatrix},\qquad [ZSK]=\begin{bmatrix}\frac{-S^1\mathbb{I}^4}{\omega{Z_\mathrm{C}}^{e*}} & \ddots & \\ & \ddots & \frac{-S^B\mathbb{I}^4}{\omega{Z_\mathrm{C}}^{e*}}\end{bmatrix}.$$

Calculating the line integral in Equation 4-20 is done by composing the matrices $[\boldsymbol{NE}]$ and $[ZL]$.

$$[\boldsymbol{NE}] = \mathrm{diag}\begin{bmatrix}\begin{bmatrix}\widehat{\mathbf{n}_{e1}}^{\,1} & 0\\ \widehat{\mathbf{n}_{e2}}^{\,1} & 0\\ \widehat{\mathbf{n}_{e3}}^{\,1} & 0\end{bmatrix} & \cdots & \begin{bmatrix}\widehat{\mathbf{n}_{e1}}^{\,B} & 0\\ \widehat{\mathbf{n}_{e2}}^{\,B} & 0\\ \widehat{\mathbf{n}_{e3}}^{\,B} & 0\end{bmatrix}\end{bmatrix} \in \mathbb{R}^{3B\times 4B},$$

$$[ZL] = \mathrm{diag}\begin{bmatrix}[ZL^1]\\ \vdots \\ [ZL^B]\end{bmatrix}, \qquad [ZL^b] = \frac{-1}{2\omega \mathrm{Z_C}^{\,l}}\begin{bmatrix}\mathbf{0}^{3\times 3} & & \\ {l^b}_1 & {l^b}_2 & 0\\ \mathbf{0}^{3\times 3} & & \\ 0 & {l^b}_2 & {l^b}_3\\ \mathbf{0}^{3\times 3} & & \\ {l^b}_1 & 0 & {l^b}_3\end{bmatrix} \in \mathbb{R}^{12\times 3}.$$

As shown in Figure 4-5, $[\boldsymbol{NE}]$ is responsible for rotating the $\nabla_s\phi_i$ with edge normal vector $\widehat{\mathbf{n}_e}$s, and $[ZL]$ is to sum the potentials along l_1, l_2 and l_3.

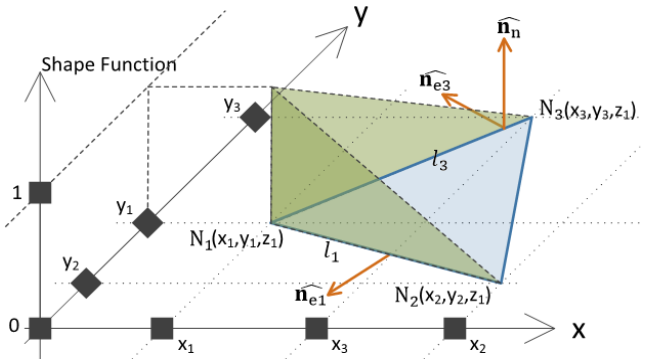

Figure 4-5 Line integral on the boundary face of an element

One more term appeared when voltage driving electrode is used, Equation 4-18 (b) leads to,

$$\sum_{j=1}^{N}\sum_{b=1}^{B_l}\frac{1}{\omega \mathrm{Z_C}^{\,l} S^b}\int_{S^b}\phi_i\phi_j\,\mathrm{d}S\,[SS_0]\begin{bmatrix}\boldsymbol{\Lambda}_{xj}\\ \boldsymbol{\Lambda}_{yj}\\ \boldsymbol{\Lambda}_{zj}\\ \mathrm{u}_j\end{bmatrix} = [BN_i]^{\mathrm{T}}[ZM][BN][SS][\mathrm{u}\boldsymbol{\Lambda}]\,.$$

Equation 4-23

Similar to the mass matrix we have introduced in Equation 4-21, however the face area S^b is cancelled in $[ZM^b]$ as,

$$[ZM^b] = \frac{-1}{12\omega \mathrm{Z_C}^{\,l}}\begin{bmatrix}2\mathbb{I}^4 & \mathbb{I}^4 & \mathbb{I}^4\\ \mathbb{I}^4 & 2\mathbb{I}^4 & \mathbb{I}^4\\ \mathbb{I}^4 & \mathbb{I}^4 & 2\mathbb{I}^4\end{bmatrix} \in \mathbb{C}^{12\times 12}, \qquad [ZM] = \mathrm{diag}\begin{bmatrix}[ZM^1]\\ \vdots \\ [ZM^B]\end{bmatrix}.$$

In all the CEM-IBC for current driving electrodes appears to be,

$$\begin{pmatrix} -[BN_i]^{\mathrm{T}}[ZSM][BN][\boldsymbol{TST}]^{\mathrm{T}} \\ -[BN_i]^{\mathrm{T}}[ZS][\boldsymbol{KKB}][SV] \\ +[SV_0]^{\mathrm{T}}[BN_i]^{\mathrm{T}}[ZS][\boldsymbol{KKB}] \\ -[SV_0]^{\mathrm{T}}[\boldsymbol{KKB}_i]^{\mathrm{T}}[ZSK][\boldsymbol{KKB}][SV] \\ +[BN_i]^{\mathrm{T}}[ZL][\boldsymbol{NE}][\boldsymbol{KKB}][SV] \end{pmatrix}.$$

Equation 4-24

For voltage driving electrodes, the RHS of Equation 4-23 has to be added to the matrix in Equation 4-24.

The CEM-IBC can be solved by adding Equation 4-24 with Equation 4-6 directly. However, the RHSs for current or voltage driving electrodes are different. The derivation of the RHSs can be simply obtained from Equation 4-17 (b) and Equation 4-18 (b) respectively. We do not detail them here.

For the measuring electrodes, the CEM-IBC for current driving electrodes can be applied with the $\mathbf{J}^{\mathbf{i}}$ set to zero. The *SINGLE* voltage on the measuring electrodes can be obtained with Equation 4-16 after the whole system matrix is solved.

4.4.2 Instrumental Electrode and Transmission Line Port Model

In the previous sections, the boundary conditions of SEM-PMC, SEM-IBC and CEM-IBC for EIT applications are introduced and detailed. However, the behaviours of EMF at the frequencies of the beta dispersion band are more complicated than the assumptions made. Three problems have been mentioned in full Maxwell's EIT electrode models, the contact impedance, the instrumental effect, and the port reflection. The first problem is solved by the CEM-IBC detailed in the previous section. The latter two problems will be discussed in this section.

An EMF decays rapidly in an unbounded media from the Maxwell's equations. In practice, the fields are guided in bounded regions when possible. Transmission lines and waveguides are typical wave-guiding systems (Rao, 1991). For EIT systems, the electrical current is used as an excitation source driven by an EMF. However, the electrode pairs used in traditional EIT systems are not suitable for guiding the EMF to excite the object.

A wave-guiding system is usually characterised by its characteristic impedance. When the EMF is propagating in a wave-guiding system, the ratio between the electric field and the magnetic field depends on the impedance. Variations, and especially discontinuities, of the characteristic impedance along the propagation direction usually cause reflections.

The EMF that surrounds the wire, drives the electric current flowing inside the wire, but only when the frequency is low. A pair of electrodes (one sourcing and one sinking) with the wires

attached to them consist of a wave-guiding system. However, the characteristic impedance of the electrodes-wires-wave-guiding system varies along the lines. For high frequency signals, the skin effects, reflections and radiations of such wave-guiding systems can be significant.

By considering the electrodes of EIT systems in pairs and each pair as a port of a wave-guiding system, the characteristic impedance Z_{P} of the port can characterise the instrumental effects that load EIT systems at high frequencies.

A pair of measuring electrodes work as a port, with a finite impedance Z_{PM}. The EMF in the object propagates into the port. Due to the difference between the object impedance and Z_{PM}, however, the EMF is partially reflected. Furthermore, as the characteristic impedance along the electrodes-wires-wave-guiding system varies from Z_{PM}, the EMF is partially reflected, partially radiated, and partially transmitted to the measuring electronic devices. In total the fields in the object is disturbed and the measurements are inaccurate.

A pair of driving electrodes also form a port, with an impedance Z_{PD}. The EMF generated by a source transmits through the electrodes-wires-wave-guiding system. Before the field even reaches the object, the variation of the characteristic impedance reflects and radiates a portion of the field. When the EMF finally reached the object (because of the difference between the object impedance and the port Z_{PD}), the EMF is partially bounced back through the electrodes-wires-wave-guiding system.

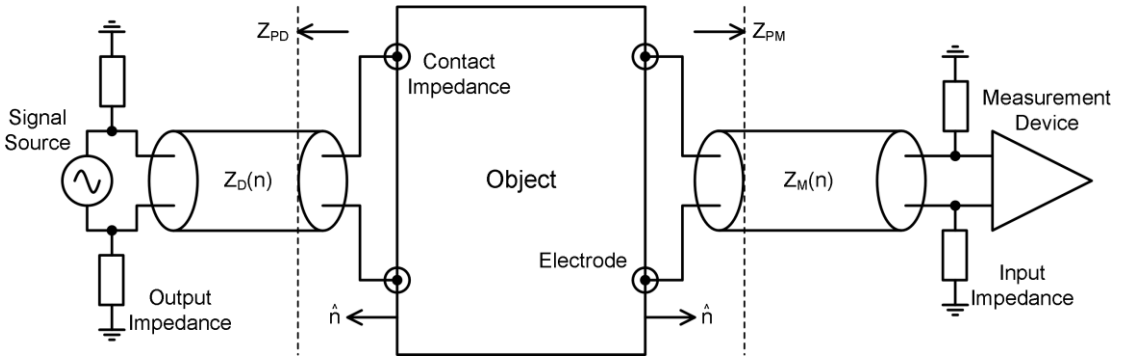

Figure 4-6 EIT System Instrument as Wave-Guiding System

Figure 4-6 shows an EIT system instrument with wave-guiding ports, modified from Figure 2-3. The electronic devices are simplified, and the connections between electronics and electrodes are detailed instead in the figure.

Figure 4-6 yields that, without applying the wave-guiding systems, any effort to enhance the output or the input impedances of the EIT electronic systems to avoid instrumental effects is futile when the frequency is in the beta-dispersion band.

The above findings suggest that traditional hardware settings of electrodes-wires-wave-guiding are not compatible with the frequency extension.

Electronic systems have been long investigated in radio frequency measurement applications, transmission lines are used to propagate a signal at a longer distance. It may overcome the problems in delivering the EMFs by slightly changing the electrode-electronic connections.

The approach we are proposing to solve the forward problem more accurately at higher frequencies has considered the issues above. By providing the BCs a step further than the electrode surface, the wave-guiding systems are included in the forward problems. The wave-guiding systems for delivering the EMFs from the sources to the object and from the object to the measuring devices, is replaced by transmission lines. The typical electrodes of EIT systems are replaced with the transmission line ports, so that the EIT system can be more suitable for high frequency excitation-measurement operations. The instrumental effects we have discussed in Chapter 3 can be included in the transmission line model and characterised by impedance matching

The transmission line requires the “electrode” of the driving pairs and the measuring pairs to have a fixed structure. This structure forms a port of the transmission line. In the transmission line, a constant characteristic impedance is maintained and normally only 1-D differential equations are needed. Two types of transmission lines are usually used in electronic applications: parallel field transmission lines (such as strip-line) and coaxial transmission lines. Differential strip-line is chosen in our study.

A cross section on the axial direction of the transmission line is shown in Figure 4-7, together with the port consisting of the electrodes. Similar to Figure 4-3, we use orange arrows to represent the fields in the object, the green ones to represent the electric field on the metal surface. The grey blocks are the conductive metal parts of the electrodes and the strip-line. The electrodes and the strip-line, although drawn separately in Figure 4-7, are physically jointed together. The electrode pair is the port of the strip-line.

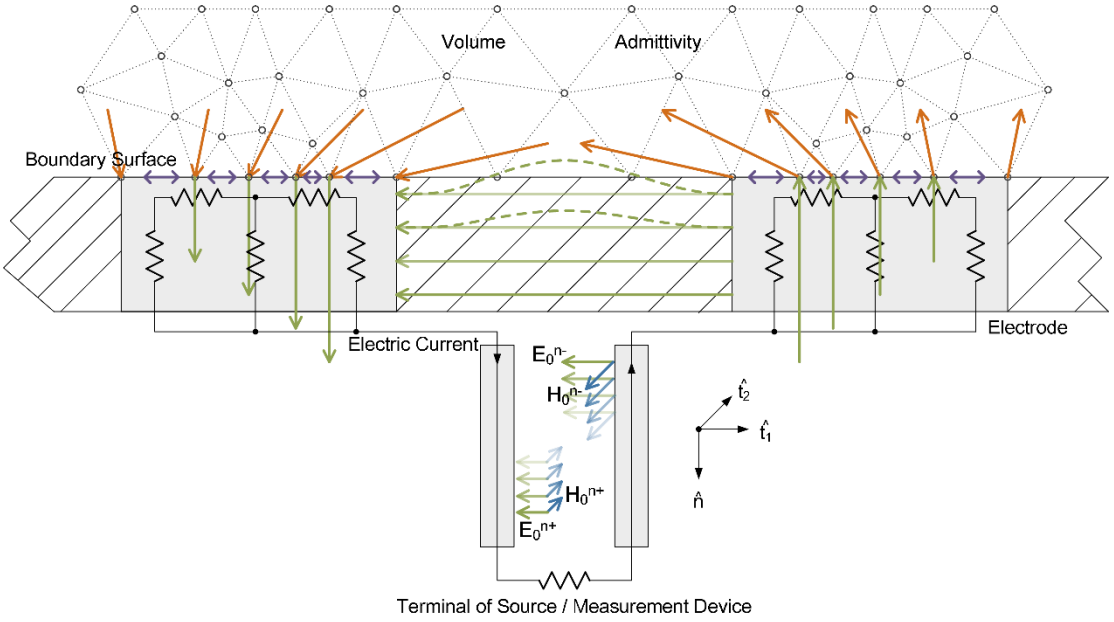

Figure 4-7 Axial Direction Cross Section of Strip-line Port

In order to derive the BCs for this transmission line port, we define a few variables. The index of this port structure is l while the two conductive surfaces touching the object (the two electrode surfaces) are l^+ and l^-. The characteristic impedance of the strip-line is Z_0. The inner distance between the metals is d, and the width of each metal piece is w (on $\hat{\mathbf{t}}_2$ direction). The transmission line is placed along $\hat{\mathbf{n}}$ direction. The source or measurement device is applied on the far-side of the transmission line, at $n = n_{\mathrm{T}}$.. The object interface is located on the near-side of the line, at $n = 0$.

Assuming the EMF in the transmission line is a Transverse Electromagnetic (TEM) wave, which obeys one-dimension Maxwell's equations (Shen & Kong, 1995), the general solution therefore can be expressed as,

$$\frac{\partial \mathbf{E}_{t1}}{\partial n} = \mathrm{j}\omega\mu\mathbf{H}_{t2}, \qquad \frac{\partial}{\partial n}\frac{1}{\mathrm{j}\omega\mu}\frac{\partial \mathbf{E}_{t1}}{\partial n} = \varepsilon^*\mathbf{E}_{t1}, \qquad k = \pm\sqrt{-\mathrm{j}\omega\mu\varepsilon^*} = \pm\sqrt{\omega^2\mu\varepsilon}\,,$$

$$\mathbf{E}_{t1} = {\mathbf{E}_0}^{n-}e^{+\mathrm{j}kn} + {\mathbf{E}_0}^{n+}e^{-\mathrm{j}kn}, \qquad \mathbf{H}_{t2} = \sqrt{\varepsilon/\mu}\left({\mathbf{E}_0}^{n-}e^{+\mathrm{j}kn} - {\mathbf{E}_0}^{n+}e^{-\mathrm{j}kn}\right).$$

Equation 4-25 (a - b)

From Equation 4-25, the EMF propagates on both directions $\pm\hat{\mathbf{n}}$ along the transmission line (also shown in Figure 4-7), with the magnitude of the electric field intensities ${\mathbf{E}_0}^{n-}$ and ${\mathbf{E}_0}^{n+}$, respectively. On each direction, the fields obey the same relationship provided by the characteristic impedance. The characteristic impedance of the transmission line is given by the ratio (Wheeler, 1964) between the voltage and the current as,

$$Z_0 = {Z_0}^{n+} = \frac{d{\mathbf{E}_0}^{n+}e^{-\mathrm{j}kn}}{w\sqrt{\varepsilon/\mu}\,{\mathbf{E}_0}^{n+}e^{-\mathrm{j}kn}} = {Z_0}^{n-} = \frac{d{\mathbf{E}_0}^{n-}e^{+\mathrm{j}kn}}{w\sqrt{\varepsilon/\mu}\,{\mathbf{E}_0}^{n-}e^{+\mathrm{j}kn}} = \frac{d}{w}\sqrt{\frac{\mu}{\varepsilon}}.$$

The voltage across the transmission line cross section, and the current along each parallel metal piece are given as,

$$U(n) = \int_{l^-}^{l^+} \mathbf{E}_{t1}\hat{\mathbf{t}_1}\cdot \mathrm{d}t_1 = d\left({\mathbf{E}_0}^{n-}e^{+\mathrm{j}kn} + {\mathbf{E}_0}^{n+}e^{-\mathrm{j}kn}\right),$$

$$I(n) = \oint_{l^\pm} \mathbf{H}_{t2}\cdot \mathrm{d}S = \pm w\sqrt{\varepsilon/\mu}\left({\mathbf{E}_0}^{n-}e^{+\mathrm{j}kn} - {\mathbf{E}_0}^{n+}e^{-\mathrm{j}kn}\right).$$

Equation 4-26 (a - b)

Different from the electrodes-wires-wave-guiding systems, the voltage and current across the transmission line are functions of location n. As $\mathbf{E}_{t1}$ and $\mathbf{H}_{t2}$ are outside the object region, the quasi-static assumption is valid considering the dielectric properties of transmission line. Therefore the voltages can represent the EMF in the transmission line. We have the voltage across the near-end port to be $U(0) = U_{l^+} - U_{l^-}$. The voltage across the far-end port is $U(n_\mathrm{T}) = U_0$. Similarly, when the signal reaches the print circuit boards (PCB) or the semiconductor devices, quasi-static fields are always assumed.

The ratio between the field intensities propagating on the two directions is the reflection coefficient Γ_O. For driving transmission lines, $\hat{\mathbf{n}}$ is the direction of reflection, and Γ_O is defined as ${\mathbf{E}_0}^{n+}/{\mathbf{E}_0}^{n-}$. Substitute Γ_O into the Equation 4-26, it can be given,

$$U(n) = d{\mathbf{E}_0}^{n-}\left(e^{+\mathrm{j}kn} + \Gamma_\mathrm{O}e^{-\mathrm{j}kn}\right),$$

$$I(n) = \pm w\sqrt{\varepsilon/\mu}\,{\mathbf{E}_0}^{n-}\left(e^{+\mathrm{j}kn} - \Gamma_\mathrm{O}e^{-\mathrm{j}kn}\right).$$

$$Z(n) = \frac{U(n)}{I(n)} = \frac{d\left(e^{+\mathrm{j}kn} + \Gamma_\mathrm{O}e^{-\mathrm{j}kn}\right)}{w\sqrt{\varepsilon/\mu}\,(e^{+\mathrm{j}kn} - \Gamma_\mathrm{O}e^{-\mathrm{j}kn})} = Z_0\frac{e^{\mathrm{j}kn} + \Gamma_\mathrm{O}e^{-\mathrm{j}kn}}{e^{\mathrm{j}kn} - \Gamma_\mathrm{O}e^{-\mathrm{j}kn}}.$$

Equation 4-27

The voltage exciting CEM-IBC is inserted with the transmission line equations. Substituting Equation 4-27 into Equation 4-18 (b) and evaluating with $n = n_\mathrm{T}$ and $n = 0$, the BCs for the two electrodes l^+ and l^- are obtained,

$$-\frac{1}{\mathrm{j}\omega}\int_{S_{l^\pm}} v\,\varepsilon^*(\mathrm{j}\omega\mathbf{A} + \nabla\Phi)\cdot\hat{\mathbf{n}}\mathrm{d}S + \frac{1}{\mathrm{j}\omega}\int_{S_{l^\pm}}\frac{v}{Z_\mathrm{C}}\nabla_\mathrm{s}\cdot(\mathrm{j}\omega\mathbf{A}_\mathrm{s} + \nabla_\mathrm{s}\Phi)\,\mathrm{d}S - \frac{1}{\mathrm{j}\omega}\int_{S_{l^\pm}}\frac{v\Phi}{Z_\mathrm{C}S_{l^\pm}}\mathrm{d}S$$
$$= -\frac{1}{\mathrm{j}\omega}\int_{S_{l^\pm}}\frac{vU_{l^\pm}}{Z_\mathrm{C}S_{l^\pm}}\mathrm{d}S\,,$$

$$\int_{S_{l^{\pm}}} \mathbf{J}^{\mathbf{i}} \cdot \hat{\mathbf{n}} \mathrm{d}S = I(0) = \pm w\sqrt{\varepsilon/\mu}\, {\mathbf{E}_0}^{n-}\left(e^{+\mathrm{j}kn} - \Gamma_{\mathrm{O}} e^{-\mathrm{j}kn}\right) = \pm w\sqrt{\varepsilon/\mu}\, {\mathbf{E}_0}^{n-}(1 - \Gamma_{\mathrm{O}}) \,,$$

$$U_{l^+} = -U_{l^-} = U(0) = \frac{d}{2} {\mathbf{E}_0}^{n-}\left(e^{+\mathrm{j}kn} + \Gamma_{\mathrm{O}} e^{-\mathrm{j}kn}\right) = \frac{d}{2} {\mathbf{E}_0}^{n-}(1 + \Gamma_{\mathrm{O}}) \,,$$

$$U_0 = U(n_{\mathrm{T}}) = d{\mathbf{E}_0}^{n-}\left(e^{+\mathrm{j}kn_{\mathrm{T}}} + \Gamma_{\mathrm{O}} e^{-\mathrm{j}kn_{\mathrm{T}}}\right).$$

Equation 4-28 (a - d)

Equation 4-28 provides the BCs for the metal pieces (electrode areas) of an exciting transmission line. Equation 4-28 (a) is same to the CEM-IBC for voltage exciting electrodes, but the voltage of the electrodes $U_{l^{\pm}}$ are unknowns. Equation 4-28 (b) provides the relationship between the $\mathbf{J}^{\mathbf{i}} \cdot \hat{\mathbf{n}}$ on the object surface and the current in the transmission line, with two extra unknowns, ${\mathbf{E}_0}^{n-}$ and ${\mathbf{E}_0}^{n-}\Gamma_{\mathrm{O}}$, added. Equation 4-28 (c - d) are the transmission line equations at the near and far end of the line. The voltage source (providing the potential difference of U_0) is applied at the far-end with the output impedance Z_0 (same as the characterisation impedance of the transmission line).

For the dielectric surface regions between the conductive pieces (electrodes) of the transmission line port, different the BCs are needed. The general IBC given in Section 2.4.3 (Soni, et al., 2006) is not appropriate for this region, as the object boundary is clearly specified.

According to the continuity condition Equation 4-3 (c), tangential components of $\mathbf{E}$ field remain the same on both sides of a boundary surface. Our assumption about the transmission line (1-D differential equations) allows only tangential components to exist. Therefore, the $\mathbf{E}$ field in the transmission line at $n = 0$ is the tangential components $\mathbf{E}$ of on the object surface.

Reconsidering Table 4-2 and Table 4-3, Type C BC can be used for the dielectric surface region as,

$$\hat{\mathbf{n}} \times (\nabla\Phi + \mathrm{j}\omega\mathbf{A}) = \frac{U_{l^+} - U_{l^-}}{d} \hat{\mathbf{t}_1},$$

$$\int_{dw_l} \left(\phi_i \frac{1}{\mu} \nabla \cdot \mathbf{A}\right) \hat{\mathbf{n}}\, \mathrm{d}S + \int_{dw_l} (\varepsilon^* \phi_i \Phi) \hat{\mathbf{n}}\, \mathrm{d}S = 0 \,,$$

$$\Phi(\mathrm{t}_1) = U_{l^-} + \frac{U_{l^+} - U_{l^-}}{d} \mathrm{t}_1 \,.$$

Equation 4-29 (a - c)

Equation 4-29 is similar to the PMC BCs used in Equation 2-39, but with the $\mathbf{M}_{\mathrm{s}}$ provided. dw_l is the area of dielectric surface region of port l. The tangential electric field is assumed to be

uniformly distributed along the $\widehat{\mathbf{t}_1}$ direction, as Equation 4-29 (a) states. The Dirichlet condition is chosen for the gauge, as Equation 4-29 (b). The extra Information of Type C is given in the form of Φ. The distribution of Φ is considered to be linear, as Equation 4-29 (c).

The BCs of an exciting transmission line port can be given by Equation 4-28 (a - d) for the conductive surface and the Equation 4-29 (a - c) for the dielectric surface.

For the measuring transmission line port, different BCs have to be applied. A terminator with the impedance Z_0 is kept the same with the characteristic impedance of the transmission line is placed at $n = n_{\mathrm{T}}$ instead of the source. The voltage across the terminator becomes one of the unknowns. Also the EMF is terminated at the terminator, which means there is no reflection when the field reaches the terminator.

The Z_0 terminator prevents the field from propagating towards the object (-$\widehat{\mathbf{n}}$ direction) in the transmission line. Only the outward field, heading to the terminator, exists. Furthermore, this outward field obeys the transmission line equations. So we can have the Equation 4-28 revised as,

$$-\frac{1}{\mathrm{j}\omega}\int_{S_{l\pm}} v\,\varepsilon^{*}(\mathrm{j}\omega\mathbf{A}+\nabla\Phi)\cdot\widehat{\mathbf{n}}\mathrm{d}S+\frac{1}{\mathrm{j}\omega}\int_{S_{l\pm}}\frac{v}{Z_{\mathrm{C}}}\nabla_{\mathrm{s}}\cdot(\mathrm{j}\omega\mathbf{A}_{\mathrm{s}}+\nabla_{\mathrm{s}}\Phi)\,\mathrm{d}S-\frac{1}{\mathrm{j}\omega}\int_{S_{l\pm}}\frac{v\Phi}{Z_{\mathrm{C}}S_{l\pm}}\mathrm{d}S$$
$$=-\frac{1}{\mathrm{j}\omega}\int_{S_{l\pm}}\frac{vU_{l\pm}}{Z_{\mathrm{C}}S_{l\pm}}\mathrm{d}S\,,$$

$$\int_{S_{l\pm}}\mathbf{J}^{\mathbf{i}}\cdot\widehat{\mathbf{n}}\mathrm{d}S=I(0)=\pm w\sqrt{\varepsilon/\mu}\,{\mathbf{E}_0}^{n+}\,,$$

$$U_{l^{+}}=-U_{l^{-}}=U(0)=\frac{d}{2}{\mathbf{E}_0}^{n+}\,,$$

$$U(n_{\mathrm{T}})=d{\mathbf{E}_0}^{n+}e^{-\mathrm{j}kn_{\mathrm{T}}}.$$

Equation 4-30 (a - d)

Equation 4-30 (b) is the current on the transmission line. The voltage across the transmission line port is given by the intensity in Equation 4-30 (c).

The dielectric surface of the transmission line behaves the same with the exciting port, and the boundary conditions, Equation 4-29 (a - c), can be used directly for the measuring ports.

The TPM for EIT forward problems are described by Equation 4-28, Equation 4-29 and Equation 4-30. The TPM covers both driving and measuring transmission line ports, including the metal

pieces of the port (electrode pair surfaces) and the dielectric surface in between. The TPM provides better accuracy and is more suitable for higher frequency applications.

We will use Section 4.5 to illuminate the difference of these approaches we have introduced.

4.5 Case Study and Discussions

We use a geometry model similar to the Tank Model used in Section 3.4.2 to illustrate the CEM-IBC and TPM. The Transmission Line Tank model is shown in Figure 4-8 given by COMSOL.

The model consists of a conductive cylinder tank and a sphere with a distribution of the conductivity inside. Five pairs of electrodes are attached along the middle line of the cylinder wall.

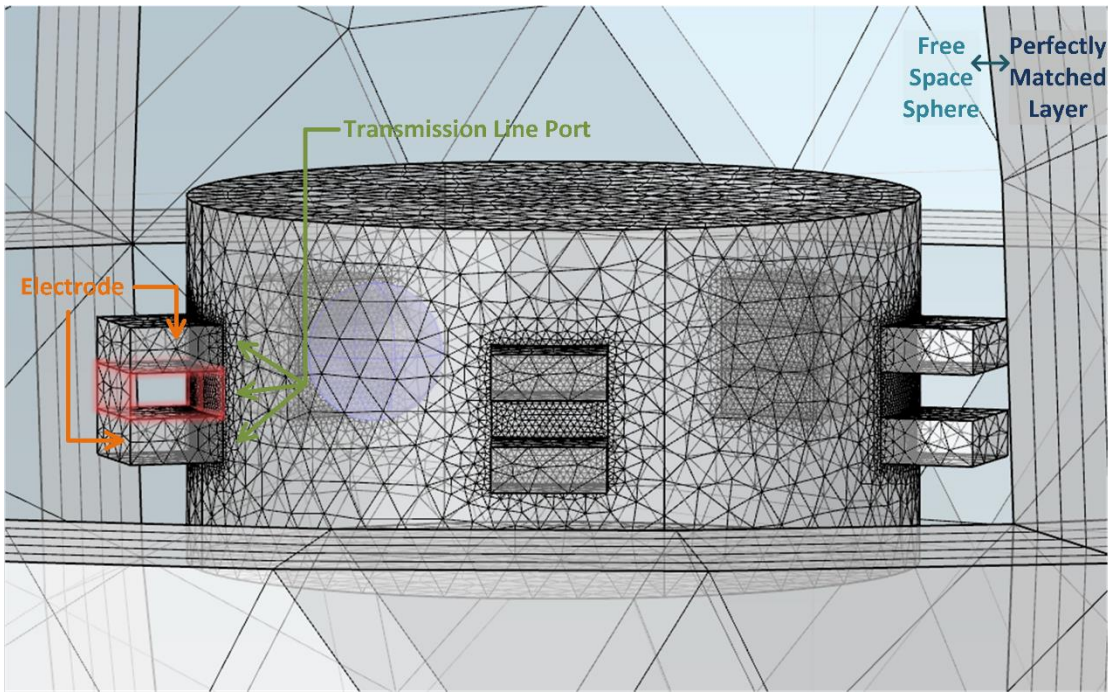

Figure 4-8 Transmission Line Tank Model

The parameters of the geometry are given as

- Material conductivity, 0.05S/m;
- Material relative permittivity, 81;
- Tank diameter, 80mm;
- Tank height, 40mm;
- Electrode width, 12.5mm;
- Electrode height, 5mm;
- Electrode gap width, 12.5mm;
- Electrode gap height, 5mm;

- Driving current, 1mA;
- Insertion sphere conductivity, 0.1S/m;
- Insertion sphere relative permittivity, 400;
- Insertion sphere diameter, 15mm;
- Insertion sphere centre position (to tank centre), [15, 25, 5] mm.

The geometry is designed to have electrodes placed as a transmission line port, which ensures that the TPM can be applied. We performed several simulations applying the following BC sets in this section, to demonstrate the effect of the contact impedance, quasi-static and port impedances, as well as the skin effect,

a) Traditional CEM;
b) IEM, we have introduced in Chapter 3;
c) SEM-PMC, the $\mathbf{A} - \Phi$ with mixed BCs used in (Soni, et al., 2006; Zhang & Li, 2014);
d) SEM-IBC, the $\mathbf{A} - \Phi$ IBC used in (Soni, et al., 2006);
e) CEM-IBC, the BCs set introduced in Section 4.4.1;
f) TPM, the BCs set introduced in Section 4.4.2;
g) COMSOL, the electromagnetic field solving software.

For the traditional CEM simulation, Case a), a pair of electrodes are set as driving electrodes, and all the other pairs are measuring ones. In order to compare the solution of the forward problem with those of other electrode models, the model is driven with voltage sources. However, the input/output impedances of any electrode are ignored and are excluded. The parameters of the simulation Case a) are,

- Driving amplitude: ±0.5V;
- Source output impedance: 0 Ohm(not available in the model);
- Measuring input impedance: infinite (not available in the model);
- Contact impedance: $\eta = 7 \times 10^{-4} - \mathrm{j}5 \times 10^{-4} \Omega \cdot \mathrm{m}^2$ (same to Section 3.4.2).

For the IEM simulation, Case b), settings are applied similar to Case a). To have the port impedance compatible with the TPM setting, the input and output impedance of the electrodes are set to be half of the port impedance. The parameters for Case b) are,

- Driving amplitude: ±0.5V;
- Source output impedance: 75 Ohm;
- Measuring input impedance: 75 Ohm;
- Contact impedance: $\eta = 7 \times 10^{-4} - \mathrm{j}5 \times 10^{-4} \Omega \cdot \mathrm{m}^2$ (same to Section 3.4.2).

For the SEM-PMC simulation, Case c), voltage driving and PEC surface on all electrode surfaces are applied. Same as a) that input/output impedances are excluded. The parameters of Case c) are,

- Driving amplitude: ±0.5V;
- Source output impedance: 0 Ohm(not available in the model);
- Measuring input impedance: infinite (not available in the model);
- Contact impedance: PEC (not available in the model).

For SEM-IBC simulation Case d), all the electrode settings are the same to SEM-PMC Case c), and only the non-electrode boundary surface is dealt with IBC. The parameters of Case d) are,

- Driving amplitude: ±0.5V;
- Source output impedance: 0 Ohm(not available in the model);
- Measuring input impedance: infinite (not available in the model);
- Contact impedance: PEC (not available in the model);
- Non-electrode surface: $\mathrm{Z} = \sqrt{\mu_0/\varepsilon_0}$.

For Case e), our CEM-IBC introduced in Section 4.4.1 is used to solve the forward problem. Compared with Case d), the contact impedances on both the driving electrodes and the measuring electrodes are considered, which allows the potentials to vary on the electrode surfaces. The parameters of Case e) are,

- Driving amplitude: ±0.5V;
- Source output impedance: 0 Ohm(not available in the model);
- Measuring input impedance: infinite (not available in the model);
- Contact impedance: : $\eta = 7 \times 10^{-4} - \mathrm{j}5 \times 10^{-4} \Omega \cdot \mathrm{m}^2$ (same to Section 3.4.2);
- Non-electrode surface: $\mathrm{Z} = \sqrt{\mu_0/\varepsilon_0}$.

For Case f), our TPM introduced in Section 4.4.2 is used to obtain the results. The ten electrodes are considered as five transmission line ports. The contact impedances are applied to the metal contact surfaces of the transmission line ports, which are considered as electrode surfaces. The input/output impedance of each transmission line port is defined by the size of the dielectric part of the transmission line port. The air is the dielectric medium of the transmission line for simplicity. The parameters of Case f) are,

- Port Driving amplitude: 1V;
- Non-electrode surface: $\mathrm{Z} = \sqrt{\mu_0/\varepsilon_0}$;
- Source output impedance: $\mathrm{Z}_0 = \left(d\sqrt{\mu_0/\varepsilon_0}\right)/w \approx 150$ Ohm;

- Measuring input terminator: $\mathrm{Z}_0 = \left(d\sqrt{\mu_0/\varepsilon_0}\right)/w \approx 150$ Ohm;
- Contact impedance: $\eta = 7 \times 10^{-4} - \mathrm{j}5 \times 10^{-4}\Omega \cdot \mathrm{m}^2$ (same to Section 3.4.2);
- Transmission line Length: $n_\mathrm{T} = 10$ mm.

For Case g), simulations using COMSOL are also included for comparison. The parameters for the COMSOL simulation are,

- Port Driving Electric Field: $1/d =$ 200V/m;
- Non-electrode surface: $\mathrm{Z} = \sqrt{\mu_0/\varepsilon_0}$;
- Source output impedance: $\mathrm{Z}_0 = \left(d\sqrt{\mu_0/\varepsilon_0}\right)/w \approx 150$ Ohm;
- Measuring input terminator: $\mathrm{Z}_0 = \left(d\sqrt{\mu_0/\varepsilon_0}\right)/w \approx 150$ Ohm;
- Contact impedance: PEC (not available in the model);
- Transmission line Length: $n_\mathrm{T} = 10$ mm;
- Free space sphere diameter: 400mm;
- PML thickness: 40mm.

The potential distributions of forward solutions for Cases a), c), d), e), f) and g) are plotted in the following figures. The potential distribution for Cases a) is obtained by solving the quasi-static problem, where vector potentials are not considered and only the electric scalar potential is plotted (Figure 4-9). The solutions for Cases c), d), e) and f) are *four potentials* and the vector potentials are shown in arrows (Figure 4-10 to Figure 4-13). The magnitude and phase are plotted and compared in terms of the voltage differences between measuring electrode pairs (or the port voltages in the TPM simulation) in the Figure 4-15 and Figure 4-16.

The COMSOL solves the prime field, similar to most electromagnetic field solvers. To obtain the scalar and vector potentials from the prime field will be too complicated to achieve, therefore we only plot the magnitude and directions of the electric field in Figure 4-14. The port voltages however can be easily obtained by applying the line integral on the solved electric field along the vertical direction. It results in the potential differences (voltages), which we used in the port voltage figures (Figure 4-15 and Figure 4-16) to compare with other simulations.

The potentials of the forward problem solution given by the traditional CEM BCs are plotted in Figure 4-9.

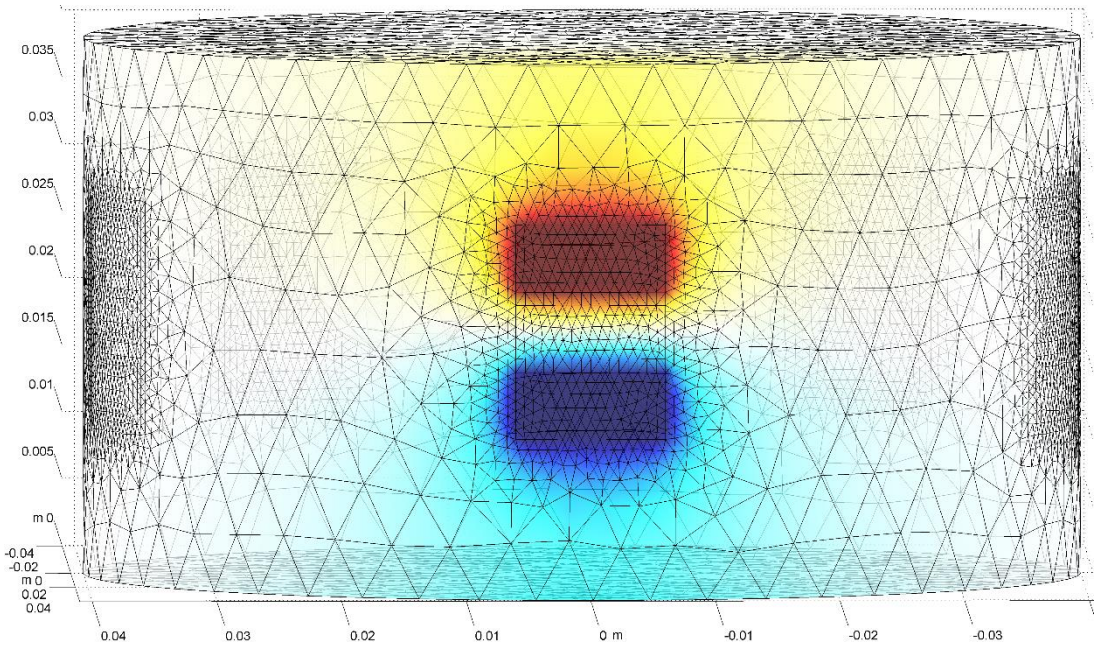

Figure 4-9 Potentials of Forward Problem Solution with Traditional CEM at 5.01MHz

The potentials of the forward problem solution given by the SEM-PMC BCs are plotted in Figure 4-10.

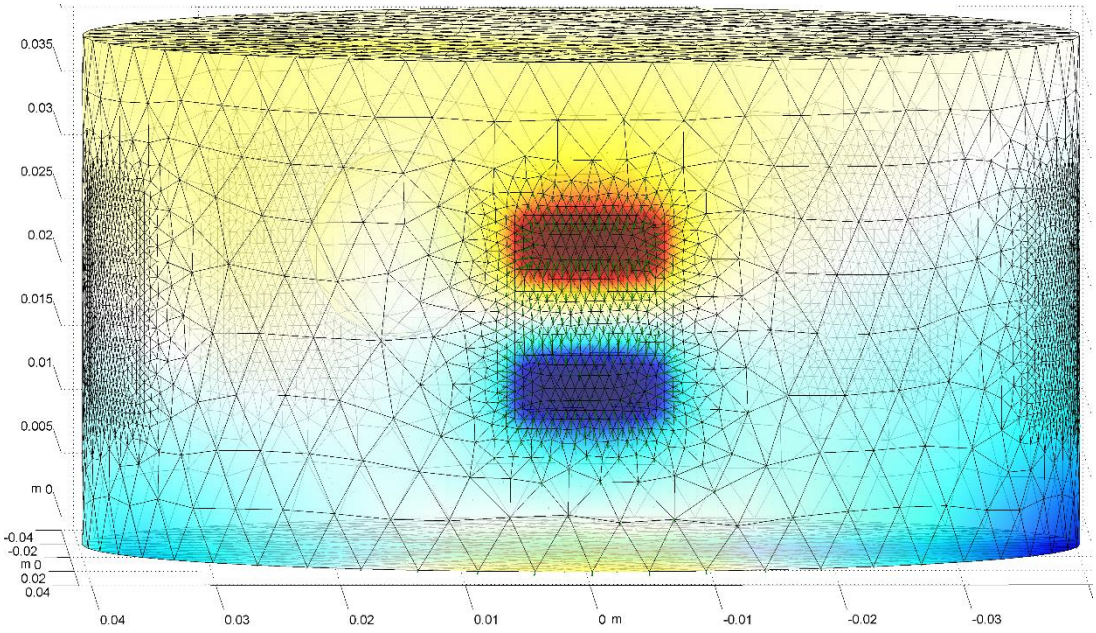

Figure 4-10 $\mathbf{A} - \Phi$ Potentials of Forward Problem Solution with SEM-PMC at 5.01MHz

The potentials of the forward problem solution given by the SEM-IBC are plotted in Figure 4-11.

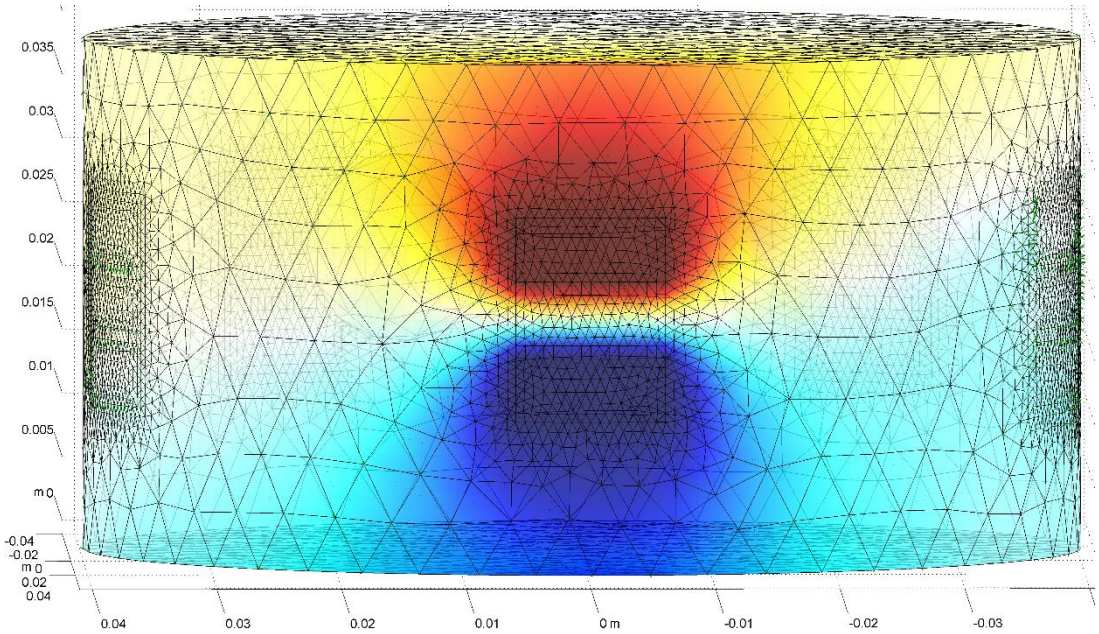

Figure 4-11 $\mathbf{A} - \Phi$ Potentials of Forward Problem Solution with SEM-IBC at 5.01MHz

The potentials of the forward problem solution given by the CEM-IBC are plotted in Figure 4-12.

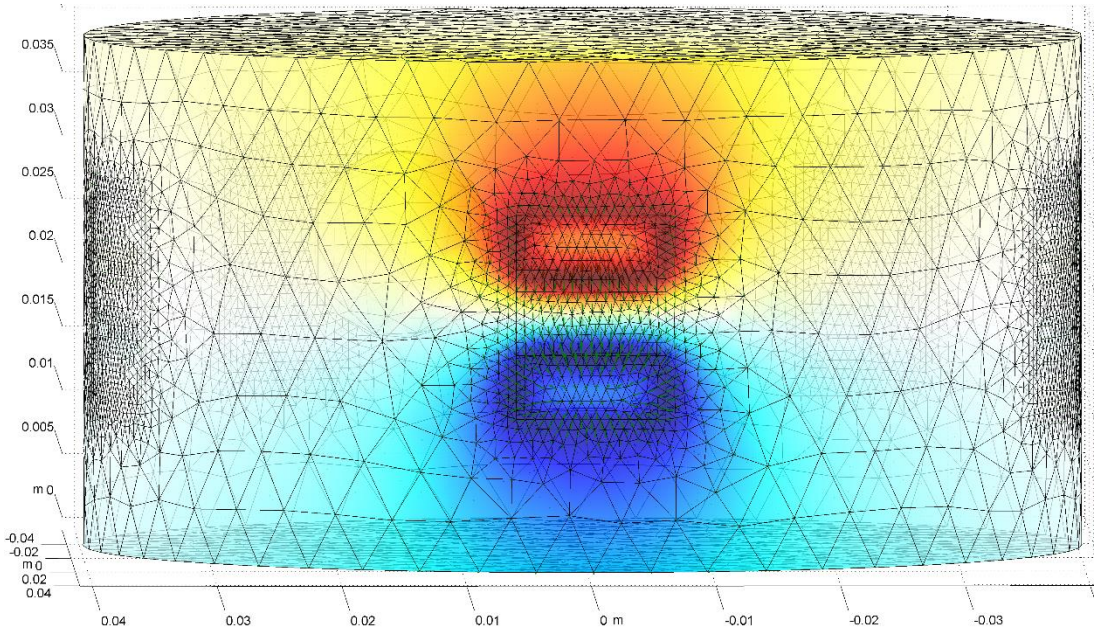

Figure 4-12 $\mathbf{A} - \Phi$ Potentials of Forward Problem Solution with CEM-IBC at 5.01MHz

The potentials of the forward problem solution given by the TPM are plotted in Figure 4-13.

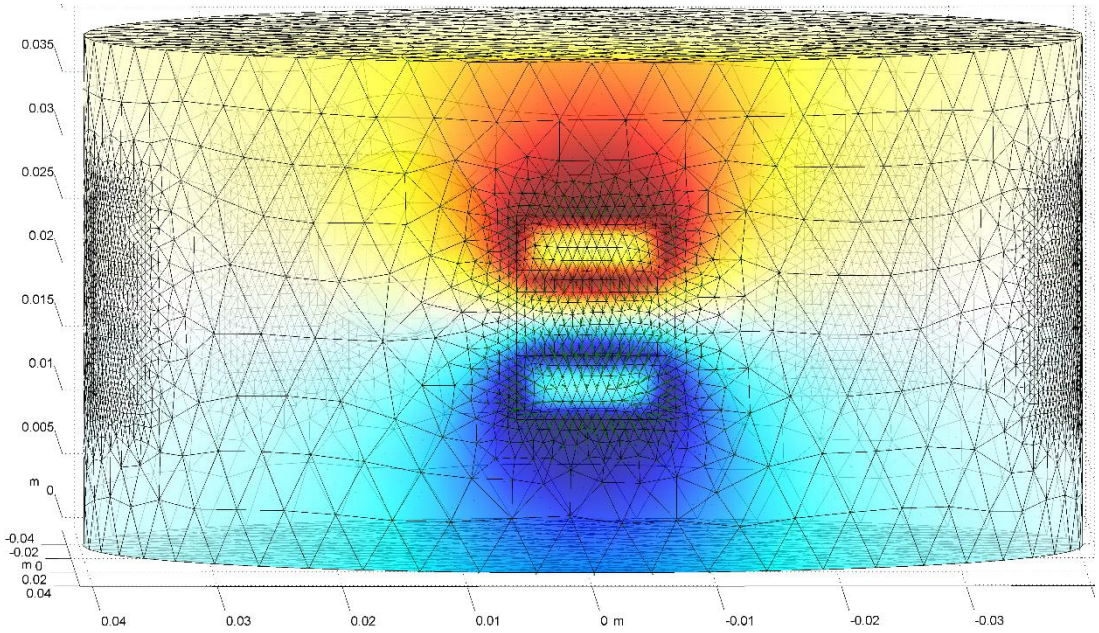

Figure 4-13 $\mathbf{A} - \Phi$ Potentials of Forward Problem Solution with TPM at 5.01MHz

The magnitude and directions of the electric field of the forward problem solution given by the COMSOL are plotted in Figure 4-14.

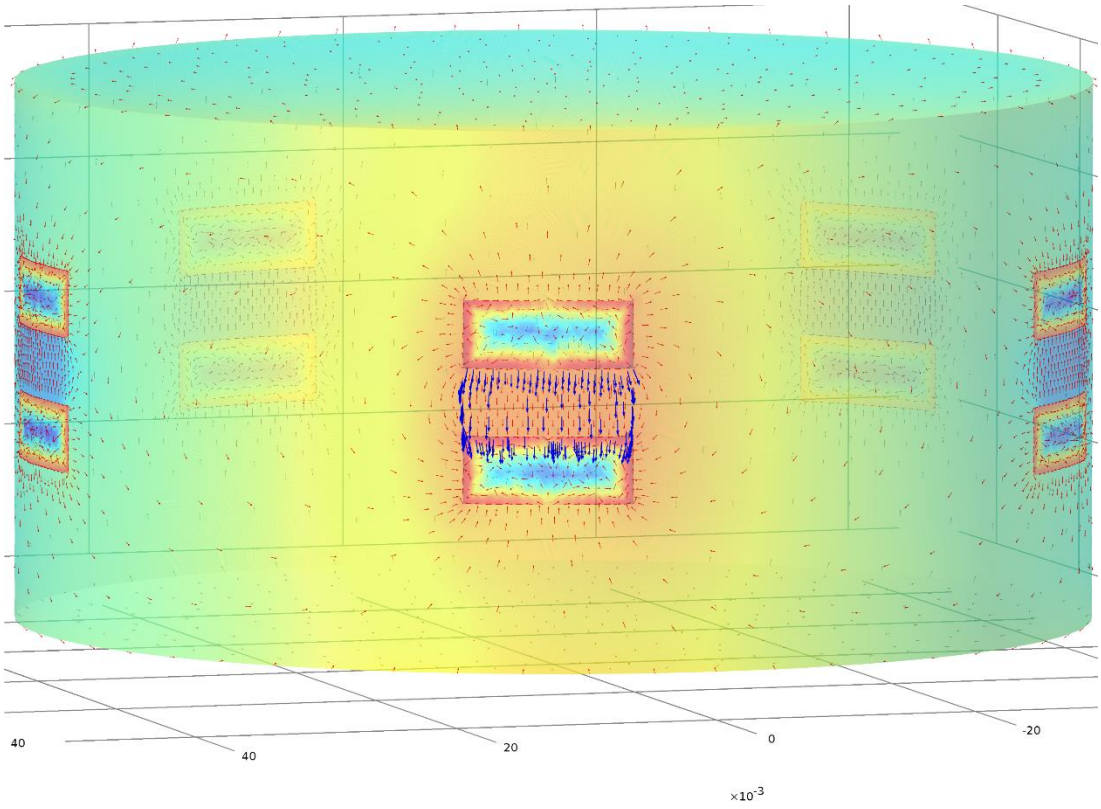

Figure 4-14 Magnitude and Directions of Forward Problem Solution with TPM at 5.01MHz

As every simulation employs a pair of voltage sources for excitation, the comparison of the voltage differences on the driving electrodes becomes meaningless. We plot the amplitudes and phases of the voltage differences on the next pair (top clockwise) of electrodes to the driving pair. For Case f), the port voltages are plotted in Figure 4-15 and Figure 4-16.

In both Figure 4-15 and Figure 4-16, there are two curves obtained from Case f). We marked the two curves with "TPM" and "TPM $\eta\downarrow$" with the contact impedance of the latter being set much smaller, as $\eta = 7 \times 10^{-5} - \mathrm{j}5 \times 10^{-5} \Omega \cdot \mathrm{m}^2$.

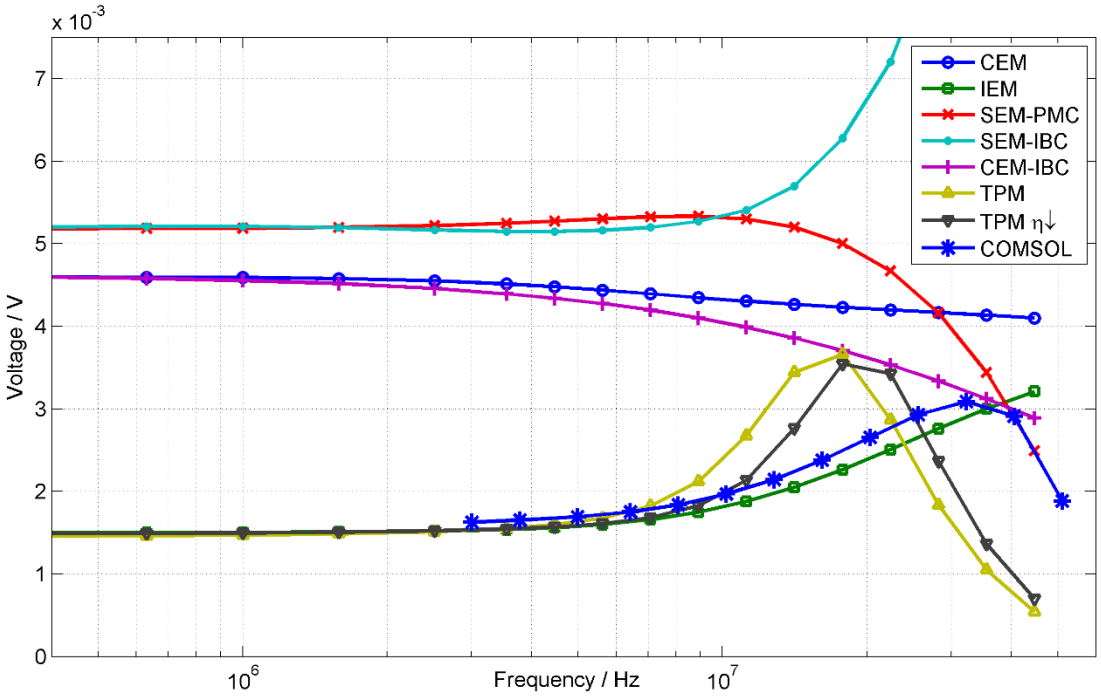

Figure 4-15 Amplitudes of the Voltage Differences on the Measuring Electrode Pair (or Transmission Line Port)

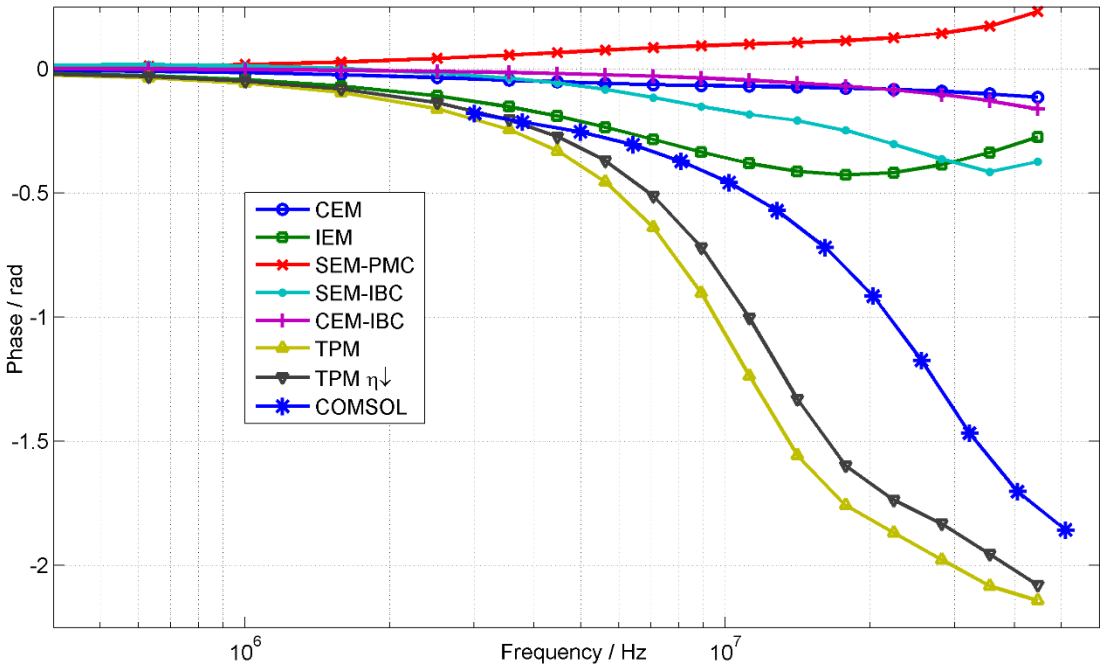

Figure 4-16 Phases of the Voltage Differences on Measuring Electrode Pair (or Transmission Line Port)

Some key findings from the various solution methods are as follows:

- The shapes of the scalar potential distributions are similar for Cases a), b), d), e) and f).
- The shape of the distribution for Case c) in Figure 4-10 is clearly distorted. The reason can be that the SEM-PMC assumes the tangential component of the $\mathbf{H}$ field disappear on the non-electrode boundary. It was also concluded by Soni et al. that, the SEM-PMC behaves badly (Soni, et al., 2006). The SEM-PMC has been used in the Tank Model (Section 3.4.2) as comparison, however we used a surrounding air sphere to avoid the effect in the tank.
- The behavior of the vector potential around the measuring electrode pairs in Case d) SEM-IBC is not correct. The reason can be that Type D BC (Table 4-2) on measuring electrodes forces the tangential electric field to vanish. However, the IBC on the non-electrode boundary dictates the tangential electric field to exist.
- The skin effect on the driving electrodes can be seen in the solutions of Case e) CEM-IBC and Case f) TPM. Equation 4-16 and Equation 4-17 (b) allow the current density to choose its path, instead of being a uniform distribution forced by other BCs. Equation 4-17 (a) allows the potentials varying on the electrode surfaces, instead of being constant forced by other BCs.
- For Case f) TPM, the excitation current density is constrained by the transmission line Equation 4-28 and characteristic impedances Z_{PM} and Z_{PD}, making the electric field more consentrated on the port dielectric surface.
- The distribution plotted in Figure 4-14 is the magnitude of electric field obtained by COMSOL (which is not the same with the scalar and vector potentials plotted in other figures). The potential distribution similar to Cases e) CEM-IBC and f) TPM is implied from the electric field intensity.
- The voltages on the measuring electrode pair (measuring port voltages) given from different simulations conflict between all Cases.
- At a relative low frequency, the magnitudes of voltages converge to three groups for three reasons:
    - Case c) and d), lack of input/output and contact impedance;
    - Case a) and e), lack of input/output impedance;
    - Case b), f) and COMSOL, with input/output (port) impedance.
- For Case g) simulations using COMSOL do not converge at frequencies lower than 2MHz.

- The solutions for Case e) are similar in both magnitude and phase to those for Case a). The CEM-IBC obtained identical results to the CEM does, when the frequency is low enough. It confirms the quasi-static assumption can be used at low frequencies. On the other hand, the full Maxwell's equation reduces the magnitudes while distorting the phases when the frequency increases.
- A peak is found in both Case f) and Case g) COMSOL. The peak appears at the frequency where the impedance of the tank matches the characteristic impedance of the transmission line. However, the two methods predict three different frequencies for the impedance matching points.
- The phase differences to the driving signal on the measuring electrode pairs (transmission line port) are similar for Cases f) and Case g) COMSOL. The same tendency is found between the two, whereas the largest derivative of phases appear at different frequencies.

Based on the above findings, we conclude the following:

- Simply solving the EIT forward problems with the full Maxwell's equations using the potential formula is not necessarily providing more accurate results than the quasi-static solutions, unless the BCs including electrode models are carefully considered.
- Solving the forward problems with the Laplace equations under quasi-static assumption is still able to find relatively accurate results at a frequency up to a few MHz with IEM.
- The CEM-IBC successfully takes the contact impedances of the electrode surfaces into account. However, a general electrode is not able to deliver the electromagnetic field to the amount it assumes.
- The COMSOL simulations verify that the TPM is able to obtain accurate forward solutions for EIT. The difference at the same frequency between the two methods may due to the PEC used on the electrode surface by COMSOL.
- The TPM gives the best predictions on the forward problems of EIT in the frequency range, among the BCs used in this case study.
- The contact impedance of the electrode (port) surface can significantly affect the accuracy of the forward problems, and has to be accurately measured.
- Experimental results are needed for verifying the proposed model.

There are also other defects that will contribute the inaccuracy of the TPM.

The accuracy of the IBC is determined by the geometry size and the medium propagation constant (Senior, 1960). In EIT applications such as our case study, however, the accuracy of the IBC limits the performance of the forward solver, especially on the non-electrode boundary surface and at low frequencies.

The transmission line equations (Equation 4-26) constraining the port excitation are one-dimension differential equations approximated from the Maxwell's equations. The normal component of the electric field is forced to vanish with Equation 4-28 (c - d), so that the transmission line equations can be applied. The normal component of the electric field can exist in reality at the dielectric region of a transmission line port, as shown in Figure 4-7 with green dash arrows. But, the EMF propagating in a differential strip-line is mainly TEM wave, and the TE and TM modes can propagate at only high frequencies (Shen & Kong, 1995). Therefore, the normal component limits the accuracy of the forward solver when the wavelengths are comparable with the port size.

4.6 Summary

This chapter investigates the full Maxwell's equations applying on the EIT forward problems. A 3-D FEM model using the potential formula is derived. More accurate BCs including electrode models for forward problems, CEM-IBC and TPM, are presented. The CEM-IBC takes the contact impedance of electrodes into the considerations for the forward modelling. The TPM treats a pair of electrodes as a transmission line port, which provides appropriate ways for injecting and measuring electromagnetic fields. Our results were verified with different BCs and also a commercial EMF solver, COMSOL. The results confirm that at a frequency range up to a few MHz, the IEM we proposed in Chapter 3 can accurately obtain the forward solutions without solving the full Maxwell's formula. The similarity in the measured voltages between TPM and COMSOL has been found in Figure 4-15 and Figure 4-16, where the difference in frequency of the peaks is contributed by the contact impedances. The TPM including the effects caused by the contact impedance, the skin effects and the instrumental loading effects, can obtain the best results (against the COMSOL results) and provide a much wider resolvability range than COMSOL.

Chapter 5 EIT Inverse Problems with IEM

5.1 Introduction

Based on the forward problem detailed in earlier sections, we know that the analytical solution does not exist. Therefore, the inverse problem $U(\mathbf{x}) \underset{\text{EIT}}{\longrightarrow} \varepsilon^*(x)$ is linearized as the variation of the measured voltage to that of the admittivity. The general concept of this linearised inverse problem is described by Equation 2-3, we rewrite the formula again as,

$$\Delta\varepsilon^* = \left[\frac{\partial F(\varepsilon^*{}_0)}{\partial \varepsilon^*}\right]^{-1} \left[U_{\varepsilon^*{}_0+\Delta\varepsilon^*} - F(\varepsilon^*{}_0)\right].$$

In order to solve the inverse problem, Equation 2-3 is obtained numerically, where $[\partial F(\varepsilon^*{}_0)/\partial \varepsilon^*]$ is usually called the Jacobian matrix.

The Jacobian matrix is derived from EIT forward problems detailed in Section 2.3.1, where BCs such as CEM are involved. As CEM does not consider the instrumental effects of EIT systems, the EIT inverse problem derived from CEM forward problems fails to describe the real scenario. However, our IEM model (introduced in Chapter 3) is designed to model the instrumental effects. Therefore, the inverse problems derived from IEM forward problems are supposed to be better in handling the data affected by instrumental loadings.

To derived inverse problems with IEM, linearisation and perturbation techniques are applied. In order to compensate the ill-posedness, regularisations and non-linear LS are used, similar to the inverse problems derived from CEM forward problems.

In this chapter I will detail the derivations of the IEM inverse problem. Two numerical experiments will be performed, and the comparison between the inverse problems based on CEM and IEM will illustrate the reduction of instrumental effects on reconstructed images. The general approaches including the regularisation methods, iterative inversion etc., introduced in the Section 2.3.2 were used to obtain the images.

5.2 Perturbation and IEM Jacobian Matrix

To obtain Jacobian matrix in Equation 2-3, the derivative $[\partial F(\varepsilon^*{}_0)/\partial \varepsilon^*]$ is calculated. Similar to the derivation of the Jacobian matrix from CEM in Section 2.3.1, Equation 2-17 can be modified when our IEM is considered. Substituting the IEM BC to the RHS of Equation 2-17, we obtain,

$$\int_{\Omega} \varepsilon^* \nabla\Phi^d \cdot \nabla\Phi^\delta \mathrm{d}V + \sum_{l=1}^{L} \eta_l \int_{S_l} \left(\varepsilon^* \nabla\Phi^\delta \cdot \hat{\mathbf{n}}\right)\left(\varepsilon^* \nabla\Phi^d \cdot \hat{\mathbf{n}}\right)\mathrm{d}S = -\sum_{l=1}^{L} {U^\delta}_l \left({I^d}_{\mathrm{S}l} + \frac{{U^d}_l}{{\mathbf{Z}_{\mathrm{F}}}_l^d}\right).$$

Equation 5-1

As realistic systems are considered, the instrumental impedance ($\mathbf{Z}_{\mathrm{F}}$ in the IEM forward problem), is impossible to maintain a constant value, on any electrode. We use ${\mathbf{Z}_{\mathrm{F}}}_l^d$ to indicate the instrumental impedance on the l^{th} electrode and when a driving/measuring pattern d is applied.

When the IEM is not involved, $\mathbf{Z}_{\mathrm{F}} \to \infty$, only the voltages on the two driving electrodes are used. All voltages on the other electrodes do not contribute to the RHS, as $I_{\mathrm{S}l} = 0$ for non-exciting electrodes. However, when IEM is included, the contribution of non-exciting electrodes becomes noticeable.

The perturbation procedure can be applied to Equation 5-1 as $\varepsilon^* \to \varepsilon^* + \Delta\varepsilon^*$, $\Phi^d \to \Phi^d + \Delta\Phi^d$, $\Phi^\delta \to \Phi^\delta + \Delta\Phi^\delta$ and ${U^\delta}_l \to {U^\delta}_l + \Delta{U^\delta}_l$, to obtain the potential and voltage variation with respective to the admittivity variation. Ignoring the high order terms, the perturbed formula becomes,

$$\int_{\Omega} \varepsilon^* \nabla\Phi^d \cdot \nabla\Phi^\delta + \varepsilon^* \nabla\left(\Delta\Phi^\delta\right) \cdot \nabla\Phi^d + \varepsilon^* \nabla\left(\Delta\Phi^d\right) \cdot \nabla\Phi^\delta + \Delta\varepsilon^* \nabla\Phi^d \cdot \nabla\Phi^\delta \mathrm{d}V$$

$$+ \sum_{l=1}^{L} \eta_l \int_{S_l} {\varepsilon^*}^2 \frac{\partial\Phi^d}{\partial n}\frac{\partial\Phi^\delta}{\partial n} + {\varepsilon^*}^2 \frac{\partial\Delta\Phi^d}{\partial n}\frac{\partial\Phi^\delta}{\partial n} + {\varepsilon^*}^2 \frac{\partial\Delta\Phi^\delta}{\partial n}\frac{\partial\Phi^d}{\partial n} + 2\Delta\varepsilon^*\varepsilon^* \frac{\partial\Phi^\delta}{\partial n}\frac{\partial\Phi^d}{\partial n} \mathrm{d}S$$

$$= -\sum_{l=1}^{L} \left({U^\delta}_l {I^d}_{\mathrm{S}l} + \frac{{U^\delta}_l {U^d}_l}{{\mathbf{Z}_{\mathrm{F}}}_l^d} + {U^\delta}_l \frac{\Delta{U^d}_l}{{\mathbf{Z}_{\mathrm{F}}}_l^d} + {U^d}_l \frac{\Delta{U^\delta}_l}{{\mathbf{Z}_{\mathrm{F}}}_l^d} + \Delta{U^\delta}_l {I^d}_{\mathrm{S}l}\right)$$

Equation 5-2

Removing all the reference terms in Equation 5-1 from Equation 5-2, and we obtain,

$$\int_{\Omega} \varepsilon^* \nabla\left(\Delta\Phi^\delta\right) \cdot \nabla\Phi^d + \varepsilon^* \nabla\left(\Delta\Phi^d\right) \cdot \nabla\Phi^\delta + \Delta\varepsilon^* \nabla\Phi^d \cdot \nabla\Phi^\delta \mathrm{d}V$$

$$+ \sum_{l=1}^{L} \eta_l \int_{S_l} {\varepsilon^*}^2 \frac{\partial\Delta\Phi^d}{\partial n}\frac{\partial\Phi^\delta}{\partial n} + {\varepsilon^*}^2 \frac{\partial\Delta\Phi^\delta}{\partial n}\frac{\partial\Phi^d}{\partial n} + 2\Delta\varepsilon^*\varepsilon^* \frac{\partial\Phi^\delta}{\partial n}\frac{\partial\Phi^d}{\partial n} \mathrm{d}S$$

$$= -\sum_{l=1}^{L} \left({U^\delta}_l \frac{\Delta{U^d}_l}{{\mathbf{Z}_{\mathrm{F}}}_l^d} + {U^d}_l \frac{\Delta{U^\delta}_l}{{\mathbf{Z}_{\mathrm{F}}}_l^d} + \Delta{U^\delta}_l {I^d}_{\mathrm{S}l}\right).$$

Equation 5-3

The first two terms in the volume integral are dependent on variation of admittivity. We use Equation 2-14 to move them into the boundary integral by replacing v with $\Delta\Phi^d$ and $\Delta\Phi^\delta$, and substituting it into Equation 5-8.

$$\int_{\partial\Omega}\Delta\Phi^\delta\varepsilon^*\nabla\Phi^d\cdot\hat{\mathbf{n}}\mathrm{d}S+\int_{\partial\Omega}\Delta\Phi^d\varepsilon^*\nabla\Phi^\delta\cdot\hat{\mathbf{n}}\mathrm{d}S+\int_{\Omega}\Delta\varepsilon^*\nabla\Phi^d\cdot\nabla\Phi^\delta\mathrm{d}V$$

$$+\sum_{l=1}^{L}\eta_l\int_{S_l}\varepsilon^{*2}\frac{\partial\Delta\Phi^\delta}{\partial n}\frac{\partial\Phi^d}{\partial n}+\varepsilon^{*2}\frac{\partial\Phi^\delta}{\partial n}\frac{\partial\Delta\Phi^d}{\partial n}+2\Delta\varepsilon^*\varepsilon^*\frac{\partial\Phi^\delta}{\partial n}\frac{\partial\Phi^d}{\partial n}\mathrm{d}S$$

$$=-\sum_{l=1}^{L}\left(U^\delta{}_l\frac{\Delta U^d{}_l}{\mathbf{Z}_{\mathrm{F}l}^{\,d}}+U^d{}_l\frac{\Delta U^\delta{}_l}{\mathbf{Z}_{\mathrm{F}l}^{\,d}}+\Delta U^\delta{}_l I^d{}_{\mathrm{S}l}\right).$$

Inserting the perturbed BC Equation 2-15 (c),

$$\Delta\Phi^\delta+\eta_l\Delta\varepsilon^*\frac{\partial\Phi^\delta}{\partial n}+\eta_l\varepsilon^*\frac{\partial\Delta\Phi^\delta}{\partial n}=\Delta U^\delta{}_l,\qquad\Delta\Phi^d+\eta_l\Delta\varepsilon^*\frac{\partial\Phi^d}{\partial n}+\eta_l\varepsilon^*\frac{\partial\Delta\Phi^d}{\partial n}=\Delta U^d{}_l\,,$$

$$\int_{\Omega}\Delta\varepsilon^*\nabla\Phi^d\cdot\nabla\Phi^\delta\mathrm{d}V+\sum_{l=1}^{L}\Delta U^\delta{}_l\int_{S_l}\varepsilon^*\frac{\partial\Phi^d}{\partial n}\mathrm{d}S+\sum_{l=1}^{L}\Delta U^d{}_l\int_{S_l}\varepsilon^*\frac{\partial\Phi^\delta}{\partial n}\mathrm{d}S$$

$$=-\sum_{l=1}^{L}\left(U^\delta{}_l\frac{\Delta U^d{}_l}{\mathbf{Z}_{\mathrm{F}l}^{\,d}}+U^d{}_l\frac{\Delta U^\delta{}_l}{\mathbf{Z}_{\mathrm{F}l}^{\,d}}+\Delta U^\delta{}_l I^d{}_{\mathrm{S}l}\right).$$

Here the IEM BCs for both excitation patterns d and δ, are used and inserted. So we obtain,

$$\int_{S_l}\varepsilon^*\frac{\partial\Phi^d}{\partial n}dS=I^d{}_l=-\left(I^d{}_{\mathrm{S}l}+\frac{U^d{}_l}{\mathbf{Z}_{\mathrm{F}l}^{\,d}}\right)$$

$$\int_{S_l}\varepsilon^*\frac{\partial\Phi^\delta}{\partial n}dS=I^\delta{}_l=-\left(I^\delta{}_{\mathrm{S}l}+\frac{U^\delta{}_l}{\mathbf{Z}_{\mathrm{F}l}^{\,\delta}}\right)$$

$$\int_{\Omega}\Delta\varepsilon^*\nabla\Phi^d\cdot\nabla\Phi^\delta\mathrm{d}V=\sum_{l=1}^{L}\Delta U^d{}_l\left[I^\delta{}_{\mathrm{S}l}+U^\delta{}_l\left(\frac{1}{\mathbf{Z}_{\mathrm{F}l}^{\,\delta}}-\frac{1}{\mathbf{Z}_{\mathrm{F}l}^{\,d}}\right)\right]$$

Equation 5-4

Equation 5-4 is the general formula for EIT inverse problems with the IEM included. Similar to the CEM inverse model, it requires to specify exciting patterns and measuring patterns.

We use the same simple example to explain Equation 5-4. Let the measuring pattern to be $\mathbf{i}^\delta=\left[I^\delta{}_0,-I^\delta{}_0,0,\cdots 0\right]^{\mathrm{T}}$, which means $I^\delta{}_1=-I^\delta{}_2=I^\delta{}_0$ and $I^\delta{}_l\big|_{3\sim L}=0$. And then, let the

driving pattern to be $\mathbf{i}^d = [0,0,{I^d}_0,-{I^d}_0,0,\cdots 0]^{\mathrm{T}}$, which means ${I^d}_3 = -{I^d}_4 = {I^d}_0$ and ${I^d}_l\big|_{1,2,5\sim L} = 0$.

Because only the 1st and the 2nd electrodes are driving when $\mathbf{i}^\delta$ applied, the sum of $\Delta {U^d}_l {I^\delta}_{\mathrm{S}l}$ is reduced to 2 terms. Between the patterns δ and d, only the instrumental impedances on electrodes 1 ~ 4 have been changed in driving and measuring modes, which means on the rest electrodes $\mathbf{Z}_{\mathrm{F}_l}^{\delta} = \mathbf{Z}_{\mathrm{F}_l}^{d}$ for $l \in \{5,\cdots,L\}$.

Together with the Equation 5-4 in this simplified case, it becomes,

$$\int_{\Omega} \Delta\varepsilon^* \nabla\Phi^d \cdot \nabla\Phi^\delta \mathrm{d}V = \left(\Delta {U^d}_1 - \Delta {U^d}_2\right) {I^\delta}_0 + \sum_{l=1}^{4} \Delta {U^d}_l {U^\delta}_l \left(\frac{1}{\mathbf{Z}_{\mathrm{F}_l}^{\delta}} - \frac{1}{\mathbf{Z}_{\mathrm{F}_l}^{d}}\right).$$

Equation 5-5

Here, $\Delta {U^d}_l$ is the voltage variation on electrodes between ${U^d}_l(\varepsilon^*)$ and ${U^d}_l(\varepsilon^* + \Delta\varepsilon^*)$, and this difference is caused by $\Delta\varepsilon^*$. Considering Equation 5-5, the following points can be conclude:

- When $\mathbf{Z}_{\mathrm{F}} \to \infty$, and the potential distributions is free from the instrumental effects. The IEM inverse problem degrades to the CEM inverse problem.
- When $\mathbf{Z}_{\mathrm{F}_l}^{\delta} = \mathbf{Z}_{\mathrm{F}_l}^{d}$, the inverse formula with IEM is the same to the CEM. The IEM is only involved in obtaining the forward solutions, and these solutions are used in the calculations of the Jacobian matrix, which we are going to derive as follows.

However, the above two are not the common cases, especially in the frequency range from hundreds kHz to a few MHz. In Section 2.4, we have explained, at such a frequency range, it is challenging to make the instrumental impedance of an electrode to be the same in the driving and measuring modes; it is also challenging to make it large enough to be free from instrumental effects.

- If the above two conditions cannot be met, then the second term (on the RHS) of Equation 5-4 comes into play. In the term, the voltage variations due to the admittivity change, as well as the voltages on electrodes, are involved.

To derive the Jacobian matrix, Equation 5-4 is first discretised to E dimensions as,

$$\sum_{e=1}^{E} \Delta {\varepsilon^*}_e \int_e \nabla\Phi^d \cdot \nabla\Phi^\delta dV = \sum_{l=1}^{L} \Delta {U^d}_l \left({I^\delta}_{\mathrm{S}l} + \frac{{U^\delta}_l}{\mathbf{Z}_{\mathrm{F}_l}^{\delta}} - \frac{{U^\delta}_l}{\mathbf{Z}_{\mathrm{F}_l}^{d}}\right)$$

$$\sum_{l=1}^{L}\frac{\Delta U^{d}{}_{l}}{\Delta\varepsilon^{*}{}_{e}}\left(I^{\delta}{}_{Sl}+\frac{U^{\delta}{}_{l}}{\mathbf{Z}_{\mathrm{F}}{}_{l}^{\delta}}-\frac{U^{\delta}{}_{l}}{\mathbf{Z}_{\mathrm{F}}{}_{l}^{d}}\right)=\int_{e}\nabla\Phi^{d}\cdot\nabla\Phi^{\delta}dV$$

Equation 5-6

We rewrite it as,

$$\sum_{l=1}^{L}\left(I^{\delta}{}_{Sl}+\frac{U^{\delta}{}_{l}}{\mathbf{Z}_{\mathrm{F}}{}_{l}^{\delta}}-\frac{U^{\delta}{}_{l}}{\mathbf{Z}_{\mathrm{F}}{}_{l}^{d}}\right)\frac{U^{d}{}_{l}(\varepsilon^{*}{}_{e}+\Delta\varepsilon^{*}{}_{e})-U^{d}{}_{l}(\varepsilon^{*}{}_{e})}{\Delta\varepsilon^{*}{}_{e}}=\int_{e}\nabla\Phi^{d}\cdot\nabla\Phi^{\delta}dV$$

$$\sum_{l=1}^{L}\left(I^{\delta}{}_{Sl}+\frac{U^{\delta}{}_{l}}{\mathbf{Z}_{\mathrm{F}}{}_{l}^{\delta}}-\frac{U^{\delta}{}_{l}}{\mathbf{Z}_{\mathrm{F}}{}_{l}^{d}}\right)\lim_{\Delta\varepsilon^{*}{}_{e}\to 0}\frac{U^{d}{}_{l}(\varepsilon^{*}{}_{e}+\Delta\varepsilon^{*}{}_{e})-U^{d}{}_{l}(\varepsilon^{*}{}_{e})}{\Delta\varepsilon^{*}{}_{e}}$$

$$=\sum_{l=1}^{L}\left(I^{\delta}{}_{Sl}+\frac{U^{\delta}{}_{l}}{\mathbf{Z}_{\mathrm{F}}{}_{l}^{\delta}}-\frac{U^{\delta}{}_{l}}{\mathbf{Z}_{\mathrm{F}}{}_{l}^{d}}\right)\frac{\partial U^{d}{}_{l}}{\partial\varepsilon^{*}{}_{e}}=\int_{e}\nabla\Phi^{d}\cdot\nabla\Phi^{\delta}dV$$

Equation 5-7

Considering the simplified case, the measuring pattern $\mathbf{i}^{\delta}$ is on a pair of electrodes $l^{\delta+}$ and $l^{\delta-}$, with the current $\pm I^{\delta}{}_{0}$ respectively, *when in the driving mode*. It causes the potential distribution in the object to be Φ^{δ}; the driving pattern $\mathbf{i}^{d}$ is exciting the object on a pair of electrodes l^{d+} and l^{d-}, with the current $\pm I^{d}{}_{0}$ respectively. The potential distribution in the object is Φ^{d}. There is $\mathbf{Z}_{\mathrm{F}}{}_{l}^{\delta}=\mathbf{Z}_{\mathrm{F}}{}_{l}^{d}$ for the electrodes apart from $l^{\delta+}$, $l^{\delta-}$, l^{d+} and l^{d-}. We have,

$$I^{\delta}{}_{0}\frac{\partial U^{d}{}_{l^{\delta+}}}{\partial\varepsilon^{*}{}_{e}}-I^{\delta}{}_{0}\frac{\partial U^{d}{}_{l^{\delta-}}}{\partial\varepsilon^{*}{}_{e}}+\sum_{l=\substack{l^{\delta+}\\l^{d+}}^{\substack{l^{\delta-}\\l^{d-}}}}U^{\delta}{}_{l}\left(\frac{1}{\mathbf{Z}_{\mathrm{F}}{}_{l}^{\delta}}-\frac{1}{\mathbf{Z}_{\mathrm{F}}{}_{l}^{d}}\right)\frac{\partial U^{d}{}_{l}}{\partial\varepsilon^{*}{}_{e}}=\int_{e}\nabla\Phi^{d}\cdot\nabla\Phi^{\delta}dV$$

$$\frac{\partial W_{d,\delta}}{\partial\varepsilon^{*}{}_{e}}=\int_{e}\nabla\Phi^{d}\cdot\nabla\Phi^{\delta}\mathrm{d}V$$

Equation 5-8 (a - b)

Then, the differential formula can be easily recognised, by comparing with Equation 2-20. We rewrite it here as,

$$\frac{\partial U_{d,\delta}}{\partial\varepsilon^{*}{}_{e}}\equiv\frac{\partial\left(U^{d}{}_{l^{+}}-U^{d}{}_{l^{-}}\right)}{\partial\varepsilon^{*}{}_{e}}=\frac{-1}{I^{\delta}{}_{0}}\int_{V_{e}}\nabla\Phi^{d}\cdot\nabla\Phi^{\delta}\mathrm{d}V\,.$$

The LHS of Equation 5-8 (a) suggests that the integral can be expressed by the linear combinations of the voltage variation on the electrodes, with respect to the admittivity. We therefore use the new notation $W_{d,\delta}$ in contrast to the $U_{d,\delta}$ in Equation 2-20, for the

combinations. Its subscripts d and δ denote the related driving pattern and measuring pattern, respectively.

With the partial derivative given, the Jacobian matrix can be easily obtained as the formula is similar to Equation 3-13 in the forward problem Section 3.3.1. Many of the matrices can be re-used in calculating the Jacobian matrix, therefore we eliminate the derivations here.

The Equation 5-8 (b) is the contribution from the integral of an element to a driving and a measuring pattern. In order to provide the Jacobian matrix, the FEM is applied on RHS of Equation 5-8 (b) with the gradient on potentials being replaced with the shape functions.

$$\frac{\partial W_{d,\delta}}{\partial \varepsilon^*{}_e} = V_e \begin{bmatrix} \mathrm{u}_{e1}{}^d \\ \vdots \\ \mathrm{u}_{e4}{}^d \end{bmatrix}^* \begin{bmatrix} \frac{\partial \phi^e{}_{e1}}{\partial x} & \cdots & \frac{\partial \phi^e{}_{e4}}{\partial x} \\ \frac{\partial \phi^e{}_{e1}}{\partial y} & \cdots & \frac{\partial \phi^e{}_{e4}}{\partial y} \\ \frac{\partial \phi^e{}_{e1}}{\partial z} & & \frac{\partial \phi^e{}_{e4}}{\partial z} \end{bmatrix}^{\mathrm{T}} \begin{bmatrix} \frac{\partial \phi^e{}_{e1}}{\partial x} & \cdots & \frac{\partial \phi^e{}_{e4}}{\partial x} \\ \frac{\partial \phi^e{}_{e1}}{\partial y} & \cdots & \frac{\partial \phi^e{}_{e4}}{\partial y} \\ \frac{\partial \phi^e{}_{e1}}{\partial z} & & \frac{\partial \phi^e{}_{e4}}{\partial z} \end{bmatrix} \begin{bmatrix} \mathrm{u}_{e1}{}^\delta \\ \vdots \\ \mathrm{u}_{e4}{}^\delta \end{bmatrix}$$

Here V_e is the volume of the e^{th} element, and note that, the inner product in complex domain is the product of the conjugate transport of the matrix and the other matrix.

By extending the local nodes to global nodes, it can be recognised as the stiffness matrix.

$$\frac{\partial W_{d,\delta}}{\partial \varepsilon^*{}_e} = \begin{bmatrix} \mathrm{u}_1{}^d \\ \vdots \\ \mathrm{u}_N{}^d \end{bmatrix}^* \begin{bmatrix} \boldsymbol{\phi}_1^e \\ \vdots \\ \boldsymbol{\phi}_N^e \end{bmatrix} [\boldsymbol{V}^e] \begin{bmatrix} \boldsymbol{\phi}_1^e \\ \vdots \\ \boldsymbol{\phi}_N^e \end{bmatrix}^{\mathrm{T}} \begin{bmatrix} \mathrm{u}_1{}^\delta \\ \vdots \\ \mathrm{u}_N{}^\delta \end{bmatrix} = \begin{bmatrix} \mathrm{u}_1{}^d \\ \vdots \\ \mathrm{u}_N{}^d \end{bmatrix}^* \boldsymbol{K}^{\mathrm{T}} [\boldsymbol{V}^e] \boldsymbol{K} \begin{bmatrix} \mathrm{u}_1{}^\delta \\ \vdots \\ \mathrm{u}_N{}^\delta \end{bmatrix}$$

Equation 5-9

In the above form, only the matrix $[\boldsymbol{V}^e]$ need to be redefined by replacing the $[\varepsilon V^e]$ term in the forward FEM matrix. The entries of the Jacobian matrix by Equation 5-8 are then given by the product of forward solutions of the two patterns d and δ.

As explained earlier, each column of the Jacobian represent the $\Delta\varepsilon^*{}_e$ at an element, and we denote a row of the Jacobian with $\boldsymbol{J}^{d,\delta}$, which related to a specific driving and measuring pattern d, δ, as following,

$$\boldsymbol{J}^{d,\delta} = \begin{bmatrix} \frac{\partial W_{d,\delta}}{\partial \varepsilon^*{}_1} & \cdots & \frac{\partial W_{d,\delta}}{\partial \varepsilon^*{}_E} \end{bmatrix} \in \mathbb{C}^{1\times E}.$$

Each entry in $\boldsymbol{J}^{d,\delta}$ is the contribution of an elements to the variation of $W_{d,\delta}$. Assume there are C driving patterns $d1 \sim dC$ with each of these driving patterns having M measurement patterns $\delta 1 \sim \delta M$, then the overall Jacobian matrix is made up as follows,

$$\boldsymbol{J} = \begin{bmatrix} \boldsymbol{J}^{d1,\delta1} \\ \vdots \\ \boldsymbol{J}^{dC,\delta M} \end{bmatrix} \in \mathbb{C}^{(MC)\times E}.$$

In order to calculate the Jacobian matrix effectively, each column of the matrix is calculated at once, by applying the forward solutions $\mathrm{u}^{d1\sim dC}$ and $\mathrm{u}^{\delta1\sim\delta M}$as Equation 5-10.

$$\boldsymbol{J}^{e} = -\begin{bmatrix} {\mathrm{u}_1}^{d1} & \cdots & {\mathrm{u}_1}^{dC} \\ \vdots & & \vdots \\ {\mathrm{u}_N}^{d1} & & {\mathrm{u}_N}^{dC} \end{bmatrix}^{*} \boldsymbol{K}^{\mathrm{T}}[\boldsymbol{V}^{e}]\boldsymbol{K} \begin{bmatrix} {\mathrm{u}_1}^{\delta1} & \cdots & {\mathrm{u}_1}^{\delta M} \\ \vdots & & \vdots \\ {\mathrm{u}_N}^{\delta1} & & {\mathrm{u}_N}^{\delta M} \end{bmatrix}$$

Equation 5-10

The differences appears on the RHS, and every element in the IEM Jacobian matrix is $\Delta W_{d,\delta}/\Delta\varepsilon^{*}$ instead of $\Delta U_{d,\delta}/\Delta\varepsilon^{*}$. Consequently, modifications are made on the RHS of Equation 2-22 corresponding to $\Delta W_{d,\delta}$.

$$\boldsymbol{J}\begin{bmatrix} {\Delta\varepsilon^{*}}_1 \\ \vdots \\ {\Delta\varepsilon^{*}}_e \\ \vdots \\ {\Delta\varepsilon^{*}}_E \end{bmatrix} = \begin{bmatrix} \Delta W_{d1,\delta1} \\ \vdots \\ \Delta W_{d,\delta} \\ \vdots \\ \Delta W_{dC,\delta M} \end{bmatrix}, \qquad \Delta W_{d,\delta} = \begin{bmatrix} {I^{\delta}}_0 + {U^{\delta}}_{l^{\delta+}}\left(\dfrac{1}{\mathbf{Z}^{\delta}_{\mathrm{F}l^{\delta+}}} - \dfrac{1}{\mathbf{Z}^{d}_{\mathrm{F}l^{\delta+}}}\right) \\ -{I^{\delta}}_0 + {U^{\delta}}_{l^{\delta-}}\left(\dfrac{1}{\mathbf{Z}^{\delta}_{\mathrm{F}l^{\delta-}}} - \dfrac{1}{\mathbf{Z}^{d}_{\mathrm{F}l^{\delta-}}}\right) \\ {U^{\delta}}_{l^{d+}}\left(\dfrac{1}{\mathbf{Z}^{\delta}_{\mathrm{F}l^{d+}}} - \dfrac{1}{\mathbf{Z}^{d}_{\mathrm{F}l^{d+}}}\right) \\ {U^{\delta}}_{l^{d-}}\left(\dfrac{1}{\mathbf{Z}^{\delta}_{\mathrm{F}l^{d-}}} - \dfrac{1}{\mathbf{Z}^{d}_{\mathrm{F}l^{d-}}}\right) \end{bmatrix}^{\mathrm{T}} \begin{bmatrix} {\Delta U^{d}}_{l^{\delta+}} \\ {\Delta U^{d}}_{l^{\delta-}} \\ {\Delta U^{d}}_{l^{d+}} \\ {\Delta U^{d}}_{l^{d-}} \end{bmatrix}.$$

Equation 5-11 (a - b)

From Equation 5-11 (b), $\Delta W_{d,\delta}$ is an inner product of two vectors corresponding to the driving and measuring patterns d and δ. We form a diagonal matrix and combine it into the Jacobian matrix.

$$\boldsymbol{J}\begin{bmatrix} {\Delta\varepsilon^{*}}_1 \\ \vdots \\ {\Delta\varepsilon^{*}}_e \\ \vdots \\ {\Delta\varepsilon^{*}}_E \end{bmatrix} = \begin{bmatrix} b^{d1,\delta1} & & & & & \\ & \ddots & & & & \\ & & b^{dC,\delta1} & & & \\ & & & \ddots & & \\ & & & & b^{d1,\delta M} & \\ & & & & & \ddots \\ & & & & & b^{dC,\delta M} \end{bmatrix} \begin{bmatrix} \Delta U^{d1,\delta1} \\ \vdots \\ \Delta U^{dC,\delta1} \\ \vdots \\ \Delta U^{d1,\delta M} \\ \vdots \\ \Delta U^{dC,\delta M} \end{bmatrix} = [\boldsymbol{JIC}] \begin{bmatrix} \Delta U^{d1,\delta1} \\ \vdots \\ \Delta U^{dC,\delta1} \\ \vdots \\ \Delta U^{d1,\delta M} \\ \vdots \\ \Delta U^{dC,\delta M} \end{bmatrix}.$$

Equation 5-12

Here, $[\boldsymbol{JIC}]$ is the instrumental correction matrix for the Jacobian consisting of $b^{d,\delta}$ in diagonal. The two vectors in the Equation 5-12 are defined as followed.

$$b^{d,\delta} = \begin{bmatrix} {I^{\delta}}_0 + {U^{\delta}}_{l^{\delta+}}\left(\frac{1}{\mathbf{Z}_{\mathrm{F}l^{\delta+}}^{\delta}} - \frac{1}{\mathbf{Z}_{\mathrm{F}l^{\delta+}}^{d}}\right) \\ -{I^{\delta}}_0 + {U^{\delta}}_{l^{\delta-}}\left(\frac{1}{\mathbf{Z}_{\mathrm{F}l^{\delta-}}^{\delta}} - \frac{1}{\mathbf{Z}_{\mathrm{F}l^{\delta-}}^{d}}\right) \\ {U^{\delta}}_{l^{d+}}\left(\frac{1}{\mathbf{Z}_{\mathrm{F}l^{d+}}^{\delta}} - \frac{1}{\mathbf{Z}_{\mathrm{F}l^{d+}}^{d}}\right) \\ {U^{\delta}}_{l^{d-}}\left(\frac{1}{\mathbf{Z}_{\mathrm{F}l^{d-}}^{\delta}} - \frac{1}{\mathbf{Z}_{\mathrm{F}l^{d-}}^{d}}\right) \end{bmatrix}^{\mathrm{T}}, \qquad \Delta U^{d,\delta} = \begin{bmatrix} \Delta{U^{d}}_{l^{\delta+}} \\ \Delta{U^{d}}_{l^{\delta-}} \\ \Delta{U^{d}}_{l^{d+}} \\ \Delta{U^{d}}_{l^{d-}} \end{bmatrix}.$$

Equation 5-12 gives the formula of inverse problems derived from IEM forward problems, in which the instrumental effects caused by the instrumental impedance are considered. However, it does not change the fact that the inverse problem of EIT is ill-posed. Therefore, the solutions can be obtained after the regularisation and non-linear LS techniques are applied.

The same procedures have been used to obtain Equation 2-29 from Equation 2-21 (b) by using the iterative regularised Gauss-Newton method. The inverse problem with IEM in Equation 5-12, therefore can be solved as,

$$x_{k+1} = x_k + ([\boldsymbol{J}_k]^*[\boldsymbol{J}_k] + \lambda^2\boldsymbol{L}^*\boldsymbol{L})^{-1}[\boldsymbol{J}_k]^*[\boldsymbol{JIC}_k]\left[\widetilde{U}_{d,\delta}(x_0 + \Delta x) - U_{d,\delta}(x_k)\right] + \lambda^2\boldsymbol{L}^*\boldsymbol{L}(x_0 - x_k).$$

Equation 5-13

5.3 Case Studies and Discussions

In the following sections, two cases are studied for illustrating the instrumental effects in the reconstructed images and the benefit provided by using the IEM inverse problem.

Both cases are numerical simulations, the input of the inverse problems are given by EIT forward problems, in which IEM is used to include the instrumental effects. The typical absolute imaging procedure of EIT is used, which has been introduced in Chapter 2 Equation 2-29. The iterative inverse solver based on iterative regularised Gauss-Newton method is included in the algorithm. For each case study, reconstructed images are obtained from both the CEM based inverse problem and the IEM based inverse problem, introduced in Section 2.3 and Section 5.2 respectively. The regularisation parameter λ in Equation 2-29 (c) and Equation 5-13 are chosen based on the residuals obtained from first iteration.

Both the foreground and the background of first case study are simulated on homogeneous admittivity distributions, therefore the difference between the foreground and the background is homogeneous. We name the case study, the homogeneous case.

The second case simulated is on a homogeneous background admittivity distribution, however for the foreground, a cylinder and a sphere of different admittivity are placed in the model. We name it the elementary object case.

5.3.1 Homogeneous Case

The homogeneous case is designed to show the artefacts in reconstructed image caused by inaccurate electrode models, or more precisely caused by the instrumental effects not being considered in the electrode model.

A cylinder tank similar to the case studied in section 3.4.2 is used. However there are 16 electrodes, placed in two rings, as shown in Figure 5-1. In order to simulate the instrumental effects, the signal frequency used in this experiment is 1.25 MHz, and typical circuit parameters are chosen for the driving and measuring instruments. The parameters of the tank and the electrode circuits are listed as,

- Tank radius, 0.06m;
- Tank height, 0.05m;
- Electrode radius, 0.004m;
- Driving current, 1mA;
- Resistance part of the driving electrode 5MΩ;
- Capacitance part of the driving electrode 20pF;
- Resistance part of the driving electrode 5MΩ;
- Capacitance part of the driving electrode 10pF.

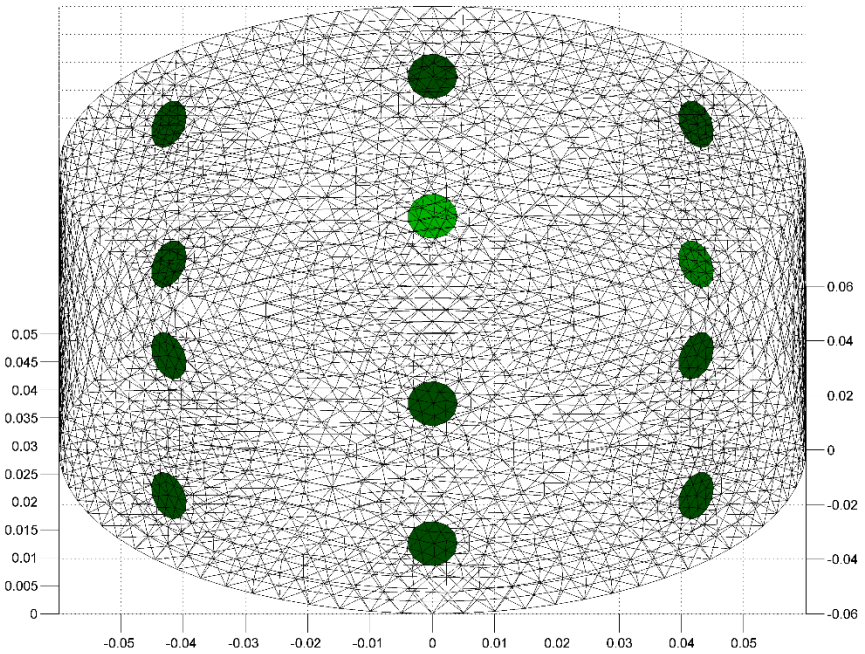

Figure 5-1 Tank Model for Homogeneous Case Study

As mentioned in Section 5.2, the instrumental impedance of each electrode is not the same, we set the standard deviation of all the instrument impedances to be within 1% of the impedance values listed previously.

The background of the simulation is a homogeneous admittivity distribution with the conductivity part being 0.05S/m while the relative permittivity being 81. This is a typical setting for saline. The foreground of the simulation is also a homogeneous admittivity distribution as mentioned. The conductivity is set to be 0.06S/m, and the relative permittivity is 200. This can be considered as a tank of conductive gel or AGAR, which is commonly used in EIT applications.

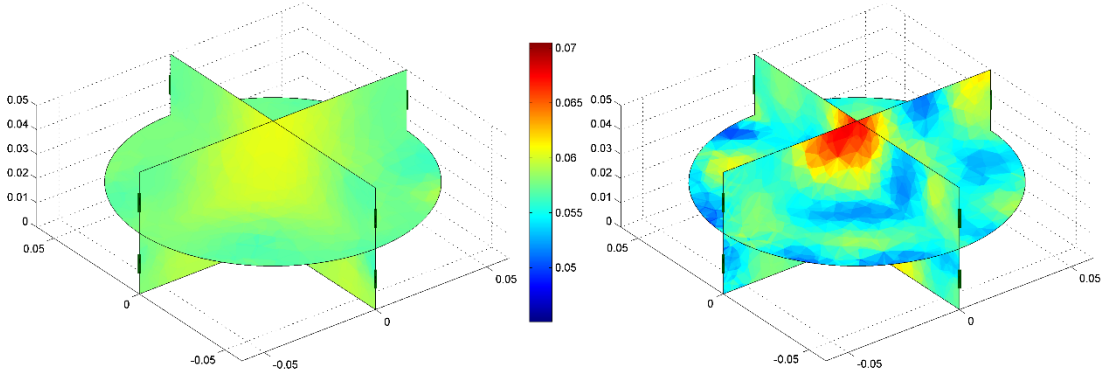

(a) Inverse Solution with IEM (b) Inverse Solution with CEM

Figure 5-2 Reconstructed Images for Homogeneous Case Study

The reconstructed images of inverse problems using IEM and CEM as electrode models respectively are shown in Figure 5-2 (a - b). The colour bar in the figures is in the unit of S/m,

while the x, y and z axes are in meters. Because the case study is designed for showing the artefact caused by the instrumental effects, the histogram of the admittivity on each mesh element is plotted in Figure 5-3. The horizontal axis is in the unit of S/m and vertical is element count. The true solution of this case study is a homogenous admittivity distribution, and the value of which equals to the foreground admittivity. Due to the ill-posedness and numerical errors, the admittivity distribution spreads along the admittivity axes across the elements in the geometry. From both figures, it can be seen, IEM provides smaller distribution in admittivity range, compared with the solution given by CEM.

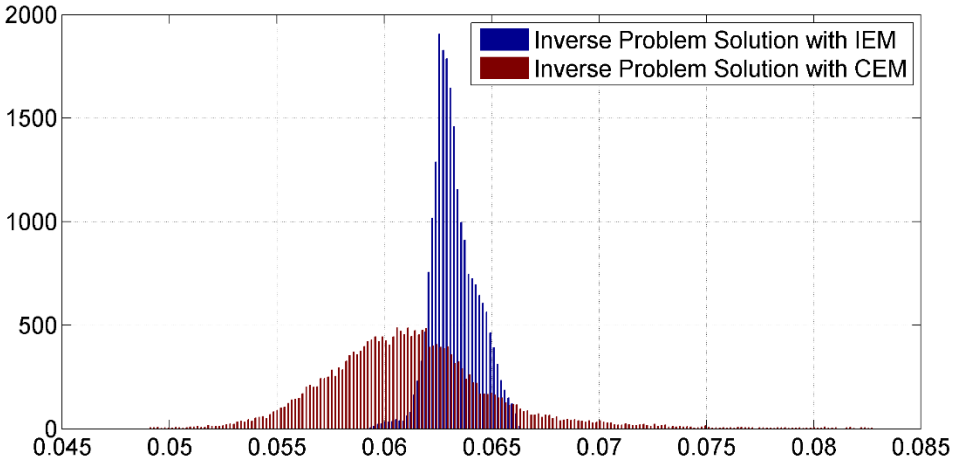

Figure 5-3 Histogram of Inverse Solutions for Homogeneous Case Study

This difference in the admittivity variation between the two reconstructions is the artefact caused by the instrumental effects. Recall Equation 2-29 (c) and Equation 5-13, the observed voltage differences on electrodes contribute to the estimation of admittivity, along with the instrumental effects on the observations. Without considering these instrumental effects, the Equation 2-29 (c) generates artefacts in the reconstruction result to compensate the *observation error*. The Equation 5-13 however uses the terms $[\boldsymbol{JIC}_k]$ to cancel the instrumental effects.

5.3.2 Elementary Objects Case

The elementary objects case is designed to show the effects on objects in the reconstructed image caused by the instrumental effects.

A cylinder tank similar to the homogeneous case studied is used, but 24 electrodes are placed in three rings one upon others on the wall of the cylinder, as shown in Figure 5-4. A higher signal frequency of 2 MHz is used in this experiment, and the electrode radii are reduced to 2.5mm for sake of image reconstruction.

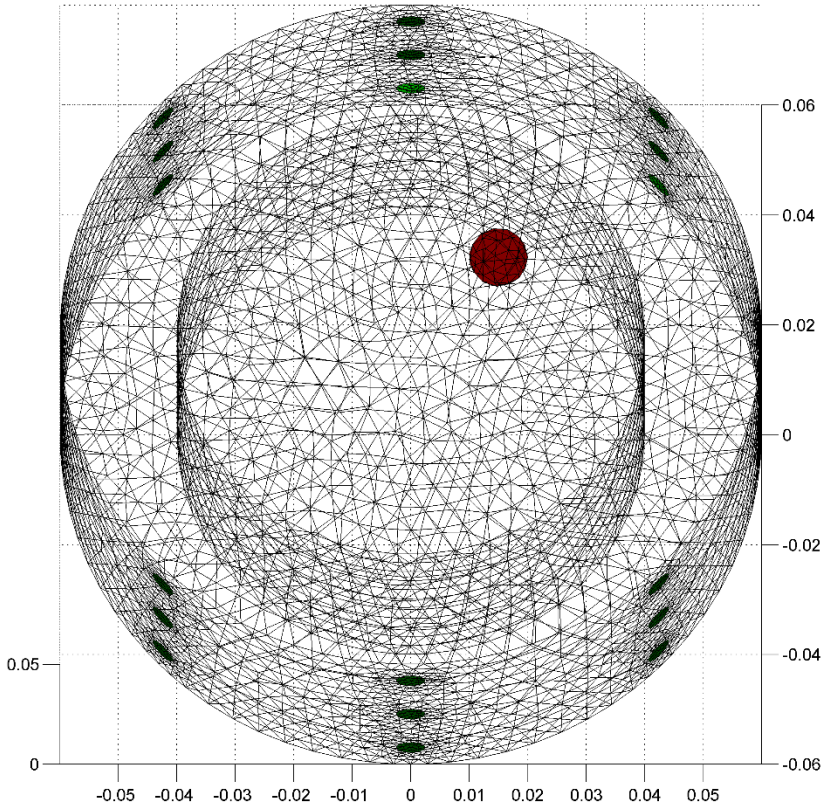

Figure 5-4 Tank Model for Elementary Objects Case Study

A cylinder with diameter 40mm is placed at the centre of the tank throughout the height. A sphere with diameter 5mm is placed inside the cylinder in the tank. The coordinates of the sphere centre is set to be (15, 10, 37.5) mm. The conductivity of the cylinder is set to be 0.06S/m, and with relative permittivity being 160. The electrical parameters of the sphere are 0.10S/m and 200, respectively.

A slice of each reconstructed image is plotted in Figure 5-5 (a - b) of the two methods. The slices are taken in parallel with the top and bottom of the tank, across the centre of the spheres.

Both solutions are given by the 5th iteration, with the same regularisation parameter. Some of the typical features mentioned in Section 1.3 can be clearly seen in the figures, including lack of sensitivity at locations far from electrodes and errors due to non-linearity, etc. The reconstructed admittivity at the centre of the tank is lower than the value it is supposed to be, whereas the admittivity at the centre of the sphere is lower as well. However, we do not discuss these common issues of EIT inverse problems, since it is not in the scope of this chapter.

Apart from these known issues, due to the instrumental effects, the artefacts appear near the electrodes and also distribute inside the elementary objects when using the CEM

reconstruction. These artefacts are significantly suppressed when using IEM inverse problem to reconstruct the image, as the instrumental effects in the observations are handled by the IEM.

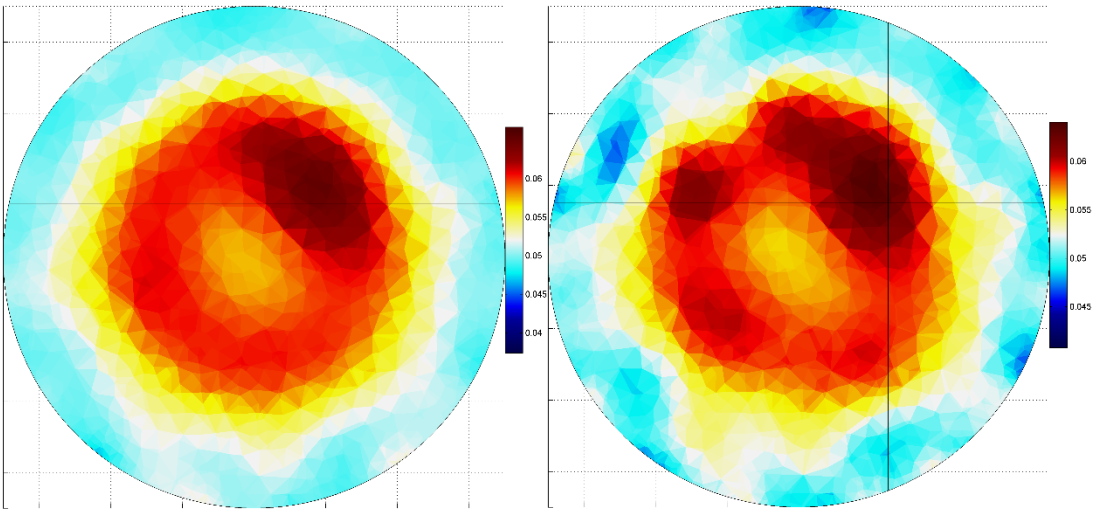

(a) Inverse Solution with IEM (b) Inverse Solution with CEM

Figure 5-5 Reconstructed Images for Elementary Objects Case Study

5.4 Summary

We have simulated and shown with the above two case studies, that the inverse problems including IEM can improve the quality of reconstructed image when the signal frequency is high enough when instrumental effects take places.

The IEM inverse problem provides a new viewpoint for the high frequency EIT applications. The instrumental problems and modelling errors (McEwan, et al., 2007) in traditional EIT instruments when operating at a high frequency can be overcome by correctly modelling these errors, and having the corrected models included in the forward and inverse problems.

Chapter 6 Summarise and Further Work

6.1 Summarise

EIT is a non-invasive imaging modality. EIT applications covering the beta-dispersion frequency are potentially capable of detecting early stage cancers. On the other hand, the ill-posedness, modelling errors and instrumental effects have been significantly preventing them from being widely applied.

In this thesis, I have investigated the electrode models and developed numerical models for EIT systems to be used in the frequency range from 500 kHz to tens of MHz.

The contributions of the research can be summarised as follows:

- An Instrumental Electrode Model (IEM) has been proposed for general EIT forward problems, with instrumental effects considered;
- A full Maxwell version of CEM, using Impedance Boundary Conditions (IBC), is proposed for full Maxwell EIT forward problems;
- A Transmission line Port Model (TPM) is proposed for full Maxwell EIT forward problems;
- An EIT inverse formula including IEM is derived and proposed with simulated results.

Promising numerical simulation results have been produced, which provides a way of using the quasi-static or full Maxwell EIT models with the realistic EIT instrumental effects considered.

6.2 Future Work

In the UK, more than 1000 people will be diagnosed with cancer everyday by the end of 2016, and almost 400 of them will die from cancer within 5 years, according to a new analysis from Macmillan Cancer Support. One of the most important factors that affects cancer survival rates in a population appears to be the stage at which cancers are diagnosed (Torre, et al., 2012), and Cancer Research UK has been urging to invest more resources in early-stage diagnosis and effective treatments.

Various medical imaging tools are available for cancer detection, and biopsies are usually carried out a definitive diagnosis on tissues of abnormality. The accuracy (rate of true outcomes to population) of the most commonly used imaging tools, such as X-rays (including X-ray CT, mammography et al.), MRI and Ultrasound, are still limited making them poorly suited for prognosis (Center, et al., 2011), although they can assist diagnosis. The cost and safety issues still prevent them from being used for screening (Wall, et al., 2006; Penfield &

Reilly, 2007). There is much unmet need still for low-cost, accurate early-stage prognostic / diagnostic tools.

Previous research found that the difference in bioimpedance between malignant and benign tissues is pronounced in the beta-dispersion band (100kHz-100MHz) (Surowiec, et al., 1988; Gabriel, et al., 1996). This phenomenon is the foundation for EIT instruments, and it has been exploited in commercial electrical impedance spectroscopy tools used in clinical trials for cervical intraepithelial neoplasia diagnosis (Tidy, et al., 2013). However, all currently available EIT instruments suffer from ill-posedness, making them sensitive to measurement noise and modelling errors (Holder, 2005). The quasi-static approximation techniques widely applied in the EIT society are not able to cover this frequency band (Soni, et al., 2006). Moreover, traditional EIT instruments require front-end circuits to have gigantic input and output impedances (Guermandi, et al., 2015), making it impossible achieve reliable imaging construction at such high frequencies. Furthermore, traditional EIT instruments use wet electrodes to physically contact with patients and therefore are prone to artefacts, greatly degrading their performances.

The research of this thesis tackled the modelling errors and front-end circuits for extending the operating frequency of EIT instruments. Moreover, 3-D full-Maxwell models for high-frequency operations without making any quasi-static assumption has been proposed. Most recent results suggest that the full-Maxwell model shows better performances against ill-posedness than the traditional EIT solutions.

With the previous work done in this thesis, the complexity of EIT system design can be greatly reduced by considering realistic instrumental effects. The full-Maxwell EIT algorithms allow robust reconstruction of the admittivity in the beta-dispersion band and therefore promise a potential non-invasive early stage diagnostic tool.

A new project, to develop a low-cost contact-free EIT instrument (denoted Electro-Magnetic Tomography, EMT, hereafter) that can well cover the beta-dispersion band and provide robust imaging reconstruction, has been established with the following objectives:

- Develop contact-free EMT front-end transceivers that allow injecting/receiving signals in the beta-dispersion band.
- Characterise the developed front-end to provide accurate parameters for the proposed full-Maxwell EMT models.

- Use full-Maxwell algorithms to ensure the stability and the well-posedness of inverse problems.

Experiments will be performed on laboratory phantoms and biological samples to verify the accuracy of the modelling and the efficiency of the reconstructions.

The proposed EMT technique probes the sample with electromagnetic fields instead of electrical currents at the beta-dispersion frequencies. It makes full use of the contrast in admittivity between malignant and benign tissues. The reconstructed images do not suffer from the artefacts introduced by the electrode-contacts or modelling errors from the quasi-static approximation. The EMT instrumentation gains benefits from well-developed commercial off-the-shelf electronics and carefully-considered theoretical modelling. It has a potential to become a non-invasive early stage cancer diagnostic tool.

References

Adler, A. et al., 2009. GREIT: a unified approach to 2D linear EIT reconstruction of lung images. *Physiological Measurement,* 30(6), p. S35–S55.

Adler, A. & Lionheart, W. R. B., 2006. Uses and abuses of EIDORS: an extensible software base for EIT. *Physiological Measurement,* Issue 27, p. 25–42.

Ahn, S. et al., 2010. *Weighted frequency-difference EIT measurement of hemisphere phantom.* s.l., s.n.

Ammari, H. et al., 2008. Electrical Impedance Tomography by Elastic Deformation. *SIAM Journal on Applied Mathematics,* 68(6), pp. 1557-1573.

Bakushinskii, A. B., 1992. The problem of the convergence of the iteratively regularized Gauss-Newton method. *Computational Mathematics and Mathematical Physics,* 32(9), pp. 1353-1359.

Barber, D. C. & Brown, B. H., 1984. Applied potential tomography. *J. Phys. E: Sci. Instrum,* Issue 17, pp. 723-733.

Barton, M. L. & Cendes, Z. J., 1987. New vector finite elements for three-dimensional magnetic field computation. *Journal of Applied Physics,* 61(8), pp. 3919-3921.

Bayford, R., 2006. Bioimpedance Tomography (Electrical Impedance Tomography). *The Annual Review of Biomedical Engineering,* Volume 8, p. 63–91.

Bayford, R., Hanquan, Y., Boone, K. & Holder, D. S., 1995. Experimental validation of a novel reconstruction algorithm for electrical impedance tomography based on backprojection of Lagrange multipliers. *Physiological Measurement,* 16(3A), pp. A237-A247.

Birgül, Ö., Eyüboğlu, B. M. & Ider, Y. Z., 2003. Experimental results for 2D magnetic resonance electrical impedance tomography (MR-EIT) using magnetic flux density in one direction. *Physics in Medicine and Biology,* 48(21), pp. 3485-3504.

Bíró, O., 1999. Edge element formulations of eddy current problems. *Computer Methods in Applied Mechanics and Engineering,* 169(3,4), pp. 391-405.

Boone, K. G. & Holder, D. S., 1996. Current approaches to analogue instrumentation design in electrical impedance tomography. *Physiological Measurement,* 17(4), p. 229–247.

Borsic, A., 2002. *Regularisation Methods for Imaging from Electrical Measurements.* PhD Thesis ed. Oxford, UK: Oxford Brookes University.

Borsic, A., Lionheart, W. & McLeod, C., 2002. Generation of anisotropic-smoothness regularization filters for EIT. *IEEE Transactions on Medical Imaging,* 21(6), pp. 579-587.

Borsic, A., McLeod, C. N. & Lionheart, W. R., 2001. *Total Variation regularisation in EIT Reconstruction.* Hannover, Germany, International Society for Industrial Process Tomography.

Boyle, A. & Adler, A., 2010. Electrode models under shape deformation in Electrical Impedance Tomography. *Journal of Physics: Conference Series,* 224(1).

Boyle, A. & Adler, A., 2011. The impact of electrode area, contact impedance and boundary shape on EIT images. *Physiological Measurement,* Issue 32, p. 745–754.

Boyse, W. E., Lynch, D. R., Paulsen, K. D. & Minerbo, G. N., 1992. Nodal-Based Finite-Element Modeling of Maxwell's Equations. *IEEE Transactions on Antennas and Propagation,* 40(6), pp. 642-651.

Boyse, W. E. & Paulsen, K. D., 1997. Accurate Solutions of Maxwell's Equations Around PEC Corners and Highly Curved Surfaces Using Nodal Finite Elements. *IEEE Transactions on Antennas and Propagation,* 45(12), pp. 1758-1767.

Breckon, W. R. & Pidcock, M. K., 1988. Data errors and reconstruction algorithms in electrical impedance tomography. *Clinical Physics and Physiological Measurement,* 9(4A), pp. 105-109.

Breckon, W. R. & Pidcock, M. K., 1988. Some Mathematical Aspects of Electrical Impedance Tomography. *Mathematics and Computer Science in Medical Imaging NATO ASI Series,* Volume 39, pp. 351-362.

Brown, B. H. & Seagar, A. D., 1987. The Sheffield data collection system. *Clinical Physics and Physiological Measurement,* 8(4A), pp. 91-97.

Calderon, A. P., 1980. *On an Inverse Boundary Value Problem.* Rio de Janeiro, Sociedade Brasileira de Matematica.

Center, M., Siegel, R. & Jemal, A., 2011. *Global cancer facts & figures 2nd Edition,* Atlanta, Georgia: American Cancer Society.

Cheney, M., Isaacson, D. & Newell, J. C., 1999. Electrical impedance tomography. *SIAM Review,* Issue 41, pp. 85-101.

Cheney, M. et al., 1990. NOSER: An algorithm for solving the inverse conductivity problem. *International Journal of Imaging Systems and Technology,* 2(2), pp. 66-75.

Cheng, K. S., Isaacson, D., Newell, J. C. & Gisser, D. G., 1989. Electrode models for electric current computed tomography. *IEEE Transactions on Biomedical Engineering,* pp. 918-924.

Chung, E. T., Chan, T. F. & Tai, X.-C., 2005. Electrical impedance tomography using level set representation and total variational regularization. *Journal of Computational Physics,* 205(1), p. 357–372.

Claasen, T. & Jongepier, A., 1981. Model for the Power Spectral Density of Quantization Noise. *IEEE Transactions on Acoustics, Speech and Signal Processing,* 29(4), pp. 914 - 917.

Daily, W., Ramirez, A., Binley, A. & LeBrecque, D., 2004. Electrical Resistance Tomography. *The Leading Edge,* 23(5), pp. 438-442.

Dai, T., Soleimani, M. & Adler, A., 2008. EIT image reconstruction with four dimensional regularization. *Medical & Biological Engineering & Computing,* 46(9), pp. 889-899.

Davies, B., Fernandez, F. & Philippou, G., 1982. Finite Element Analysis of All Modes in Cavities with Circular Symmetry. *IEEE Transactions on Microwave Theory and Techniques,* 30(11), pp. 1975-1980.

Denyer, C. W., Lidgey, F. J., Zhu, Q. S. & McLeod, C. N., 1994. A high output impedance current source. *Physiological Measurement,* 15(2A), pp. A79-A82.

Devaney, A. J., 1983. A Computer Simulation Study of Diffraction Tomography. *IEEE Transactions on Biomedical Engineering,* BME-30(7), pp. 377-386.

Dobson, D. C. & Santosa, F., 1994. An image-enhancement technique for electrical impedance tomography. *Inverse Problems,* 10(2), pp. 317-334.

Dorn, O., Bertete-Aguirre, H., Berryman, J. G. & Papanicolaou, G. C., 1999. A nonlinear inversion method for 3D electromagnetic imaging using adjoint fields. *Inverse Problems,* 15(6), pp. 1523-1558.

Dutta, M., Rakshit, A. & Bhattacharyya, S. N., 2001. Development and study of an automatic AC bridge for impedance measurement. *IEEE Transactions on Instrumentation and Measurement,* 50(5), pp. 1048-1052.

Dyck, D., Lowther, D. & Freeman, E., 1994. A method of computing the sensitivity of electromagnetic quantities to changes in materials and sources. *IEEE Transactions on Magnetics,* 30(5), pp. 3415-3418.

Eisenberg, M. A. & Malvern, L. E., 1973. On finite element integration in natural co-ordinates. *International Journal for Numerical Methods in Engineering,* 7(4), pp. 574-575.

Firoozabadi, R. & Miller, E. L., 2010 . *Finite Element Modeling of Electromagnetic Scattering for Microwave Breast Cancer Detection.* Boston, s.n.

Flores, M. G. C., Negreiros, M., Carro, L. & Susin, A. A., 2004. INL and DNL estimation based on noise for ADC test. *IEEE Transactions on Instrumentation and Measurement,* 53(5), pp. 1391-1395.

Flores-Tapia, D., O'Halloran, M. & Pistorius, S., 2011. A BIMODAL RECONSTRUCTION METHOD FOR BREAST CANCER IMAGING. *Progress In Electromagnetics Research,* 118(1), pp. 461-486.

Fu, J., Hou, C. & Zhao, Z., 2012. MIMO-OFDM scheme using ApFFT over 3GPP SCM channels. *Transactions of Tianjin University,* 18(2), pp. 128-134.

Gabriel, C., Gabriel, S. & Corthout, E., 1996. The dielectric properties of biological tissues: I. Literature. *Physics in Medicine and Biology,* 41(11), pp. 2231-2249.

Gisser, D. G., Isaacson, D. & Newell, J. C., 1990. Electric Current Computed Tomography and Eigenvalues. *SIAM Journal on Applied Mathematics,* 50(6), pp. 1623-1634.

Griffiths, D. J., 1998. *Introduction to Electrodynamics.* 3rd ed. Upper Saddle River: Pearson Education (US).

Griffiths, H., 2001. Magnetic induction tomography. *MEASUREMENT SCIENCE AND TECHNOLOGY,* Volume 12, pp. 1126-1131.

Griffiths, H., Stewart, W. R. & Gough, W., 1999. Magnetic Induction Tomography: A Measuring System for Biological Tissues. *Annals of the New York Academy of Sciences,* 873(1), pp. 335-345.

Grimnes, S. & Martinsen, O., 2008. *Bioimpedance and Bioelectricity Basics.* Oxford, UK: Elsevier Ltd.

Guermandi, M., Cardu, R., Franchi Scarselli, E. & Guerrieri, R., 2015. Active Electrode IC for EEG and Electrical Impedance Tomography With Continuous Monitoring of Contact Impedance. *IEEE Trans Biomed Circuits Syst.,* 9(1), pp. 21-33.

Halter, R., Hartov, A. & Paulsen, K. D., 2004. Design and implementation of a high frequency electrical impedance tomography system. *Physiological Measurement,* Issue 25, p. 379–390.

Halter, R. J., Hartov, A. & Paulsen, K. D., 2008. A Broadband High-Frequency Electrical Impedance Tomography System for Breast Imaging. *IEEE Transactions on Biomedical Engineering,* 55(2), pp. 650-659.

Harrach, B., Seo, J. K. & Woo, E. J., 2010. Factorization Method and Its Physical Justification in Frequency-Difference Electrical Impedance Tomography. *IEEE Transactions on Medical Imaging,* 29(11), p. 1918.

Harrington, R. F., 1961. *Time-Harmonic Electromagnetic Fields.* New York: McGraw-Hill.

Hartinger, A. E., Gagnon, H. & Guardo, R., 2006. A method for modelling and optimizing an electrical impedance tomography system. *Physiological Measurement,* Volume 27, pp. 51-64.

Hartinger, A. E., Gagnon, H. & Guardo, R., 2007. Accounting for hardware imperfections in EIT image reconstruction algorithms. *Physiological Measurement,* Volume 28, pp. 13-27.

Hasanov, K. F., Ma, A. W., Nachman, A. I. & Joy, M. L., 2008. Current density impedance imaging. *IEEE Transactions on Medical Imaging,* 27(9), pp. 1301-1309.

Hayt, W., Kemmerly, J. & Durbin, S., 2011. *Engineering Circuit Analysis.* 8 ed. s.l.:McGraw-Hill Companies.

Henderson, R. P. & Webster, J. G., 1978. An Impedance Camera for Spatially Specific Measurements of the Thorax. *IEEE Transactions on Biomedical Engineering,* 25(3), pp. 250-254.

Herman, G. T., 2009. *Fundamentals of computerized tomography: Image reconstruction from projection.* 2nd ed. s.l.:Springe.

Holder, D., 2005. *Electrical Impedance Tomography: Methods, History and Applications.* Bristol: Institute of Physics Publishing.

IEEE-SA Standards Board, 2000. IEEE Standard for Terminology and Test Methods for Analog-to-Digital Converters. *IEEE Std 1241-2000,* 1(12), pp. 1-98.

Iniewski, K., 2008. *Wireless Technologies: Circuits, Systems, and Devices.* 1st ed. London: CRC Press, Taylor & Francis Group.

Isaacson, D., 1986. Distinguishability of Conductivities by Electric Current Computed Tomography. *IEEE Transactions on Medical Imaging,* 5(2), pp. 91-95.

Isaacson, D., Mueller, J., Newell, J. & Siltanen, S., 2004. Reconstructions of Chest Phantoms by the D-Bar Method for Electrical Impedance Tomography. *IEEE Transactions on Medical Imaging,* 23(7), pp. 821-828.

Jackson, J. D., 2002. From Lorenz to Coulomb and other explicit gauge transformations. *American Journal of Physics,* 70(9), pp. 917-928.

Jackson, V. P., Hendrick, R. E., Feig, S. A. & Kopans, D. B., 1993. Imaging of the radiographically dense breast. *Radiology,* 188(2), pp. 297-301.

Jerri, A. J., 1977. The Shannon sampling theorem—Its various extensions and applications: A tutorial review. *Proceedings of the IEEE,* 65(11), pp. 1565-1596.

Jin, B., Khan, T. & Maass, P., 2012. A reconstruction algorithm for electrical impedance tomography. *INTERNATIONAL JOURNAL FOR NUMERICAL METHODS IN ENGINEERING,* 89(3), p. 337–353.

Jones, P. W. & Smith, P., 2010. *Stochastic Processes: An Introduction.* 2nd ed. London, UK: CRC Press.

Jun, S. C. et al., 2009. Frequency-difference EIT (fdEIT) using weighted difference and equivalent homogeneous admittivity: validation by simulation and tank experiment. *Physiological Measurement,* p. 1087–1099.

Kaipio, J. P., Kolehmainen, V., Somersalo, E. & Vauhkonen, M., 2000. Statistical inversion and Monte Carlo sampling methods in electrical impedance tomography. *Inverse Problems,* 16(5), p. 1487–1522.

Kaipio, J. P., Kolehmainen, V., Vauhkonen, M. & Somersalo, E., 1999. Inverse problems with structural prior information. *Inverse Problems,* 15(3), pp. 713-729.

Kaltenbacher, B., Neubauer, A. & Scherzer, O., 2008. *Iterative regularization methods for nonlinear ill-posed problems.* s.l.:Berlin : Walter de Gruyter & Co.

Khang, H. S. et al., 2002. J-substitution algorithm in magnetic resonance electrical impedance tomography (MREIT): phantom experiments for static resistivity images. *IEEE Transactions on Medical Imaging,* 21(6), pp. 695-702.

Kohn, R. V. & Vogelius, M., 1985. Determining conductivity by boundary measurements II. Interior results. *Communications on Pure and Applied Mathematics,* 38(5), p. 643–667.

Kolehmainen, V., Vauhkonen, M., Karjalainen, P. A. & Kaipio, J. P., 1997. Assessment of errors in static electrical impedance tomography with adjacent and trigonometric current patterns. *Physiological Measurement,* 18(4), pp. 289-303.

Korjenevsky, A., Cherepenin, V. & Sapetsky, S., 2000. Magnetic induction tomography: experimental realization. *Physiological Measurement,* 21(1), p. 89–94.

Kwon, O., Lee, J.-Y. & Yoon, J.-R., 2002. Equipotential line method for magnetic resonance electrical impedance tomography. *Inverse Problems,* 18(4), pp. 1089-1100.

Kwon, O., Woo, E. J., Yoon, J.-R. & Seo, J. K., 2002. Magnetic resonance electrical impedance tomography (MREIT): simulation study of J-substitution algorithm. *IEEE Transactions on Biomedical Engineering,* 49(2), pp. 160-167.

Larsson, J., 2007. Electromagnetics from a quasistatic perspective. *Am. J. Phys.,* 75(3), pp. 230-239.

Lazebnik, M. et al., 2007. A large-scale study of the ultrawideband microwave dielectric properties of normal, benign and malignant breast tissues obtained from cancer surgeries. *Physics in Medicine and Biology,* 52(20), pp. 6093-6115.

Li, N., 2014. *DEVELOPMENT OF A REAL-TIME CELLULAR IMPEDANCE ANALYSIS SYSTEM.* PhD Thesis ed. Brighton: University of Sussex.

Li, N. et al., 2013. A high-speed bioelectrical impedance spectroscopy system based on the digital auto-balancing bridge method. *Measurement Science and Technology,* 24(6), p. 065701.

Lionheart, W. R. B., 2004. EIT reconstruction algorithms: pitfalls, challenges and recent developments. *Physiological Measurement,* Issue 25, p. 125–142.

Lynch, D. R. & Paulsen, K. D., 1991. Origin of Vector Parasites in Numerical Maxwell Solutions. *IEEE Transactions on Microwave Theory and Techniques,* 39(3), pp. 383-394.

Marquardt, D. W., 1963. An Algorithm for Least-Squares Estimation of Nonlinear Parameters. *Journal of the Society for Industrial and Applied Mathematics,* 11(2), pp. 431-441.

McEwan, A., Cusick, G. & Holder, D. S., 2007. A review of errors in multi-frequency EIT instrumentation. *Physiological Measurement,* 28(7), p. S197–S215.

McEwan, A. et al., 2006. Design and calibration of a compact multi-frequency EIT system for acute stroke imaging. *Physiological Measurement,* 27(5), pp. 199-210.

Meaney, P. M. et al., 2000. A Clinical Prototype for Active Microwave Imaging of the Breast. *IEEE Transactions on Microwave Theory and Techniques,* 48(11), pp. 1841-1853.

Meaney, P. M., Paulsen, K. D. & Chang, J. T., 1998. Near-field microwave imaging of biologically-based materials using a monopole transceiver system. *IEEE Transactions on Microwave Theory and Techniques,* 46(1), pp. 31 - 45.

Meeson, S., 1997. *An investigation of optimal performance criteria in Electrical Impedance Tomography.* PhD Thesis ed. Southampton, UK: University of Southampton.

Merwa, R., Hollaus, K., Brandstätter, B. & Scharfetter, H., 2003. Numerical solution of the general 3D eddy current problem for magnetic induction tomography (spectroscopy). *Physiological Measurement,* 24(2), p. 545–554.

Merwa, R., Hollaus, K., Brunner, P. & Scharfetter, H., 2005. Solution of the inverse problem of magnetic induction tomography (MIT). *Physiological Measurement,* 26(2), pp. S241-S250.

Metherall, P., Barber, D. C., Smallwood, R. H. & Brown, B. H., 1996. Three-dimensional electrical impedance tomography. *Nature,* Issue 380, pp. 509-512.

Mirtaheri, P., Grimnes, S. & Martinsen, O. G., 2005. Electrode Polarization Impedance in Weak NaCl Aqueous Solutions. *IEEE Transactions on Biomedical Engineering,* 52(12), pp. 2093-2099.

Moré, J. J., 1978. The Levenberg-Marquardt algorithm: Implementation and theory. *Numerical Analysis,* Volume 630, pp. 105-116.

Morucci, J. P. et al., 1995. 3D reconstruction in electrical impedance imaging using a direct sensitivity matrix approach. *Physiological Measurement,* 16(3A), pp. A123-A128.

Mueller, J. L., Siltanen, S. & Isaacson, D., 2002. A direct reconstruction algorithm for electrical impedance tomography. *IEEE Transactions on Medical Imaging,* 21(6), pp. 555-559.

Murai, T. & Kagawa, Y., 1985. Electrical Impedance Computed Tomography Based on a Finite Element Model. *IEEE Transactions on Biomedical Engineering,* BME-32(3), pp. 177-184.

Nissinen, A., Kolehmainen, V. & Kaipio, J., 2011. Compensation of Modelling Errors Due to Unknown Domain Boundary in Electrical Impedance Tomography. *IEEE Transactions on Medical Imaging,* 30(2), pp. 231-242.

Oh, T. I. et al., 2007. Calibration methods for a multi-channel multi-frequency EIT system. *Physiological Measurement,* 28(10), p. 1175.

Oh, T. I. et al., 2011. A fully parallel multi-frequency EIT system with flexible electrode configuration: KHU Mark2. *Physiological Measurement,* Issue 32, p. 835–849.

Oh, T. I., Woo, E. J. & Holder, D., 2007. Multi-frequency EIT system with radially symmetric architecture: KHU Mark1. *Physiological Measurement,* Issue 28, p. S183–S196.

Paulsen, K. D., Boyse, W. E. & Lynch, D. R., 1992. Continuous Potential Maxwell Solutions on Nodal-Based Finite Elements. *IEEE Transactions on Antennas and Propagation,* 40(10), pp. 1192-1200.

Penfield, J. G. & Reilly, R. F., 2007. What nephrologists need to know about gadolinium. *Nature Clinical Practice Nephrology,* 3(12), p. 654–68.

Penfield, P., Spence, R. & Duinker, S., 1970. *Tellegen's theorem and electrical networks.* 1 ed. Cambridge, Massachusetts, US: M.I.T. Press.

Peyton, A. J. et al., 1996. An overview of electromagnetic inductance tomography: description of three different systems. *Meas. Sci. Technol.,* 7(3), pp. 261-271.

Platonov, A. A., Jedrzejewski, K., Małkiewicz, Ł. & Jasnos, J., 2006. Principles of optimisation, modelling and testing of intelligent cyclic A/D converters. *Measurement,* 39(3), pp. 213-231.

Polydorides, N. & Lionheart, W. R. B., 2002. A Matlab toolkit for three-dimensional electrical impedance tomography: a contribution to the. *MEASUREMENT SCIENCE AND TECHNOLOGY,* Issue 13, p. 1871–1883.

Rahman, B. M. A. & Davies, B. J., 1984. Penalty Function Improvement of Waveguide Solution by Finite Elements. *IEEE Transactions on Microwave Theory and Techniques,* 32(8), pp. 922-928.

Rao, N. N., 1991. *Elements of Engineering Electromagnetics.* 3rd ed. New Jersey, US: Prentice-Hall, Inc..

Ross, A. S., Saulnier, G. J., Newell, J. C. & Isaacson, D., 2003. Current source design for electrical impedance tomography. *Physiological Measurement,* 24(2), pp. 509-516.

Säbel, M. & Aichinger, H., 1996. Recent developments in breast imaging. *Physics in Medicine and Biology,* 41(3), pp. 315-368.

Sarpeshkar, R., Delbruck, T. & Mead, C., 1993. White noise in MOS transistors and resistors. *IEEE Circuits and Devices Magazine,* 9(6), pp. 23-29.

Saulnier, G. J. et al., 2001. Electrical impedance tomography. *IEEE Sig. Proc. Mag.,* Issue 18, pp. 31-43.

Saulnier, G. J., Ross, A. S. & Liu, N., 2006. A high-precision voltage source for EIT. *Physiological Measurement,* 27(5), pp. 221-236.

Schwan, H., 1957. Electrical properties of tissue and cell suspensions. *Adv Biol Med Phys.,* Volume 5, pp. 147-209.

Scott, G. C., Joy, M. L. G., Armstrong, R. L. & Henkelman, R. M., 1992. Sensitivity of magnetic-resonance current-density imaging. *Journal of Magnetic Resonance,* 97(2), pp. 235-254.

Scott, G., Joy, M., Armstrong, R. & Henkelman, R., 1991. Measurement of nonuniform current density by magnetic resonance. *IEEE Transactions on Medical Imaging,* 10(3), pp. 362-374.

Seagar, A. D., Barber, D. C. & Brown, B. H., 1987. Theoretical limits to sensitivity and resolution in impedance imaging. *Clinical Physics and Physiological Measurement,* 8(4A), pp. 13-31.

Semenov, S., 2009. Microwave tomography: review of the progress towards clinical applications. *Philosophical Transactions A,* 367(1900), pp. 3021-3042.

Semenov, S. Y. et al., 1998. Microwave Tomography: Theoretical and Experimental Investigation of the Iteration Reconstruction Algorithm. *IEEE Transactions on Microwave Theory and Techniques,* 46(2), pp. 133-141.

Senior, T. B. A., 1960. Impedance boundary conditions for imperfectly conducting surfaces. *Applied Scientific Research, Section B,* 8(1), pp. 418-436.

Seo, J. K. et al., 2008. Frequency-difference electrical impedance tomography (fdEIT): algorithm development and feasibility study. *Physiological Measurement,* 29(8), p. 929.

Seo, J. K. & Woo, E. J., 2011. Magnetic Resonance Electrical Impedance Tomography (MREIT). *SIAM Review,* 53(1), pp. 40-68.

Seo, J. K., Yoon, J.-R., Woo, E. J. & Kwon, O., 2003. Reconstruction of conductivity and current density images using only one component of magnetic field measurements. *IEEE Transactions on Biomedical Engineering,* 50(9), pp. 1121-1124.

Sheng, X.-Q. & Song, W., 2012. *Essentials of Comupational Electromagnetics.* Singapore: John Wiley & Sons Singapore Pte..

Shen, L. C. & Kong, J. A., 1995. *Applied Electromagnetism.* 3rd ed. Boston: PWS Publishing Co..

Soleimani, M. & Lionheart, W., 2005. Image Reconstruction in Three-Dimensional Magnetostatic Permeability Tomography. *IEEE Transactions on Magnetics,* 41(4), pp. 1274-1279.

Soleimani, M. et al., 2006. A three-dimensional inverse finite-element method applied to experimental eddy-current imaging data. *IEEE Transactions on Magnetics,* 42(5), pp. 1560-1567.

Somersalo, E., Cheney, M. & Isaacson, D., 1992. Existence and uniqueness for electrode models for electric current computed tomography. *SIAM Journal on Applied Mathematics,* p. 1023 1040.

Somersalo, E., Cheney, M., Isaacson, D. & Isaacson, E., 1991. Layer stripping: a direct numerical method for impedance imaging. *Inverse Problems,* 7(6), pp. 899-926.

Somersalo, E. et al., 1997. *Impedance imaging and Markov chain Monte Carlo methods.* San Diego, CA, SPIE.

Soni, N. K., Paulsen, K. D., Dehghani, H. & Hartov, A., 2006. Finite Element Implementation of Maxwell's Equations for Image Reconstruction in Electrical Impedance Tomography. *IEEE Transactions on Medical Imaging,* 25(1), pp. 55-61.

Souvorov, A. E. et al., 1998. Microwave Tomography: A Two-Dimensional Newton Iterative Scheme. *IEEE Transactions on Microwave Theory and Techniques,* 46(11), pp. 1654-1659.

Strang, G. & Fix, G. J., 1973. *An analysis of the finite element method.* 1st ed. New Jersey, US: Prentice-Hall Englewood Cliffs, NJ.

Stratton, J. A., 1941. *Electromagnetic Theory.* New York: McGraw-Hill.

Surowiec, A., Stuchly, S., Barr, J. & Swarup, A., 1988. Dielectric Properties of Breast Carcinoma and the Surrounding Tissues. *IEEE Transactions on Biomedical Engineering,* 35(4), pp. 257 - 263.

Sylvester, J. & Uhlmann, G., 1987. A Global Uniqueness Theorem for an Inverse Boundary Value Problem. *Annals of Mathematics,* 125(1), pp. 153-169.

Tang, M. et al., 2002. The number of electrodes and basis functions in EIT image reconstruction. *Physiological Measurement,* 23(1), p. 129–140.

Tidy, J. A. et al., 2013. Accuracy of detection of high-grade cervical intraepithelial neoplasia using electrical impedance spectroscopy with colposcopy. *An International Journal of Obstetrics & Gynaecology,* 120(4), pp. 400-411.

Torre, L., Siegel, R. & Jemal, A., 2012. *Global cancer facts & figures 3rd Edition,* Atlanta, Georgia: American Cancer Society.

Van Bladel, J., 1964. *Electromagnetic Fields.* Revised printing by Hemisphere Publishing, New York, 1985 ed. New York: McGraw-Hill.

Vasilescu, G., 2006. *Electronic Noise and Interfering Signals.* 2nd ed. Berlin : Springer.

Vauhkonen, M., Kaipio, J. P., Somersalo, E. & Karjalainen, P. A., 1997. Electrical impedance tomography with basis constraints. *Inverse Problems,* 13(2), p. 523–530.

Vauhkonen, M. et al., 1998. Tikhonov Regularization and Prior Information in Electrical Impedance Tomography. *IEEE Transactions on Medical Imaging,* 17(2), pp. 285-293.

Vauhkonen, P. J., Vauhkonen, M., Savolainen, T. & Kaipio, J. P., 1999. Three-dimensional electrical impedance tomography based on the complete electrode model. *IEEE Transactions on Biomedical Engineering,* Issue 46, pp. 1150-1160.

Wall, B. F. et al., 2006. What are the risks from medical X-rays and other low dose radiation?. *The British Journal of Radiology,* 79(940), pp. 285-294.

Wangsness, R. K., 1986. *Electromagnetic Fields.* 2nd Edition ed. Chichester: John Wiley & sons.

Webster, G. J., 1990. *Electrical Impedance Tomography.* Bristol, UK: Adam Hilger.

Westgard, J. B., 1997. *Electrodynamics: A Concise Introduction.* New York: Springer-Verlag New York, Inc..

Wexler, A., 1988. Electrical impedance imaging in two and three dimensions. *Clinical Physics and Physiological Measurement,* 9(4A), pp. 29-33.

Wheeler, H., 1964. Transmission-line properties of parallel wide strips by a conformal-mapping approximation. *IEEE Transactions on Microwave Theory and Techniques,* 12(3), pp. 280-289.

Widrow, B. & István, K., 2008. Spectrum of Quantization Noise and Conditions of Whiteness. In: *Quantization Noise.* Cambridge: Cambridge University Press, pp. 529-562.

Woo, E., Hua, P., Webster, J. & Tompkins, W. J., 1993. A robust image reconstruction algorithm and its parallel implementation in electrical impedance tomography. *IEEE Transactions on Medical Imaging,* 12(2), pp. 137-146.

Yang, W. Q. & Peng, L., 2003. Image reconstruction algorithms for electrical capacitance tomography. *Measurement Science and Technology,* 14(1), p. R1.

Yorkey, T., 1986. *Comparing reconstruction algorithms for electrical impedance tomography.* PhD Thesis ed. Madison, US: University of Wisconsin and madison.

Yorkey, T. J., Webster, J. & Tompkins, W. J., 1987. Comparing Reconstruction Algorithms for Electrical Impedance Tomography. *IEEE Transactions on Biomedical Engineering,* BME-34(11), pp. 843-852.

Yu, Z. et al., 1993. Imaging system based on electromagnetic tomography (EMT). *Electronics Letters,* 29(7), pp. 625-626.

Zhang, W. & Li, D., 2014. An instrumental electrode model for solving EIT forward problems. *Physiological Measurement,* 35(10), pp. 2001-2026.